# *Contributions in the design and research of air-hydro-mechanic equipment of actuation and force*

-HABILITATION THESIS-

*Associate Professor Dr. Ing.* ***Daniel Cătălin STROIȚĂ***

***Timișoara 2025***

# Content

# Rezumat

Prezenta teză de abilitare este structurată pe **3** capitole:

**- Capitolul I. Retrospectiva realizărilor profesionale din momentul obținerii titlului de doctor și până în prezent (studii în domeniul hidrodinamicii);**

**- Capitolul II. Rezultatele activității de cercetare din domeniul acționărilor hidraulice și al identificării dinamice a sistemelor de acționare a turbinelor de vânt, proiectarea și punerea în funcțiune a Standului de încercare a echipamentelor hidraulice**;

**- Capitolul III. Planul de dezvoltare a carierei profesionale și academice.**

## Capitolul I. Retrospectiva realizărilor profesionale din momentul obținerii titlului de doctor și până în prezent

Acest capitol prezintă activitatea mea profesională și academică de după susținerea tezei de doctorat. În anul 2009 am susținut teza de doctorat intitulată ***Identificarea dinamică a turbinelor cu dublu flux***, în cadrul Facultății de Mecanică a Universității Politehnica din Timișoara, sub conducerea ilustrului *Prof.Dr.Ing.**Mircea Bărglăzan***, obținând titlul de Doctor în domeniul **Inginerie Mecanică**, în baza Ordinului Ministrului Educației, Cercetării și Tineretului numărul 4698 din 14.08.2009.

Din anul 2009 până în anul 2012 am activat ca Asistent Universitar la Catedra de Mașini Hidraulice a Facultății de Mecanică, unde am predat partea aplicativă (laborator, seminar și proiect ) la diverse discipline de specialitate.

Din anul 2012 până în 2017 am lucrat în domeniul de proiectare al instalațiilor de manipulare a țevilor de foraj marin, la National Oilwell Varco, în Kristiansand, Norvegia, unde, pe deoparte am putut utiliza noțiunile teoretice și practice învățate în cadrul facultății, iar pe de altă parte am acumulat noi cunoștințe în utilizarea servomecanismelor electro hidraulice de ultimă generație.

În anul 2017 am revenit la Facultatea de Mecanică și până în prezent activez în cadrul departamentului de *Mașini Mecanice Utilaje și Transporturi* unde am parcurs toate etapele didactice: 2017-2020 Asistent Universitar, 2020-2024 Șef de Lucrări, 2024 până în prezent Conferențiar Universitar.

Din momentul întoarcerii din Norvegia am pus în funcțiune 2 standuri de acționări hidraulice și pneumatice realizând în același timp și un îndrumător de laborator pentru studenții și masteranzii specializărilor la care predau, am fost membru în colectivul de proiectare și realizare a standului de testare a aparaturii hidraulice din

Laboratorul de Acționări Hidraulice și Pneumatice și am coordonat studenți și masteranzi la elaborarea lucrărilor de diplomă și disertație.
În tot acest timp am publicat ca prim autor/coordonator și coautor un număr de 4 cărți de specialitate din domeniul disciplinelor predate, 2 îndrumătoare de laborator și am fost membru în echipa de cercetare în cadrul a 16 Contracte de cercetare naționale și internaționale. De asemenea am publicat un număr de 39 lucrări, 12 ISI (5 cu factor de impact, 4 ca prim autor/autor corespondent), 4 BDI, 23 în reviste naționale și internaționale.

**- Capitolul II. Rezultatele activității de cercetare din domeniul identificării dinamice a sistemelor de acționare hidraulică a mecanismului de reglare a paletelor turbinelor de vânt, precum și a proiectării/punerii în funcțiune a Standului de încercare a echipamentului hidraulic**
Acest capitol reprezintă de fapt o continuare a studiului abordat în teza de doctorat, identificarea dinamică experimentală, însă aplicată în domeniul acționărilor hidraulice și mai concret pe un sistem hidraulic care reglează paletele unei turbine eoliene. În acest capitol sunt prezentate metodele utilizate în identificarea dinamică experimentală, standul experimental, precum și aparatura de măsură utilizată. Scopul acestei cercetări îl constituie determinarea funcțiilor de transfer, precum și determinarea a caracteristicilor de frecvență, pe baza diverselor criterii din domeniul automatizărilor.

**- Capitolul III. Planul de dezvoltare a carierei profesionale și academice**
În acest capitol voi prezenta un plan de dezvoltare a activității profesionale din punct de vedere al disciplinelor predate adaptat la cerințele pieței actuale, în formarea viitorilor doctori ai specializării noastre și un plan al integrării acestora precum și al studenților și masteranzilor în diversele obiective de cercetare din domeniul acționărilor hidraulice și al hidrodinamicii.

## Summary

This thesis is structured in 3 chapters:
**- Chapter I. Retrospective of professional achievements from the moment of obtaining the doctorate until now (studies in the field of hydrodynamics);**
**- Chapter II. The results of the research activity in the field of dynamic identification of wind turbine pitch drive systems and the design and setup of the Hydraulic equipment testing stand;**
**- Chapter III. Professional and academic career development plan.**

**Chapter I. Retrospective of professional achievements from the moment of obtaining the PhD. degree until present**

This chapter presents my professional and academic experience after defending my doctoral thesis. In 2009, I defended my doctoral thesis entitled ***Dynamic identification of double-flux turbines***, within the Faculty of Mechanics of the Politehnica University of Timișoara, under the coordination of the illustrious *Prof.Dr.Ing.**Mircea Bărglăzan***, obtaining the title of Doctor in the field of Mechanical Engineering, based on the Order of the Minister of Education, Research and Youth number 4698 of 14.08.2009.
From 2009 to 2012, I worked as an Assistant at the Department of Hydraulic Machines of the Faculty of Mechanics, where I taught the applied part (laboratory and seminar) in various specialized disciplines.
From 2012 to 2017, I worked in the design field of marine drilling pipe handling, at National Oilwell Varco, in Kristiansand, Norway, where, on the one hand, I could use the theoretical and practical notions learned in the faculty, and on the other hand I gained new knowledge in the use of ultimate generation electro-hydraulic servomechanisms.
In 2017 I returned to the Faculty of Mechanics and until present I activate in the Department of Mechanical Machinery, Equipment and Transport, where I completed all teaching stages: 2017-2020 University Assistant, 2020-2024 Lecturer, 2024-present Associate Professor.
From the moment of my return from Norway, I put into operation 2 stands of hydraulic and pneumatic drives, at the same time creating a laboratory guide for the students and master students of our specializations and I was a member of the design and realization collective of the test stand of the hydraulic equipment from our Hydraulic and Pneumatic Drives Laboratory.

During all this time I published as first author/coordinator and co-author a number of 4 specialized books in the field of taught subjects, 2 laboratory guides and I was a member of the research team within 16 national and international research contracts. I also published a number of 39 papers 12 ISI (5 with impact factor, 4 as first author/corresponding author), 4 BDI, 23 in national and international journals.

**- Chapter II. The results of the research activity in the field of dynamic identification of wind turbine drive systems**

This chapter actually represents a continuation of the studies done in the doctoral thesis, the experimental dynamic identification, but applied in the field of hydraulic drives and more concretely on a hydraulic system that adjusts the blades of a wind turbine. In this chapter are presented the experimental stand, the measuring equipment used as well as the methods used in the experimental dynamic identification. The purpose of this research is determination of the transfer functions and the frequency characteristics based on various criteria in the field of automation.

**- Chapter III. Professional and academic career development plan**

In this chapter I will present the plan for the development of my professional activity from the point of view of the taught disciplines adapted to the requirements of the current market, in the training of future doctors of our specialization and a plan for their integration as well as the students and master students in the various research objectives in the field of hydrodynamics and hydraulic drives.

# Chapter I. The retrospective of professional achievements from the moment of obtaining the PhD. title until present

This chapter is divided into 3 subchapters:
I.1. The didactic activity
I.2. The work as a design engineer in the field of hydraulic installations for handling marine drill pipes
I.3. The research activity

## I.1. The didactic activity

My teaching activity started in 2006, after obtaining the title of engineer, where together with the acceptance to PhD. studies, as a full-time doctoral student, in addition to the obligation to finish the doctoral thesis in a period of 3 years, I had to teach the applied part at various disciplines belonging to the field of hydraulic and pneumatic drives, fluid mechanics and hydraulic turbomachines. Specifically, I held the application part (laboratory, seminar, project) at the following disciplines:

- *Hydraulic and pneumatic drives;*
- *Hydro-pneumatic actuation and automation systems;*
- *Fluid mechanics and hydraulic machines;*
- *Hydraulics and hydraulic machines;*
- *The thermal and hydro part of the power plants;*
- *Turbomachines;*

In 2009, after completing the doctoral thesis entitled *"Dynamic identification of double-flow turbines"* under the supervision of *Prof.Dr.Ing.* **Mircea Bărglăzan** and obtaining the doctor title, I continued teaching as University Assistant until 2012, when I made the decision to apply the theoretical part learned into practice and got a job at a company which designs and produces hydraulic drive equipment, in Kristiansand, Norway. This part of my work/research will be detailed separately.
In 2017, I returned to the Hydraulic Machinery Collective, of the Department of Mechanical Machinery, Equipment and Transportation, as University Assistant.
Thus, between the years 2017-2020, while I held the position of University Assistant, I put into operation two Festo test stands, one for the hydraulic actuation part and one for the pneumatic one, for the use of students, for which together with my colleagues from the collective conceived and carried out various laboratory works on them.

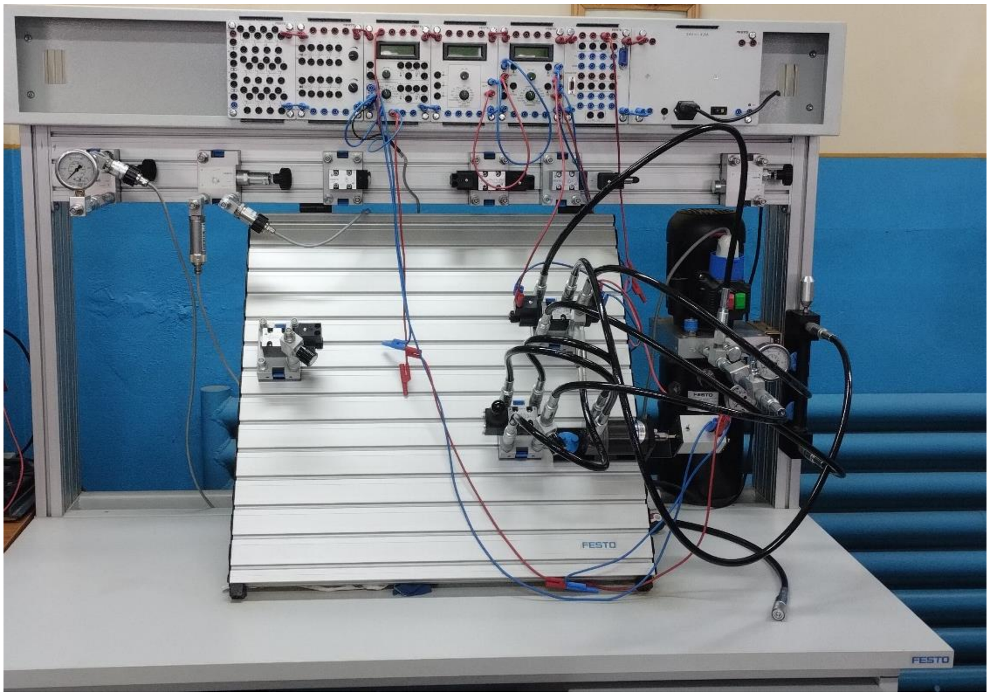


*Fig.1. Festo stand for power acting*

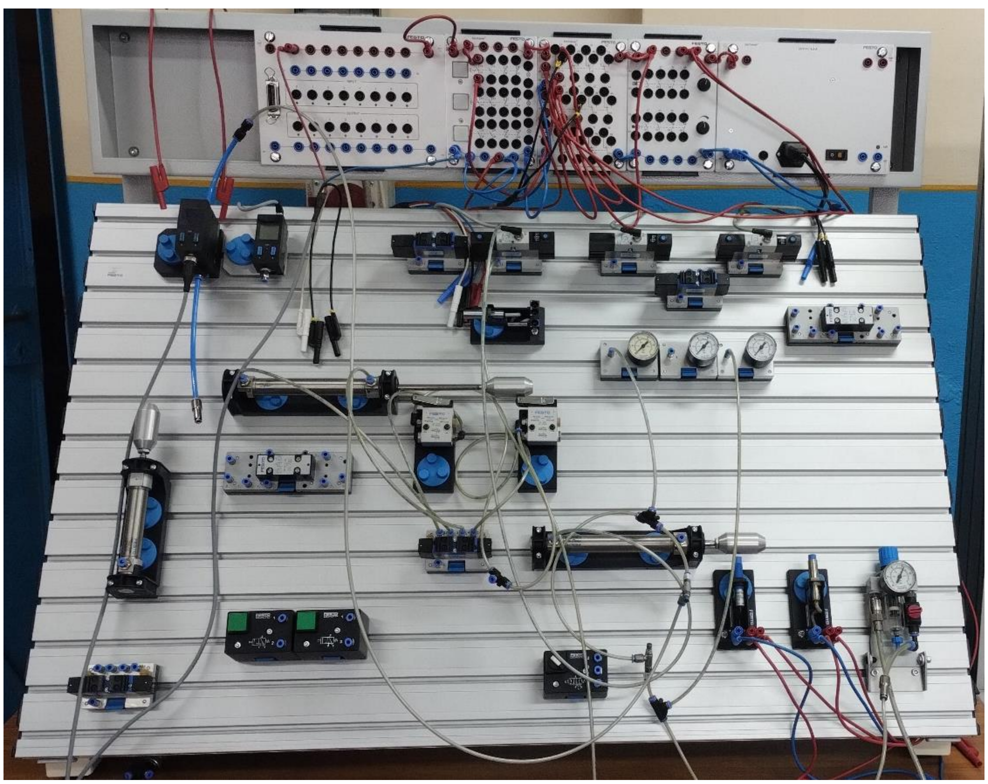

*Fig.2. Festo stand for pneumatics*

During this period, teaching the applied part in various disciplines of Fluid mechanics and hydraulic machines, I published as a co-author in 2019, together with

Mrs. *Conf. Dr. Ing.* **Adriana-Sida Manea**, a guide for the applied part entitled "Hidraulică și mașini hidraulice". Also, in addition to this, together with Mr. *Prof. Dr. Ing.* **Ilare Bordeașu**, I have rethought the laboratory and project part of the discipline entitled *"Sisteme de acționare și automatizare hidropneumatice"* from the *"Hidrodinamica mașinilor și sistemelor hidromecanice"* master, introducing students to the use of proportional electro-hydraulic equipment, as well as Festo Fluid Sim software, received together with the 2 stands.

In 2020, I advanced to the position of Lecturer (Șef de lucrări), occupied until 2024. During this period, I published a number of 4 books in the field of taught disciplines, 3 in printed format and one in electronic format, which can be found on the UPT Virtual Campus, as follows:

- **Daniel Cătălin Stroiță**, *Sisteme de acționare și automatizare hidropneumatice,* format electronic *CV UPT, 2020.*
- Ilare Bordeașu, Cristian Ghera, Cornelia Laura Sălcianu, **Daniel-Cătălin Stroiță**, *Elemente de proiectare și tehnologie de fabricație a reperelor mașinilor și sistemelor hidro-pneumatice*, Ed. Politehnica, 2020;
- Adriana Sida Manea, **Daniel Cătălin Stroiță**, *Hidraulică și mașini hidraulice,* Ed. Politehnica, 2023;

**Daniel Cătălin Stroiță**, Cristian Ghera, *Acționări hidraulice*, Ed. Politehnica, 2023.

Also, together with Mr. *Ș.L.Dr.Ing. Cristian Ghera* and *Ms. Conf.Dr.Ing.Adriana-Sida Manea*, I created a laboratory guide for students and master students from the Faculty of Mechanics, that are studying the discipline of Acționări hidraulice și pneumatice, Daniel Cătălin Stroiță, Cristian Ghera, Adriana Sida Manea, *Acționări hidraulice și pneumatice. Aplicații*, Ed. Politehnica 2023.

From 2024 until now, I hold the position of Associate Professor (Conferentiar). During this period, I continued the publishing activity, coordinating the book, C. Ghera, I Bordeasu, A.N. Luca, L. Salcianu, *Acționări pneumatice*, Ed. Politehnica, 2024, which represents a continuation of the work started in the first book, entitled *Acționări hidraulice.*

All these didactic materials, at the writing of which I participated, both as the first author/coordinator and as a co-author, had the main purpose of bringing the disciplines taught to the level of understanding and assimilation of the engineering concepts by the students, preparing them for the current market requirements.

Throughout this teaching period, I managed several diploma and dissertation projects, from 2022 being a member of the Dissertation Committee of the master entitled *"Hidrodinamica mașinilor și sistemelor hidromecanice"*. Among the students coordinated at the diploma work, one managed to go further in the academic environment, obtaining his Phd. title and even becoming a colleague of ours.

I am also a member of the guidance committee of 2 PhD students.

## I.2. The activity as a design/project engineer in the field of hydraulic installations for handling marine drill pipes

Between 2012-2017, I worked as a hydraulic systems design engineer for marine drill pipe handling equipment, between 2012-2013 as a Design Engineer (being hired by a consultancy company XACT) and from 2013 until 2017 as a Project Engineer for National Oilwell Varco as internal employee.
Due to the confidentiality policy of the company where I worked, I cannot give detailed technical details, only general data about the equipment I was responsible for. In the first phase, I started with relatively simple equipment such as the nacelles used for various repairs called "Service and access baskets" (Fig.3) and hydraulic pipe handling machines called "Catwalks" (Fig.4). Here I made various improvements in terms of their maneuverability by optimizing the hydraulic equipment used.


*Fig.3. Service and access basket [1]*


*Fig.4. Catwalk machine [1]*

Also, during this early period, I was hydraulically responsible for a number of equipment such as DFMA (Fig. 5), Top Drive, etc., working with the vast majority of drill pipe handling equipment produced by NOV

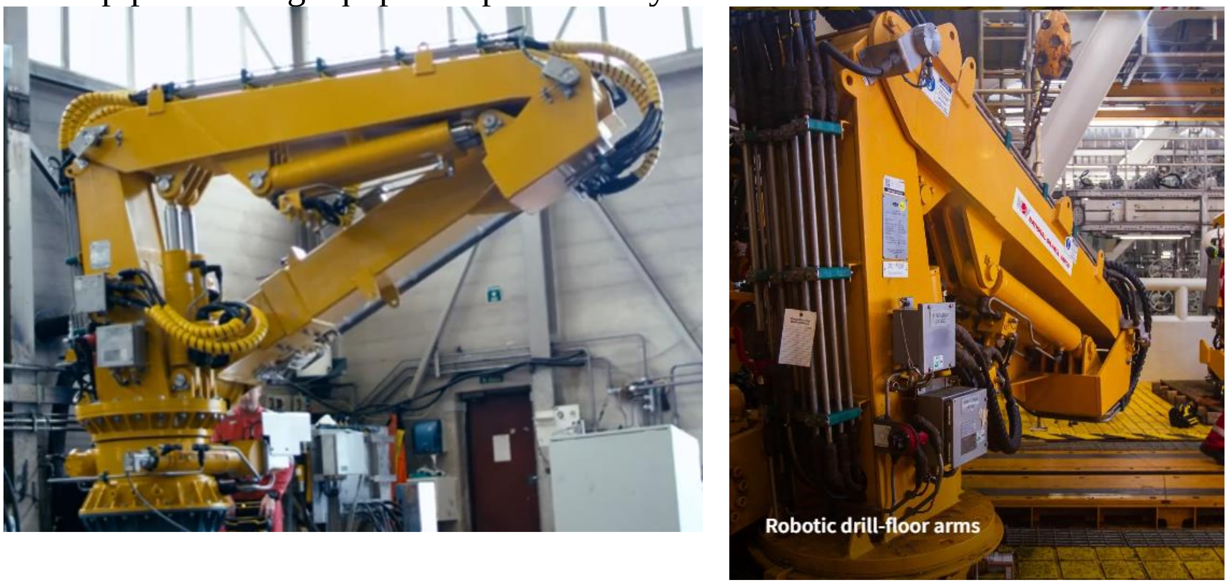


*Fig.5. Drill floor manipulator arm DFMA [1]*


*Fig.6. Top drive [2]*

The most exciting part for me came when I was given the hydraulic design responsibility for the Lifting Rig and Dead Line Compensator (DLC) systems. Here I had the chance to be responsible on the hydraulic side for the most complex system that NOV produces, the power installed in the BOOST system being impressive, in the order of megawatts. The complexity of the hydraulic design of these systems is very high, both from the point of view of the drilling drive system and from the point of view of the wave compensator. Two of these complex systems were designed and built for the Frigstad company (Fig.7, 8) with me in charge of the hydraulic side.

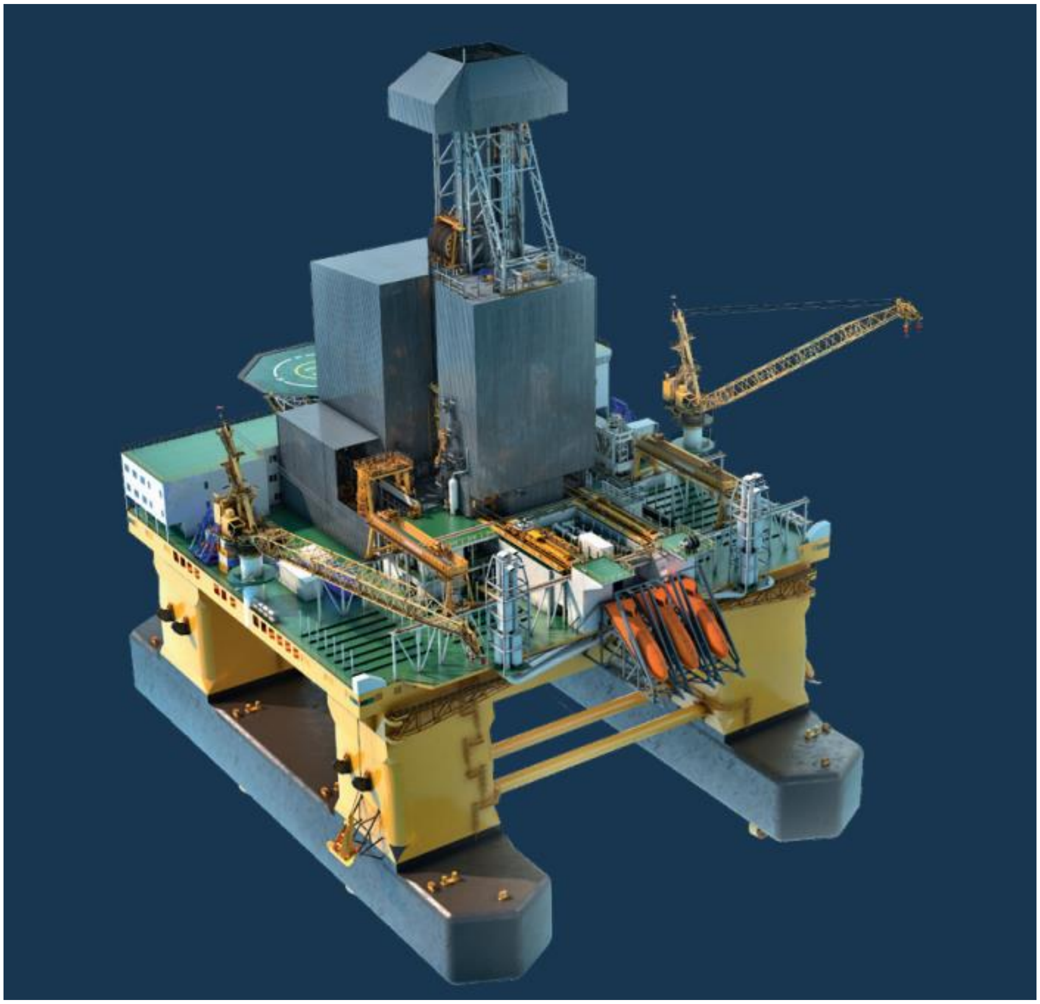

*Fig.7. Frigstad D90 [3]*

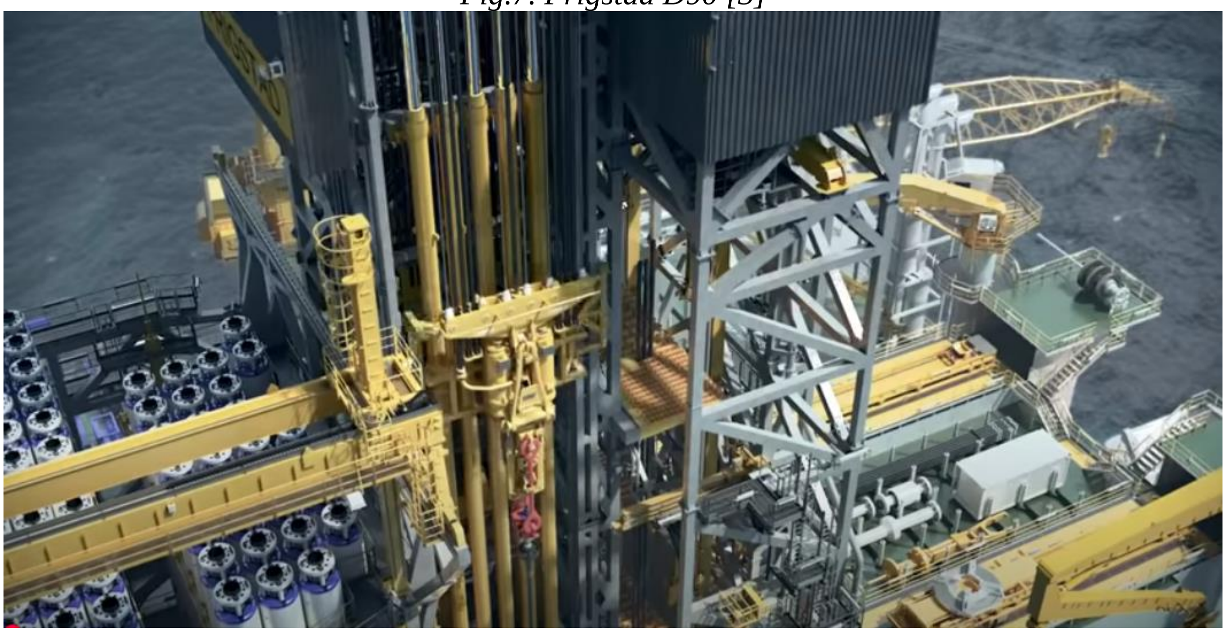

*Fig.8. Frigstad D90, view of Top Drive driving system [4]*

Also, during this time when I worked for the National Oilwell Varco company, I designed the hydraulic, braking and cooling installation for a concept at the time called the Single Layer Winch (Fig.9). One of the key points here was to achieve a braking time in the order of milliseconds for a winch operating several hundred tons.

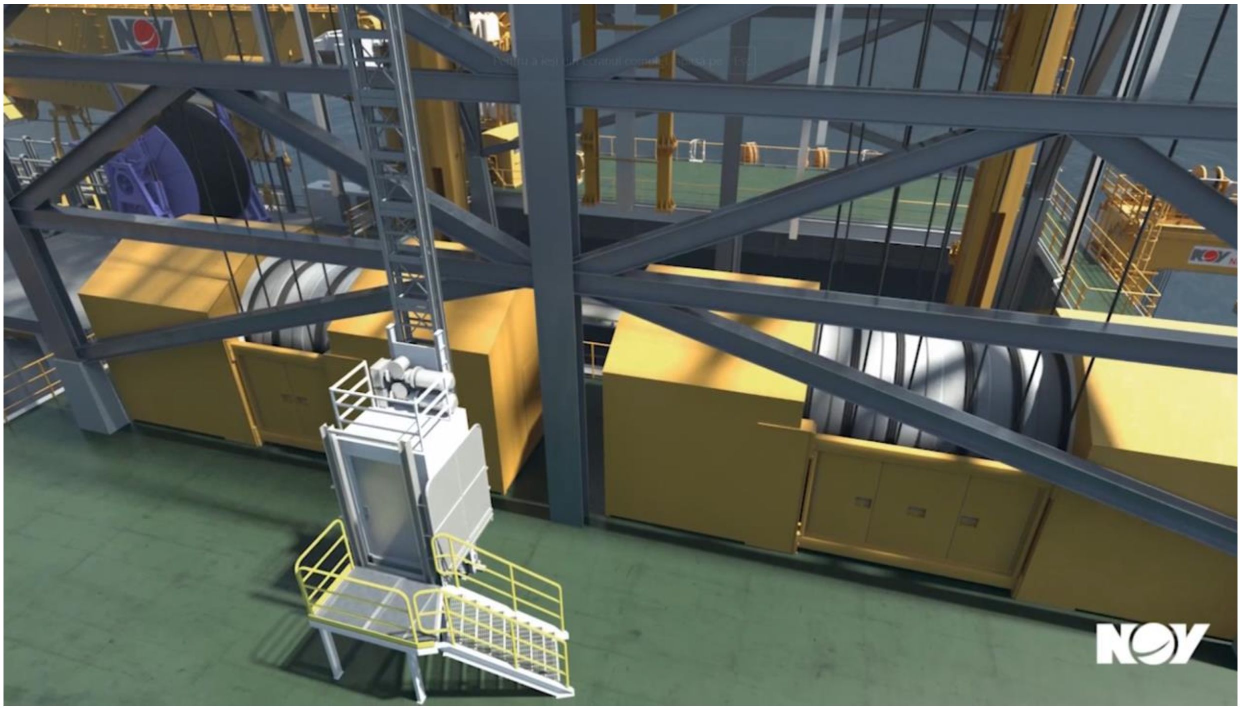

*Fig.9. Single layer winch [2]*

During this period of more than 5 years, working as a design engineer, I had the chance to interact with major manufacturers of hydraulic equipment such as Rexroth, Montan Hydraulic, Fjero, Hydratech (hydraulic cylinders), Parker Hanifin, Hydman Oy, (hydraulic blocks), Brevini (hydraulic equipment and gearboxes) etc.
In the various projects for which I was responsible, I actively participated in the design of new solutions as well as in the improvement of existing ones.
I also attach as a part of this thesis the proof of my work in Norway and the confirmation that my resignation from NOV was voluntary and unconditioned.

XACT

# Work certificate

**Iht. Arbeidsmiljøloven § 15-15**

| | |
|---|---|
| **EMPLOYEE** | |
| **Name:** | Daniel Stroita |
| **Address:** | Fidjeåsen 8F, 4639 Kristiansand S, Norway |
| **Date of birth:** | 280882-23529 |
| **Employed:** | 01.02.2012-31.03.2013 |
| **Info about employer:** | Xact Consultance AS is an actor in technical consulting. We are an engineering and consulting company for the energy and industrial markets. |
| **Info about employee:** | Daniel Stroita had, during this period at Xact, a contract within hydraulic engineering. Daniel was working full time in Kristiansand, Norway, as a hydraulic engineer on an assignment for National Oilwell Varco. Daniel carried out his duties as expected as an Xact consultant towards our customer. |
| **EMPLOYER** | |
| **Name:** | Xact Consultance AS |
| **Contactperson:** | Fredrik Alkenhoff |

Oslo, 01.04.2013

City/date

Signature employer

To whom it may concern

Ref.: 95192747 NO, Kristiansand, 15-Feb-2017

**LETTER OF REFERENCE**

Daniel Catalin Stroita, born 28-Aug-1982, has from 01-Apr-2013 to 31-May-2017 been employed at National Oilwell Varco Norway AS.

At the time of resignation, Daniel Catalin Stroita was employed as Project Engineer, Hydraulics Drilling.

National Oilwell Varco Norway AS is a 100 % owned subsidiary of National Oilwell Varco, a global leading supplier of innovative, high technology systems and solutions for the oil and gas industry.

Daniel Catalin Stroita resigned voluntarily and we wish good luck with future challenges.

National Oilwell Varco Norway AS

Kjell Hammen
Director HR NOV Norway

## I.3. Research activity

Both from the moment of obtaining the doctor title and before, I actively participated as a member in the research groups of various national and international projects of which I mention, only those included after or actually in the year 2009, the year in which I defended my doctoral thesis:

1. *Transmisii hidrodinamice inteligente*, ID929/2008 nr 679/2009 PN II Idei, 2009-2010;
2. *Improvement of the Structures and Efficiency of Small Horizontal Axis Wind Generators with Non-Regulated Blades, Research and Development Group "Wind Turbine and Mechanical Structure"*, RO 0018, 2009-2011;
3. *Deservirea energetica a unei comunitati locale utilizand curentii de aer*, 3416/21-036/2007, 2009-2010;
4. *Optimizarea sistemelor energetice inteligente de transport a apei pt creșterea eficienței energetice și economia de energie*, 1365/21-041/2007, 2009-2010;
5. *Studiul fenomenelor hidrodinamice și de cavitație în sistemele de acționare și automatizare și de forță*, IDEI cod 35/nr. 68, 2009;
6. *Sisteme hidraulice adaptive pentru turbine eoliene de mică putere*, PC 1467 SHATEMP 2-ENERGIE CNMP 21-047, 2009.

Based on the theme of the research projects, but also on studies carried out independently of them, I would divide my research activity in the field of hydrodynamics and turbomachinery into 5 large categories:

**I.3.1. The research in the domain of Hydrodynamic Torque Converters**
**I.3.2. The research in the domain of Hydraulic Turbines**
**I.3.3. The research in the domain of Turbo Pumps and in Water Feeding Networks**
**I.3.4. The research in Wind Turbines domain**
**I.3.5. The research in Cavitation domain**

A good part of the results of these researches have been published both in technical articles and in various reports for the grants in question. As representative papers within this subchapter I would mention:

- **Stroita Daniel Catalin**, Adriana Sida Manea, *Blade Polymeric Material Study of a Cross-Flow Water Turbine Runner*, MATERIALE PLASTICE, ISSN 2537-5741 ISSN-L 0025-5289, Vol 56(2), pag. 366-369, 2019.
- Manea A. S., Muntean S., **Stroiță D.C**, *Analitycal approach and numerical methodology validated against experimental data on S shape airfoil for wide flow angles of attack*, Proceedings of the Romanian Academy Series A -

Mathematics Physics Technical Sciences Information Science/1454-9069, Vol 21/2, 2020

- Manea, AS; Dobanda, E; Barglazan, M; **Stroita, DC**, Two-Phase Flow In Hydrodynamic Torque Converter, Proceedings of The 20th International DAAAM Symposium, DAAAM Int Vienna, 1726-9679, 2009
- Miloş T., Bej, A., Dobândă E., Manea A., Bădărău R., **Stroiţă D**., Blade Design using CAD Technique for Small Power Wind Turbine, IEEE International Joint Conferences on Computational Cybernetics and Technical Informatics ICCC-CONTI 2010, IEEE Catalog Number CFP10575-CDR, ISBN 978-1-4244-7431-8, 27-29 May 2010, Timisoara, Romania, pg,571-575, 2010.
- Miloş T., Dobândă E., Manea A., Bădărău R., **Stroiţă D**., Computational Graph Theory for Find out Optimal Routes of Pipeline Supply, IEEE International Joint Conferences on Computational Cybernetics and Technical Informatics ICCC-CONTI 2010, IEEE Catalog Number CFP10575-CDR, ISBN 978-1-4244-7431-8, 27-29 May 2010, Timisoara, Romania, pg,577-580, 2010
- Danut Tokar, **Catalin Stroita**, Adriana Tokar, Alexandra Rusen, Hybrid System that Integrates the Lost Energy Recovery on the Water-Water Heat Pump Exhaust Circuit, IOP Conf. Series: Materials Science and Engineering 603 (2019) 042002 IOP Publishing doi:10.1088/1757-899X/603/4/042002, 2019
- Tanasa C., Stuparu A., Stroita C., Popescu C., Susan-Resiga R., *3D numerical analysis of pulsating water jet in the draft tube cone of hydraulic machinery*, AIP Conference Proceedings, Vol 2186, Article Number180002, 2019.
- Ilare Bordeasu, Cristian Ghera, Alexandru-Nicolae Luca, Adriana-Sida Manea, **Daniel-Catalin Stroita**, Cornelia Laura Salcianu, Brandusa Ghiban, Lavinia Madalina Micu, *Investigation of Cavitation Resistance of Biocompatible ZincBased Alloys for Biomedical Applications*, KOD 2024.
- Adriana Sida Manea, **Daniel Catalin Stroita**, Ilare Bordeasu, Cristian Ghera, Alexandru Nicolae Luca, *Air-Dynamic Measurements on "S" Shape Hydrofoils*, KOD 2024.
- Cristian Ghera, Iosif Lazăr, Daniela Alexa, Ilare Bordeaşu, Nicuşor Alin Sîrbu, Daniel Ostoia, Mihai Hluscu, Cornelia Laura Salcianu, **Daniel Catalin Stroita**, Dumitru Viorel Bazavan, Marcela Sava, Lavinia Madalina Micu, *New Results Regarding the Cavitation Destruction Behavior of Heat-Treated CuZn39Pb3 Brass with Different Parameters,* Advanced Materials Research, Vol. 1172, Pag. 1-8, 2022.

### I.3.1. The research in the domain of Hydrodynamic Torque Converters [6, 7, 8]

The research in the field of hydrodynamic torque converters began within a national research contract, in the group led by Mr. *Prof.Dr.Ing.* ***Mircea Bărglăzan***, some of the results being published even before the undersigned obtained his doctorate.

Since these researches are not directly related to the subject of the doctoral thesis, I considered it important to present them in this habilitation thesis.

The studies continued in the framework of the second research grant, the collective being led this time by Mrs. *Conf.Dr.Ing. Adriana Sida Manea*.

In the following, I will briefly present the theme of the research in this field and the results obtained. The research was focused on the theoretical and experimental study of the operation of hydrodynamic torque converters, Lysholm-Smith type (consisting of a pump rotor and three stages of turbine rotors that have two stator stages between them), operating with different degrees of filling with two-phase oil-air medium, with the cooling circuit turned off.

The chosen theoretical model allowed us to analyze the behavior of the hydrodynamic torque converter in various operating regimes, both stationary and transient.

The main parameters of the model are:

- pump shaft speed;
- turbine shaft speed;
- the physical parameters of the fluid.

The main stage in the modeling process is the calculation of the kinematics of the elements of the cascade machines, that is, the elements of the velocity triangles. For this purpose, the geometry elements of the hydrodynamic torque converter will be considered as constant and as variable, the speed at the primary shaft and the load at the secondary shaft.

The specific energy transferred to the fluid by the pump is given by (1):

$$H_P = \frac{1}{g}\cdot(u_2\cdot v_{u2} - u_1\cdot v_{u1}) = \frac{r_2\cdot\omega}{g}\cdot\left(r_2\cdot\omega - \frac{Q}{\rho_2\cdot S_2\cdot tg(\beta_2)} - \frac{r_1}{r_2}\cdot\frac{Q}{\rho_1\cdot S_1\cdot tg(\alpha_1)}\right) \quad (1)$$

The specific energy transferred to the turbines is given by (2):

$$H_{Tj} = \frac{1}{g}\cdot\left(u_{1j}\cdot v_{u1j} - u_{2j}\cdot v_{u2j}\right) = \frac{r_{1j}\cdot\omega}{g}\cdot\left(r_{1j}\cdot\omega - \frac{Q}{\rho_{1j}\cdot S_{1j}\cdot tg(\beta_1)} - \frac{r_{2j}}{r_{1j}}\cdot\frac{Q}{\rho_{2j}\cdot S_{2j}\cdot tg(\alpha_{2j})}\right) \quad (2)$$

where j represents the number of turbine stages.

$$H_T = \sum_j H_{Tj} \quad (3)$$

The hydraulic losses are calculated with Borda-Carnot relation:

$$h_p = \zeta \cdot \frac{v_0^2}{2 \cdot g} \tag{4}$$

with characteristic velocity $v_0$, given by the volumetric flow rate of the machine, and the local hydraulic loss coefficient $\zeta$ is calculated through the Reynolds number, considering the working fluid changing with temperature and the filling degree.
Modeling the normal working regime, at standard asynchronous speed of 975 rev/min shows a variation of torques at primary and secondary shaft machines, as a function of speed ratio s = $n_T$ / $n_P$ as presented in Fig. 10:

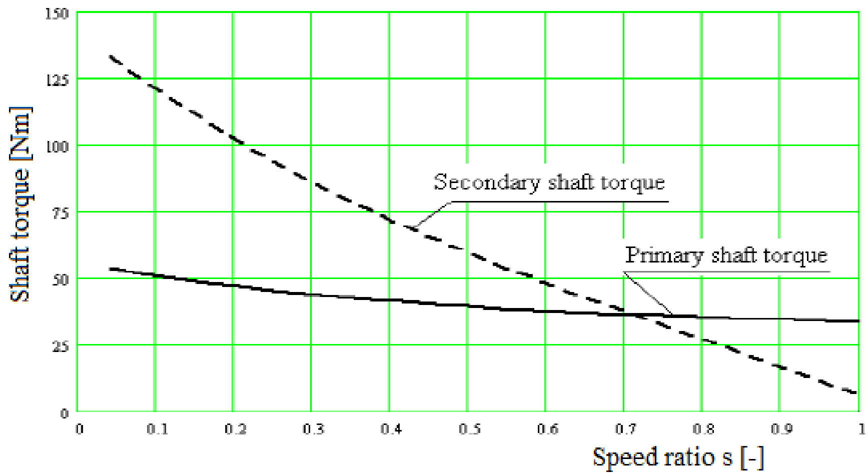


*Fig.10. Variation of shafts torques as function of speed ratio*

The different filling degrees can be modeled by introducing the definition of a two-phase fluid, composed from the main liquid and air.
The volume of the domain occupied by the multiphase flow represents the sum of partial volumes of components phases:

$$V = \sum_{i=1}^{n} V_i \tag{5}$$

Volumetric concentration of component "i" will be given by:

$$C_i = \frac{V_i}{V} \tag{6}$$

Considering the specific masses:

$$\rho = \rho_{mix} = \rho_1 \cdot C_1 + \cdots + \rho_i \cdot C_i + \cdots + \rho_N \cdot C_N = \sum_{i=1}^{N} \rho_i \cdot C_i \tag{7}$$

The term $\rho_{mix}$ define the mean density of the two-phase flow fluid, considered as a homogeneous fluid, and having this specific mass.

Reconsidering the way which has defined the degree of filling, mean density of the working fluid, considered as a two - phase flow is:

$$\rho_{mix} = C \cdot \rho_{air} + (1 + C) \cdot \rho_{oil} = \rho_{oil} + C \cdot (\rho_{am} - \rho_{oil}) \tag{8}$$

where $C$ is the main liquid concentration (oil).
Judging in a similar way the two-phase fluid viscosity, the constitutive dynamic viscosity coefficient will be:

$$\eta_{mix} = C \cdot \eta_{air} + (1 - C) \cdot \eta_{oil} \tag{9}$$

Using the presented model and considering different degrees of filling of hydraulic circuit were considered as 100 %, 95 %, 90 %, 85 %, 80 % and 70 %, as ratio between liquid (mineral oil) and total volume (liquid + gas, respectively oil + air volumes), we obtain the variation presented in Fig. 11 and Fig. 12.

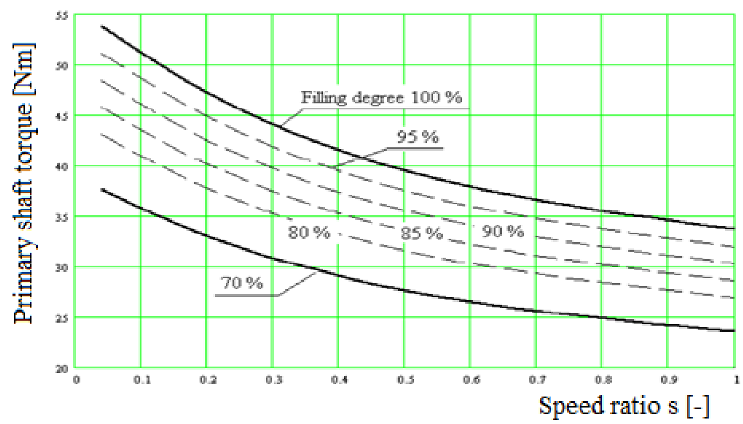


*Fig.11. Variation of primary shaft torque with speeds ratio in function of degree of filling*

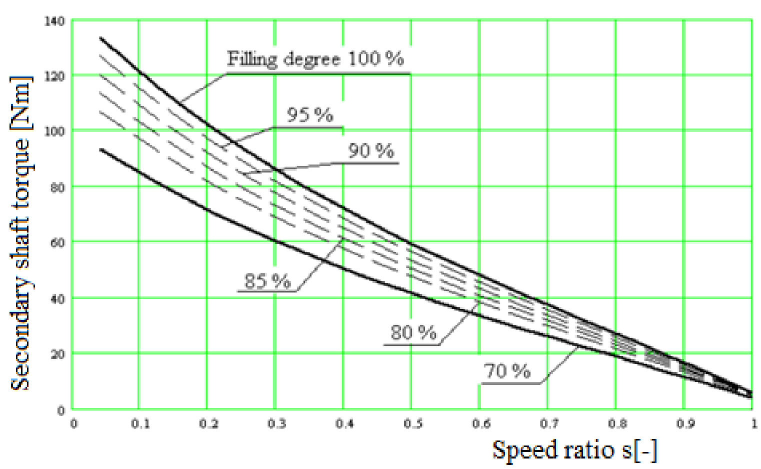


*Fig.12. Variation of secondary shaft torque with speeds ratio in function of degree of filling*

Considering the temperature we obtain:

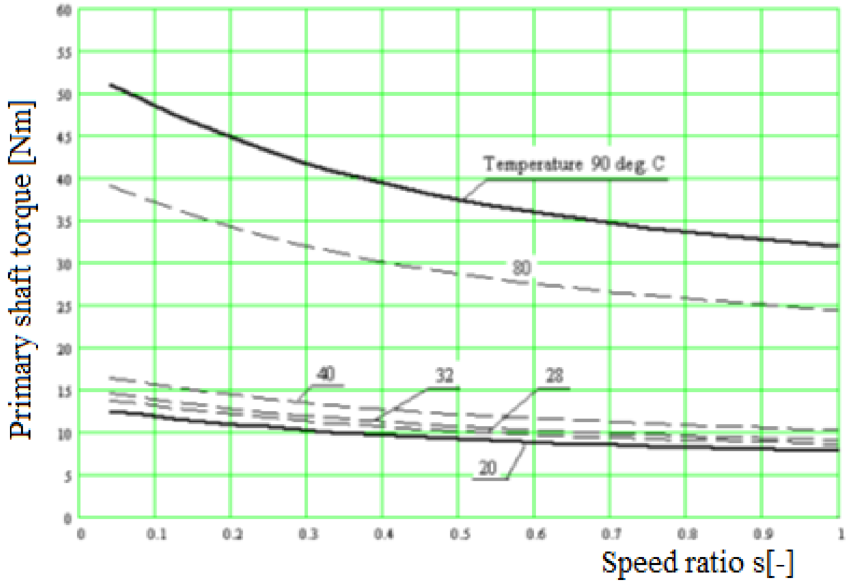


*Fig.13. Variation of primary shaft torque with the speeds ratio as function of the temperature at degree of filling 100 %*

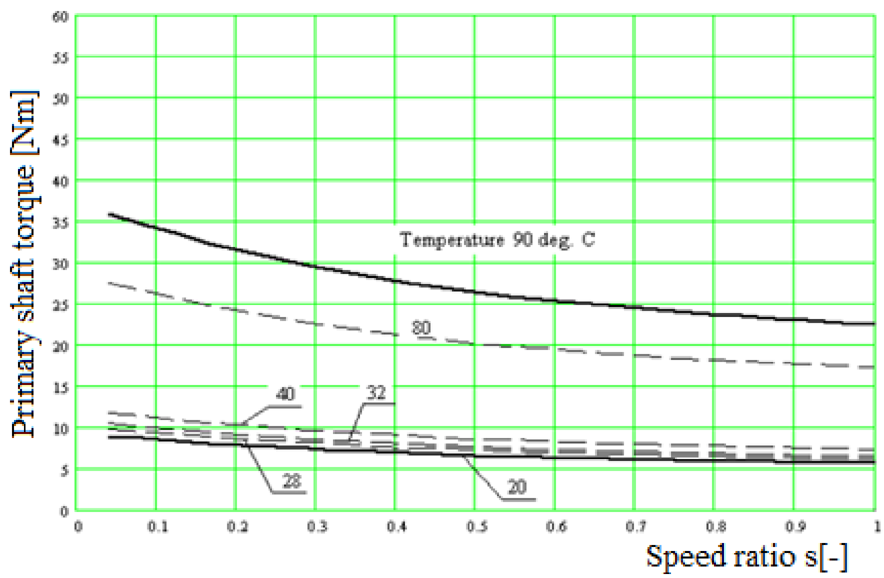


*Fig.14. Variation of primary shaft torque with the speeds ratio as function of the temperature at degree of filling 70 %*

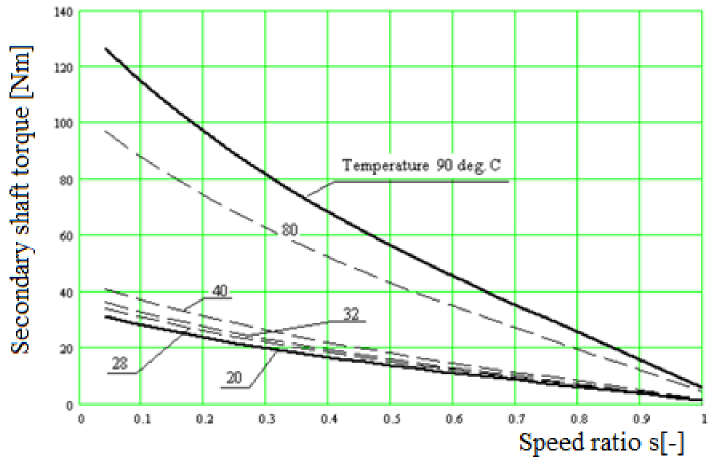


*Fig.15. Variation of secondary shaft torque with speeds ratio as function of the temperature at degree of filling 100 %*

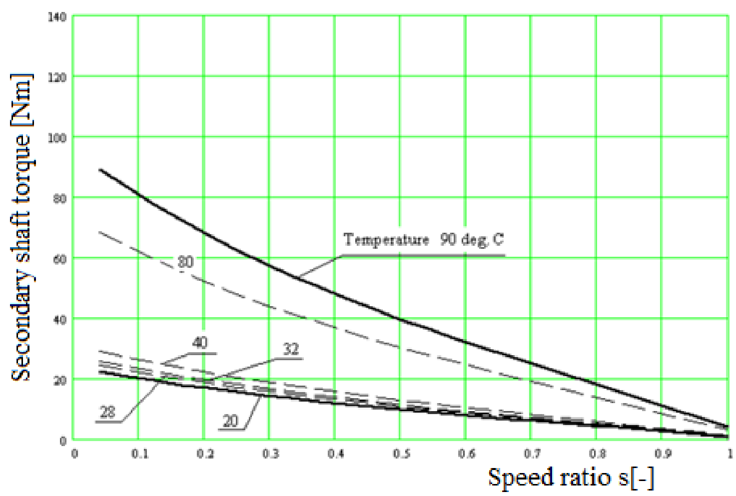


*Fig.16. Variation of secondary shaft torque with speeds ratio as function of the temperature at degree of filling 70 %*

On the basis of the theoretical results obtained, it can be said that the mathematical model allowed us to analyze the behavior of a complex machine as a torque converter in dynamic regimes generated in exploitation through:

- the modification of the degree of filling – modeled as a modification of the volumetric concentration of working fluid;
- the change of physical proprieties of the working fluid as consequence of rise of the temperature in the hydraulic circuit.

It is important to establish what happens when a blocking (closing) of the cooling circuit occurs. The running time until the optimum temperature is touched varies with the degree of filling. In the following, an experimental analysis of the temperature variation with the degree of filling in the CHC-350 torque converter was experimented.

In the Laboratory for Hydraulic Machines of the "Politehnica" University of Timisoara, Romania, exists an experimental facility for hydraulic transmissions.

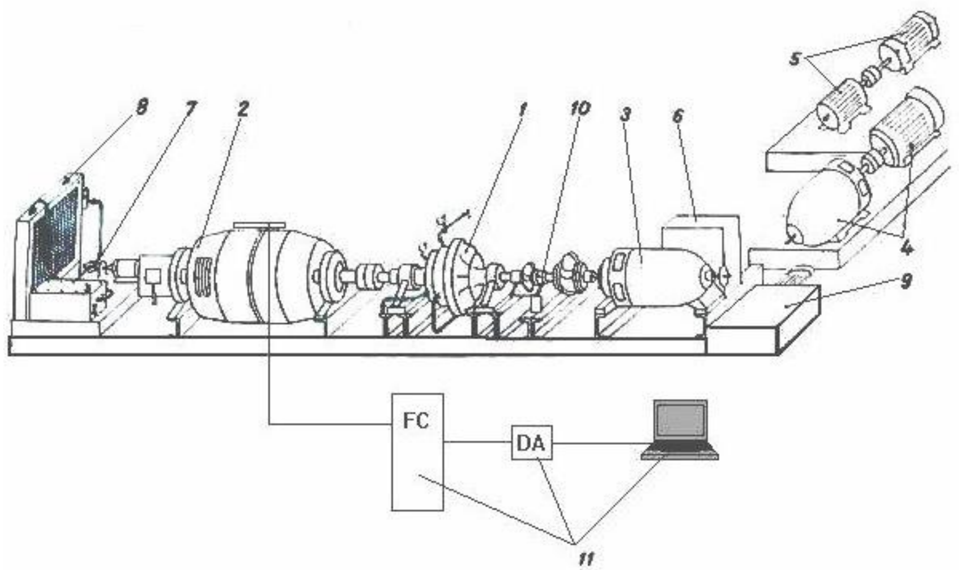


*Fig.17. The testing rig for hydrodynamic torque converters*

The facility consists from a testing rig as it is shown in Fig. 17, with the following components: 1-torque converter Lysholm – Smith type; 2-multiple speed induction motor; 3-dynamo for load; 4-Ward – Leonard system for power regeneration; 5-additional electric aggregate for excitation; 6-closed circuit for coupling brake circuit; 7-gear pump; 8-radiator; 9-starter equipment; 10-gauge for torque; 11-data acquisition system: FC – frequency converter, DA – data acquisition equipment, and computer.

The parameters of the system are: the degree of filling with oil of the torque converter; the constant resistant torque; the initial oil temperature and the pressure. The flow structure is monitored by different speeds red in revolution per minute.

Thermal power balance of the torque converter is:

$$P_{dis} = P_{tme} + P_{lic} \tag{10}$$

where:

- the power dissipated through the operation of the torque converter is:

$$P_{dis} = (1 - \eta_{tc}) \cdot P_1 \tag{11}$$

- the power transited to environment is:

$$P_{tme} = \sum \lambda_i \cdot A_i \cdot \Delta\theta_i \tag{12}$$

- the thermal power transported by cooling liquid is:

$$P_{lic} = \rho_0 \cdot Q_a \cdot c_u \cdot \Delta\theta \tag{13}$$

The functional performances of the torque converters can be influenced by the variation of the entrance speed, $\mathbf{n}_1$, the modification of the geometry of pump impeller and turbine runner blades and the modification of the degree of filling respectively through using a two-phase working fluid (liquid-gas).
In this study, there are presented a part of the experimental results obtained, considering the thermal regime in a Lysholm-Smith torque converter, operating with two-phase fluid type, mineral oil-air.
Thus, the experimental research, put in evidence that temperature variation in time in two-phase fluid mineral oil-air, is strongly influenced by the working regime of the torque converter (CHC - 350), through the turbine load.
Therefore, the tests were organized in accord to transmission loading, minimal loading, idle regime, (M2=0) and maximal loading/braking of the turbine for different degrees of filling using constant input speed $n_1$=1000 rev/min. The experimental results obtained are presented in Fig. 18, 19.

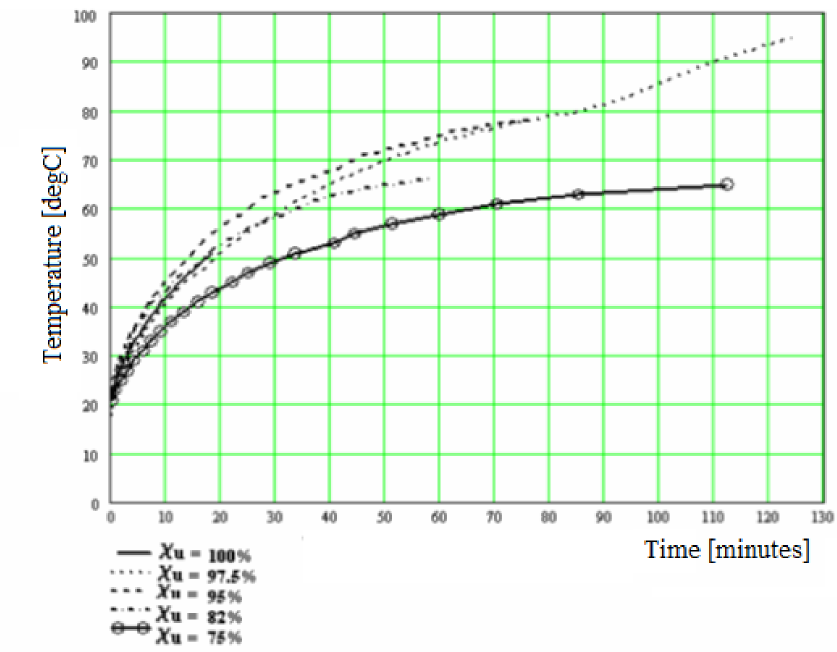


*Fig.18. Temperature variation in time in idle regime ($M_2$=0) for different degrees of filling*

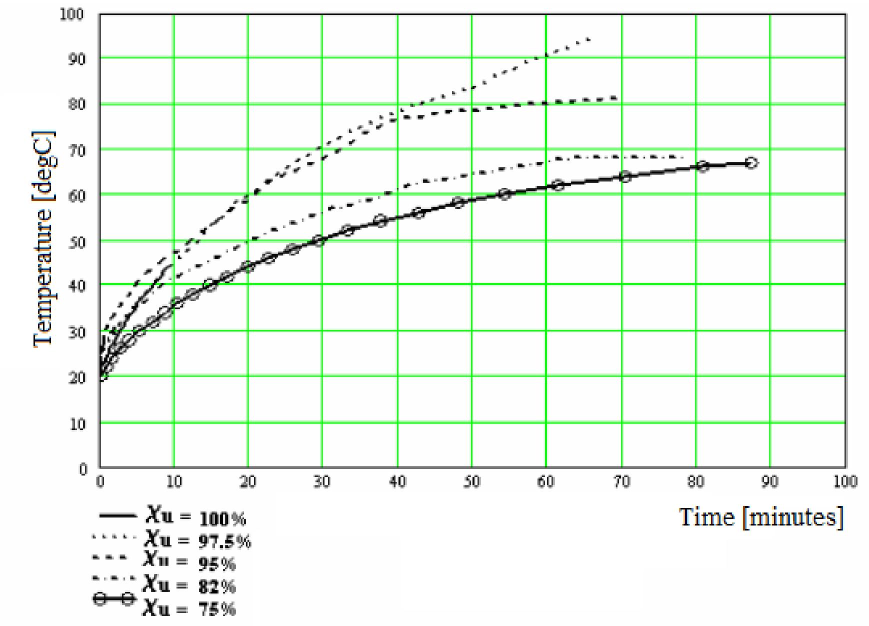


*Fig.19. Temperature variation in time with maximum load regime ($M_2$= $M_{2max}$=70…270 Nm) for different degrees of filling*

The analysis of the experimental curves presented in Fig.18 and Fig.19 show that the warming of the two-phase flow is produced faster in the case of maximum loading of the turbine and generally, the warming process is strongly influenced by the hydrodynamic transmission degree of filling, respectively through the balance of each constituent, mineral oil or air, in the two-phase flow.

The cause of the strong warming at higher degrees of filling could be the difference between the physical properties of the mineral oil and of the air and in other words that the maximum loading/braking of the turbine is followed by irreversible heat transfer of one additional part from kinetic energy of two-phase flow, which because of the braking are transformed into heat and pressure potential energy.

The maximum rise of temperature by a transient starting regime occurs at a degree of filling of $\chi_u = 95\%$ by idle regime and $\chi_u = 97.5\%$ at maximum loading of the torque converter.

The global effect of the two-phase working fluid warming, respectively of the parametric modification of the degree of filling can be better appreciated trough mechanical parameters of the turbine outlet, respectively the mechanical torque $\mathbf{M_2}$ and the outlet speed of rotation $\mathbf{n_2}$.

It has been observed that at the same constant input speed $\mathbf{n_1}$, indifferently which is the degree of filling and the loading level of the torque converter, the pressure in the transmission gets higher with the growing of the working fluid temperature. The outlet speed $\mathbf{n_2}$ grows with the growing of the two-phase fluid temperature, by high degrees of filling. At smaller degrees of filling, the outlet speed $\mathbf{n_2}$ decreases with the raising of the temperature (Fig. 20, 21).

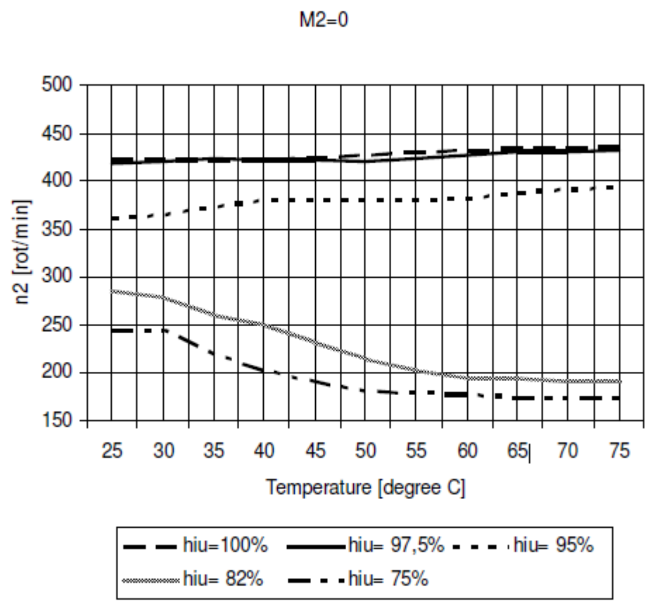


*Fig.20. Speed as a function of temperature for different degrees of filling, without load on the torque converter*

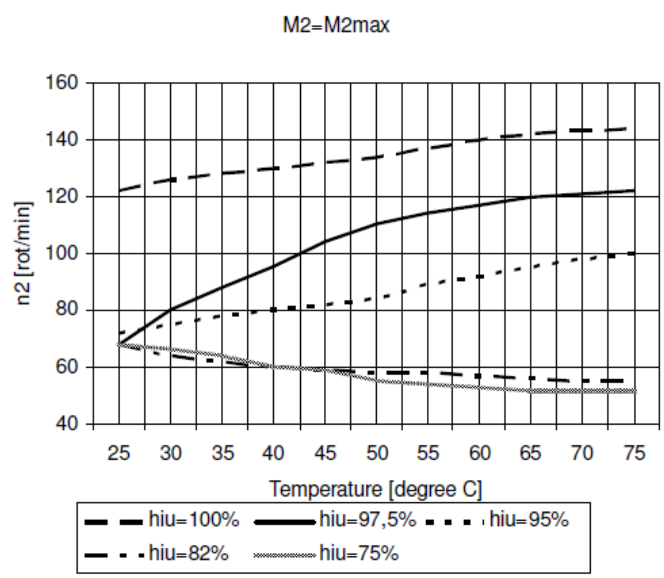


*Fig.21. Speed as a function of temperature for different degrees of filling, with maximum load on the torque converter*

Considering the running of the torque converters, seeing that, at higher degrees of filling, with the growing of the two-phase flow temperature grows the outlet mechanical torque $\mathbf{M_2}$ and the speed $\mathbf{n_2}$, appears a contradiction (probably accountable through the extremely complex thermo-hydrodynamic behavior of the two-phase liquid-gas components, generally) if we take into account the working characteristics of the torque converters obtained with the cooling equipment in operation.

From Fig. 20 and Fig. 21, it can be observed that for different degrees of filling $\chi_u = constant$ and for the same speed of rotation **$n_1$ = constant**, the speed of rotation **$n_2$** has different variations, monotonous, increasing or decreasing, with the temperature increase of the two-phase working fluid.
Hence, it results that there exists a degree of filling $\chi_{u0} = constant$ at which, the speed remains constant, indifferently of the temperature variation in time.
Thus, if a gradient is defined as follows:

$$grad\Pi = \frac{\Delta n_2}{\Delta\theta}\left[\frac{rev/min}{℃}\right] \tag{14}$$

then, $grad\Pi = 0$, for the degree of filling $\chi_{u0} = 85\%$, for maximum loading and $\chi_{u0}{}^* = 91\%$ for minimal loading and $grad\Pi > 0$, for different degrees of filling $\chi_u > \chi_{u0}$ or $\chi_u > \chi_{u0}{}^*$ and $grad\Pi < 0$ for different degrees of filling $\chi_u < \chi_{u0}$ or $\chi_u < \chi_{u0}{}^*$, respectively (Fig. 22).

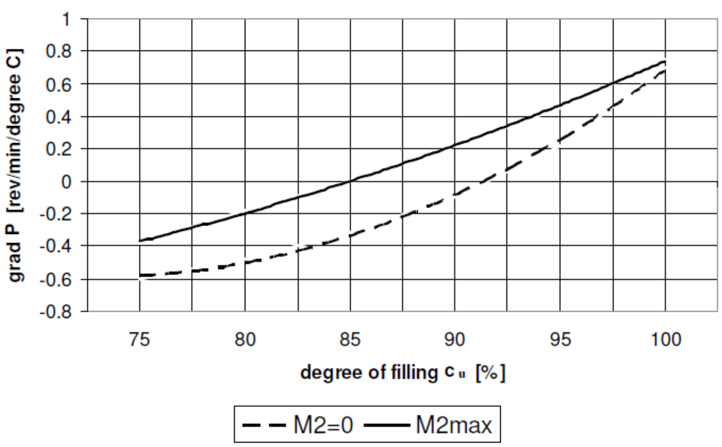


*Fig.22. Gradient of the speed with temperature in function of the degree of filling, for idle regime and maximum load regime of the torque converter at constant entrance speed $n_1$ =1000 rev/min.*

The unique thermo-hydrodynamic case, when $grad\Pi = 0$, or when the speed $n_2$ = const., respectively, it is taught that is the result of different response of the mineral oil and air from the two-phase flow, with the temperature increase. The filling degree $\chi_{u0} = 85\%$, or the gradient $grad\Pi = 0$, respectively, or ($n_2$ = const.), offers outstanding assignments concerning the two-phase components, mineral oil-air, respectively, as for the influence of temperature about of the physical properties of two-phase flow. On the other way, with the two-phase components, mineral oil-air, we can maintain the normal speed $n_2$ constant, indifferently of the temperature variation in time of the hydrodynamic transmission.

In conclusion, the filling degree, $\chi_{u0} = 85\%$, respectively, $\chi_{u0}{}^{*} = 91\%$, corresponding to entrance speed of rotation **$n_1$ = 1000 rev/min**, ensures a stationary regime in the hydrodynamic transmission.

### I.3.2. The research in the domain of Hydraulic Turbines [9, 10, 11, 12, 13, 14, 15, 16, 17]

Considering the importance of using green energy and especially energy recovery where possible, we have continued research in the field of small power hydraulic turbines and their use in various locations where energy can be recovered.
The following analysis was done over the Cross-Flow hydraulic turbines, that don't need very complex hydro settlements, being very suitable for small and medium power hydro plants. Also, a quite big potential in the use of this type of hydraulic machines is the energy recovery in the water treatment and sewage plants.
The turbine's blades surfaces enters in contact with the pressurized water jet, which creates a hydrodynamic force that tends to stress the blade. Mainly the Cross-flow turbine blades are made from steel, but this study presents the hydrodynamic design of a Cross-Flow water turbine and the possibility of using new polymeric material as Delrin ®AF for the runner blades.
Generally, the Cross-Flow turbine blades are circle arcs with constant width. The variable thickness blade has the advantage of smoothly modification of the inter blade channel. In our case the blade shape was designed using O. Popa method, the geometry being generated using a trigonometrical 6th grade polynomial, (Fig. 23). The sharp blade edge ensures with minimal losses the stream distribution at the runner inlet. Although with classic machining was quite difficult and expensive to make the shape of the blade, the new methods and materials make this possible in quite an easy manor.

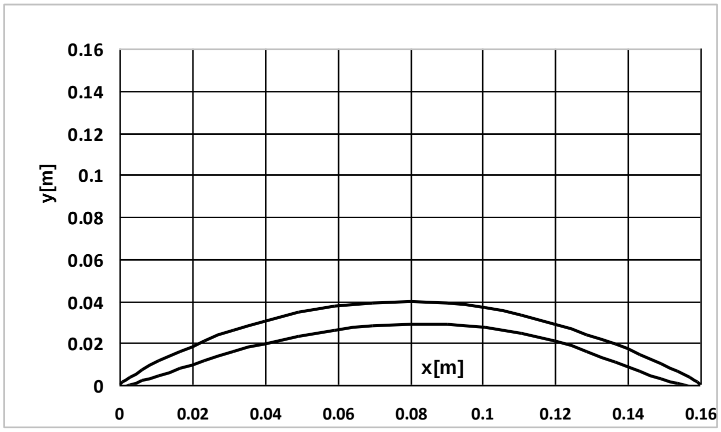


*Fig.23. Cross-Flow turbine blade with variable thickness, designed with O. Popa conformal mapping method*

Usually, the Cross-Flow turbine blades are made from steel, but the development of the new polymeric materials and of the new technologies make possible the implementation of these two in the Cross- Flow runners and blades manufacturing. Further, it is presented the hydro-dynamic design of the blade and a study from the point of view of strength of materials of some suitable polymeric materials class for the turbine blades.

The blade design was done for a Cross-Flow turbine with a head of H=40 m and a volumetric flow rate of Q=1.8 m$^3$/s. The stereo-mechanical power of the turbine is:

$$P_s = \rho g Q H_T \eta_T \tag{15}$$

in which it is assumed an efficiency $\eta_T = 0.8$, water density $\rho = 1000$ kg/m$^3$ and gravitational acceleration $g=9.8065$ m/s$^2$. The speed of rotation of the hydraulic turbine's runner is selected between the synchronization speeds with a.c. frequency 50 Hz namely:

$$n = \frac{3000}{pp} \text{ [rev/min]}, \quad n_s = n\frac{\sqrt{P_S[kW]}}{{H_T}^{5/4}} \tag{16}$$

in which $pp = \overline{1, N}$ are the pole pairs of the electric generator.

The specific speeds for the Cross-Flow hydraulic turbines are $n_s = 50\ldots150$.

Runner diameter is:

$$D_1 = \frac{n_{11}\sqrt{H_T}}{n} \text{ [m]}, \quad n_{11} = 40 \text{ rev/min} \tag{17}$$

Absolute flow velocity at the entrance in the runner:

$$v_1 = k_{v1}\sqrt{2gH_T} \text{ [m/s]} \tag{18}$$

where $k_{v1}$=0.98 depends on the nozzle hydrodynamics. Runner tangential velocity is:

$$u_1 = \frac{\pi D_1 n}{60} \text{ [m/s]} \tag{19}$$

Absolute velocity angle is:

$$\alpha_1 = a\,tan\frac{\sqrt{v_1^2 - 4u_1^2}}{2u_1} \tag{20}$$

Runner angles are:

$$\beta_4 = a\,tan(\,2\,tan\,\alpha_1) \qquad (21)$$

$$\beta_1 = 180° - \beta_4 = 150°,\ \beta_4 = 30° \text{ also it is assumed: } \beta_2 = 90° = \beta_3 \qquad (22)$$

Inner runner diameter was obtained through an iterative procedure:

$$D_2 = D_1 \sqrt{\frac{-\,sin^2\,\beta_4 + \sqrt{sin^4\,\beta_4 + 4\frac{sin^2\,\beta_1}{sin^2\,\beta_2} cos^2\,\beta_4}}{2\,cos^2\,\beta_4}} \qquad (23)$$

The relative velocities are:

$$w_1 = -\frac{v_1\,cos\,\alpha_1}{2\,cos\,\beta_1} \qquad w_2 = w_1 \frac{D_1}{D_2}\frac{sin\,\beta_1}{sin\,\beta_2} \qquad (24)$$

The literature gives different formulas for turbine’s hydraulic efficiency. For our case it is accepted:

$$\eta_{hT} = 0.887 - \frac{D_1}{H_T} 0.717 \qquad (25)$$

It can be considered acceptable the estimated overall efficiency of the Cross-flow hydraulic turbine $\eta_T = 0.8$.

The blades number after an empirical formula:

$$z = 4xINT(10 \cdot D_1 - 1) = 24 \qquad (26)$$

The transport velocity by the inner diameter of the runner:

$$u_2 = u_1 \frac{D_2}{D_1}\,[\text{m/s}] \qquad (27)$$

The flow angle here is:

$$\alpha_2 = a\,tan \frac{w_2\,sin\,\beta_2}{u_2 - w_2\,cos\,\beta_2}\,[\text{rad}] \qquad \varepsilon = 2\alpha_2 \qquad (28)$$

$$v_2 = \frac{u_2 - w_2\,cos\,\beta_2}{cos\,\alpha_2}\,[\text{m/s}] \qquad (29)$$

Runner width:

$$b_r = \frac{Q}{k \cdot k_{v1} \cdot D_1 \sqrt{2gH_T}} + 0.02 \text{ [m]}, \quad k=0.1 \tag{30}$$

The Cross-Flow turbine runner has the main geometric sizes $D_1$=0.76 m, $D_2$=0.44 m and the width L=0.884 m.

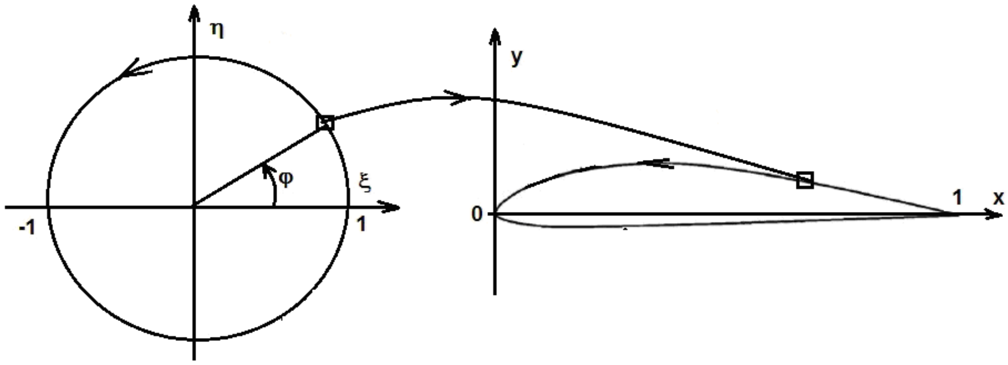


*Fig. 24. Conformal mapping of the unit circle external domain into the external domain of an airfoil*

The turbine blade geometry has been generated transposing the circles network in an airfoils network, fig. 24.

The network characteristics result from the singularization of the network, obtaining the coefficients of approximation trigonometric polynomial. The blade geometry was approximated through a 6$^{th}$ order trigonometric polynomial. The blade coordinates are:

$$X = \frac{1}{2}(1 + cos\,\phi), \; Y = \frac{a_0}{2} + \sum_{n=1}^{N}[a_n\, cos(n\phi) + b_n\, sin(n\phi)] \tag{31}$$

$Y$=$Y$(φ), φ∈[0, 2π],. For N=6 coefficients, is considered $\Delta\phi = \frac{\pi}{6}$. In order to obtain the trigonometrical polynomial coefficients are considered 12 values for $Y_p$, p = 0, 1, 2 …. (2N-1). With these values are calculated the coefficients of the trigonometrical polynomial:

$$a_{n=}\frac{1}{N}\sum_{p=0}^{2N-1} Y_p\, cos(p\frac{n\pi}{N}), \; b_{n=}\frac{1}{N}\sum_{p=0}^{2N-1} Y_p\, sin(p\frac{n\pi}{N}) \tag{32}$$

For the studied blade, the trigonometrical polynomial coefficients are presented in table 1:

*Table 1*

| **n** | 0 | 1 | 2 | 3 | 4 | 5 | 6 |
|---|---|---|---|---|---|---|---|
| **$a_n$** | 0.205 | -0.002476 | -0.108 | 0.0003333 | 0.0045 | 0.002143 | 0.001 |
| **$b_n$** | 0 | 0.036 | -0.002309 | 0.003667 | 0.002887 | 0.001224 | 0 |

In order to analyze the force distribution on the blade, it was considered the hardest condition, when the runner is completely blocked and on it acts the whole force of the water jet.
From fluid mechanics theory the force of the jet is:

$$F_j = \rho Q \Delta v \tag{33}$$

Where:$\rho$ =1000 [kg/m$^3$] is the water density, Q=1.8 [m$^3$/s] is the volumetric flow rate, $\Delta v$ =28 [m/s] is the absolute velocity variation (it was considered the hardest condition, when the velocity variation is equal with the velocity from the pipe). As we know from the geometry the jet attacks three blade channels, it means that for one blade force calculation we must consider the formula:

$$F_{jb} = \rho \frac{Q}{3} \Delta v \tag{34}$$

After calculus results that $F_{jb}$=16800 N.
In many mechanical solutions, thermo-plastic resins are a very good alternative solution instead of conventional materials. From this material class, the acetal homo polymer presents a combination of physical and mechanical properties which permits them to compete easy with metals. The acetals are formed from a group of aldehyde or ketone which reacts nucleophile with alcohol in the presence of an acid catalyst. The acetal ensures a high resistance and rigidity associated with a good dimensional stability and machinability. Also, it is characterized through a low friction coefficient and good wear properties, especially in wet medium. The acetal absorbs minimal humidity quantities, keeping its properties constant in a big variety of media. The low water absorption confers excellent dimensional stability for the parts machined with high precision. From acetals homo polymers Delrin®AF gain a large scale recognition because of its reliability and performance in many domains of mechanical engineering [8]. From the producer datasheet Delrin®AF presents the following mechanical properties given in table 2:

*Table 2. Delrin ®AF material mechanical properties*:

| Material | Modulus of elasticity, E [MPa] | Tensile strength $\sigma_r$ [MPa] | Elongation at break A [%] |
|---|---|---|---|
| Delrin®AF | 3200 | 70 | 15 |

Taking into account the blade geometry and the load resulted from hydro dynamic calculus, Fig. 25, a numerical analysis of the blade stress and strain has been made. The material is defined elastic linear with properties similar with the acetal Delrin®AF. The blade support conditions have been established according to its mounting solution in the runner, considering also two intermediary supports, Fig. 26.

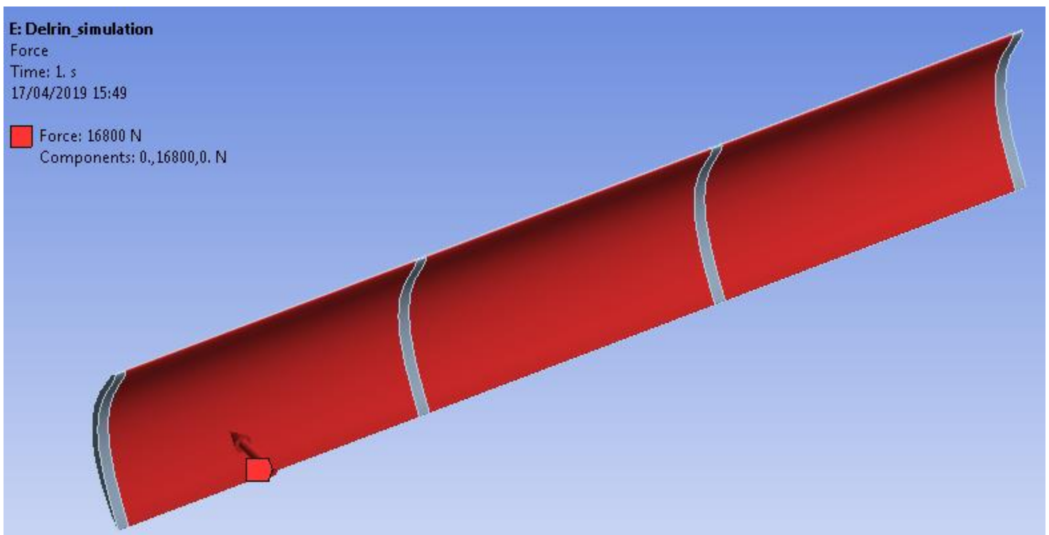


*Fig. 25. The hydro dynamic force applied on blade inner surface*

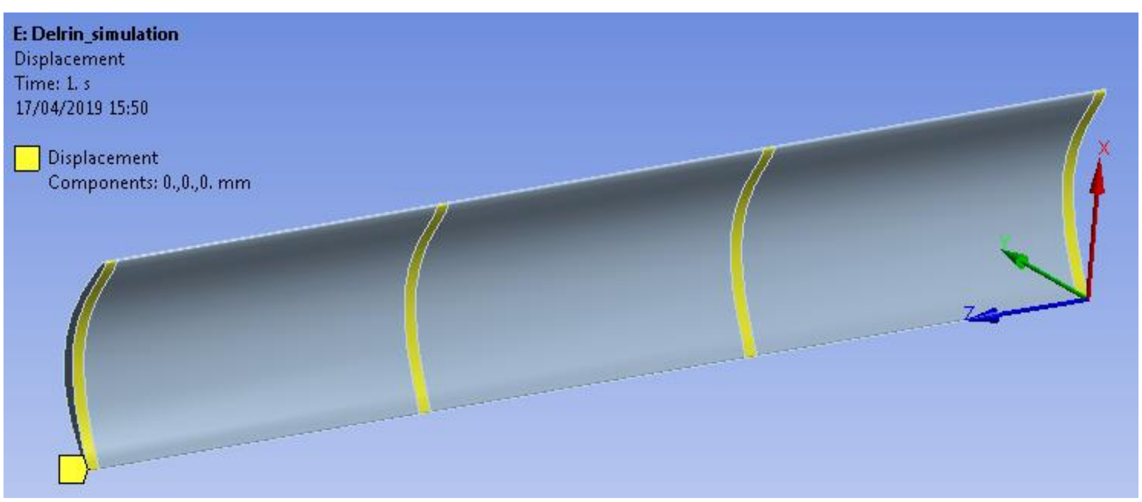


*Fig. 26. Supports applied on both blade surfaces*

Fig. 27 and 28 present the Von-Mises equivalent stress and strain distributions for the considered loading case. As a result of blade geometry and deformation modulus can be seen stress concentrations in the blade's upper part, nearby the supports. However, these stresses concentrations give a relatively good safety coefficient accepted in the design standards of these components, fig. 29.

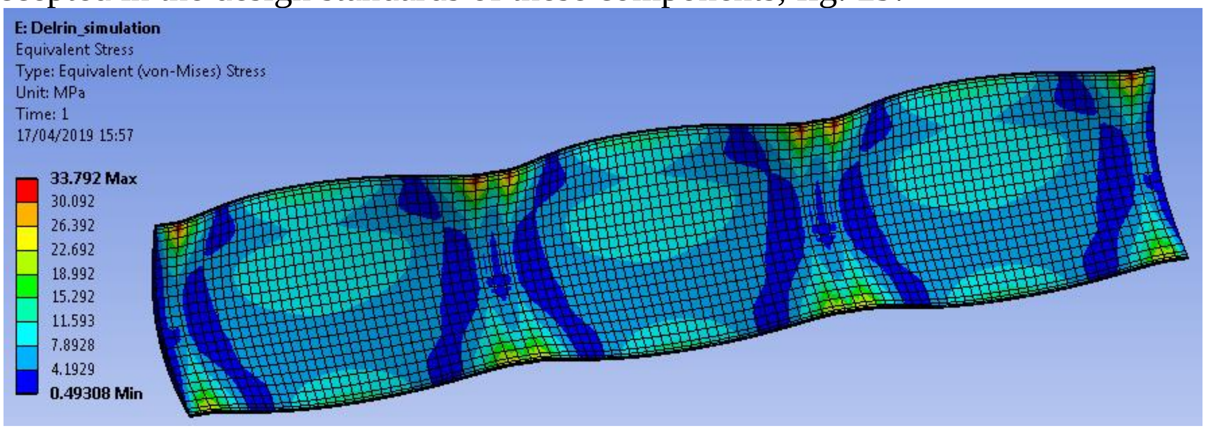


*Fig. 27. The equivalent Von Mises stress distribution*

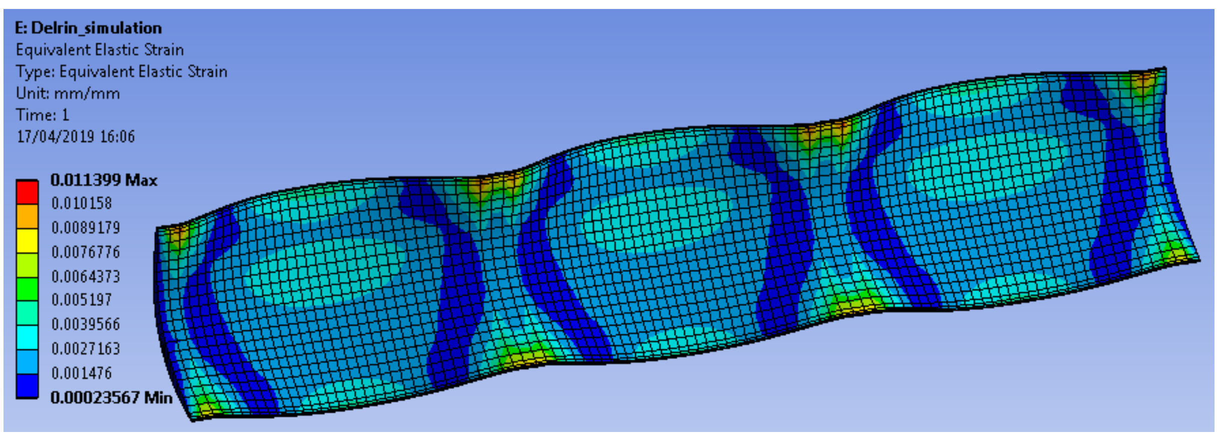


*Fig. 28. The equivalent Von Mises strain field*

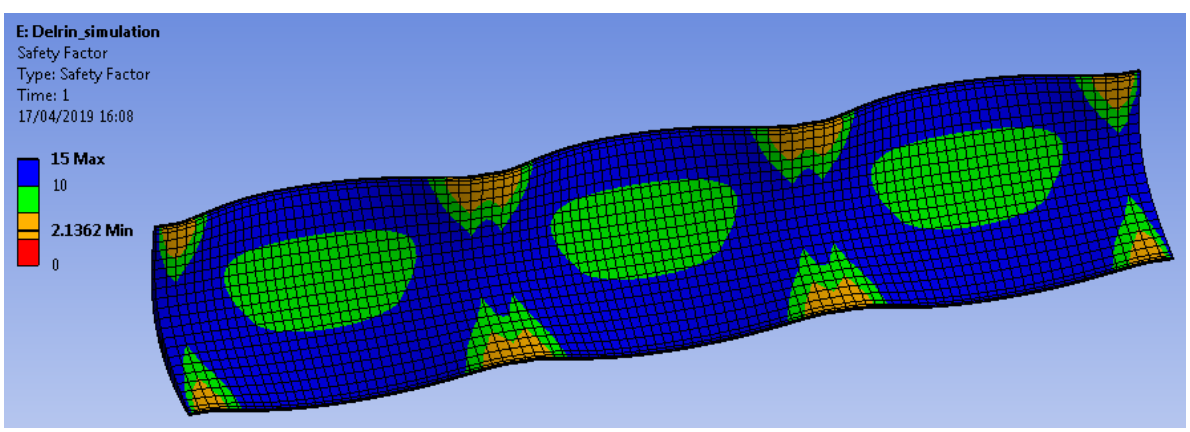


*Fig. 29. The safety factor distribution*

The use of thermoplastic materials in Cross-Flow hydraulic turbines blades and runners has many advantages: good mechanical resistance, easy machining because of lower density than metals, the hydraulic machine components having a reduced weight. For the studied case the blade volume is de 0.00127652 m$^3$. In the case in which the blade will be machined from steel, for a medium steel density of 7850 kg/m$^3$, it will give a blade mass of 10 kg. If Delrin material is used, having a density of 1420 kg/m$^3$, the blade will have a mass of 1.812 kg, being almost 5.5 times lighter.

Further, together with my colleagues from Department of Civil Engineering and Building Services, of Politehnica University of Timișoara, it has been made an analysis of how to store electricity by approach a Pelton water-water turbine hybrid system. The heat pump consumes the electrical energy for action, producing a thermal effect. By integrating a system with Pelton water storage tank and a turbine on the heat pump outlet circuit, the lost hydraulic energy can be recovered. The experimental hybrid system was made to develop **HRES** (Hybrid renewable energy system) optimization models. Hybrid systems may exceed the limits of individual generators in terms of efficiency, economy, reliability and flexibility. An energy storage system can alleviate the problems associated with uncertainties and fluctuations from renewable sources. The large number of random variables and parameters in a hybrid energy system requires optimization to increase the efficiency of hybrid system components to achieve economic and technical benefits.
The proposed experimental installation (Fig. 30) highlights the conversion and storage of energy and the possibility of recovering the lost energy from the technical systems.

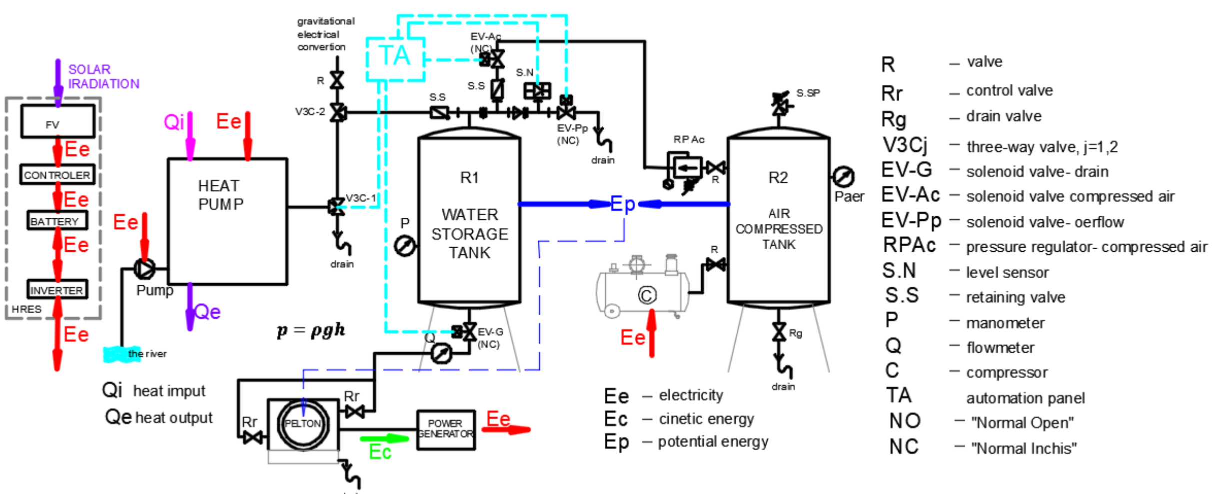


*Fig. 30. Functional scheme of the experimental installation*

The water discharged from the primary circuit of a water-water heat pump is stored into a storage tank R1, coupled via a solenoid valve to the Pelton turbine. The head

of the hydraulic turbine is achieved with the compressed air stored in the R2 tank. The compressed air is pre-stressed by the C-powered compressor from a hybrid photovoltaic conversion system (**PV)**. The experimental installation doesn't practically consume the electricity from the **NES** (National Energy System), the electrical energy required for the operation of the heat pump and for the production of the compressed air is provided by **HRES** (Hybrid renewable energy system). In order to confirm this, a small scale laboratory Pelton turbine was tested from the point of efficiency.
In Fig. 31 and 32, are presented the characteristic curves, torque and efficiency as a function of speed. The results are obtained for 3 testing regimes:

- regime 1: turbine head H=16.5 m and the volumetric flow rate Q=0.37 l/s;

- regime 2: turbine head H=12 m and the volumetric flow rate Q=0.52 l/s;

- regime 3: turbine head H=8 m and the volumetric flow rate Q=0.62 l/s.

Utile power for the hydraulic turbine, in this case is mechanical power defined as:

$$M_P = T \cdot \omega \; [W] \qquad (35)$$

where T [Nm] represents the mechanical torque at turbine shaft and $\omega$ [rad/s] is the angular speed.
The absorbed power is the hydraulic power:

$$H_P = \rho \cdot g \cdot Q \cdot H \; [W] \qquad (36)$$

where $\rho$=1000 [kg/m$^3$] is water density, g=9.80665 [m/s$^2$] is gravitational acceleration, H[m] represents the turbine head and Q [m$^3$/s] is the volumetric flow rate.
The hydraulic turbine efficiency is the ratio between the util and absorbed power:

$$Efficiency = \frac{M_P}{H_P} \cdot 100 \; [\%] \qquad (37)$$

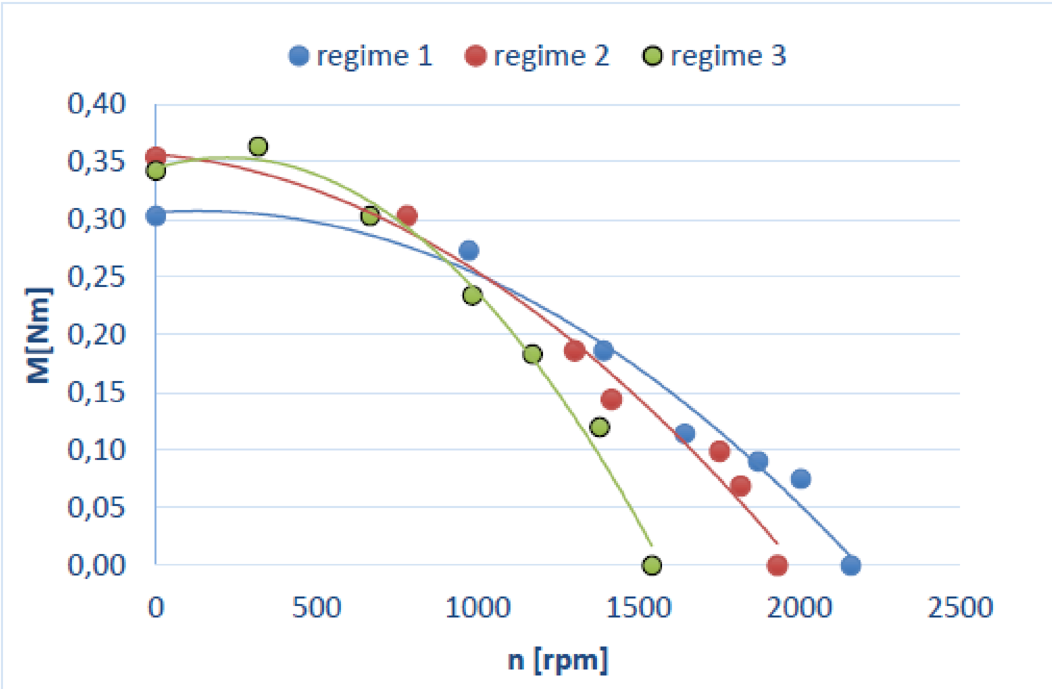


*Fig. 31. Torque as a function of speed for a Pelton turbine*

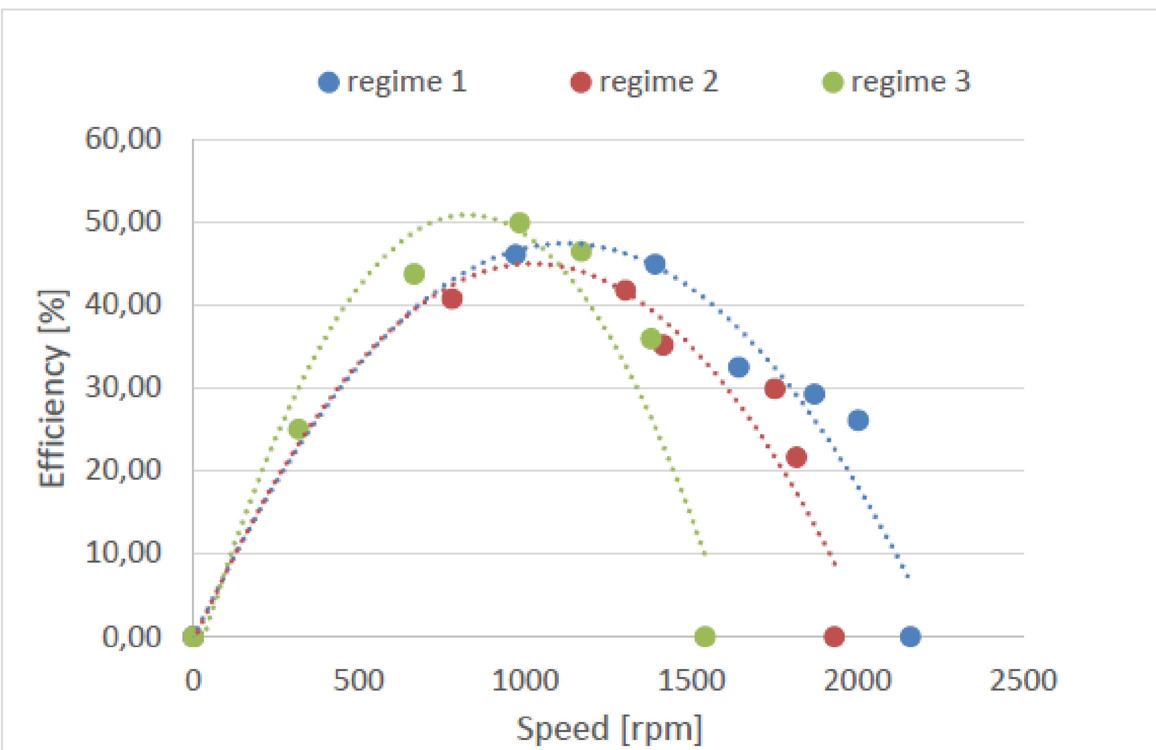


*Fig. 32. Efficiency as a function of speed for a Pelton turbine*

Another study in the domain of hydraulic turbines was done through a numerical analysis of the pulsating water jet in the draft tube cone of hydraulic machinery and concluded in an ISI paper together with *Scientific Researcher Grade1* Constantin Tănasă, from *Research Institute for Renewable Energy of Politehnica University of Timisoara* and with my colleagues from the Faculty of Mechanical Engineering, Hydraulic Machinery Collective: Conf. Dr. Ing. Adrian Stuparu and Prof.Dr.Ing. Romeo Susan-Resiga.

The main problem that the paper treats is developing the pulsating water jet method in order to mitigate or eliminate the vortex rope associated with the pressure pulsations. The numerical domain, the energy losses coefficient and kinetic to potential conversion ratio distributions are plotted along to the cone length in order to evaluate the energetic performances, also being evaluated the unsteady pressure fluctuations with and without pulsating water jet.

The numerical domain corresponds to the test section with a convergent-divergent shape, which is part of the swirling flow apparatus from the test rig from Politehnica University Timisoara, studied in several research grants by Professor Resiga and his team. The structured mesh with 2.1M cell generated on the domain and the boundary conditions imposed uses velocity profile at the inlet and mean pressure at the outlet. The runner speed was 925 rpm, the nominal discharge 30 l/s and the jet discharge was 11.5% from the nominal one. For the numerical simulations were used the FLUENT code and RSM turbulence model. The time step for both cases (with and without pulsating jet) was 0.1 ms.

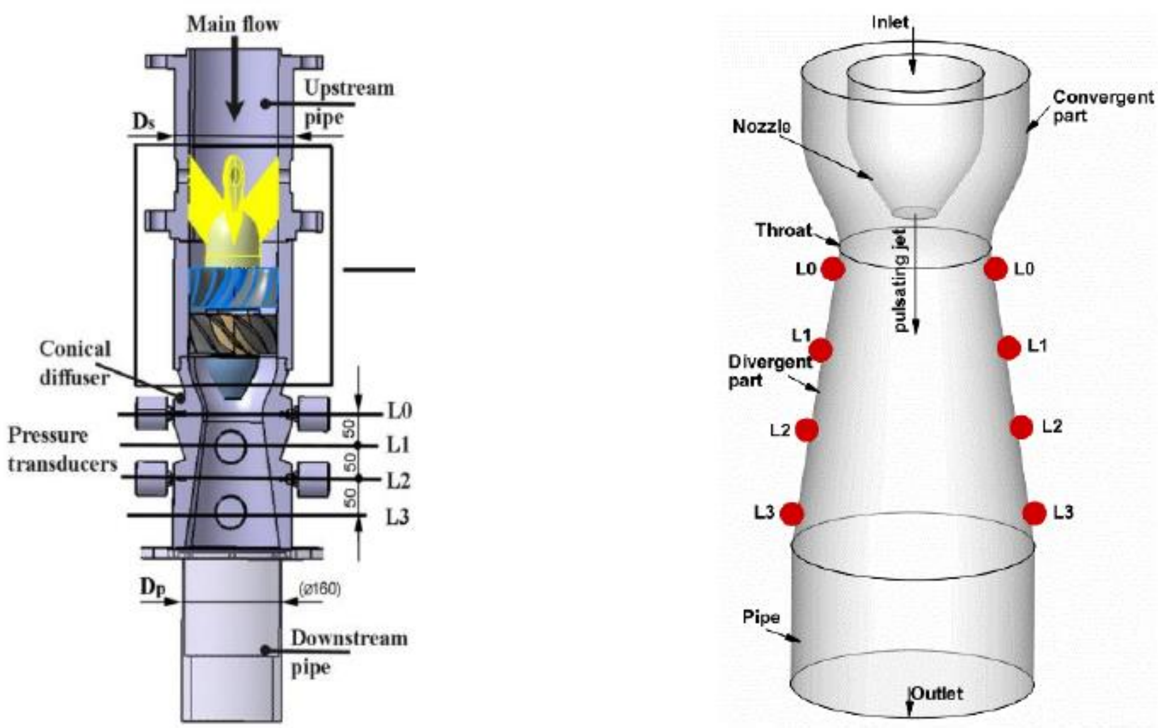


*Fig. 33. Swirling flow apparatus and 3D computational domain*

The simulation results are resented in Fig.34 to Fig.39.

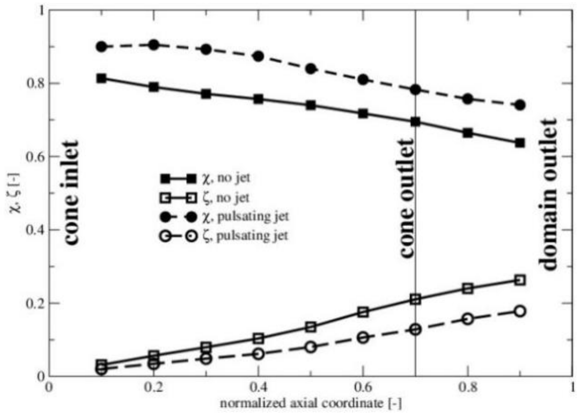


*Fig. 34. Energy conversion (χ) and the loss coefficient (ζ) along the draft tube cone axis*

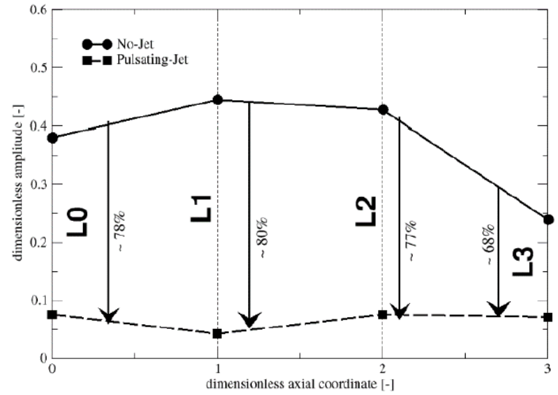


*Fig. 35. Dimensionless amplitude along the axis of the draft tube cone*

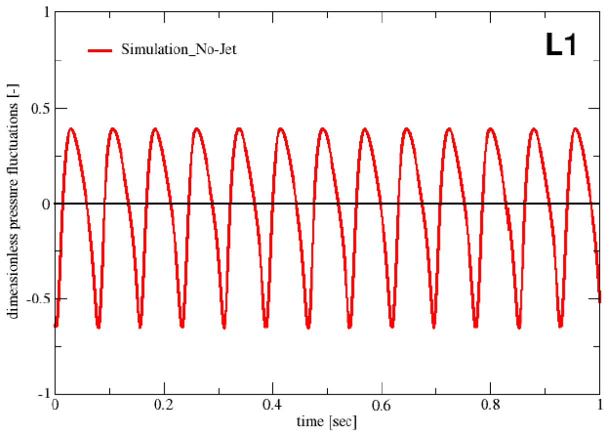


*Fig. 36. Pressure fluctuation without pulsating jet*

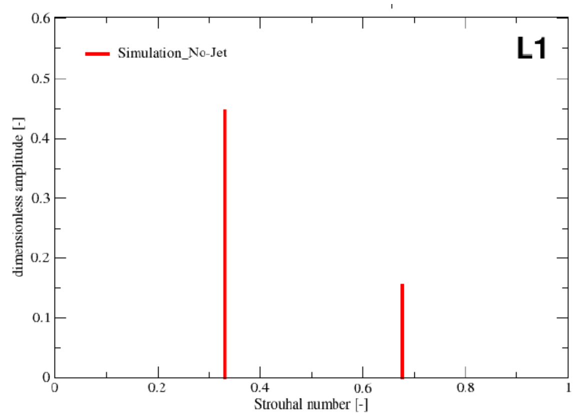


*Fig. 37. Fourier spectra for L1 level monitoring at the cone wall without pulsating jet*

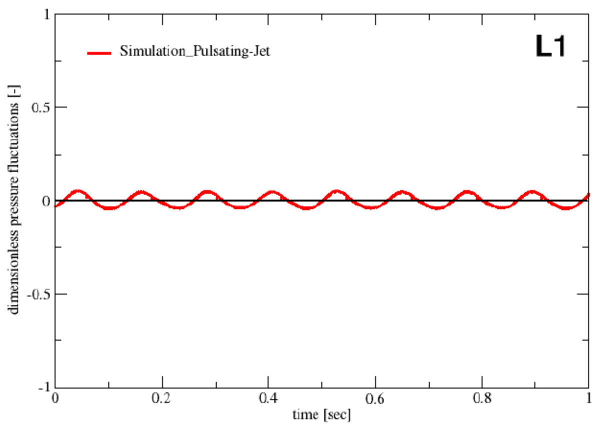


*Fig. 38. Pressure fluctuation with pulsating jet*

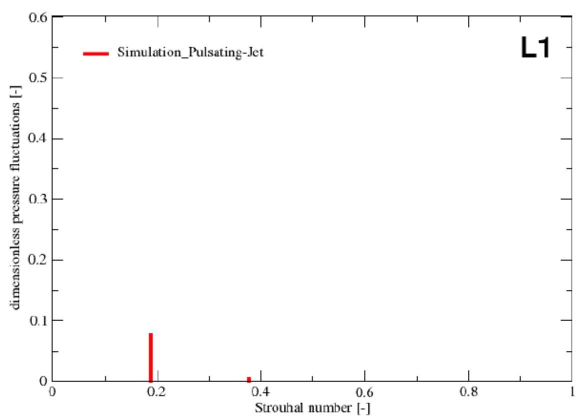


*Fig. 39 Fourier spectra for L1 level monitoring at the cone wall with pulsating jet*

Since the unsteady part of the pressure signal is periodic, we characterize it using the vortex rope precessing frequency and the dominant amplitude. In dimensionless form, the precessing frequency is expressed using the Strouhal number**:**

$$Sh = f \frac{D_t}{V_t} \tag{38}$$

where $f$ is oscillation frequency, and $D_t$ represents the test section diameter.
The pressure fluctuation is dimensionless with the kinetic term:

$$\rho \cdot \frac{V_t^2}{2} \tag{39}$$

where *Vt* is the reference velocity from the test section throat.
As a general conclusion we can say that using this method, the vortex rope is practically eliminated because the rotating component is negligible when the pulsating jet is introduced, mitigating the low-frequency pressure fluctuations.

Another interesting and important study in the domain of hydraulic turbines was done together with the collective composed by: Prof. Dr. Ing. M. Bărglăzan, Prof. Dr. Ing. I. Bordeaşu, Prof. Dr. Ing. M Popoviciu, Prof. Dr. Ing. V. Bălăşoiu and Prof. Dr. Ing. L. Mădăras and had the purpose to notice the elements that can produce incidents during the running of the regulating apparatus of bulb turbines.
The analyzed regulating device has a robust construction, but it has a critical element, which is the connecting rod.
For bulb-type units the guide vane regulating device has a conical shape and consists of the following important elements: the guide vane servomotors with the afferent rods, the regulating ring with the joining bolts, the connecting rods, the cranks and the guide vanes.
In the following are presented the Guide Vane Regulating Apparatus, its components and the modality of operation.
Fig. 40 presents the view of a regulating apparatus segment, seen from inside the bulb. One guide vane is presented in both extreme positions: completely closed and completely open.

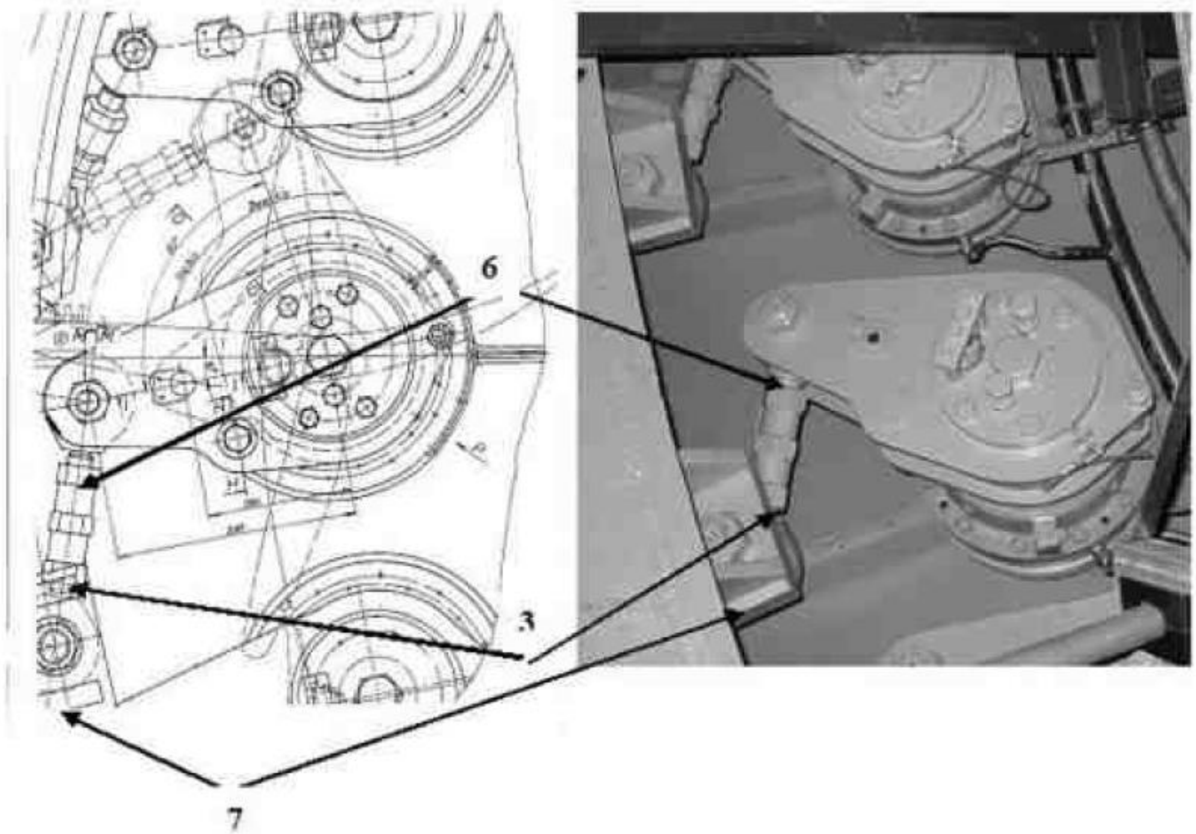


*Fig. 40. Inner view of the regulating apparatus*

The regulating device is actuated with two servomotors placed inside and at the lower part of the bulb. On the regulating ring are welded 16 vanes inclined at 60º. The joining bolts are mounted on these vanes.

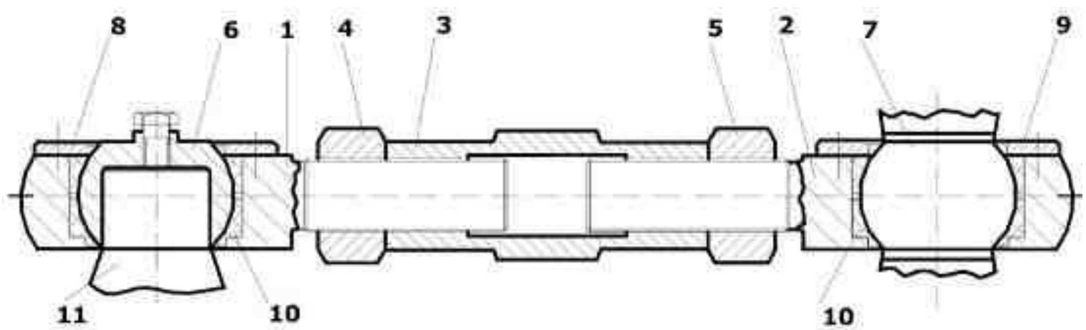


*Fig. 41. The guide vane connecting rod*

The connecting-rod presented in Fig. 41, is a complex detail having the following main parts: the left thread link ring (1), the right thread link ring (2), the lids (8, 9), the antifriction spherical bushings (10) and the joint bolt (11).

Besides the transmission of the maneuvering force, the connecting rod fulfills two other important functions:

- The first is represented by the spatial movement of the connecting rod, realized through the sliding of the bushings (10) over the metallic spheres (6, 7). These sliding allow the necessary spatial movement of the connecting rod in order to maintain the center of the sphere (6) in the movement plan of the regulating ring, concomitantly with the rotation of the link ring eyes (1, 2) in such a manner that the center of the sphere (7) has the possibility to remain in the rotation plane of the crank.
- The second function of the connecting rod is to close the dimension chain. This function is fulfilled only in the assembling period and is carried out as follows: after assembling all the involved parts in the closed position, the connecting rod is put in its normal position. The lengths of the connecting rod being adjustable through the rotation of the sleeve (3), provided with left/right thread, the dimensional chain is closed in an easy way.

The crank is also a complex element, composed of 26 individual pieces. The most important are: the proper crank, the inner cover plate, the outer cover plate, the shearing bolt and the joint with the connecting rod (the spherical arm 7 in Fig. 41). The leading part played by the crank is to move the guide vane at the right angle demanded by the turbine. This movement is obtained as a result of the force delivered by the connecting rod.

Supplementary the crank has also two secondary functions:

a) the protection against the deterioration of the guide vane in the eventuality when a great solid object gets between two consecutive guide vanes;

b) the possibility to rotate the guide vane in the opening direction even if the shearing bolt is fractured by the external forces.

These two supplementary functions will be analyzed separately.

***Guide vane protection***

In order to fulfill this function, the crank is realized from three distinct parts: the proper crank, the inner cover plate and the outer cover plate. These three parts are bounded together by three types of bolts: the shearing one, the massive support and two slender supports. The shearing bolt is a cylindrical piece, manufactured from steel (OLC 45), heat treated, with a diameter of 50 mm and provided with two shearing cross sections. These shearing sections are realized by cutting two notches at 60º (stress raisers) that reduces the diameter to 40 mm. If a massive solid object is caught between two consecutive guide vanes and the regulating apparatus is moved towards closing, these guide vanes cannot effectuate the movement. As a result, the oil pressure increases in the hydraulic actuating system together with the acting force delivered to the crank. If this force exceeds with 40…50% the normal value of the tension, the notched sections resistance is exceeded and the shearing bolt will be fractured. In this way the bounds between the proper crank and the cover plates are interrupted. The cover plates can follow the movement imposed by the regulating ring, but in the same time the proper crank and the guide vane are not obliged to follow this movement.

***Possibility to actuate the guide vanes even if the shearing bolt is fractured***

The designer offered the possibility to move the guide vanes toward opening even when the shear bolt is fractured. When the regulating ring is moved toward opening, the body of the massive support enters in the 120º clearance provided in the crank arm (Fig. 40) and allows the actuation of the system crank/guide vane. The movement towards closing is not possible and the guide vane can occupy casual positions dictated by hydrodynamic forces with the restriction given by the position of the massive support.

In the following section are analyzed the possibilities for casual events.

The shaft of the joining bolt (11) and the metallic sphere (6) are united by three threaded screws „M 16x35 group 5” (12) secured with Grower washers (13). For two up to four guide vanes, namely for those placed at the lower part of the bulb, when the Grower washers are out of use the monolith (11)-(6) is compromised. As a result of the vibrations and without the Grower washers, all the M16x35 bolts get unscrewed and finally fall at the bottom of the bulb. Under the influence of gravitation, the assembly formed by the left thread link ring (1), the antifriction bushing (10), the lid (8) and the metallic sphere (6) can slide over the cylindrical journal of the bolt (11). For an easy assembling the fitting between the metallic sphere (6) and the cylindrical journal of the bolt (11) is H7/g6. Consequently, the minimum clearance of the sphere is zero and the maximum clearance is 0.03 mm. The joining bolt journal minimum clearance is 0.013 and the maximum is 0.062. This means that the minimum clearance of the assembly is 0.013 mm and the maximum is 0.065 mm. The length of the journal being 54 mm, the maximum inclination in the first moment can reach a hexadecimal minute.

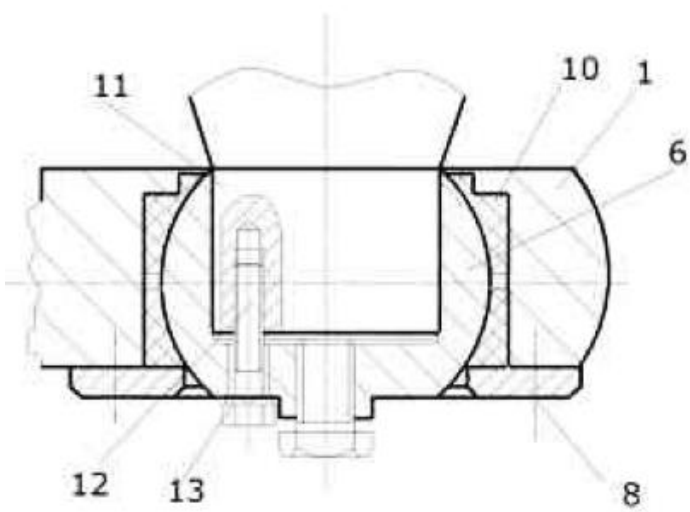


*Fig. 42. Detail of the left thread link*

The total mass of the parts subjected to gravitation is about 19.914 kg. Taking into account the inclination of the thread link ring, the force in the direction of the journal axis is approximately 9,75 N and can gradually rotate the metallic sphere in the antifriction bushing and finally the connecting rod fall from the joint. Evidently, this process is a slow one, especially the unscrewing of the three M16x35 bolts. An extremely critical circumstance is the fact that, during the periodic inspections, the intermediate phases of the detachment are very difficult to see.

Even the loss of the Grower washers cannot be observed at the periodical inspections. From discussions with the inspection personnel resulted that they found fragments of Grower washers in the bulb's interior, but they can't say if these fragments result from the assembling period or from the running period.

In the literature [14], the Grower washers are recommended till the group 8.5. Because the used screws are in group 5, they enter in the recommended interval. In [15] it is specified: "The Grower washer is a spitted one, manufactured from spring steels and in disassembled state the branches are in a far-off position. This elastic washer is mounted between the part and the nut and is compressed by screwing the nut so that the sharp end penetrates both in the part and the nut. In this way the unscrewing of the nut is prevented. Although, this method does not offer absolute assurance, so the assembly must be verified periodically." In [16] is mentioned: "The unscrewing of the hexagonal head bolt can be prevented by passing a wire through their heads." In literature there are presented also other safety solutions as for example split plates applied to the screw head. This solution is difficult to be applied in our condition because the lack of space (the free end of the plate must be fastened by a distinct screw).

Upon our opinion, ensuring this very important bond only with Grower washers does not offer the necessary confidence and the detachment of the bond regulating ring connecting rod, in peculiar conditions, can generate important injuries followed by expensive repair jobs. The fact that, in this area, there were found washer fragments, leads to the conclusion that after the heat treatment they are in some cases too fragile so they can crack and fall from the joint. Consequently, the bound can be detached by unscrewing of the three threaded screws.

A rough analysis of the probability for the connecting rod to go out from the regulating mechanism can be realized simply, by examining the possibility of inclining the right link ring in the distance between the crank plates. It resulted that the inclination of the connecting rod overcame 6º, which allows the metallic sphere (6) to go over the superior end of the joint bolt journal (11).

Another possible malfunction is generated by the rotation of the whole assembly sleeve (3) - securing nuts (4, 5) as a result of the vibrations. If the distance between the axes of the sphere (6) and the bolt (7) increases, the respective guide vane will be heavily pressed on the adjacent vanes, which leads to the deterioration of the tightness of the rubber cords.

When the rotation is in the contrary direction (the length of connecting rod is reduced), in the closed position of the regulating mechanism, it remains a clearance between the vanes and important leakages can occur.

In the other positions of the regulating apparatus, the hydrodynamic field is perturbed and the hydraulic efficiency of the turbine is reduced.

Conducting a kinematic analysis of guide vane apparatus, presented in detail in [13], it has been reached to the conclusion that the spatial movement of the connecting rod allows the detachment from the joining bolt if the Grower washers do not play their role.

From the analysis carried out on the conical guide vane regulating apparatus results that for the solution adopted by the designer, the deterioration of a low cost piece (the Grower washer) can lead, in favorable situations, to the detachment of the connecting rod from the regulating ring. In such a situation the respective guide vane has free movement under the action of the hydrodynamic forces. The connecting rod, which remains bounded to the crank, follows a chaotic movement generated by the guide vane, perhaps amplified as the result of the articulation.

If by misfortune, the free end of the connecting rod is blocked by another part there are possible great damages such as for example: the fracture of the shearing bolt or the push of the crank into that of the guide vane situated in proximity with the possibility to block up both guide vanes. As a consequence, occur important deterioration of some parts of the regulating apparatus.

Even if the detachment of the connecting rod is a slow process it has the great disadvantage of not being easy to be seen, at the regular inspections. The deterioration becomes evident only when the injury is so great that the running of regulating apparatus is impossible.

Consequently, there were proposed for the connections of the regulating apparatus parts, two supplementary safety measures.

The first, extremely economical and efficient is ***passing a wire through the heads of the joining screws***. As an experiment, it was proposed also the more elegant solution to use Nord-Lock washers [17]. Those washers have the advantages of ensuring maximum security for the bounding subjected to vibrations, they are not influenced by temperature and technical lubricants do not influence the blocking function. To avoid corrosion effects, there were proposed stainless steel washers (A4, AISI 316).

It was also recommended for the future a careful examination of the guide vane apparatus also from other points of view, especially the reliability of the tightness, the behavior of the journal bearings, the behavior of the crank details.

### I.3.3. Research in the field of turbopumps and water supplies [18, 19, 20, 21]

The following studies were done in a national grant supported by the Romanian Government – Ministry of Education, Research and Innovation, The National Centre for Programs Management (CNMP) through, CNMP project no. 21-036/2007 and CNMP project no. 21-41/2007. This grant started in 2007 and finished in 2010 and was directed by Conf. Dr. Ing. Teodor Milos, where I was part of the team.

The problem of the automatic adjustment of the operating point correlated with the requirements of the water supply arises for many pumping systems. In the conditions of our days the equipment for the adjustment of the operating point can be designed so that the pump efficiency to be at maximum and the energy consumption to be at minimum.

This adjustment can be done, using intelligent pumps. The intelligent pump has the ability to regulate and control the flow or the pressure. The typical savings of these systems are lifetime and energy advantages, improvements and system cost reductions. The results presented in what follows, were obtained from a study realized on a typical water supply using an intelligent pump.

The software commands the adjustment of pump speed, such as the operating point is at optimum with respect to the energetic consumption and the pressure value to the consumers will be maintained at the initial recommended limits.

The intelligent pumping systems with embedded sensors and controls provide smoother startups with tighter control during continuous operation. The adaptation of the operating parameters of the pumping stations to the dynamics of the consumption and the most efficient exploitation is a serious challenge for the decision factors of water delivery.

*Characteristics of the pump for water supply*

For this study in the first phase were reproduced the energetic parameters Q, H, $P_{ab}$ with the reference data given by the pump manufacturer.

The curves from the catalogue were interpolated at 5 different pump speeds, $n_1$=2900 rot/min as a maximum reference speed (100%), $n_2$= 2610 rpm (90%), $n_3$= 2320 rpm (80%), $n_4$ = 2030 rpm (70%) and $n_5$ = 1740 rpm (60%)

Reading the values of head and power from the catalogue for the flow rates between 0 and 2.1 [1 / s] the analytical curves were interpolated using polynomial functions (third degree for head and seventh degree for power and efficiency). In Fig. 43, 44 and 45 are presented the pumping head vs. flow rate, power vs. flow rate and pump efficiency vs. flow rate. The analyzed pump type was WILO Cor MVIE-204.

With the two categories of curves, pumping head and efficiency, we can build the pump operation characteristic which gives us information about the optimum operating point of the pump. The identification of the equal efficiency curves was made analytically, using a program developed by us and the graphic postprocessor program used was developed in AutoCAD under AutoLisp. The results obtained for the pump operation characteristic are shown in Fig.46.

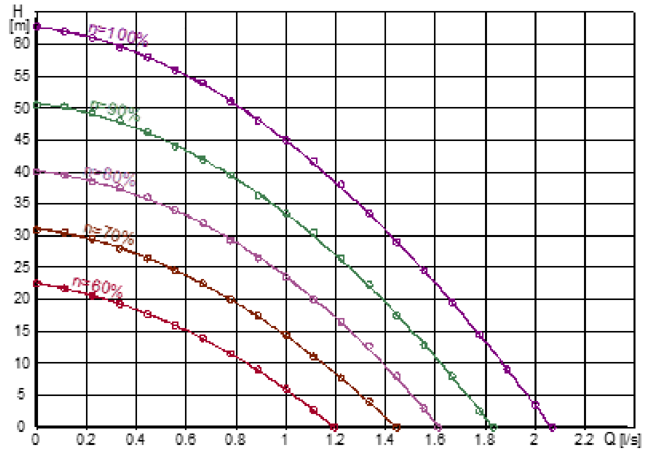


*Fig. 43. Pumping heads versus flow rate interpolated*

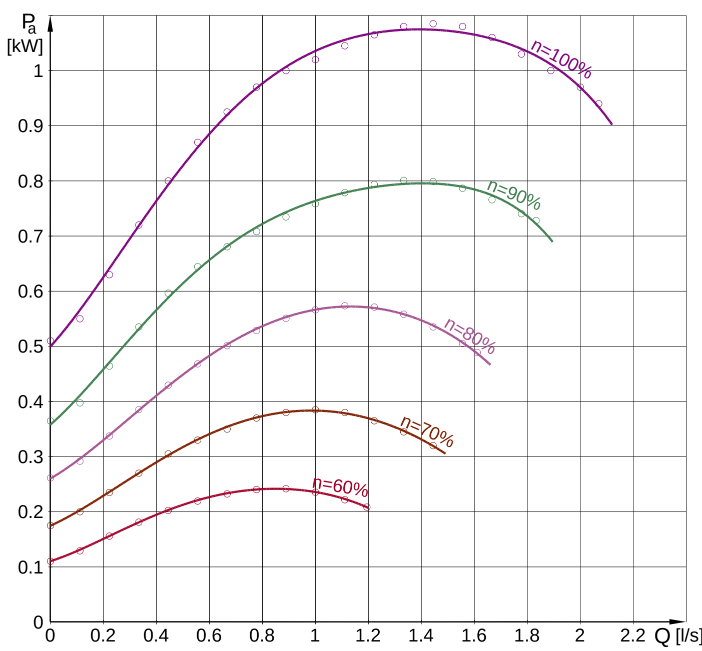


*Fig.44. Power shaft versus flow rate interpolated*

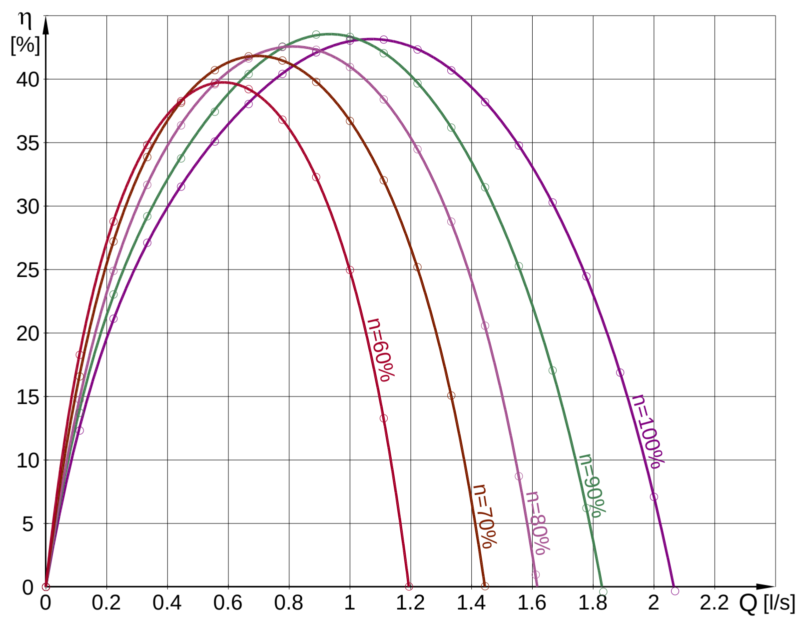


*Fig.45. Efficiencies versus flow rate for the five pump speeds*

*The characteristics of the hydraulic network help in solving the problem*

The pipe network operation characteristic $H_{pn}$ represents the amount of the losses from the hydraulic network, exterior to the pump and it is calculated with the formula (where $H_g$[m] represents the pump geodesic head):

$$H_{pn} = H_g + C_{hl} \cdot Q^2 \tag{40}$$

The hydraulic losses constant, $C_{hl}$ is calculated for an operating point measured from the pump characteristic knowing that $H_{pn} = H$ and from equation (40) results:

$$C_{hl} = \frac{H_{pn} - H_g}{Q^2} \tag{41}$$

As the network is a closed hydraulic circuit, $H_g = 0$. The other points of the pipe network operation characteristics are calculated giving values to flow rate from zero to the maximum value.

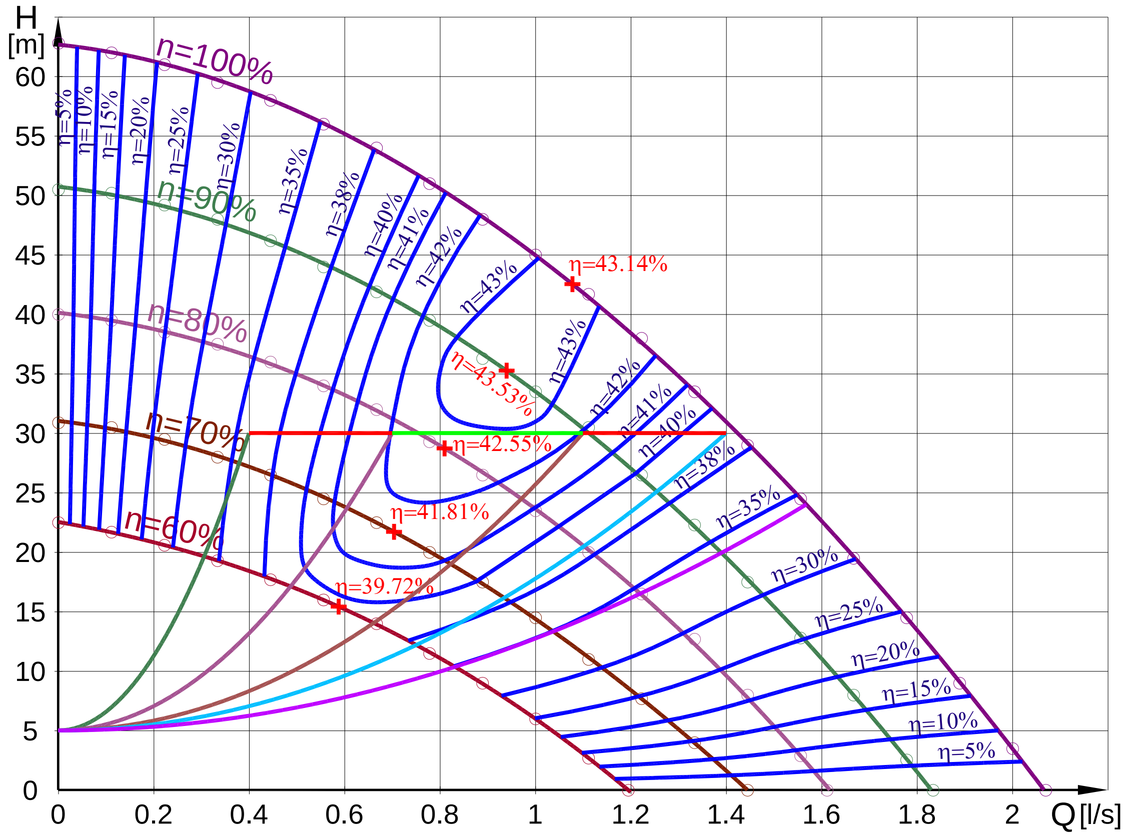

*Fig.46. The pump operation characteristic with the equal efficiency curves*

Having an installation with variable speed, the pipe network operation characteristic can be obtained adjusting the flow rate through the modification of the pump speed. If the pump delivers in the pipes network and requires the pressure (the pumping head) to be maintained constant for any flow rate, then all working points of the pump will be located on a horizontal line, $H = H_{ct}$ , figure 47.

For the working flow rate $Q_A$, adjusted with wicket and the pump operating at maximum speed, n = 100%, the characteristic corresponds to a feature of the network parabola AP. The constant of this parabola is obtained with equation (42):

$$C_{hlA} = \frac{H_{pnA} - H_g}{Q_A^2} \tag{42}$$

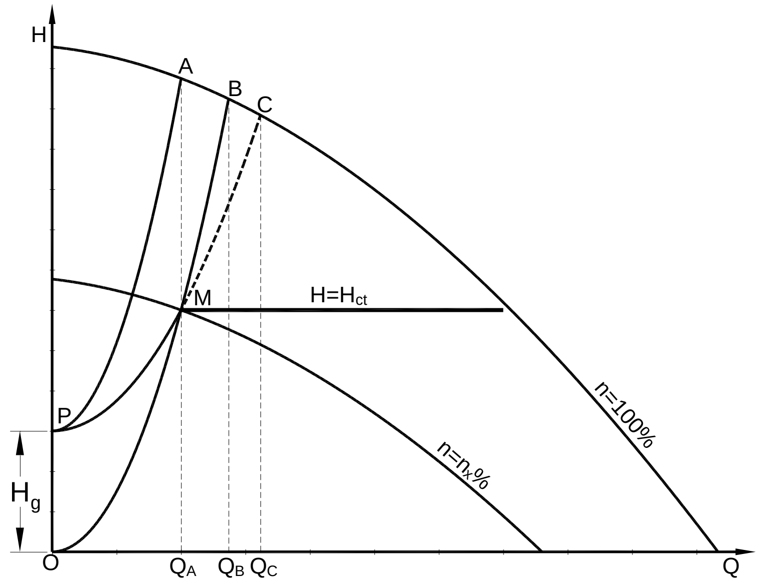


*Fig.47. The three parabolas of the flow rate $Q_A$ adjustment.*

If the same flow rate $Q_A$ is adjusted by lowering the speed $n = n_x$, the network of pipelines feature corresponds to a parabolic network form, MP. The constant of this parabola is determined by the equation (43):

$$C_{hlM} = \frac{H_{pnM} - H_g}{Q_M^2} \tag{43}$$

The operating point B results from the parabola crossing M with the curve H = f(Q) as 3th degree polynomial. Crossroads are numerically resolved.
To find through similarity, the pump's necessary speed for point M, the parabola of similar regimes shall be identified. It passes through the origin, 0 and M.
The constant necessary in this case resulting from:

$$C_{hlC} = \frac{H_{pnM}}{Q_M^2} = \frac{H_{pnC}}{Q_C^2} \tag{44}$$

The point C results from the parabola crossing O and M with the curve H = f(Q), as 3th degree polynomial. Crossroads is numerically resolved.
Using similar relations and having all data, is necessary to calculate the speed for point M with the equation:

$$n_x = n_M = n_C \cdot \frac{Q_M}{Q_C} = n_{100\%} \cdot \frac{Q_A}{Q_C} \tag{45}$$

Transposition is recommended to be done on the nearest curve H = f (Q) from point M. Otherwise transposition error may be unacceptably high, because of the difference in yields. Intelligent pumps can make automatically this adjustment through the software implemented in its own automation system.

*The energy saving achieved by regulating the flow with the pump speed compared to the flow adjustment through the outlet vane*

The energy saving results from the electric power used by the pump during operation. This is shown by the ratio between the hydraulic power of the fluid and the pump and electric motor efficiency. If the pump runs at maximum speed and the flow rate $Q_A$ (see Fig. 48) would be adjusted through the outlet vane in the hydraulic network, the power would be calculated with:

$$P_{elA} = \frac{P_h}{\eta_{em} \cdot \eta_{pA}} = \frac{\rho \cdot g \cdot Q_A \cdot H_A}{\eta_{em} \cdot \eta_{pA}} \tag{46}$$

where $Q_A \cdot H_A$ product represents the hatched area, AA'OQ, in Fig. 48.

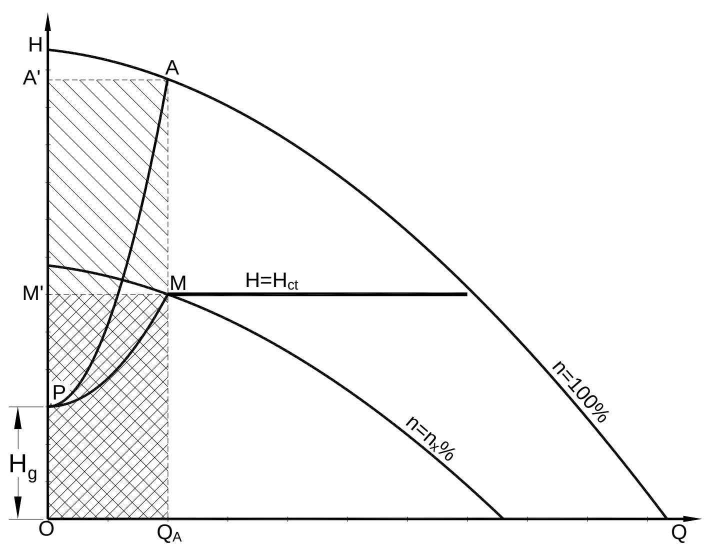


*Fig.48. Geometric areas of hydraulic powers*

If the same flow $Q_A$, is regulated by the pump speed at the pumping head required in the hydraulic network, $H = H_M$, the electric power absorbed is:

$$P_{elM} = \frac{P_h}{\eta_{em} \cdot \eta_{pM}} = \frac{\rho \cdot g \cdot Q_M \cdot H_M}{\eta_{em} \cdot \eta_{pM}} \tag{47}$$

The difference of powers will be the difference of the areas on each considered domain. The equation deduced from (46) and (47) is:

$$\Delta P_{el} = \frac{\rho \cdot g \cdot Q_A}{\eta_{em}} \cdot \left(\frac{H_A}{\eta_{pA}} - \frac{H_M}{\eta_{pM}}\right) \quad (48)$$

*A case study on energy saving*

The pumping station behavior results from overlapping the pump operation characteristic at variable speed over the pipe network operation characteristic. A minimum flow rate $Q_{min}$, a medium flow rate $Q_{med}$ and a maximum flow rate $Q_{max}$ can be estimated taking into account the requirements of the consumers from the supplied network. The share of these flow rates in the exploitation is expressed in percents through a coefficient, $C_{ut}$, which results from a statistical study. Also, for the closed hydraulic loop from this case we assume that it has to ensure constant pressure in conformation with a constant pumping head, $H_{rq} = 30\ m$, for the following domains of flow rate, (Kudo, 1994):
$\Delta Q_{min} = 0.4 - 0.7\ 1/s$ with a coefficient $C_{utmin} = 20\%$
$\Delta Q_{med} = 0.7 - 1.1\ 1/s$ with a coefficient $C_{utmed} = 65\%$
$\Delta Q_{max} = 1.1 - 1.4\ 1/s$ with a coefficient $C_{utmax} = 15\%$
The corresponding flow rates for the three domains are: $Q_1$ = 0.4 l/s; $Q_2$ = 0.7 l/s; $Q_3$ = 1.1 l/s; $Q_4$=1.4 l/s. To these flow rates, are corresponding the following pumping heads $H_1$, $H_2$, $H_3$ and $H_4$, according to the pumping head characteristic for the maximum pump speed. If the pumping station would not have the possibility to adjust the speed, then the flow rate adjustment on the consumers would be realized only through the outlet vane and on the given domain will be provided a covering pumping head between 31 m and 58 m, although in the pipes network would be sufficient a 30 m pumping head.
Even if the pump efficiency is relatively good in this domain, it can be proved that a big part of the energy consumed is unnecessarily wasted. If we consider the possibility of adjusting the speed, then it becomes possible the adjustment of the installation so that the pumping head to be maintained constant, $H_{rq}$ = 30 m and to provide to any consumer from the network the optimum operating conditions.
In the industrial installations the adjusting through outlet vane is realized at the consumer and the adjustment through speed is performed in the pumping station. The operating of the pump at three domains of flow rate show that the efficiencies and the pumping heads are sensible different, from one operating point to another. This is why in the following section is presented an averaging method of the power on the three exploitation domains.
The shaft-power of pump results from the formula:

$$(\Delta P_{el})_{med} = \frac{\sum_{k=0}^{N} \Delta P_{elk}}{N+1} \tag{49}$$

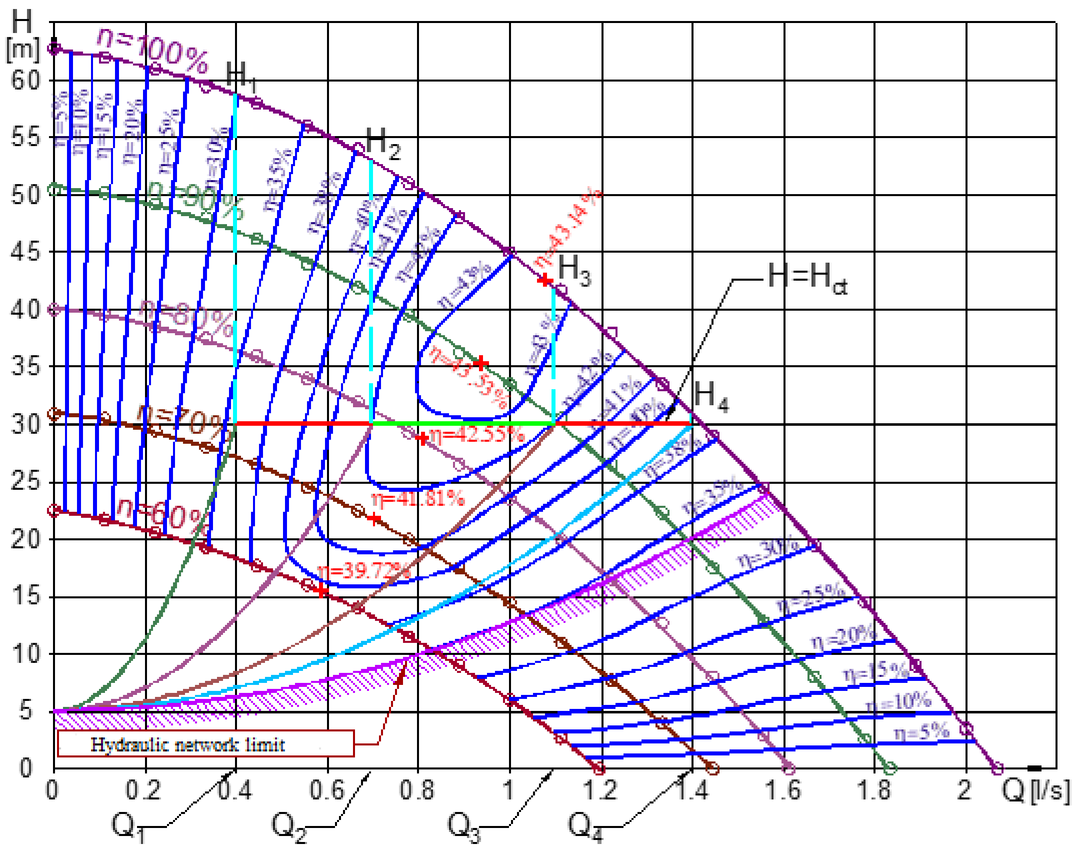


*Fig.49. Characteristic curves of the pump with pipes network characteristics and the exploitation domains*

The saving of the energy consumed depends on the running time according to the equation:

$$\Delta E = (\Delta P_{el})_{med} \cdot N_{dy} \cdot N_{hd} \cdot C_{ut} \; [kWh] \tag{50}$$

where $N_{dy}$-number of the days from a year (365), $N_{hd}$-number of hours of a day (24).

The results obtained for the three domains are presented in Table 3 and 4. It is noted that the share of energy savings can reach up to 35% of the total energy consumed if the flow rate adjustment would have been made only through the outlet vane.

*Table 3. The results obtained for the three domains*:

| Flow rate domains | $Q_1 = 0.4\ [\frac{l}{s}]$ | $Q_2 = 0.7\ [\frac{l}{s}]$ | $Q_3 = 1.1\ [\frac{l}{s}]$ | $Q_4 = 1.4\ [\frac{l}{s}]$ |
|---|---|---|---|---|
| $H_{n=100\%}[m]$ | 58.75 | 52.99 | 41.81 | 30.96 |
| $\eta_{n=100\%}[\%]$ | 29.59 | 38.81 | 43.14 | 39.30 |
| $\eta_{H=30m}$ [%] | 36.00 | 41.95 | 41.96 | 38.8 |

*Table 4. Energy saving for the three domains*:

| Flow rate domains | $C_{ut}$ [%] | $(P_{el})_{med}$ $(n = 100\%)$ [kW] | $(P_{el})_{med}$ $H = 30m$ [kW] | $(\Delta P_{el})_{med}$ [kW] | $\Delta E$ [kW] |
|---|---|---|---|---|---|
| $Q_1 \div Q_2$ | 20 | 1.005 | 0.481 | 0.524 | 918 |
| $Q_2 \div Q_3$ | 65 | 1.167 | 0.743 | 0.424 | 2414 |
| $Q_3 \div Q_4$ | 15 | 1.252 | 1.078 | 0.173 | 228 |
| $(\Delta E)_{total}$ [kWh] | | | | | 3560 |
| $E_{total}(case\ n = n_{max})$ [kWh] | | | | | 10049 |
| $Economy = \frac{(\Delta E)_{total}}{E_{total}}$ [%] | | | | | 35.42 |

Another study in the same grant was done in the application of graphs theory in order to determine the optimal route of a pipeline supply, which is at a great distance from the target consumer (the pipeline network of a city). This applies when the distance from the source to the target, because of the configuration of the landscape, has several variants of routes passing through some mandatory points. In this way, the route has **n** sections, and on each section the total cost (investment plus operating for one year) has a certain value. If the route can be browsed by more than two ways, then the method becomes profitable. Implementation of the method was through a special program, using the Borland Pascal programming and Bellman-Kalaba algorithm.
Through investment and energy consumption, the water adductions have a significant share in the water supplies systems and it is important to optimize their routes. Modern mathematical disciplines, by operational calculation, put at specialist's disposition a vast apparatus of scientific analysis in determining the optimal decisions for the design of water supply. In this context the following study describes a deterministic mathematical model optimization of the route of the water supply networks, based on the theory of graphs.

*The Calculation algorithm*

Modeling this problem is achieved through representation related directed graph *G=(X, U)* consisting of the source as the origin, route as required arcs and points as vertices. For each arc $u_j^i \in U$ is associated a number $\lambda(u_j^i) \geq 0$, in conventional units, depending on the optimization criterion adopted. The route is the best way to graph the minimum value which is determined by applying the algorithm Bellman-Kalaba. The Graph G= (X, U) is attached to a matrix M whose elements $m_{ij}$ are:

$$\boldsymbol{m_{ij}} = \begin{cases} \boldsymbol{\lambda(u_j^i)} \ - \ the\ arc\ value\ from\ \boldsymbol{x_i}\ to\ \boldsymbol{x_j} \\ \infty \ - \ if\ the\ verticies\ \boldsymbol{x_i}\ and\ \boldsymbol{x_j}\ are\ not\ adjacent \\ \boldsymbol{0} \ - \ for\ \boldsymbol{i = j} \end{cases} \tag{51}$$

The optimal route is the best way of graph **μ**, with the total value:

$$\lambda(\mu) = \sum_{u_j^i \in \mu} \lambda(u_j^i) \rightarrow min \tag{52}$$

If the notes with $V_i$ the minimum value of the road in $\mu_n^i, (i = \overline{0,n})$ existing from the tip of $x_i$ to the tip of $x_n$ :

$$V_i = \lambda(\mu_n^i), \quad (i = \overline{0,n}) \tag{53}$$

hence:

$$V_n = 0 \tag{54}$$

then, under the principle of optimality:

$$V_i = \min_{j \neq i}(V_j + m_{ij}), \quad (i = \overline{0,n-1};\ j = \overline{0,n}) \quad \text{and} \quad V_n = 0 \tag{55}$$

In order to solve the system (55) iteratively, we note with $V_i^k$ the value of $V_i$ obtained at the iteration $k$, namely:

$$V_i^0 = m_{in} \quad (i = \overline{0,n-1}); \qquad V_n^0 = 0 \tag{56}$$

We calculate:

$$V_i^1 = \min_{j \neq i}(V_j^0 + m_{ij}), \quad (i = \overline{0,n-1};\ j = \overline{0,n}) \quad \text{and} \quad V_n^1 = 0 \tag{57}$$

and then:

$$V_i^k = \min_{j \neq i}(V_j^{k-1} + m_{ij}), \quad (i = \overline{0,n-1};\ j = \overline{0,n}) \quad \text{and} \quad V_n^k = 0 \tag{58}$$

The iteration of $k$ order expressed by the relations (58) gives values only for the finite length of roads at most $k + 1$ arriving at $x_n$, choosing between them the minimum.
From one iteration to the next:

$$V_i^k \leq V_i^{k-1}, \qquad \forall j \tag{59}$$

The numbers $V_i^k$ $(i \neq n\,;\, k = 0, 1, \ldots)$ form monotone decreasing patterns, so that a minimum is necessarily reached, after a finite number of iterations that does not exceed $n - 1$. So, the algorithm stops when it reaches an iteration k, such that $V_i^k = V_i^{k-1},\ i = \overline{0,n-1}$ and the minimum road value between the peaks $x_0$ and $x_n$ is $V_0^k = V_0^{k-1}$.
In order to identify which roads have the minimum values, we found from (58) that among them we have at the last iteration:

$$V_i^k = m_{ij} + V_j^{k-1} = m_{ij} + V_j^k \tag{60}$$

Based on the algorithm described, a computer program named BEL_KAL was designed in

Borland PASCAL language.

There were made following nomenclatures: *N* is the order of the graph, *V (I, J)* is the column vector built at each iteration *k*, *X (I)* is the sequence of minimum road; *VAL*- the minimum road graph, *M(I, J)* - matrix associated with graph, whose elements are:

$$m_{ij} = \begin{cases} \lambda(u_j^i) \; - \; if \; arc \; (x_i, x_j) \; exists \\ \sum_{i,j=1}^{n} \lambda(u_j^i) \; - \; if \; arc \; (x_i, x_j) \; does \; not \; exists \\ 0 \; - \; for \; i = j \end{cases} \tag{61}$$

As entries data, are introduced the graph order and its associated matrix, on lines, whose elements are considered equal to $\lambda(u_j^i)$, if the arc $(x_i, x_j)$ exists, or equal to 0, otherwise (MATR_EX1.dat file).
As output data, we obtain the sequence of the minimum values of road peaks and their values.

*A case study*

It is considered a water adduction main for a locality L, starting from two catchment locations S1 and S2 (Fig.50). The possible routes pass through the bound points A, B, C, D, E, forming three sectors.

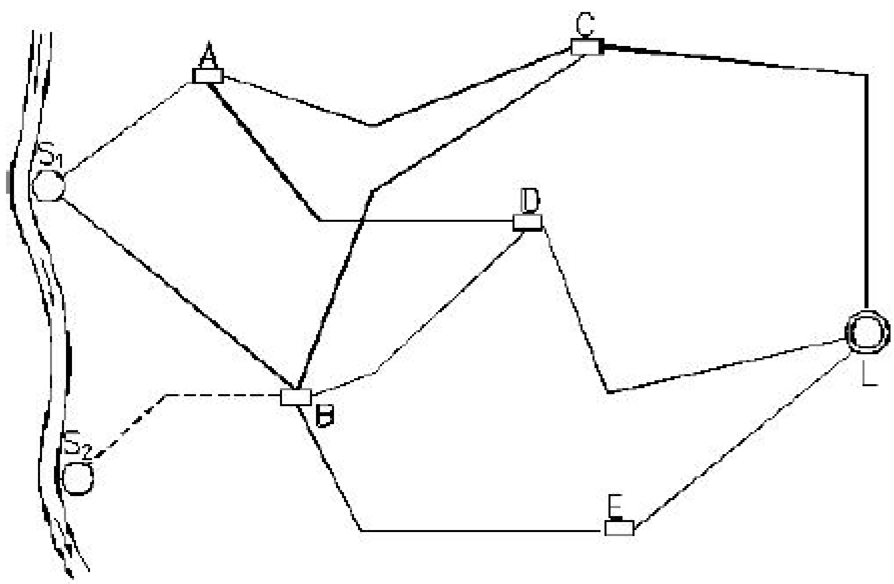


*Fig.50. Variants of the adduction route*

Putting the problem of determining the route for which the total cost is minimum, the investments for each track are determined and prepared the partial sequence graph in Fig. 50, where each arc is associated with a cost, in conventional units. The decision variables for each sector are noted with $x_1$, $x_2$, $x_3$ and $x_4$. These variables will not have numerical values, but they will be vertices of graph that are on the same alignment.
It exemplifies the application of Bellman-Kalaba algorithm to determine the optimal bus route for L locality from the water source S1 (Fig.50).
Modeling problem is achieved through the representation of the related directed graph $G = (X, U)$ of order $n = 7$, consisting of the source point of origin, route as required arcs and points as vertices. For each arc $u_j^i \in U$, there is assigned a cost in conventional units (Fig. 51) and a matrix M attached to graph $G = (X, U)$ are the elements $m_{i,j}$ defined by relations (51), where $\lambda(u_j^i)$ is the value attributed to edge $u_j^i \in U$.

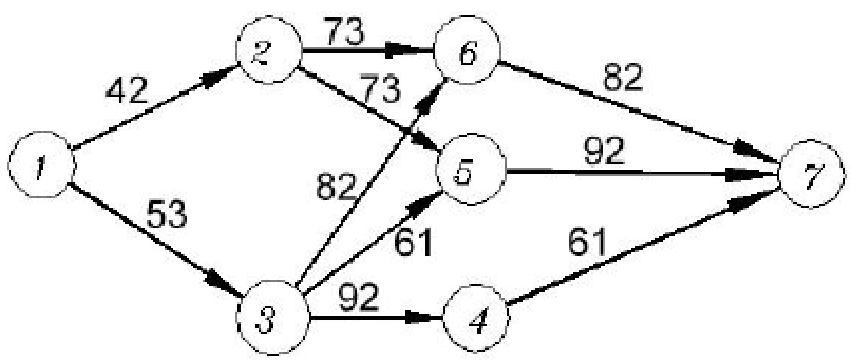


*Fig.51. Graph adduction routes*

$$M = \begin{array}{c|ccccccc|cccc}
 & 1 & 2 & 3 & 4 & 5 & 6 & 7 & V_i^0 & V_i^1 & V_i^2 & V_i^3 \\
1 & 0 & 42 & 53 & \infty & \infty & \infty & \infty & \infty & \infty & 197 & 197 \\
2 & \infty & 0 & \infty & \infty & 73 & 73 & \infty & \infty & 153 & 153 & 153 \\
3 & \infty & \infty & 0 & 92 & 61 & 82 & \infty & \infty & 153 & 153 & 153 \\
4 & \infty & \infty & \infty & 0 & \infty & \infty & 61 & 61 & 61 & 61 & 61 \\
5 & \infty & \infty & \infty & \infty & 0 & \infty & 92 & 92 & 92 & 92 & 92 \\
6 & \infty & \infty & \infty & \infty & \infty & 0 & 82 & 82 & 82 & 82 & 82 \\
7 & \infty & \infty & \infty & \infty & \infty & \infty & 0 & 0 & 0 & 0 & 0
\end{array} \quad (62)$$

The route with the minimum total cost is given by the way of minimum value in this graph, which is determined using Bellman-Kalaba algorithm.
For each $V_i^k$ $(k = 0,1,\dots)$ a column is added to the previous matrix in which values are inserted properly. The calculus is done successively:
a) There are calculated the values $V_i^0 = m_{i7}$, ($i$= 1, ..., 7), written into the column $V_i^0$.
b) There are calculated the values $V_i^1 = m_{i7}$, $i$= 1, ..., 7, ($j$= 1, ..., 7), and written into (63):

$$\begin{cases} V_1^1 = \min\limits_{j\neq 1}\left(V_j^0 + m_{1j}\right) = \min\left(V_2^0 + m_{12},\ V_3^0 + m_{13}, \dots,\ V_7^0 + m_{17}\right) = \infty \\ V_2^1 = \min\limits_{j\neq 2}\left(V_j^0 + m_{2j}\right) = \min\left(V_1^0 + m_{21},\ V_3^0 + m_{23}, \dots,\ V_7^0 + m_{27}\right) = 153 \\ V_3^1 = \min\limits_{j\neq 3}\left(V_j^0 + m_{3j}\right) = \min\left(V_1^0 + m_{31},\ V_2^0 + m_{32}, \dots,\ V_7^0 + m_{37}\right) = 153 \\ V_4^1 = \min\limits_{j\neq 4}\left(V_j^0 + m_{4j}\right) = \min\left(V_1^0 + m_{41},\ V_2^0 + m_{42}, \dots,\ V_7^0 + m_{47}\right) = 61 \\ V_5^1 = \min\limits_{j\neq 5}\left(V_j^0 + m_{5j}\right) = \min\left(V_1^0 + m_{51},\ V_2^0 + m_{52}, \dots,\ V_7^0 + m_{57}\right) = 92 \\ V_6^1 = \min\limits_{j\neq 6}\left(V_j^0 + m_{6j}\right) = \min\left(V_1^0 + m_{61},\ V_2^0 + m_{62}, \dots,\ V_7^0 + m_{67}\right) = 82 \\ V_7^1 = 0 \end{cases} \tag{63}$$

c) There are calculated the values $V_i^2$, for $i$= 1, ..., 7, ($j$= 1, ..., 7) and written into (64):

$$\begin{cases} V_1^2 = \min\limits_{j\neq 1}\left(V_j^1 + m_{1j}\right) = \min\left(V_2^1 + m_{12},\ V_3^1 + m_{13}, \dots,\ V_7^1 + m_{17}\right) = 197 \\ V_2^2 = \min\limits_{j\neq 2}\left(V_j^1 + m_{2j}\right) = \min\left(V_1^1 + m_{21},\ V_3^1 + m_{23}, \dots,\ V_7^1 + m_{27}\right) = 153 \\ V_3^2 = \min\limits_{j\neq 3}\left(V_j^1 + m_{3j}\right) = \min\left(V_1^1 + m_{31},\ V_2^1 + m_{32}, \dots,\ V_7^1 + m_{37}\right) = 153 \\ V_4^2 = \min\limits_{j\neq 4}\left(V_j^1 + m_{4j}\right) = \min\left(V_1^1 + m_{41},\ V_2^1 + m_{42}, \dots,\ V_7^1 + m_{47}\right) = 61 \\ V_5^2 = \min\limits_{j\neq 5}\left(V_j^1 + m_{5j}\right) = \min\left(V_1^1 + m_{51},\ V_2^1 + m_{52}, \dots,\ V_7^1 + m_{57}\right) = 92 \\ V_6^2 = \min\limits_{j\neq 6}\left(V_j^1 + m_{6j}\right) = \min\left(V_1^1 + m_{61},\ V_2^1 + m_{62}, \dots,\ V_7^1 + m_{67}\right) = 82 \\ V_7^2 = 0 \end{cases} \tag{64}$$

d) There are calculated the values $V_i^3$, for $i$= 1, ..., 7, ($j$= 1, ..., 7) and written in (65). Since $V_i^2 = V_i^3$ for $i$= 1, ..., 7, the algorithm stops and the road is the minimum of $V_i^2 = V_i^3 = 197$. This value is reached on the way (1, 2, 6, 7), thus resulting in optimal route of adduction as: *S1, A, C, and L*. To solve this problem the computer program BEL_KAL was used.

$$\begin{cases} V_1^3 = \min\limits_{j \neq 1}\left(V_j^2 + m_{1j}\right) = 197 \\ V_2^3 = \min\limits_{j \neq 2}\left(V_j^2 + m_{2j}\right) = 153 \\ V_3^3 = \min\limits_{j \neq 3}\left(V_j^2 + m_{3j}\right) = 153 \\ V_4^3 = \min\limits_{j \neq 4}\left(V_j^2 + m_{4j}\right) == 61 \\ V_5^3 = \min\limits_{j \neq 5}\left(V_j^2 + m_{5j}\right) = 92 \\ V_6^3 = \min\limits_{j \neq 6}\left(V_j^2 + m_{6j}\right) = 82 \\ V_7^3 = 0 \end{cases} \tag{65}$$

As conclusions for this study, the mathematical model is easily programmable in an evolved language, obtaining immediate results. The only problem is populating the matrix attached graph.

Although Bellman-Kalaba algorithm was originally designed for economy, the adaptation in water supplies routes calculation was possible with quite good results.

**I.3.4. Research in the field of wind turbines and air dynamics [21, 22, 23, 24, 25, 26]**

One of the studies in this domain was done during the research partnership project with the title „Energetically servicing of a local community using air currents", an electrical wind unit of small power designated for the rural households in Romania, coordinated by Politehnica" University of Timisoara.

The wind turbine was designed for emplacements with moderate wind speeds (middle speed 3-6 (m/s)) with possibilities of adaptation at different wind regimes.

The characteristics of the wind turbine are: runner diameter (4.4 m), tip-speed ratio (3-4), runner speed (100-160 rpm), nominal power (3.5 kW), number of blades (4), chord of profiles in active zone (200-380 mm).

All the profiles used were NACA with 4 digits type and their geometry was determined from loading conditions of the blade with the radius and wind speed of upstream of the rotor.

It resulted in 9 active sections situated between the radius of 600 mm and 2200 mm. From the radius 300 mm to 600 mm was made a transition streamlined to rectangular shape of blade axle pin. At the peripheral, the blade was prolonged with a progressive reverberation to 90° unto pressure side, in order to avoid as much as possible the air stream which appears at finite wing span between pressure side and suction side.

Next phase of blade construction was to create the 3Dsolid in AutoCAD Mechanical Desktop so that the derived file to be used in the machine program from the collaborator factory.

*The geometrical characteristics of the airfoils of the wind turbine blade*

Based on the hydrodynamic calculus, the geometric characteristics of the airfoil were obtained from each calculated section. The ordering and numbering of the calculus sections was from 0 to n, beginning with the hub section (section 0) and finishing with tip section (section n). The total number of sections was 12.

*Table 5. Geometrical characteristics of the blade sections designed with Naca airfoils*

| *Number of section* | *NACA Profile code* | *Radius of calculus section r [mm]* | *Length of the profile l [mm]* | *Stagger angle $\beta s$ [°]* | *Relative thickness d/l [%]* |
|---|---|---|---|---|---|
| H1 | 14.586 | 300 | 140 | 6 | 58.6 |
| H2 | 24.406 | 400 | 220 | 12 | 40.6 |
| H3 | 34.300 | 500 | 310 | 17 | 30.0 |
| A1 | 44.263 | 600 | 380 | 23 | 26.3 |
| A2 | 44.236 | 800 | 361.12 | 16.75 | 23.6 |
| A3 | 44.220 | 1000 | 338.90 | 13.0 | 22.0 |
| A4 | 44.204 | 1200 | 316.60 | 10.5 | 5 20.4 |
| A5 | 44.188 | 1400 | 294.46 | 8.71 | 18.8 |
| A6 | 44.172 | 1600 | 272.24 | 7.38 | 17.2 |
| A7 | 44.156 | 1800 | 250.02 | 6.33 | 15.6 |
| A8 | 44.140 | 2000 | 227.80 | 5.5 | 14.0 |
| A9 | 44.124 | 2200 | 205.58 | 4.82 | 12.4 |
| P1 | 00.124 | 2207.76 | 195.63 | 4.01 | 12.36 |
| P2 | 00.118 | 2215 | 185.67 | 3.21 | 11.8 |
| P3 | 00.109 | 2221.21 | 175.72 | 2.41 | 10.9 |
| P4 | 00.104 | 2226.0 | 165.77 | 1.61 | 10.4 |
| P5 | 00.100 | 2229.0 | 155.81 | 0.80 | 10.0 |
| P6 | 00.95 | 2230.0 | 145.86 | 0.0 | 9.5 |
| P7 | 00.90 | 2230.0 | 135.91 | 0.0 | 9.0 |
| P8 | 00.85 | 2230.0 | 125.95 | 0.0 | 8.5 |
| P9 | 00.80 | 2230.0 | 116.0 | 0.0 | 8.0 |

*The Design of the airfoils in own system of Representation*

Initially the geometry of the airfoils is according to datum from catalogue or codification and relations gives for the NACA airfoil numerical code (four, five or six digits), but for the theoretical airfoils according with conformal mapping.
At first works in dimensionless (all dimensions are reported to length "l" of the profiles). The NACA airfoils are given by camber line function, $\frac{y_f}{l}\left(\frac{x}{l}\right)$ and thickness function, $\frac{y_d}{l}\left(\frac{x}{l}\right)$. The thickness function defines semithickness of the profile measured to the normal of the camber line, Fig. 52. Relative abscissa of the maximum thickness is at $\frac{x_{dmax}}{l} = 0.3$,

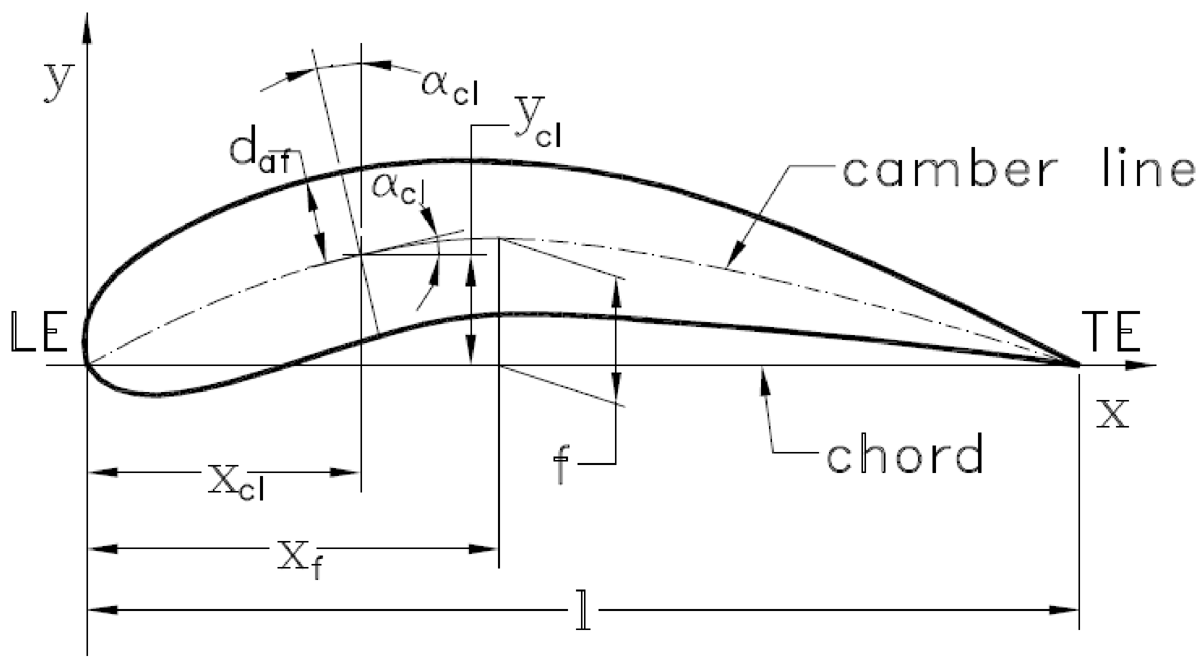


*Fig.52. Geometrical construction of NACA airfoil*

It can be seen that the camber function is defined by two parabola arcs perfectly jointed so that, airfoil camber line to continue in the interval [0, 1]. The profile construction and implicitness of the blade was made through N points calculated and distributed onto pressure side and respectively onto suction side. The simplest distribution (discretization) of the points is the uniform distribution, which realizes equal intervals for x between 0 and 1. This discretization has the disadvantage that in any zone where the curvature of the profile boundary is more pronounced (leading edge) makes that, the smoothness of curve in not quite proper.

Therefore, the option is for a non-uniform discretization of the domain, thickening the number of points at the leading edge. Working in the interval [0, 1], the best non-uniform distribution is offered by trigonometric functions.

If N is the maximum number of intervals and $i$ is the index of a current point, $i=0...N$, let $t_i$ be the argument of the trigonometric function defined as:

$$t_i = \frac{\pi}{2} \cdot \frac{1}{N} \cdot i \tag{66}$$

The abscissa of the discretization, $x_i$, is calculated with the relation:

$$x_i = 1 - cos(t_i) \tag{67}$$

It can be observed that at the extremities, $i=0$ and $i=N$, there are obtained just extremes values 0, respectively 1, but in the domain area the maximum density is at the proximity of 0, i.e. at the leading edge of the profile. This option will be reflected in all ulterior calculus and will favorably affect the accuracy and smoothness of the obtained surfaces for the blade. Forwards, for simplifications of relations, will abandon expression of the variables and functions used by reporting to "l" (length of the profile) although it was calculated at a given moment to dimensionless.

• ($x_{ex}$, $y_{ex}$), the coordinate of the current point from the suction side of the airfoil
• ($x_{in}$, $y_{in}$), the coordinate of the current point from the pressure side of the airfoil
• ($x_{cl}$, $y_{cl}$), the coordinate of the current point from the camber line of the airfoil
• $d_{af}(x_{cl})$, thickness function

The abscissa $x_{cl}$ is identically with $x_i$, the abscissa of nonuniform discretization.
According to Fig. 52, and using the calculated values for the camber line function and thickness function, there were determined the points from the pressure side and the suction side with the following relations:

$$\begin{cases} x_{in} = x_{cl} + d_{af} sin(\alpha_{cl}) \\ y_{in} = y_{cl} - d_{af} cos(\alpha_{cl}) \end{cases} \tag{68}$$

$$\begin{cases} x_{ex} = x_{cl} - d_{af} sin(\alpha_{cl}) \\ y_{ex} = y_{cl} + d_{af} cos(\alpha_{cl}) \end{cases} \tag{69}$$

The angle $\alpha_{cl}$ represents the angle of the tangent at the chamber line in the calculus point. It results from the derivative of camber line function in corresponding points. At NACA profile with four digits the derivatives of the two parabola arcs are like the relations:

$$\begin{cases} y'_{f1} = \frac{f_{max}}{x^2_{fmax}}\left(2 \cdot x_{fmax} - 2x\right) \\ y'_{f2} = \frac{f_{max}}{\left(1 - x_{fmax}\right)^2}\left(2 \cdot x_{fmax} - 2x\right) \end{cases} \tag{70}$$

*The design of transposition of the airfoils stagger angle, βs, into the plane section*

Starting from the representation from Fig.52, the profile will be transposed in the specific working position, in the cascade airfoil of the corresponding section from the runner. This operation is done in the developed plane of the calculus section. Treating this transposition in order, it can be said that it is realized in two stages:

- stage I: translation in axis of blade spindle;

- stage II: rotation around axis of blade spindle until the stagger angle βs;

The two stages are illustrated accordingly in Fig. 53 respectively Fig.54.

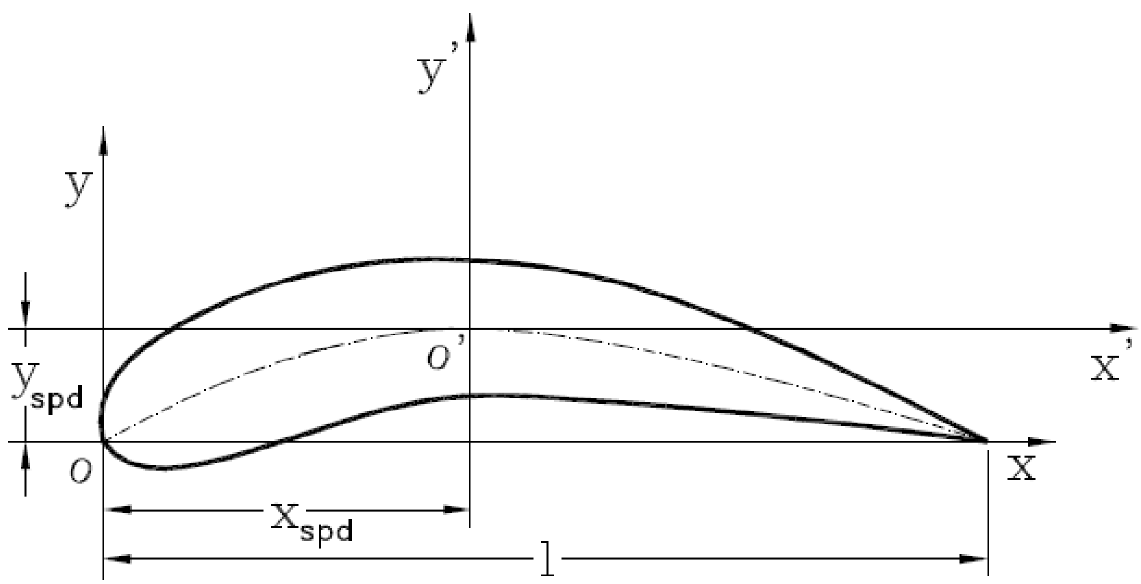


*Fig.53. Stage I, translation of the axis system into the spindle axis of the blade*

The relations through which is made the translation of the axis system into the spindle axis of the blade are:

$$\begin{cases} x' = x - x_{spd} \\ y' = y - y_{spd} \end{cases} \tag{71}$$

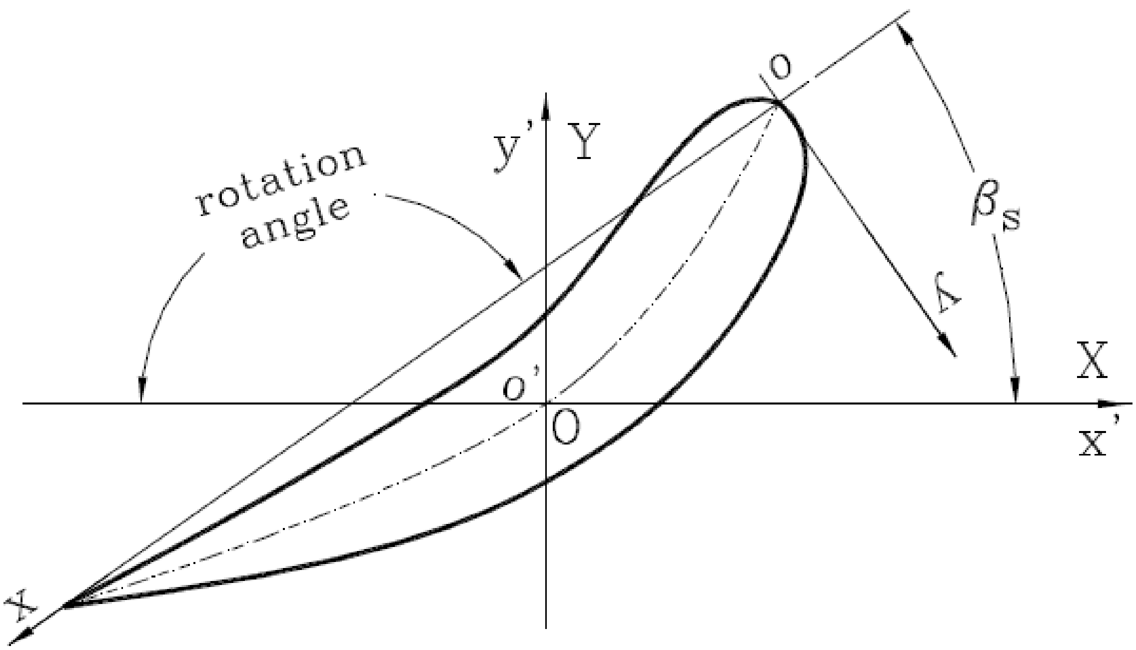


*Fig.54. Stage II: the rotation around axis of blade spindle until the stagger angle, βs*

The relations used for the rotation around the axis of the blade spindle at the stagger angle, βs, are:

$$\begin{cases} X = -x'cos(\beta_s)+y'sin(\beta_s) \\ Y = -x'sin(\beta_s)-y'cos(\beta_s) \end{cases} \quad (72)$$

Fig. 55, 56, 57, 58 and 59 present the profiles for each section and the 3D image of the blade and the wind turbine. This mode of representation has great importance in the design phase because it admits the visualization of every detail of blade's surface from whatever angle should be seen the runner.

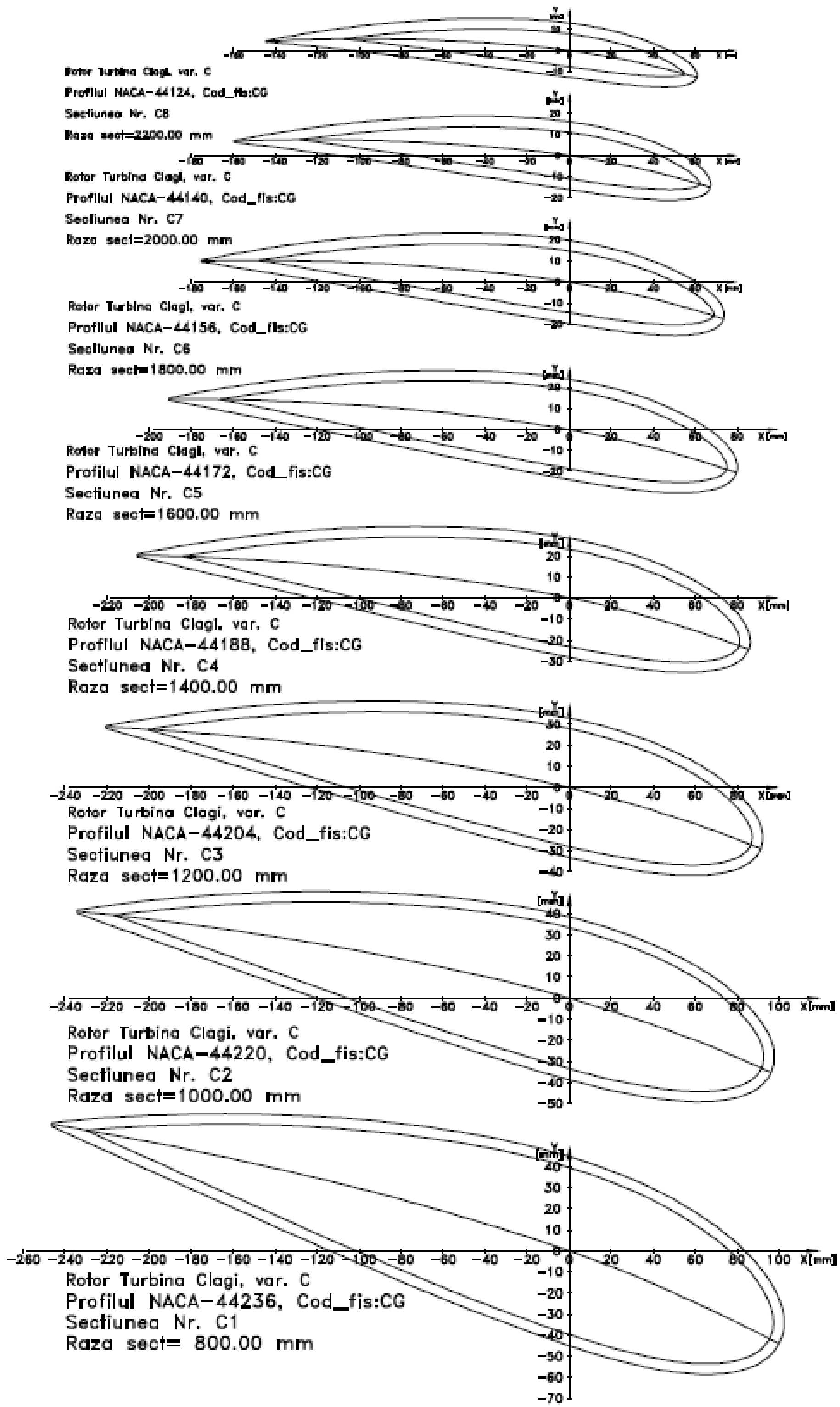


*Fig.55. The profiles obtained for the active zone*

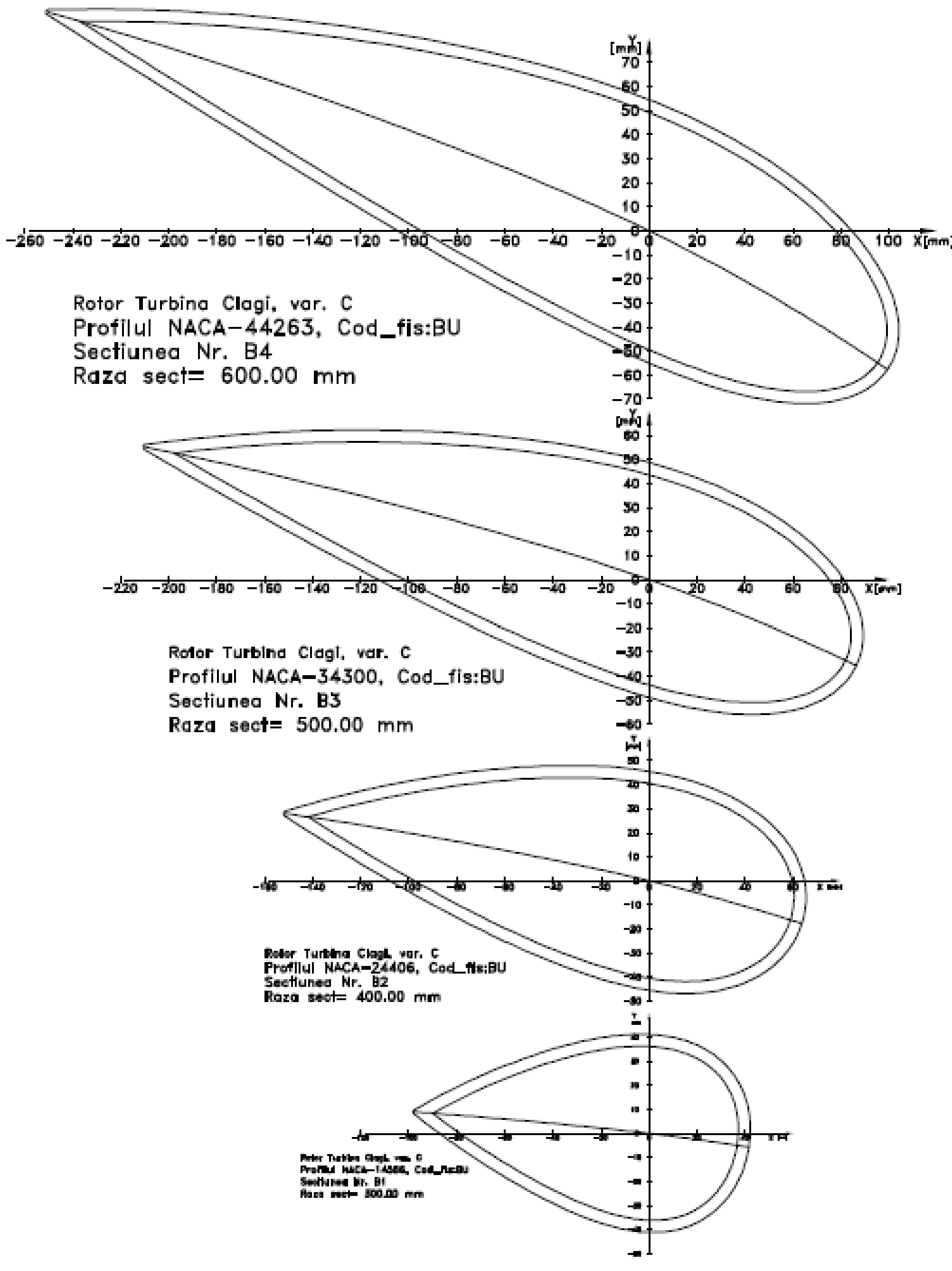


*Fig.56. The profiles obtained for the hub zone*

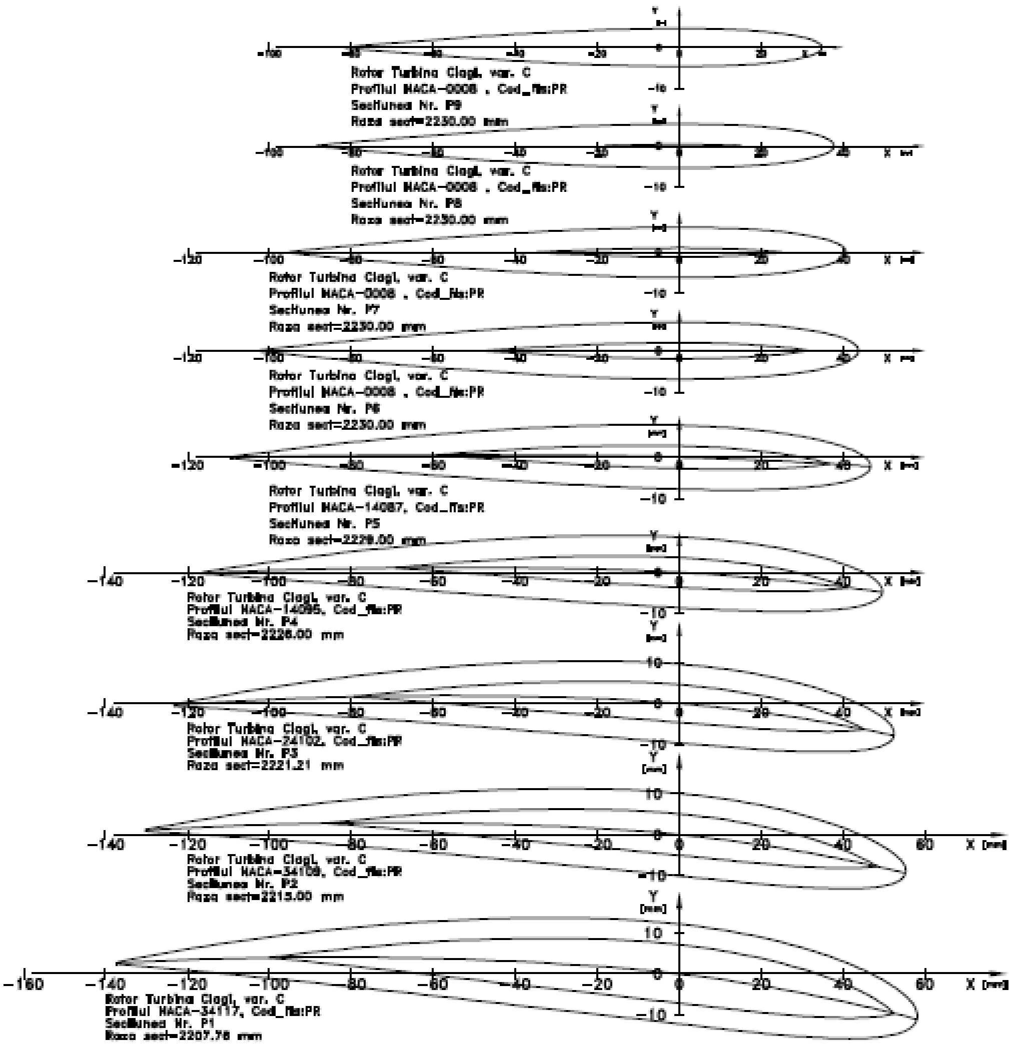


*Fig.57. The profiles obtained for the peripheral zone*

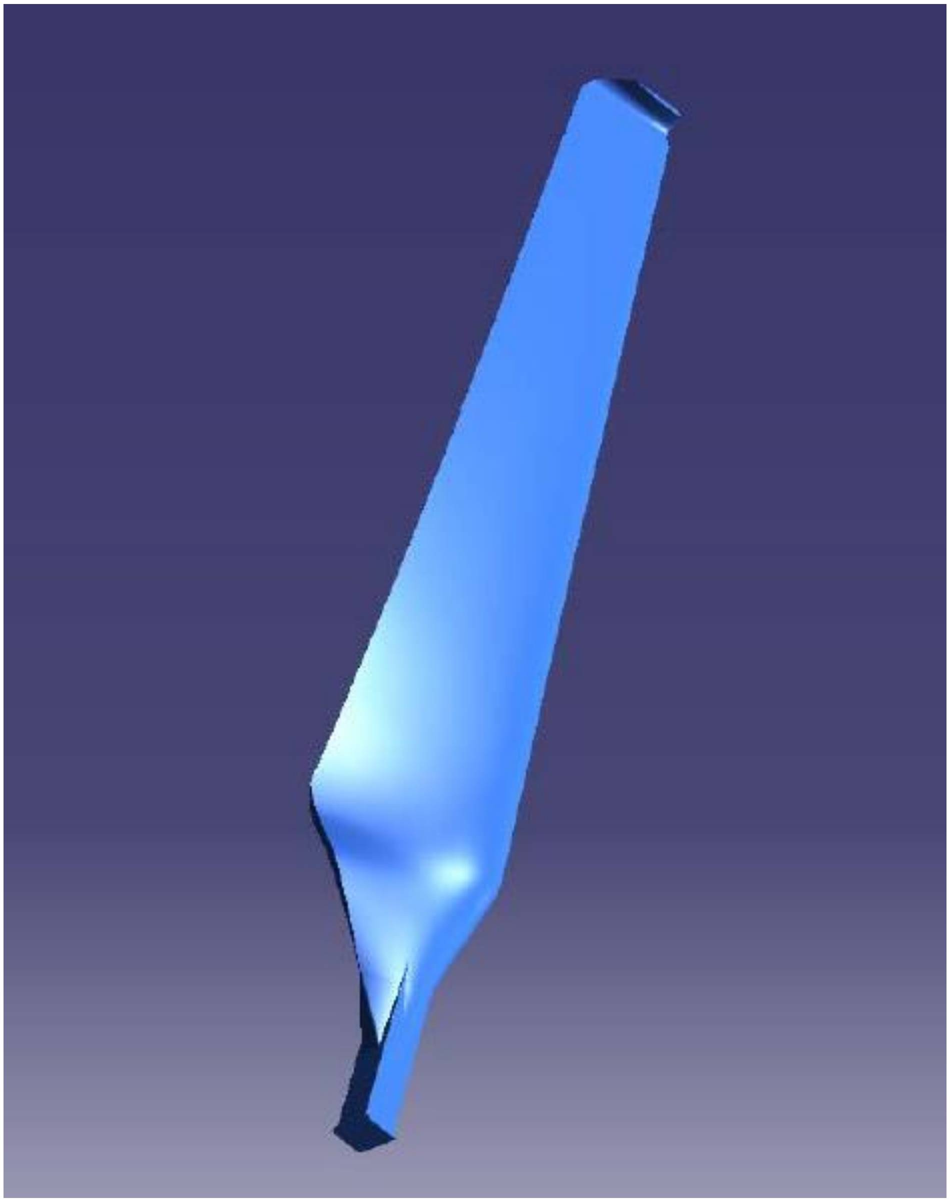

*Fig.58. The blade of the wind turbine*

*Fig.58. The Catia Wind turbine model*

The method presented was fully computerized and has some of the advantages of data processing:
- increases the working speed if the programs are arranged.
- immediately verification of blade geometrical shape giving indices about some little corrections in the hydrodynamic calculus of the airfoil's length and thicknesses;
- a great part of graphical representations and tables can enter directly in the execution project of the blade;
- the data being in electronic format is transposable immediately to scale down for manufacturing the runner model;
- the cogging torque is small enough that the turbine can start at a wind speed of 2-3 m/s.

The study presented above is the base of the design of the wind turbine blades, that was built and placed in the area of Marga Commune of Caraş-Severin County for supplying electricity to the Sanatorium Complex of the CHRISTIAN MEDICAL ASSOCIATION "IZVORUL TĂMĂDUIRII".

One important part of this project was the static tests of the wind turbine blade for the Marga aggregate. The tests were conducted by regretted Prof. Dr. Ing. Francisc Gyulay. There were done two tests, one in which the blade spindle broke at a load corresponding to a mass of 150 kg and one in which the blade spindle was redesigned and broke at 250 Kg. The test stand and the load tests for the initial blade spindle are presented on Fig. 59, 60 and 61.

*Fig.59. The test stand for the blade*


*Fig.60. The blade variant 1 loaded with 100 kg*

*Fig.61. The blade spindle broken at 150 kg*

The redesigned blade spindle tests are presented in Fig. 62 and Fig. 63.

*Fig.62. The blade variant 2 loaded with 175 kg*

*Fig.63. The blade variant 2 loaded with 200 kg*

*Fig.64. The blade variant 2 with broken spindle at 250 kg*

*Fig.65. The blade broken spindle view*

Fig. 64 and 65 present the redesigned spindle breaking at 250 kg load and the broken section. After these tests the spindle design was improved even better, the blade manufacturer did static loading tests with 350kg, which ensured $\sigma_r$=600 daN/cm$^2$ as specified in the design data.
Fig. 66 up to 69 present some pictures with the manufactured wind turbine and its commissioning.

*Fig.66. The wind turbine at Clagi manufacturing center front view*

*Fig.67. The wind turbine at Clagi manufacturing center lateral view*

*Fig.68. The wind turbine pillar mounted*

*Fig.69. The wind turbine assembled mounted on the intermediate pillar*

This wind turbine was the first one designed and made using fiber glass technology and permanent magnet motors by the collective of Hydraulic Machinery from Politehnica University of Timisoara. The automation part was also conducted “in house” by our colleagues from Automation Department.
The hydraulic machinery collective was driven by Conf. Dr. Ing. Teodor Milos and carefully checked by Prof.Dr.Ing. Francisc Gyulai, with me a young PhD. Assistant as member, together with Conf. Dr. Ing Adriana Sida Manea, S.L.Dr. Ing. Eugen Dobândă, S. L. Dr. Ing. Rodica Bădărău and regretted Technical assistant Ioan Potorac.
I am very happy and glad that I could see the design work of a wonderful team in practice.

Another experimental study in the domain of hydrofoils and air-hydrodynamics was conducted over the measurement methodology and the experimental results for a “S” type hydrofoil used for the wicket gate of a reversible hydraulic machine.
The measurements were done in an open circuit wind tunnel of the Air-dynamic Laboratory of Mechanical Faculty, designed and made by the Hydraulic Machinery Team, presented in Fig. 70.

*Fig.70. The MHT open circuit wind tunnel.*

The hydrofoil is mounted in the tunnel, such as to achieve the conditions of infinite span, to avoid the formation of end vortices and the appearance of induced resistance, presented in Fig. 71, together with the switching of the pressure taps magneto fluidic switch, designed and manufactured within the collective of Magnetic Liquids from Timisoara, Fig. 72.

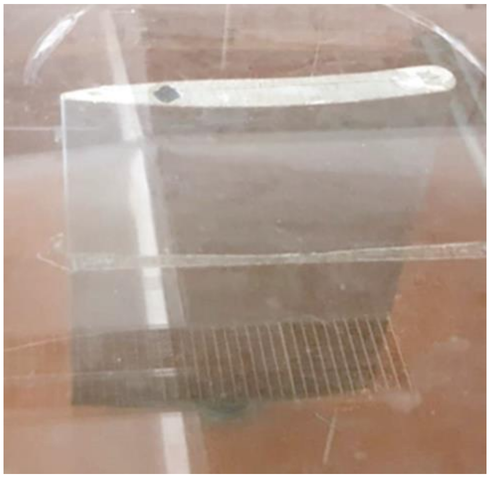

*Fig.71. The MHT-S hydrofoil in wind tunnel working zone*

*Fig.72. The magneto fluidic switch together with the instrument for measuring the differential pressure*

Further there were determined the pressure distributions on the hydrofoil for the incidence angles α = 0°, 5°, 10°, 15°, 25° and there were calculated the lift and drag coefficients presented in Fig. 73.

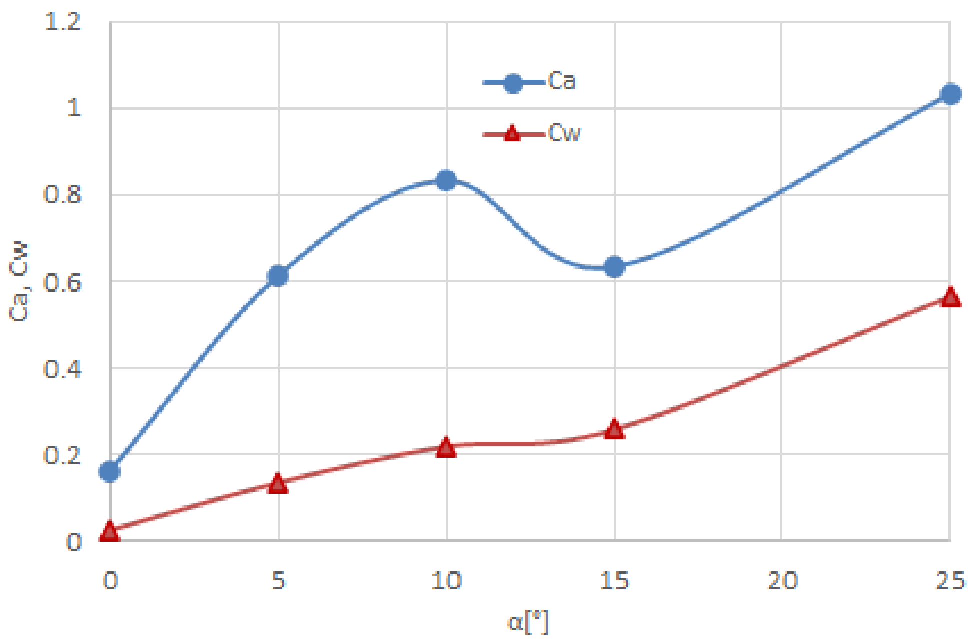


*Fig.73. The lift and drag coefficients variation with the attack angle*

Another study in the air-hydro-dynamics domain was done in the paper "*Analitycal approach and numerical methodology validated against experimental data on S shape airfoil for wide flow angles of attack*" together with Conf. Dr. Ing. Adriana-Sida Manea and C.S.I. Sebastian Muntean, where the accuracy of the results was presented with both, the analytical approach developed by Prof. O. Popa and the numerical methodology, against experimental data obtained on S shape airfoil for a wide range of attack angles, but this will not be presented in this habilitation thesis, the reference can be studied separately.

### I.3.5. Research in the field of cavitation [27, 28, 29, 30, 31, 32]

All the studies in the cavitation domain were done within the collective led by Prof. Dr. Ing**.** Ilare BORDEASU, the head of *Cavitation Erosion Research Laboratory* of the Faculty of Mechanical Engineering of Politehnica University of Timisoara. In this manor different studies were conducted resulting in several published articles that presented the research work.
The phenomenon of cavitation is present in all areas of industry where liquids are in motion. The recognition of its effects is given by the destruction of the material structure through erosion, by vibrations and noise, as well as by the modification of the hydrodynamic field leading to a decrease in energy performance (efficiency). Correlated with the current trends in the use of aluminum alloys in various components, such as boat engine propellers and cooling pump rotors of car mills, the problem arises of improving the characteristics that determine their increased resistance to cavitation erosive stresses.
In this regard, the following study presents the results of research into the behavior and resistance to erosion by vibratory cavitation of the structure of the 7075-aluminum alloy in the T451 state hardened by TIG remelting.
The behavior and structural strength of the 7075 alloy in the T451 state to the stresses of cavitational microjets is very little known, although it is used in strength structures in the military and aeronautical fields, where mechanical properties, especially hardness, close to those of low-alloy carbon steels are required. In the literature, the only data on the cavitation resistance of alloy 7075, cast or rolled, are those obtained at Politehnica University of Timișoara, in the Cavitation Erosion Research Laboratory, which refer to the semi-finished states and those resulting from artificial aging heat treatments at 180ºC, 140ºC and 120ºC, but the analysis of these data does not provide a clear picture of the dependence of resistance and behavior to cavitation stresses on the parameters of the treatment regime (temperature) and the values of mechanical properties, further cavitation investigations being necessary.
The **researched material** is the ***7075-aluminum alloy in T451*** condition, cast in the Specialized Laboratory of the Special Materials Expertise Center of the National University of Science and Technology Politehnica Bucharest, hardened by remelting using the **WIG (Wolfram Inert Gas)** method. The reason for analyzing this alloy is that its behavior and resistance to cavitation erosion were investigated for the cast semi-finished product state and for three structural states resulting from artificial aging heat treatments at 180ºC, 140ºC and 120ºC, with a holding time of 12 hours

and the desired increase in strength was not achieved, compared to the cast semi-finished product state. Wishing to expand its application to parts such as valves, directional valves, boat propellers, pump rotors, which are part of the construction of hydraulic machines and equipment, which work in various intensities of cavitation, the research was carried out on the structure of this alloy hardened by the TIG remelting method.

The material properties are:

- Chemical composition: 0.37% Si, 0.45% Fe, 1.6% Cu, 0.27% Mn, 2.15% Mg, 0.19% Cr, 5.8% Zn, 0.19% Ti, rest Al.
- Mechanical properties: breaking strength Rm = 225 MPa, yield strength $Rp_{0.2}$ = 175 MPa, breaking elongation $A_5$ = 6%, hardness = 74.5 HB, resilience KCU = 9.5 J/cm$^2$.

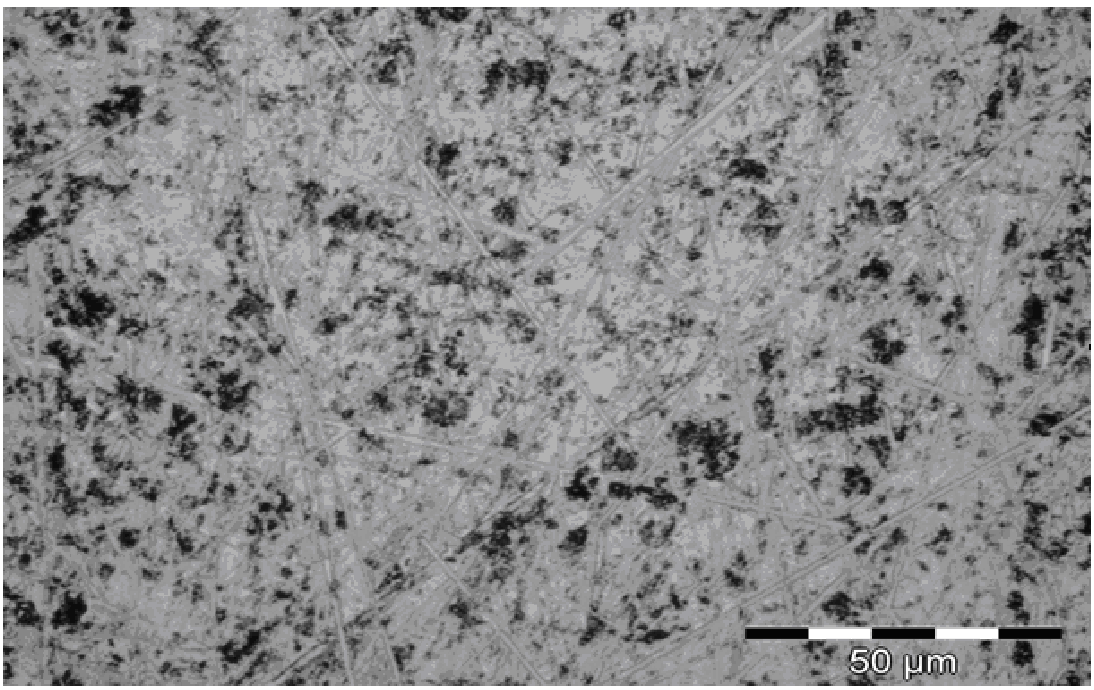

*Fig.74. The Metallographic analysis of the structure*

The metallographic analysis of the structure, Fig.74, performed with the REICHERT UnivaR microscope, shows that in the structure of this alloy the most common precipitates include $MgZn_2$ and $Al_3Zr$.

The remelting of the surface of the samples was done in the laboratory of the National Institute for Research and Development in Welding and Materials Testing (ISIM) Timisoara, on the WIG welding machine, shown in Fig. 75.

*Fig.75. The experimental stand for WIG remelting*

The parameters of the technological regime are:

- Welding current: Is = 70 A;
- Arc voltage: Ua = 11.7 V (RMS = Root Mean Square);
- Arc length: 2 mm;
- Welding speed: Vs = 12 cm/min;
- Linear energy: $E_1$ = 10.4 J/cm;
- Remelting time: 15 seconds;
- Electrode de 2.4 mm;
- ARGON gas 100 %;
- Gas flow: 8 L/min;
- Balancing 60/40 %.

The steps in the procedure for remelting were:

- the base material was preheated to 100°C and the temperature between passes was maintained between 120°C and 150°C;
- the constant welding speed, was ensured with the WIG welding head mounted on an automated welding machine;
- in order to remelt the surface, parallel passes were made with a step between them equal to 2/3 of the width of a pass, thus ensuring an overlap of approximately 1/3 of the width of the pass.

Like this it was obtained, a smooth melted surface, without welding defects. Fig. 76 a) presents the surface appearance after the completion of remelting. In Fig. 76 b) it can be seen the appearance after flat turning, grinding and finishing with abrasive paper to a roughness Ra = 3.2 μm.

*a)*

*b)*

*Fig.76. The material appearance after TIG remelting*

After the hardness measurements, performed at 5 points on the surface of the sample for the experiment, it was obtained an average value of 154 HB.

The **cavitation tests** were carried out in the *Cavitation Erosion Research Laboratory* of the Politehnica University of Timisoara, on the vibrating apparatus with piezoceramic crystals, presented in Fig.77, using cylindrical test samples with a diameter of 15.8 mm and a length of 16 mm.

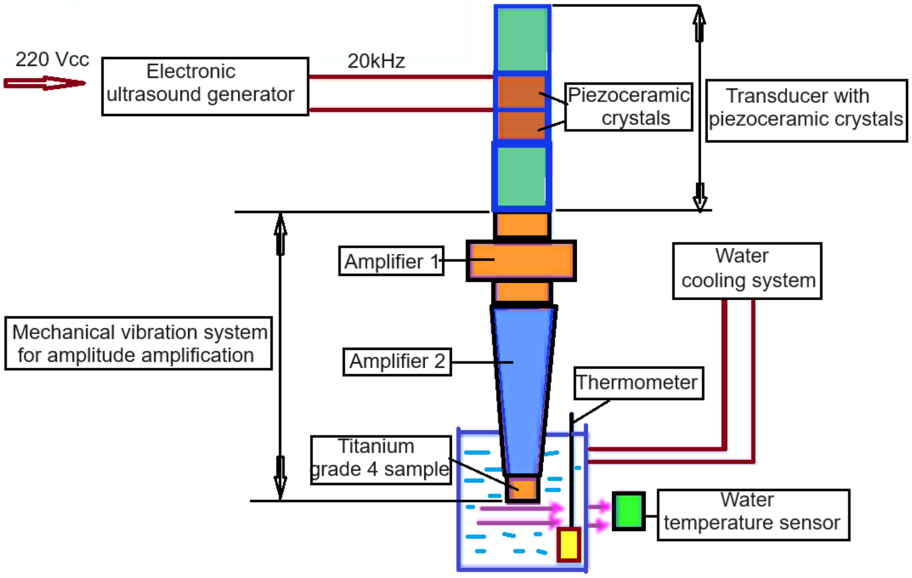


*Fig.77. Functional construction diagram of the vibratory device*

The experimental procedure and research conditions regarding: the number of samples tested (three), the total duration of cavitation exposure (165 minutes), the intermediate periods (one of 5 and 10 minutes and 10 of 15 minutes each), the liquid medium (distilled water with a temperature of 22 ± 1ºC), the processing and interpretation of the recorded data, comply with the laboratory specifications and the provisions of the international standard ASTM G32-2016.
The mass losses, necessary for determining the average erosion depth during each intermediate cavitation period, were determined with the Kern ABT 100-5NM analytical balance, with the accuracy of 0.00001 g. The measurements were performed at an ambient temperature of 21...26°C and a humidity of 62...78 %.
The diagrams in Fig. 78 and 79 show both the analytical forms of the relationships with which the averaging curves of the experimental values were constructed, the values of the $MDE_{max}$ and $MDER_s$. These parameters are necessary for evaluating the structure's resistance to cavitation erosion and the values of the statistical parameters, that provide information about the accuracy of the experimental test and about the compliance with the parameters of the WIG remelting technological regime (the average standard deviation σ and the degree of precision expressed by the tolerance interval in which the averaged experimental values are distributed).

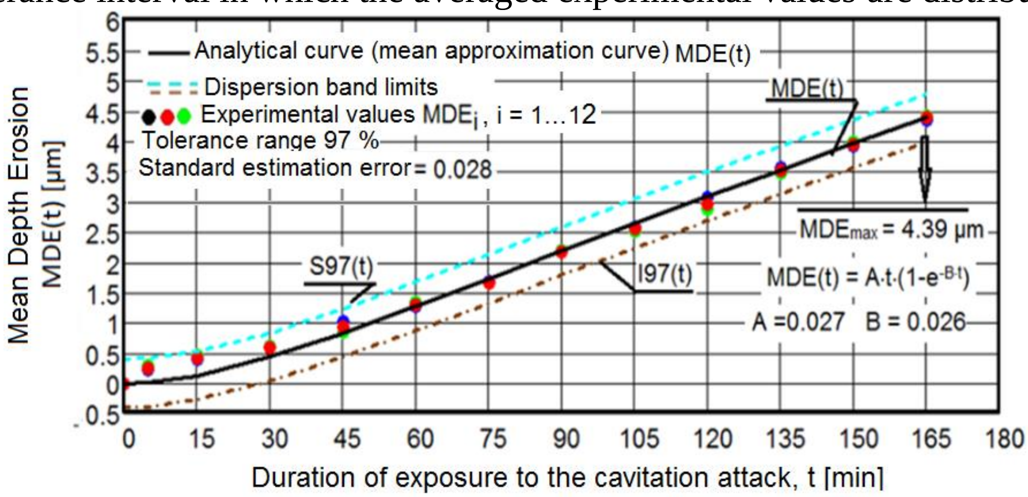


*Fig.78. Variation of the average cumulative erosion depth with the duration of cavitation exposure (**i** = is the number of the intermediate period; the first of 5 minutes, the second of 10 minutes and the next ten of 15 minutes each)*

The data in Fig. 78 show:
- the three samples have similar behaviors, in some situations the cumulative material losses of the three samples, expressed by the cumulative average depths being equal (30 min, 75 min, 90 min, 135 min). These aspects show that for all three samples, the parameters of the WIG remelting technological regime were respected;
- an increase in MDE values is observed in the interval of 0...15 minutes, which suggests that from these moments the surface structure is eroded by cavitation. This

suggestion is false, because, according to previous studies from the Cavitation Erosion Research Laboratory and those provided by bibliographic references [31], this period (0...15) min is characterized by the elimination of the asperity peak, elastic-plastic deformations and the creation of crack networks;
- the limits of the 97% tolerance interval with the value of the average standard deviation σ = 0.028 show the accuracy of the experimental program, as a result of the rigorous control of the functional parameters of the vibratory device, through the software implemented in the computer with which the cavitation process was conducted;
- the averaging curve suggests an exponential increase with a linearization trend starting from minute 45. This evolution mode suggests two aspects: (1) damping of the impact pressures exerted by the cavitational microjets on the attacked surface, (2) increasing the hardness of the layer in the eroded structure.

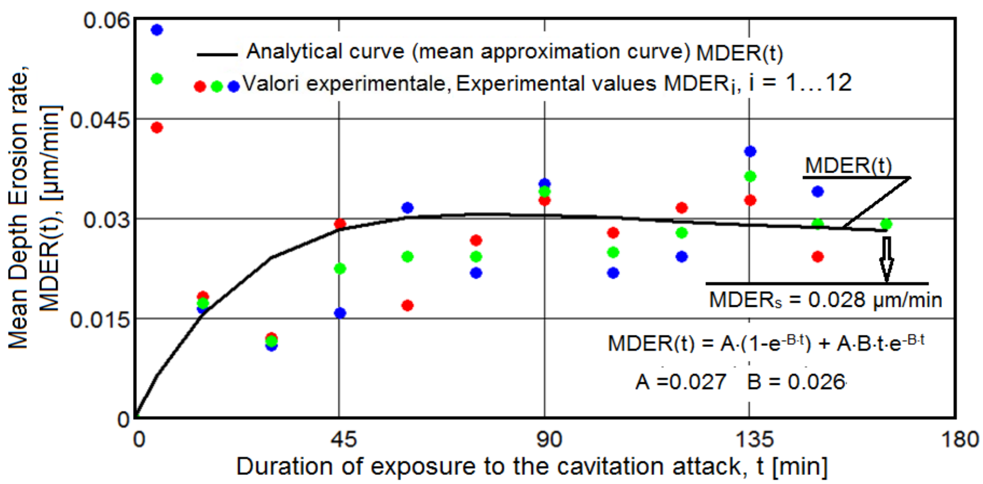


*Fig.79. Variation of the average erosion rate with the duration of cavitation exposure (**i** = is the number of the intermediate period; the first of 5 minutes, the second of 10 minutes and the next ten of 15 minutes each)*

The data in Fig. 79 shows:
- small relative differences between the velocity values determined in the intermediate intervals, which confirms the hardness of the layer attacked by cavitation, obtained by WIG remelting;
- high values of the speeds in the first minutes (5 minutes), which confirms that the structure did not suffer significant losses of base metal, but that these values are the effect of the elimination of abrasive dust and the tip of the asperities remaining after grinding;
- the relatively uniform dispersion of the experimental values compared to the averaging curve MDER(t), which reconfirms the accuracy of the experimental

program while simultaneously respecting the remelting regime of the layer required by cavitation.
The morphology of structural degradation is illustrated by photo and micro fractographic images. The illustration of how the erosion caused by vibratory cavitation extends, both on the exposed surface and in depth, is shown in Fig. 80 by macro images of the surface appearance at 6 significant times, defined by the shapes of the curves MDE(t), Fig.78 and MDER(t), Fig.79.

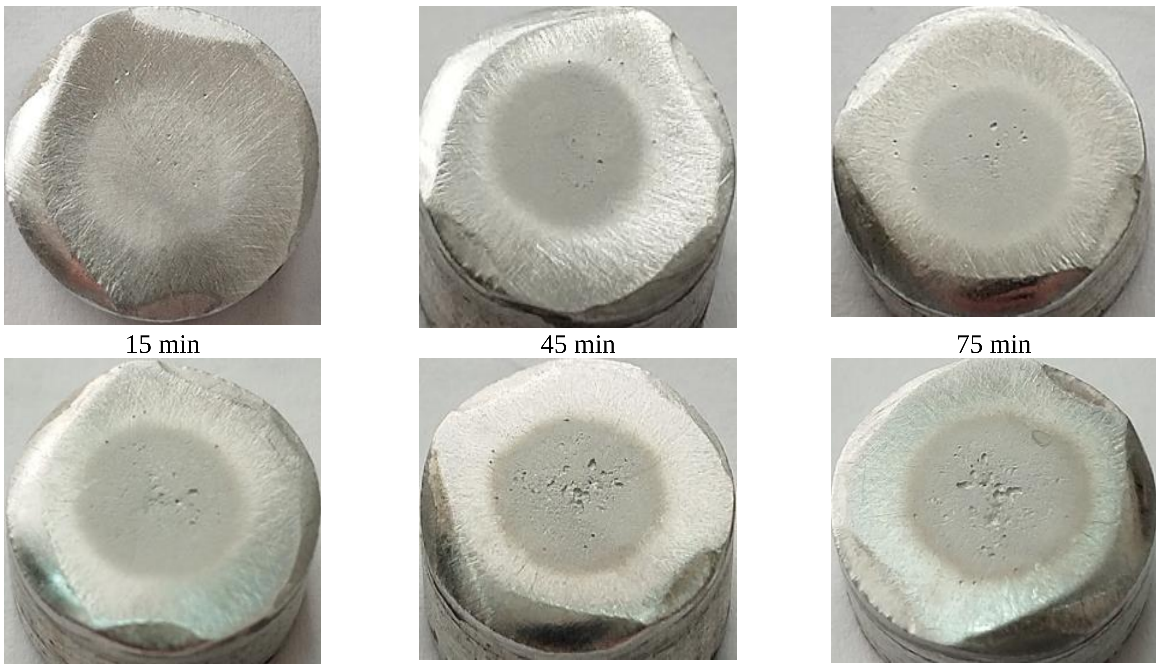

15 min 45 min 75 min

105 min 150 min 165 min

*Fig.80. The images of the evolution of erosion in the sample surface structure*

The images presented in Fig. 80 suggest that:
- the cavitation matting and incubation period is shorter, maximum 15 minutes, it can be seen in the image with 15 minutes, where the micro caverns are already visible on the cavitated surface;
- increasing the duration of the cavitation attack leads to the development of caverns, their size and number increases;
- the shape of the caverns is pinched, with a crow-like appearance, which shows that the material was torn out and expelled under the shapes of the grains;
- starting with minute 105, the differences become increasingly difficult to notice, which explains the decrease in impact force, through the damping effect of the water and air that penetrated them, during the contraction period of the sonotrode.
In order to understand the mechanism of destruction of the surface structure, remelted by WIG the fractography was performed by scanning electron microscope (SEM), combined with energy dispersive X-ray spectroscopy (EDX), Fig.81.

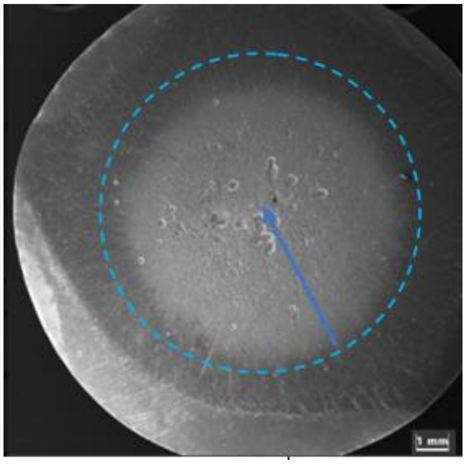


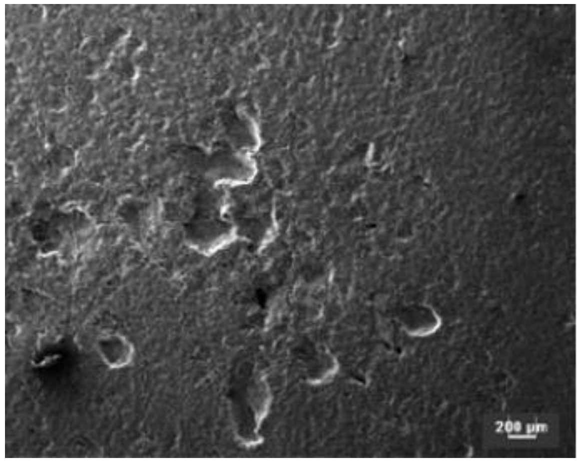


*a)zoom 15x* *b)zoom 50x*

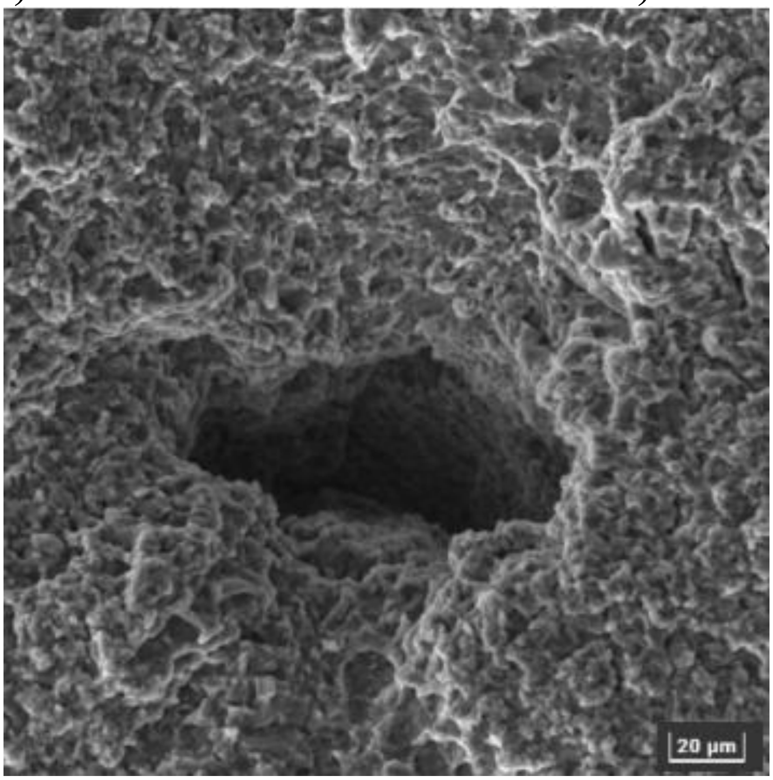


*c)zoom 1500x*

*Fig.81. SEM analysis of experimental specimens of alloy 7075, cavitation tested after 165 hours and different microscope magnification powers*

The SEM images in Fig.81a) and Fig.81b) show the irregular shapes of the caverns, randomly distributed in the area affected by cavitation, and the image in Fig.81c), a detail of the previous figures, shows a rough, spongy sponge-like surface.

From the measurements made under the microscope, these caverns have small dimensions, from 10 µm to 50 µm. The shape of the caverns and the dispersion in the microscope objective, classify the structure hardened by WIG remelting as one with very high resistance to cavitation erosion.

The image in Fig.81a) also shows that the deformations and the caverns in the cavitated area appear to be localized in the central area where the cavities are present, indicating plastic deformation before fracture.

Fig.81b) shows that the surfaces are relatively smooth around the edges, with a central area showing multiple cavities – material pull-outs. The sizes of the cavities vary and are evenly distributed in the central area. The edges of the samples show fine lines, suggesting possible cracks or deformation zones.

From the point of view of the degradation mechanism, the fracture has a mixed character, either ductile or brittle; ductile fracture being characterized by the formation of micro voids and plastic deformation before fracture, and brittle fracture occurring suddenly, with very little prior plastic deformation.

The texture of the fractures is a general one, in which the micro voids are coalesced to form multiple cavities.

SEM images show the presence of fine lines indicating intergranular (along grain boundaries) and trans granular (through grains) cracks. We believe that intergranularity indicates that grain boundaries were points of weakness, caused by the presence of impurities or secondary phases at these boundaries. We also believe that transgranularity suggests a higher intrinsic strength of the grain boundary and may indicate a more homogeneous material.

Based on microscopic analysis, the cavitation resistance of the analyzed structure is strongly dependent on the presence of impurities, phase segregation and local structural variability that can increase the susceptibility to cracking and breakage.

The metallographic image, Fig.82 presents the depths of the caverns in different areas, which exceed by over 40 times the calculated average $MDE_{max}$ value (see Fig.78), which supports the breaking force of the pressures developed upon the impact of the structure with the cavitational microjets.

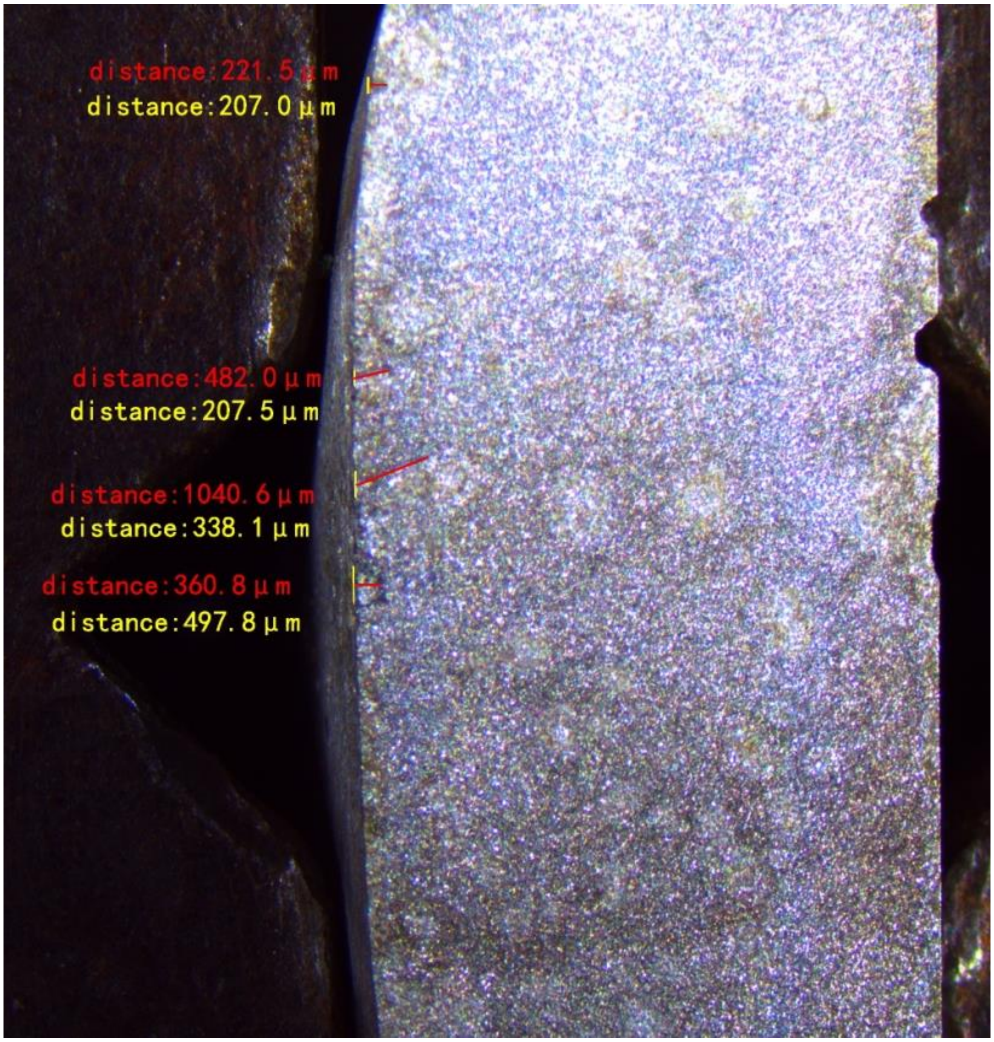


*Fig.82. Structural appearance of maximum erosion penetration depth*

The assessment of the resistance of the remelted WIG structure to vibratory cavitation attacks, according to the data shown in the histogram in Fig.82, is given by the values of the parameters $MDE_{max}$ and $R_{cav}$ = 1/$MDER_s$ (resistance of the structure to cavitation), compared with those of the structures of the same alloy for the semi-finished product states in the cast state and resulted from the volumetric heat treatments of artificial aging at 180ºC (TT180/12h), 140ºC (TT140/12h) and 120ºC (TT120/12h), with holding times of 12 hours.
The differences between these strengths are dictated by the differences in hardness values (74.55 HB for the cast semi-finished state, 91.3 HB for TT180/12h, 95.5 HB for TT140/12h and 76.5 HB for TT120/12h).

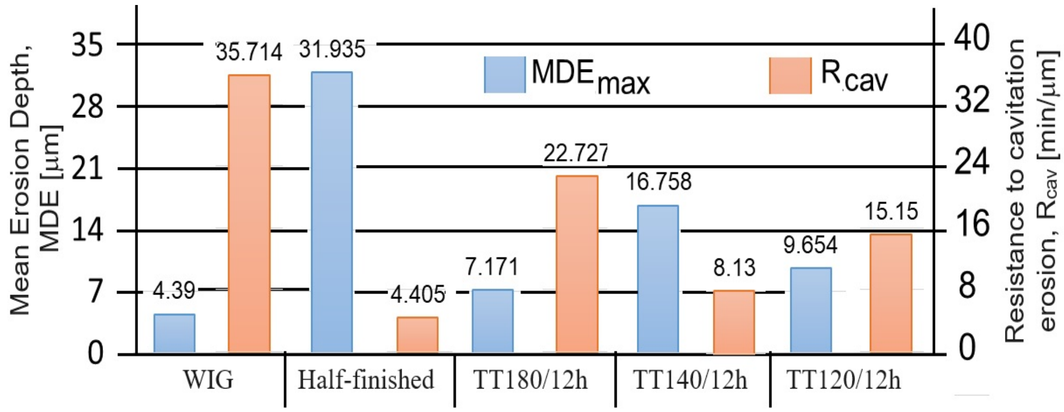


*Fig. 83. Histogram of comparison of resistance to vibratory cavitation erosion*

The histogram data shows an increase in the resistance to erosion caused by the cavitation phenomenon, conferred by WIG remelting, according to the values of the $MDE_{max}$ parameter, from 63% compared to the structure obtained by the TT 180°C/12h artificial aging heat treatment to over 7 times compared to the structure obtained by the TT 120°C/12h. And the values of the cavitation resistance parameter Rcav, show a significant increase, from 55% compared to the structure obtained by the TT 180°C/12h treatment, to over 8 times compared to the structure obtained by the 120°C/12h treatment.

*Therefore, the application of WIG remelting technology to strengthen the hardness of the surface structure of the 7075-aluminum alloy is beneficial, because it will lead to a substantial increase in its service life in hydrodynamic operating environments, characterized by a strong cavitation regime, specific to pump rotors and motorboat propellers.*

Another interesting study was done in the cavitation resistance of biocompatible zinc-based alloys for biomedical applications.

Zinc and magnesium are biocompatible metals and through their combination, respectively with copper, they found their application in stents and heart valves for personnel with cardiac problems.

As the human body is a network of veins through which the blood circulates, the heart plays the role of a pump, similar to hydraulic networks, through which fluids circulate under pressure, hydrodynamic phenomena occur in the blood circulatory network when the pressure changes its values. The sudden decrease in pressure, below the vaporization one, followed by a sudden increase, leads to cavitation-type manifestations with all its effects known and presented in literature (shocks, burglaries of veins, etc.).

Starting from these reasons, this study presents the results of cavitation tests, carried out on two biocompatible alloys (ZnMg and ZnCuMg) created in the laboratories of the University of Natural Sciences and Technology Politehnica Bucharest.

Due to the biocompatibility of the three materials, the objective of the research is to identify the best alloy suitable for heart valves, or stents, that can withstand the shocks produced by the implosions of cavitation bubbles in the blood.

*The researched material*

The researched alloys were developed in the specialized Laboratory of the Special Materials Expertise Center of the National University of Science and Technology Politehnica Bucharest (NUSTPB) in a crucible flame furnace at 650 °C, using elements with advanced purity, respectively Zn 99.99%, Mg 99.99% and Cu 99.99%.
Casting was done in stainless steel ingot. The chemical composition of the three alloys is:
– for the ZnMg alloy: Mg=3.30%, Fe=0.85%, S=0.36%, P=0.019%, Si=1.06%, Al = 0.87%, Ni = 0.02%, Zn = the rest;
– for the ZnCuMg alloy: Mg = 3.66%; Fe = 0.95%; S = 0.14%; Cu = 3.09%: Si = 0.36%; Al = 1.05%; P = 0.001%; Ni = 0.02%; Zn = the rest.
The characteristic of these alloys is that the magnesium and copper harden and brittles zinc due to the formation of hard intermetallic phases ($Mg_xZn_y$, $Cu_xZn_y$).
The structures of these cast alloys, Fig.84, have dendritic segregation, where the dendritic arms are located in the range of 100 ÷ 180 μm, with a chaotic arrangement in the metal matrix.

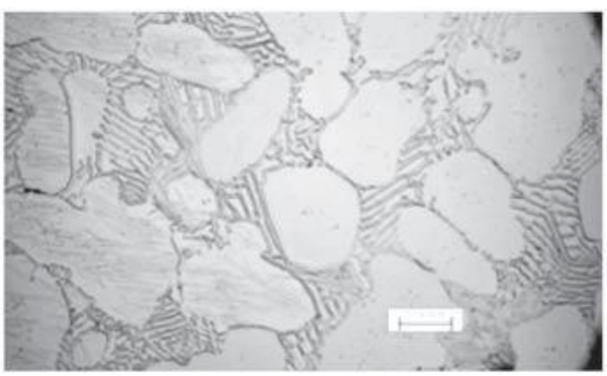

*a) ZnMg (25x)*

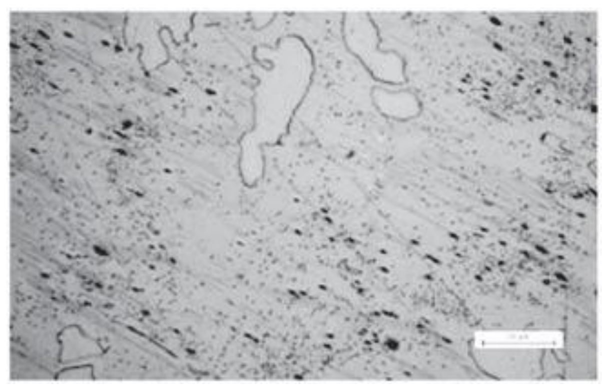

*b) ZnCuMg (25x)*

*Fig. 84. Structural analysis of Zn-Mg alloy - specimens attacked with Nital 2%.*

The values of the characteristics of mechanical resistance to breaking and HB hardness, determined in the laboratory of the Special Materials Expertise Center, are shown in Table 6.

*Table 6. The values of mechanical properties.*

| Alloy type | Rm [MPa] | Rp0.2 [MPa] | A5 [%] | Hardness HB |
|---|---|---|---|---|
| Zn-Mg | 108 | 30.7 | 3.69 | 74 |
| Zn -Cu-Mg | **123** | 84.23 | 2.42 | 76 |

The data in Table 6 shows that significant differences exist between the characteristics of mechanical resistance to breaking of 13.88% between the values of Rm, 2.8 times between the values of Rp0.2 and of 52.4% between the values of A5. The differences between hardnesses being reduced (3 ÷ 5)%. So, the differences in behavior and resistance to cavitation, for these alloys, according to the older research done by Garcia and recorded by Franc, will be dictated by the values of these mechanical characteristics.

*The Apparatus and Cavitation Testing Methodology*

The cavitation test program took place in the *Cavitation Erosion Research Laboratory* of University Politehnica of Timișoara, on the standard vibrating device with piezo ceramic crystals, respecting the requirements of the international standards ASTM G32-2016 on the stationary sample test method (indirect method). Also, the experimental procedure respected the laboratory's custom regarding: total test time (165 min), the duration of i=12 intermediate periods (each of 5 and 10 min and 10 of 15 min each), the washing method and drying.

The determination of mass losses and the processing of the experimental data in the determination of the mean depth of erosion (MDE), the mean depth erosion rate (MDER), the upper (S) and lower (I) limits of the dispersion band, the mean standard error (σ) and when evaluating the resistance to the erosion of vibrating cavitation, by comparing the values of the specific parameters, was also done according to laboratory procedure.

The functional parameters of the device, which determined the erosive intensity of the cavitation are: the power of the electronic ultrasound generator = 500W, the double vibration amplitude = 50 μm, the vibration frequency = 20 ± 0.01 kHz. The values of these parameters are consistent with the requirements of ASTM G32-2016 standards.

Also, according toASTMG32-2016 the requirements are the diameter of the circular surface of the cylindrical sample, exposed to cavitation (d = 15.8 mm) and the temperature (t =22 ± 1 °C) of the distilled water used as liquid (kinematic viscosity∼=$1.01\cdot10^{-6}$ $m^2/s$).

The mass eroded by cavitation, during the intermediate durations, was determined

with the KERN ABT 100-5NM digital electronic balance with a precision of 0.01 mg.
For the accuracy of the research results from each heat treatment regime, were taken into account the tests of at least 3 samples, where the results fell within the precision error accepted by the laboratory custom (maximum 10%).
The distance between the surface of the tested sample (stationary sample) and the surface of the vibrating sample was 1.00 mm.

*The Cavitation Test Results*

In order to follow and analyze the behavior of the structures during cavitation attacks, based on the mass losses in each intermediate period Δti, with the relationships in were determined the values of the mean depth of erosion were determined ΔMDEi and of the mean depth erosion rate MDERi = ΔMDEi /Δti (where: i-testing period, Δti – the duration of the intermediate period "i" (at 0, 5, 10 and15)).
For the construction of specific diagrams (see Fig.85), which present the variations of the experimental values of the mean depth of erosion and mean depth erosion rate with the duration of the cavitation attack, as well as the averaging curves of these values (MDE(t) and MDER(t)), the formulas below have been used:
– for the cumulative mean depth of erosion obtained on the basis of experimentally determined mass values after each intermediate period:

$$MDE_i = \sum_{i=1}^{13} \Delta MDE_i \; [\mu m] \tag{73}$$

– for the analytical curve averaging the experimental values of the mean depth erosion:

$$MDE(t) = A \cdot t \cdot (1 - e^{-B \cdot t}) \tag{74}$$

– for the analytical curve averaging the experimental values obtained for the mean depth erosion rate:

$$MDER(t) = A \cdot t \cdot (1 - e^{-B \cdot t}) + A \cdot B \cdot t \cdot e^{-B \cdot t} \qquad (74)$$

where: for $i = 1$, $\Delta t_i = 0$, $MDE_i = 0$;
**A-** is the scale parameter, statistically established on the basis of the experimental values, for constructing their approximation/averaging curve, provided that their deviations from it are minimal (±10% deviation);

**B-** is the shape parameter of the curve, established statistically based on experimental values.
The values of parameters A and B were determined with a model created in the MathCad program by the group of researchers of the Cavitation Erosion Research Laboratory.

*The Diagrams and the Parameters Specific to Cavitation Resistance Behavior*

The data in Fig. 85 show that the two alloys, created for the manufacture of stents and valves used in cardiology, have similarities and differences in their behavior to the demands of the developed microjets, thus:
– The different behavior of the ZnMg alloy (Fig. 85c) from the ZnMg alloy (Fig. 85a) in the interval 0…30 min, by increasing the losses, (large values of the mean depth of erosion (experimental values), followed by a decrease over the interval (30 ÷ 75) minutes and then linearly increasing until the test duration is completed (165 min);
– The different behaviors of the two alloys, expressed by the experimental values, are determined by the response of the structures to the specific mechanism of destruction of the roughness peaks, through the creation of deformations and the generation of microcraters and respectively by the response to the impact with the pressure forces developed by the cavitational microjets, influenced by the dendritic microstructures, the number and dispersion of brittle compounds of the three basic chemical elements (Zn, Mg, Cu), as well as the use of pressure potential energy for deformations, cracking, breaking and hardening;
– The sizes of the dispersion bands, given by the values of the tolerance fields (97 ÷ 98)% and the average standard deviations $\sigma = 0.087$ and 0.272, show that the two tested samples, from each type of alloy, are structurally identical and also in the values of the mechanical properties, in the volume of the samples and in the cavitation surface area.
The diagrams containing the variations of the erosion speeds (Fig. 85b and 85d) confirm the similar behavior of the two samples from each alloy, and in addition, compared to those from the diagrams from Fig. 85a and 85c, is observed the similar evolutions of the curves MDER(t), with a tendency to increase up to the stabilization values MDERs, which leads us to believe that, from the point of view of potential energy absorption, created by the surface impact pressure with microjets and shock waves, the structures of these alloys behave similarly.
The difference in the value of the MDERs parameter being given by the values of the mechanical properties (see Table 6), the microstructure and the mode of hardening under the cyclic stresses of cavitational microjets, a very important aspect for the behavior of stents and heart valves at people with heart problems.

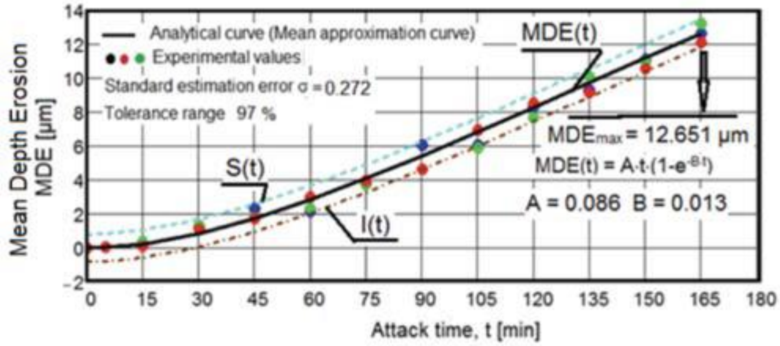


a)ZnMg

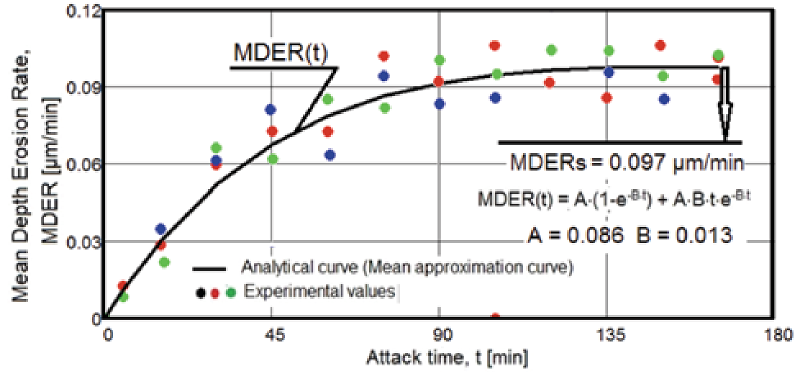


b)ZnMg

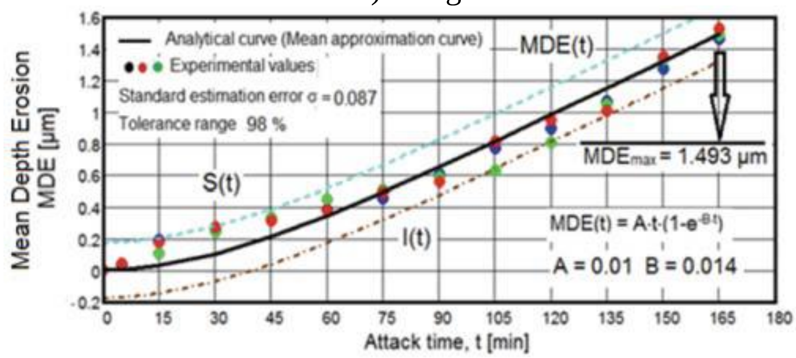


c)ZnCuMg

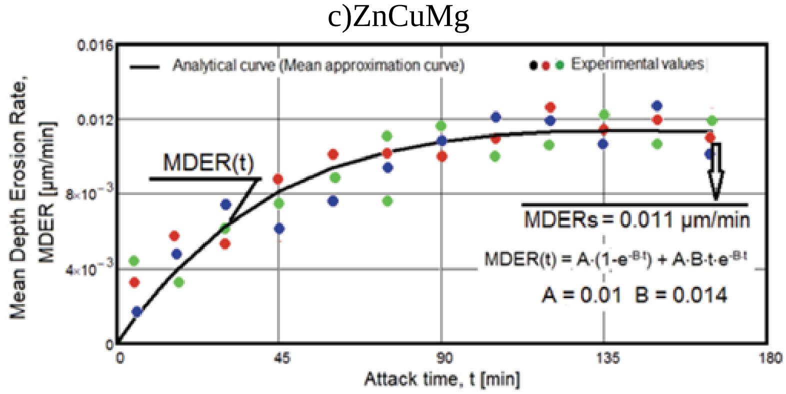


d)ZnCuMg

*Fig. 85. Cavitation characteristic curves: a), c) The variation of the mean depth erosion with the duration of cavitation exposure b), d) The variation of the mean depth erosion rate with the cavitation duration.*

*Morphology of Structure Degradation*

In Fig.86 and 87 are shown macroscopic, microscopic and stereomicroscopic images, taken on the eroded surface after the completion of the cavitation test.
The macro images, obtained by photography with the Canon Power Shot A 480, and the microscopic (SEM) images, show that cyclic stresses cause caverns of different sizes, which give the surface a spongy appearance.

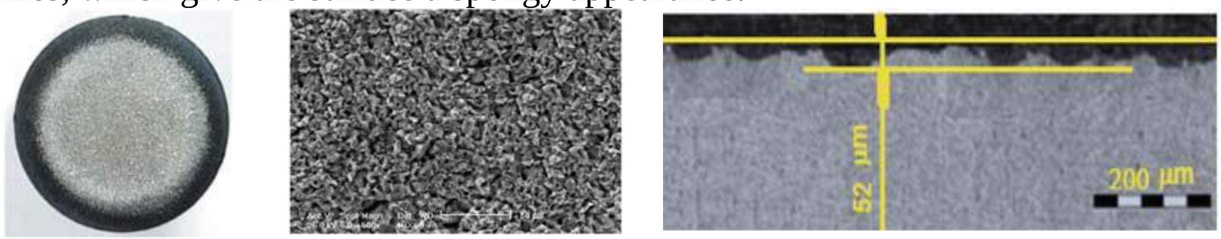


*a) Eroded area after 165 min* *b) SEM image (500x)* *c)The caverns in the eroded surface after completion of 165- minute test recorded on stereomicroscope*

*Fig. 86. Macroscopic and microstructural images with the evolution of erosion in the cavition surface area (ZnMg).*

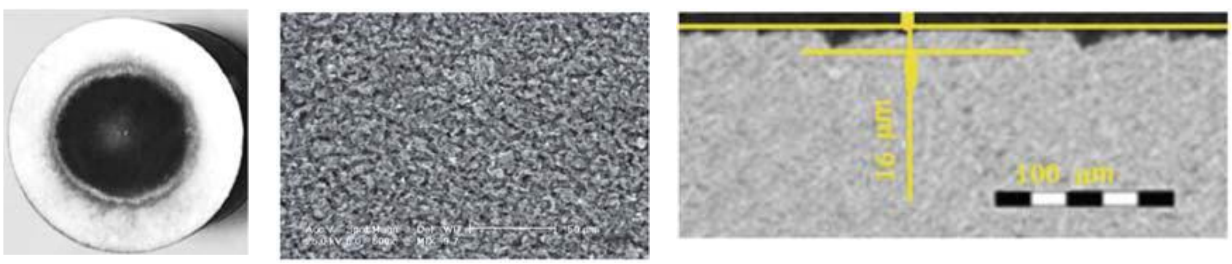


*a) Eroded area after 165 min* *b) SEM image (500x)* *c)The caverns in the eroded surface after completion of 165- minute test recorded on stereomicroscope*

*Fig. 87. Macroscopic and microstructural images with the evolution of erosion in the cavition surface area (ZnCuMg).*

The extent of erosion in the plane of the cavity surface and in depth are dependent on the type of alloy, the values of the mechanical properties (see Table 6), the nature, dimensions and the number of intermetallic compounds MgxZny and CuxZny. These images, supplemented by the microscopic ones (SEM) and cells obtained with the stereomicroscope, confirm the statements made in the analysis made on the data from the diagrams in Fig. 85.
**Clarification:** The images from Figs. 86c and 87c are obtained with the stereomicroscope, after sectioning the sample perpendicularly and along the diameter of the cavity surface.
The shape of the caverns in these photos and microscopic images show that the sizes of the grains ejected upon impact with the cavitational microjets are small, specific

to structures with high resistance to cavitational stresses which, through biodegradation, can quickly dissolve in the blood circulatory system. Like this the life of devices used in cardiovascular surgery is long and does not endanger life. Aspects captured at 500x magnification (SEM images from Fig.86b) and Fig.87b)) show a brittle, shiny crystalline appearance with flattened caverns.

However, the shapes of the caverns (see Fig.86c) and Fig.87c)) urge caution/medical assistance, in the case of cardiac devices with devices made of these alloys, because, from the point of view of the hydrodynamics of the flow in the blood circulatory system the use of stents is necessary, beneficial, but can also be disadvantageous for two reasons, because they degrade quickly and because these caverns change the configuration of the hydrodynamic field, generating strong turbulence and pressure variations, with effects that can become problematic (even destructive) for the cardiac stability of the patient.

Both photographic and microscopic images, through profilograms, but also through the maximum depths of the measured caverns (see Fig.86c) and Fig.87c)) suggest that the most degraded structure, with the lowest resistance to the vibrational cavitation stress, is that of the ZnMg alloy, due to the very low value of the yield strength $Rp_{0.2}$, in relation to the other alloy.

The histogram from Fig.88 shows the differences between the values of the parameters $MDE_{max}$ , $MDE_{cav}$ (cavern depth measured in the sectional plane see in Figures 86c and 87c) and $R_{cav}$ = 1 / MDERs (resistance to cavitation) as an expression of the effect on the resistance of the surface structure to the cavitational stresses by the type of alloy, by its microstructure and by its mechanical properties.

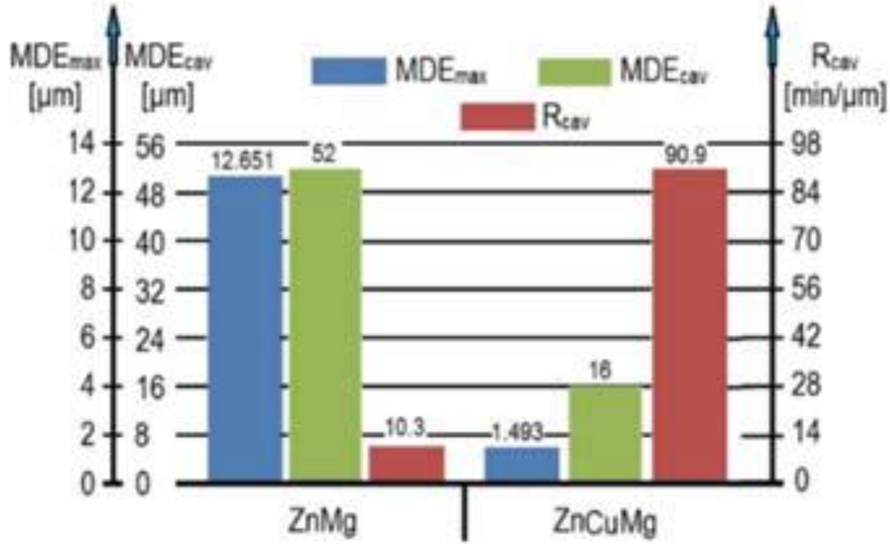


*Fig. 88. Histogram of comparison of cavitation resistance reference parameter values*

The histogram data shows that the strength of ZnCuMg alloy is higher than that of ZnMg alloy, thus:
– according to the values of the $MDE_{max}$ parameter, it is about 4.81 times higher;
– according to the values of the $MDE_{cav}$ parameter, it is about 3.25 times higher;
– according to the values of the $R_{cav}$ parameter, it is about 8.82 times higher.

The zinc-based alloys, researched in the work, are technological solutions for the use in the manufacture of stents and valves intended for cardiovascular surgery, due to their biocompatibility and biodegradation and to the fact that the intensity of cavitation produced by pressure oscillations in the circulatory system is much reduced compared to the intensity of vibratory cavitation in distilled water.
The results of the research, expressed by the values of parameters specific to cavitation erosion, show that, from the point of view of behavior and resistance, the ZnCuMg alloy ensures a longer life (more than 8 times compared to the ZnMg alloy).
The macro and microscopic images of the eroded surfaces confirm the dependence of the behavior and resistance to cavitation on the type of microstructure and correlation of the values of the main mechanical properties ($R_m$, $Rp_{02}$, $A_5$ and HB).

## Chapter II. The results of the research activity in the field of dynamic identification of wind turbine pitch systems [33-52]

As the European Union 2030 energy strategy aims to reduce its greenhouse gas emissions by at least 55%, increasing the share of renewable energy to at least 45% and considering the enormous potential of offshore wind, which could meet Europe's energy demand seven times, it is expected that the offshore wind will become one of the main electricity generators in Europe.

The offshore wind turbines advantages are:

- low greenhouse gas emissions compared to gas and coal-powered energy;
- allows the energy to be produced while saving land and reducing to almost zero the visual, noise, and shadow impacts compared to onshore wind turbines;
- better output due to larger turbines, compared to the onshore wind turbines and due to running with more qualitative wind (higher speed with a steady performance).

The main disadvantages of offshore wind turbines compared to the onshore ones consist of high operating expenses, due to accessibility conditioned by the weather, increase in installation and transmission expenses as well as new issues concerning saltwater corrosion and the substructure inspection in an offshore environment.

The reduction of operating expenses can be achieved by increasing the operational performance standards on each turbine. To optimize offshore wind energy production and reduce costs, unscheduled maintenance must be minimized and continuous operation must be ensured.

In literature [35] is provided a detailed analysis of wind turbine subsystems, identifying the hydraulic pitch system as the primary contributor to overall failure rates, accounting for 13% of all failures. Auxiliary components such as lifts, ladders, and nacelle seals are grouped under 'Other Components', contributing 12.2% to the failure rate, while the generator, gearbox, and blades account for 12.1%, 7.6%, and 6.2%, respectively. Given the significant impact of hydraulic pitch system failures on wind turbine reliability from the above research background, this system is selected as the focus of our investigation.

The primary function of the hydraulic pitch system is to precisely control the pitch angle of the turbine blades, ensuring both safe operation and optimal power output.

The objective of this research is to identify experimentally the mathematical model of a servo-valve controlled hydraulic cylinder operating under a variable load, necessary for the proper development, analysis, and synthesis of an optimized, robust, reliable, and efficient pitch control system.

In the following research is presented the experimental identification of the wind turbine pitch system with periodical sine signals as input and the actuating cylinder position as output.

The use of these types of test signals, to determine the dynamic characteristics of the systems, presents many advantages, the investigated installation being brought into the regime of forced oscillations, the influence of the noises appearing in the process and of various disturbances on the useful output signal can be more easily discriminated. Another advantage is that using zero-mean periodic sample signals allows the use of larger amplitude signals compared to non-periodic signals. This method also has the advantage that it ensures a uniform precision for the entire frequency band, specific to the researched process.

The main advantage of using this method is the fact that it allows the direct determination of the frequency response of the researched process, which can be used directly in the design calculations of the automatic system. Also, this method also allows the determination of dynamic characteristics for non-linear elements, even obtaining their description functions.

Accordingly, this chapter is divided into 3 subchapters:

**II. 1. The experimental setup**, where it is presented the experimental stand, with its components and the data acquisition system.

**II. 2. The mathematical model** which presents a proposed mathematical model for the setup.

**II. 3. Experimental system identification** were there are presented the experimentally determined transfer functions and the Margin and Nyquist plots for different frequencies and amplitudes chosen as reference.

**II. 1. The experimental setup**, this part is composed of the hydraulic stand and the data acquisition system.

### II.1.1 The hydraulic stand

The test rig and the hydraulic diagram of the stand which emulates the blade pitch mechanism of the wind turbine are depicted in Fig.89.a) and 89.b).

*Fig.89.a). The test rig for the pitch mechanism of the wind turbine*

In principle the test rig consists of two main systems, one which is the actuating system, which emulates the blade pitch mechanism and one which is the loading system, which emulates the load on the blade.

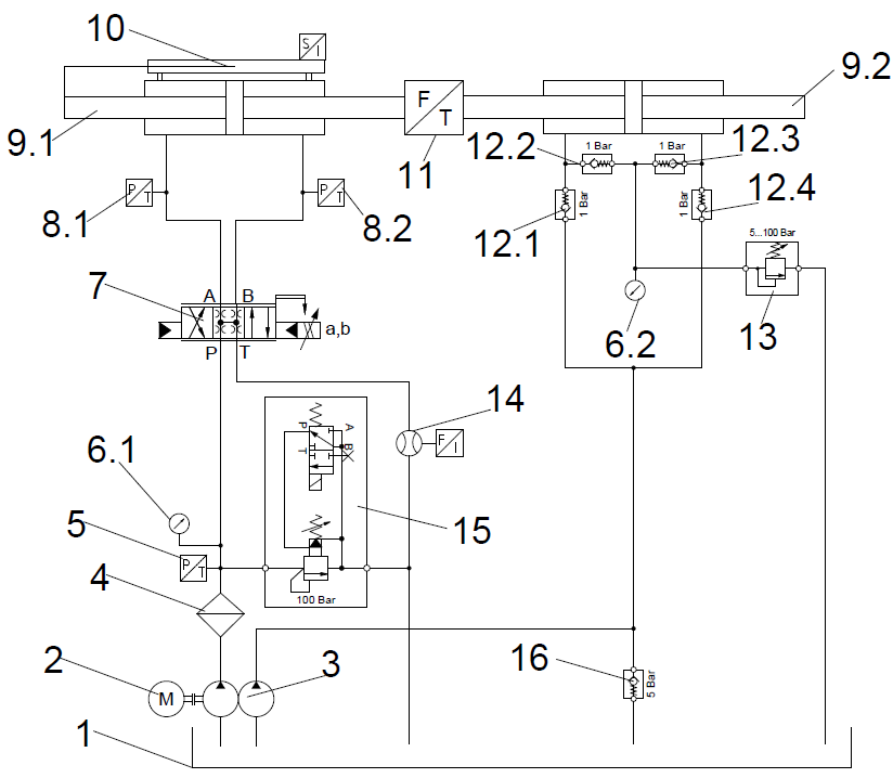


*Fig.89.b). The hydraulic diagram of the test rig*

The actuating system consists of: the main hydraulic pump 3, actuated by the electrical motor 1, the pressure filter 4, the main line pressure sensor 5, the manometer 6.1, the servo valve 7, the actuating cylinder pressure sensors 8.1 and 8.2, the actuating cylinder 9.1, the LVDT position transducer 10, the force transducer 11, the flow meter 14 and the pressure relief valve 15.
The pressure relief valve is set at 100 bar and can be actuated from the stand panel, when it is actuated the pressure in the system is 100 bar and that can be easily checked either with the manometer 6.1, either with the main line pressure sensor 5.
The servo-valve 6, feeds oil to the actuating cylinder which can be moved either to left or right. The electrical command for the servo-valve is given from a signal generator which can generate step, sine and triangular signals with different amplitudes and frequencies.
The pressure on either sides of the actuating cylinder is measured with the pressure sensors 8.1 and 8.2.
The flow in the actuating system is measured with the turbine flow meter 14.
The loading system consists of the following parts: the oil feeding pump of the loading system, the other pump of the twin one, which feeds oil to the loading cylinder 9.2., the check valves 12.1…12.4 which ensure a specific oil flow path, the load pressure setting valve 13 with the manometer 6.2 and the check valve 16 which ensures a pressure of 5 bar in the loading system when the stand is running, protecting it for cavitation occurrence.
The force given by the loading system, which emulates the load on the blade is measured with the force transducer 11.
The testing rig consists of the following parts:
**1-The reservoir,** which has a volume of 300 liters and it is equipped with breather and oil level indicator. This has the role to store and also to cool the working fluid (ISO VG 46 hydraulic oil).
**2- The electrical drive motor type ATF 32M 4A** has a maximum electrical power of 7.5 kW. The electric motor drives the hydraulic pumps converting the electrical power into mechanical power.
**3- Twin hydraulic gear pump,** with fixed displacement produced by Uzina Mecanică Plopeni, type **PRD22-2188D** [36]
The twin hydraulic pump transforms the mechanical power at the electrical motor shaft into hydraulic power feeding both systems with oil. The main pump ensures the oil flow at a maximum pressure set by the relief valve and secondary one feeds the part that is not pressurized of the loading cylinder through the check valves system.

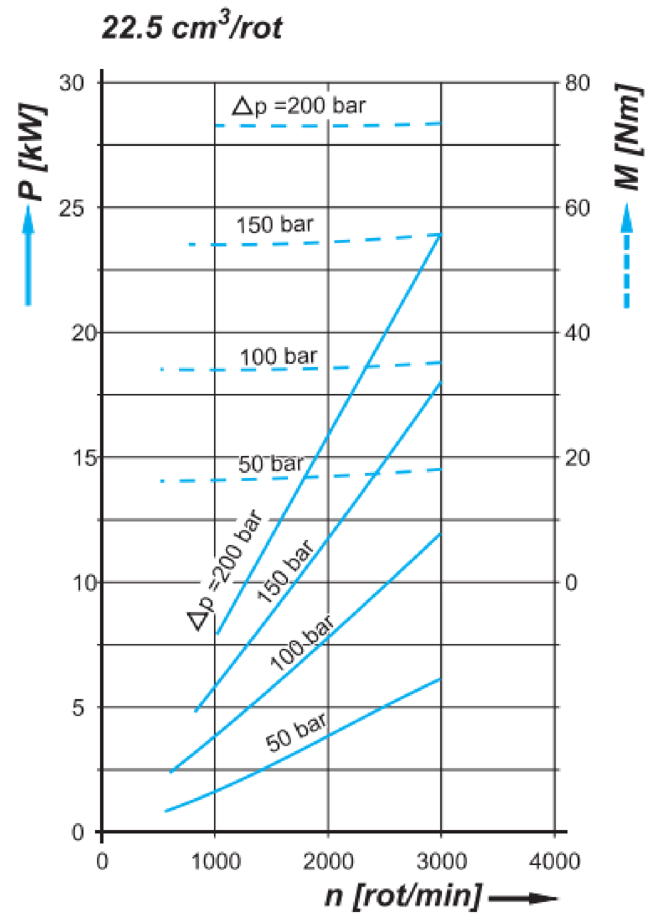


*Fig.90. The hydraulic pump diagram*

**4- Pressure line filter** [37]

The pressure line filter has the role to feed the system with clean oil without any contamination in it. Its functional scheme and the parts are presented in Fig. 91 and it consists of the filter head (1), a screw-in filter housing (2), the filter element (3) as well as a clogging indicator (4) (connection provided as a standard). The oil is passed via port A to the filter element (3), where it is cleaned. The dirt particles filtered out settle in the filter housing (2) and the filter element (3). The filtered hydraulic fluid is directed via port B back into the hydraulic circuit.

The filter housing and all the connecting elements are designed so that pressure peaks – caused, e.g. by accelerated fluid volumes when large control valves suddenly open – can be safely taken up.

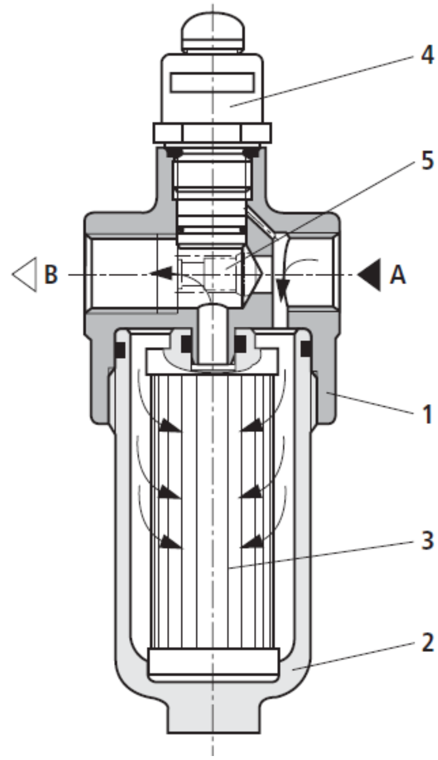


*Fig.91. The pressure line filter*

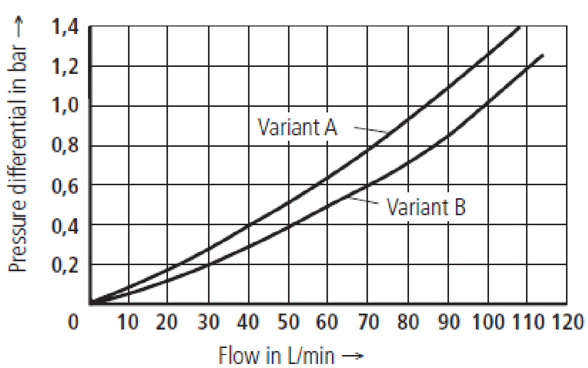


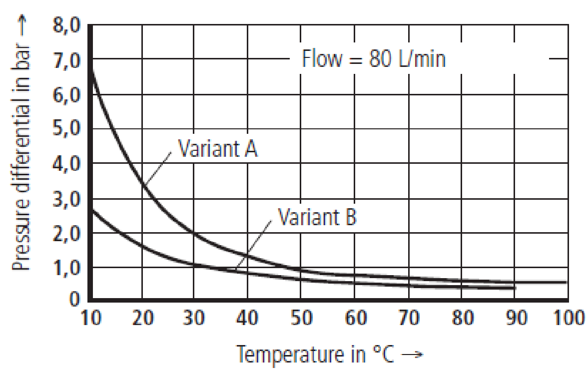


*Fig.92. The pressure line filter characteristic curves*

The filter element is made of an-organic fiber has a high filtration degree, with a 5 micrometer mesh, suitable for servo-valves systems.

**5- The pressure line pressure transducer Mannesman Rexroth HM-15-1X/600** [38]

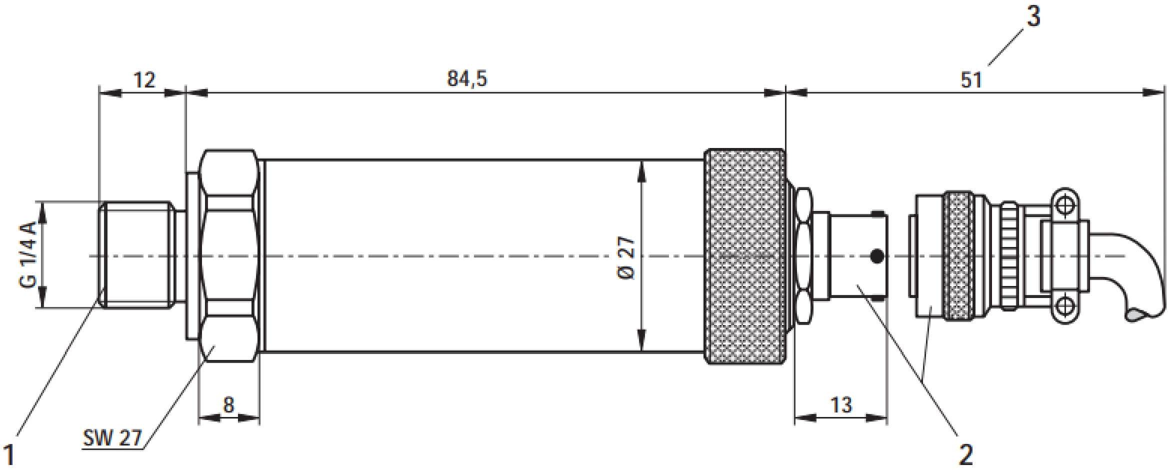


*Fig.93. The main pressure line pressure sensor*

The pressure sensor has the following parts and sizes:
1-Pressure connection G 1/4 form A to DIN 3852 part 2; with soft seal.
2-Electrical connections via a 4-pin plug;
3- Minimum installation length
It has the following characteristics
Input values:
Operating voltage: + 10 V to + 30 V
Current consumption I max: 10 mA
Measuring range: 0…600 Bar
Over-load protection: 900 Bar
Burst pressure: 2000 Bar
Dead volume V approx. 450 mm3
Output values:
Output signal: 4 to 20 mA (2 conductors)
Temperature compensation:
– Zero point type ≤ 0.08 %/ 10 K; max. ≤ 0,15 %/ 10 K
– Range type ≤ 0.08 %/ 10 K; max. ≤ 0,15 %/ 10 K
Linearity tolerance type ≤ 0.1 % 1); max. ≤ 0,3 % 1) (from 100 bar max. ≤ 0.2 %)
Hysteresis type ≤ 0.05 % 1); max. ≤ 0.1 % 1)
Repeatability ≤ 0.05 % 1)
Rise time t ≤ 0.5 ms
Long term drift (6 months):
– Zero signal ≤ 0.1 % 1)
– Range ≤ 0.1 % 1)
Ambient conditions

Nominal temperature range ϑ – 25 to + 85 °C
Operating temperature range ϑ – 40 to + 85 °C
Storage temperature range ϑ – 40 to + 100 °C
Medium temperature range ϑ – 40 to + 100 °C
EMC compatibility to IEC 801-4 severity class 3
Shock 500 g / 1 ms
Vibration resistance to IEC 68-2-6 (at 10 to 500 Hz) 20 g
Protection to DIN 40 050 IP 65

**6.1, 6.2- Manometer**

The manometers used are HansaFlex GMM 100-160 H, Class 1, with a maximum indicating pressure of 160 bar.

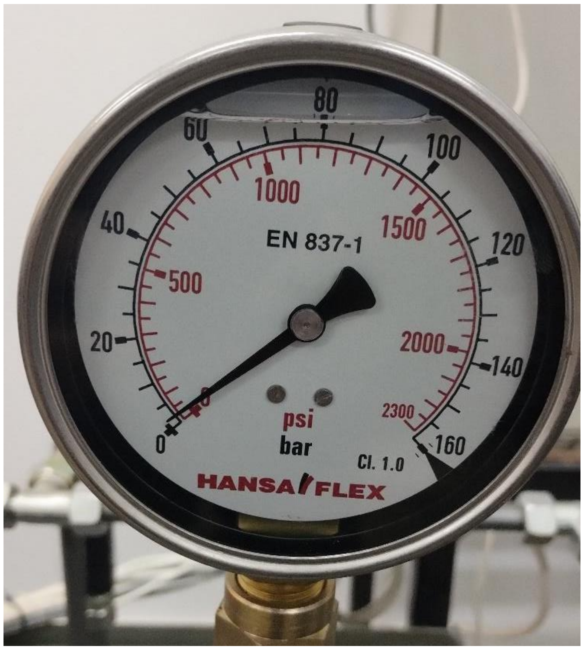


*Fig.94. The manometer*

**7- Rexroth Servo-valve type *4WS2EM10-51/45B11ET210K31EV*** [39]

*Servo-valve coding explanation*
4WS2EM -Directional servo-valve in 4-way design for external control electronics, with mechanical return;
**10** -Size 10;
**51**- Component series 50 to 59;
**45**- Rated flow of 45 l/min at 70 bar pressure drop. The rated flow refers to a 100 % command value signal at 70 bar valve pressure differential (35 bar per control edge). The valve pressure differential must be regarded as reference. Other values result in the flow being changed. A possible rated flow tolerance of ±10 % must be taken into account.
**11**- Valves for external control electronics: Coil no. 11 (30 mA / 85 Ω per coil);
**ET** - Internal supply, internal return;
**210**- Inlet pressure range of 210 bar;
**K31**- Without mating connector with connector according to EN 175201-804;
**E**- Spool overlap 0 to 0.5 % negative;
**V**- FKM seals, suitable for mineral oil (HL, HLP) according to DIN 51524;
Valves of type 4WS(E)2EM10-5X/... are electrically operated, 2-stage directional servo-valves. They are mainly used to control position, force and velocity. These valves consist of an electro-mechanical converter (torque motor) (1), a hydraulic amplifier (nozzle flapper plate principle) (2) and a control spool (3) in a sleeve (2nd stage), which is connected to the torque motor via a mechanical return.
An electrical input signal at the coils (4) of the torque motor generates a force by means of a permanent magnet which acts on the armature (5), and in connection with a torque tube (6) results in a torque. This causes the flapper plate (7) which is connected to the torque tube (6) via a pin to move from the central position between the two control nozzles (8), and a pressure differential is created across the front faces of the control spool. This pressure differential results in the control spool changing its position, which results in the pressure port being connected to one actuator port and, at the same time, the other actuator port being connected to the return flow port.
The control spool is connected to the flapper plate or the torque motor by means of a bending spring (mechanical return) (9). The position of the control spool is changed until the feedback torque across the bending spring and the electromagnetic torque of the torque motor are balanced and the pressure differential at the nozzle flapper plate system becomes zero.
The stroke of the control spool and consequently the flow of the servo valve are controlled in proportion to the electrical input signal. It must be noted that the flow depends on the valve pressure drop. External control electronics (servo amplifier)

serve the actuation of the valve, amplifying an analog input signal (command value) so that with the output signal, the servo valve is actuated in a flow-controlled form.

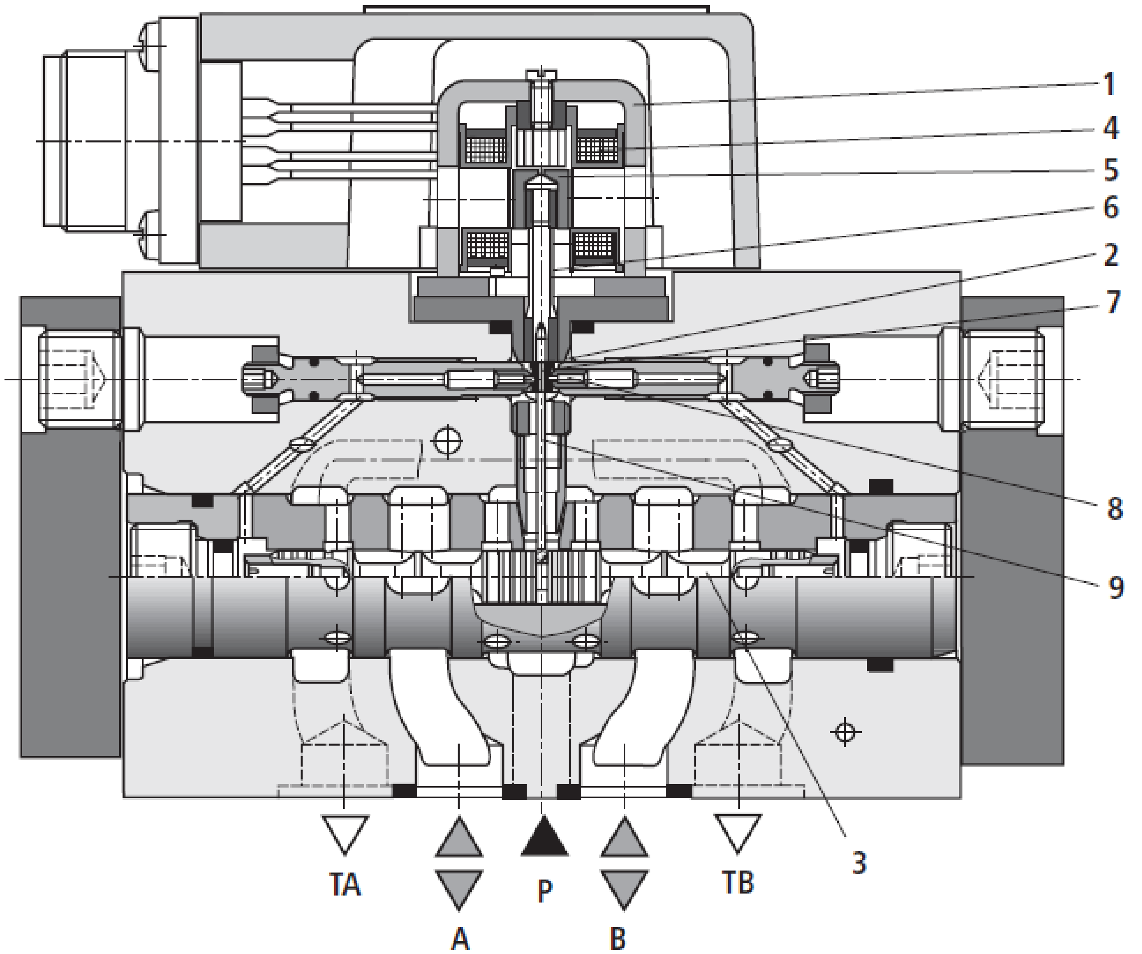


*Fig.95. The servo-valve elements*

The zero flow of the valve can be calculated with:

$$Q_{zero} = \sqrt{\frac{inlet\ pressure\ [bar]}{70\ bar}} \cdot 1.2 = \sqrt{\frac{100\ [bar]}{70\ bar}} \cdot 1.2 = 1.43 [\frac{l}{min}] \qquad (75)$$

The characteristic curves (measured with HLP 32, Toil = 40 °C ± 5 °C) are presented in Figure 96, 97, 98 and 99.

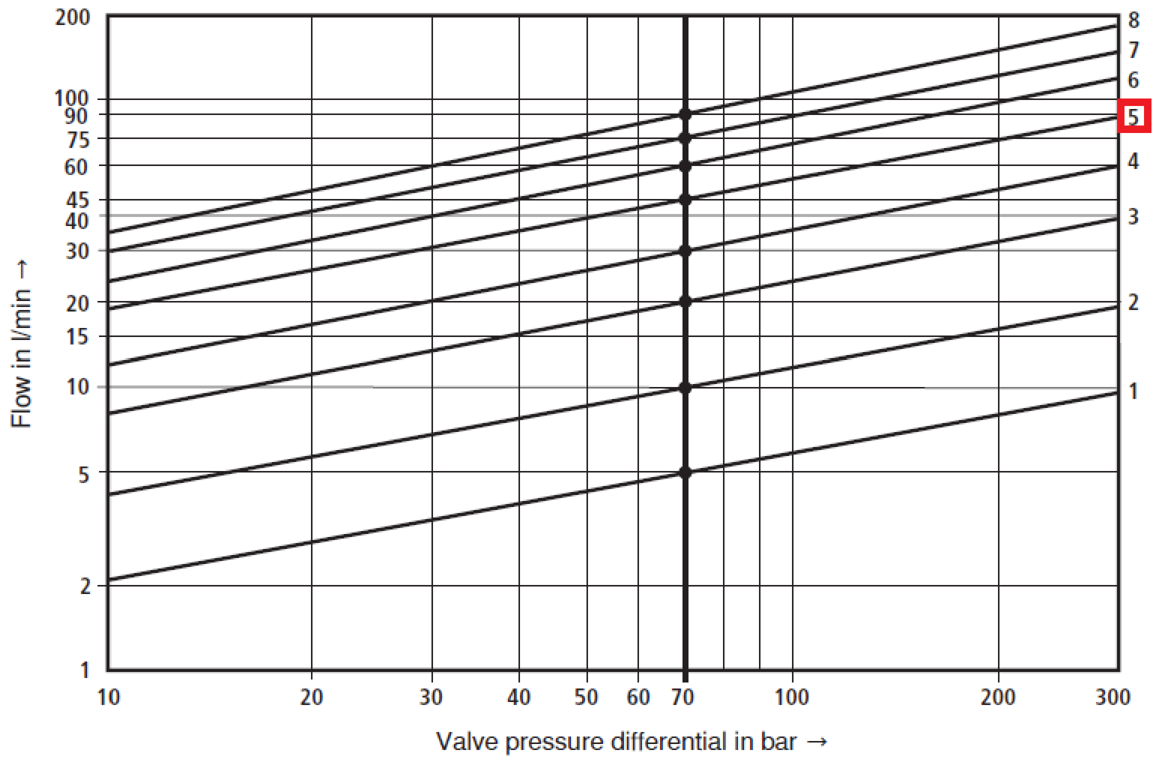


*Fig.96. Flow/load function with 100 % command value signal (tolerance ±10 %)*

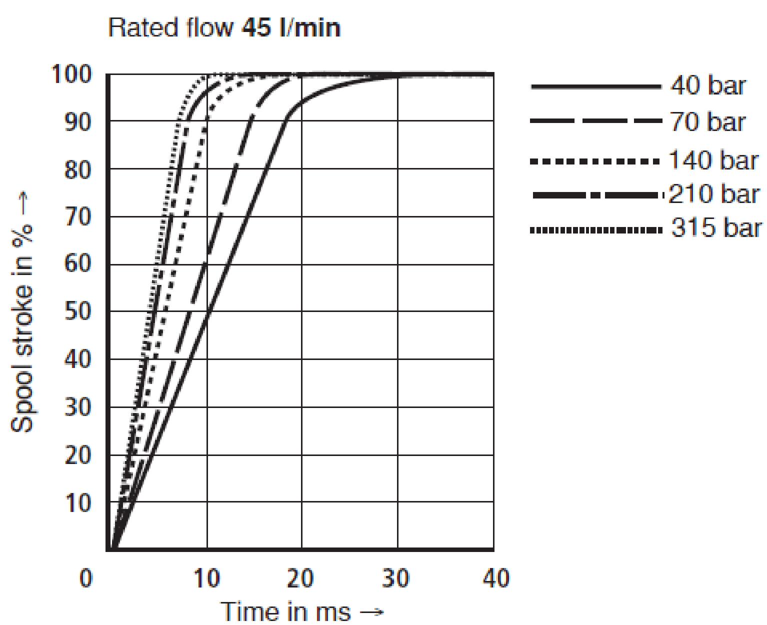


*Fig.97. Transition function with step response without flow*

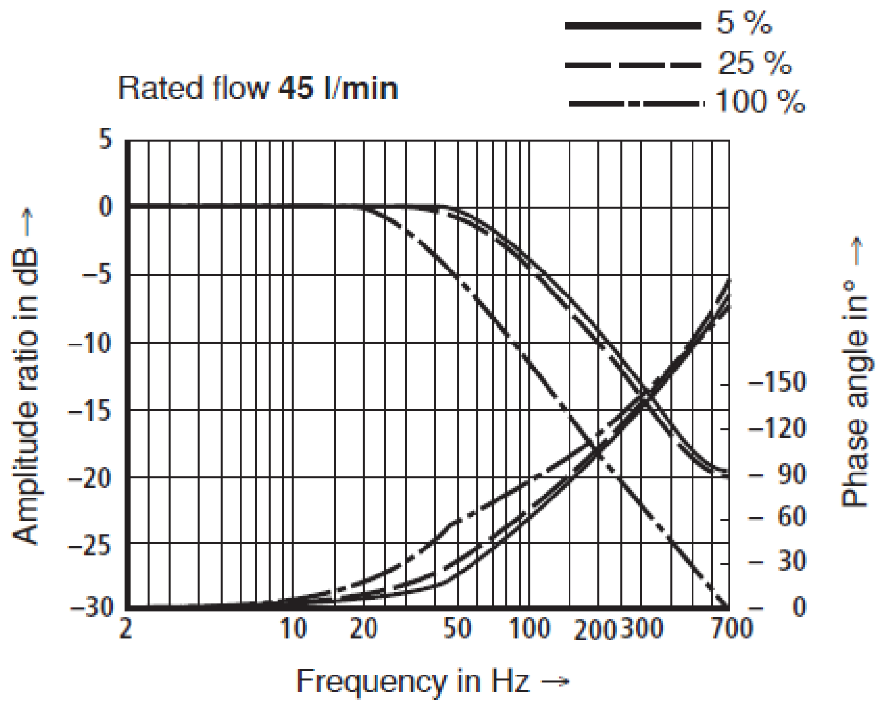


*Fig.98. Frequency response with stroke frequency without flow*

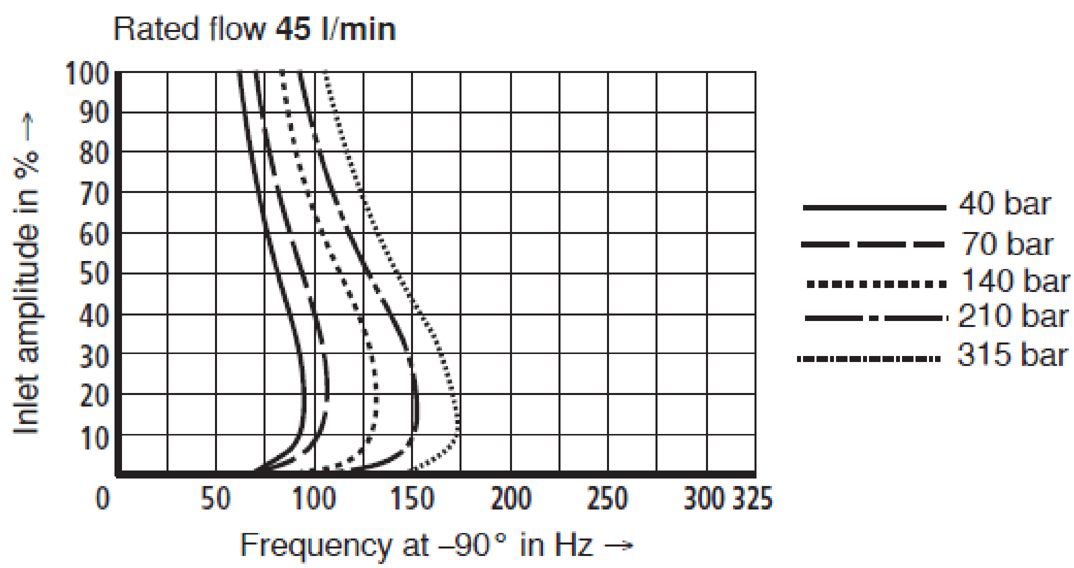


*Fig.99. Dependency of the frequency **f** at –90° on the operating pressure p and the inlet amplitude*

**8.1, 8.2- Actuating cylinder pressure sensor**

Model No: *PS-200-D-G2-1;*
Range: 0-200 Bar;
Output: 4-20 mA;
Operating temperature:-10…+85 degC;
Accuracy: +-5% F.S.
Power:18…36VDC.


*Fig.100. Actuating cylinder pressure sensor*

***9.1, 9.2- Double rod double acting hydraulic cylinder, CGT3MS2/40/28/300F11/B11HEUTAWF15845*** [40]

Both hydraulic cylinders, the actuating cylinder and the loading one have same dimensions being mechanically connected through the force transducer.

***Cylinder coding explanation***

**CG -**Double rod cylinder;
Series: **T3;**
**MS2-** Foot mounting;
**40-** Piston Ø [mm**];**
**28-** Rod Ø [mm];
**300-**Stroke [mm];
**F-** Head and base connected by tie rods with guide bush;

**11-** Series type;
**B-** Pipe threads (ISO 8138);
**1-** Pipe connections / location at head;
**1-** Pipe connections / location at base;
**H-** Piston rod surface hardened and hard chromium plated;
**E-** Piston rod end with internal thread;
**U-** Without end position cushioning;
**T-** Seal version with reduced friction;
**A-** with test point on both sides;
**W-**without option 2.

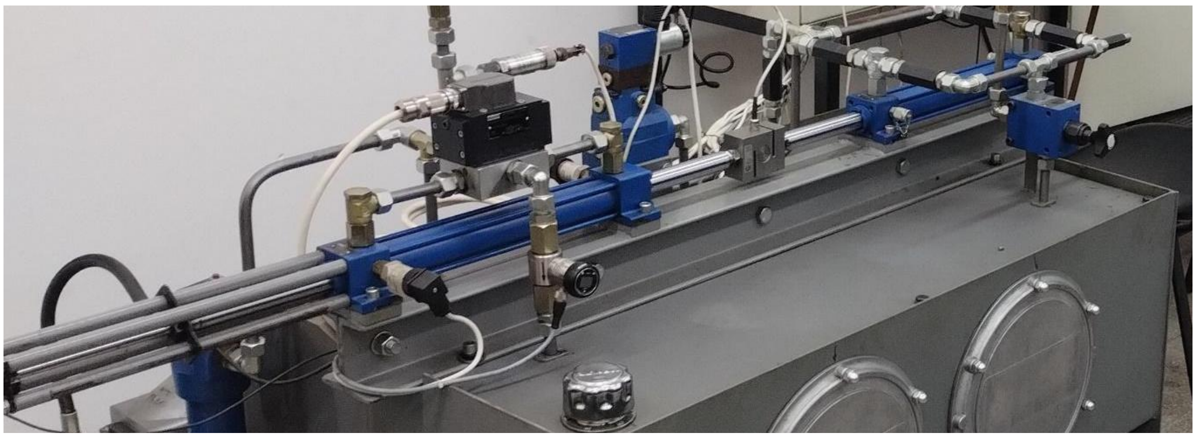

*Fig.101. The hydraulic cylinders*

**10-LVDT position transducer Monitran MTN/EICR150** [41, 42]

This transducer has the role of measuring the stroke of the actuating cylinder. The LVDT, Linear Variable Differential Transformer has been used throughout many decades for the accurate measurement of displacement and within closed loops for the control of positioning. In its simplest form, the design consists of a cylindrical array of primary and secondary windings with a separate cylindrical core which passes through the center (Fig.102.A).
The primary windings (P) are energized with a constant amplitude A.C. supply at a frequency of 1 to 10 kHz. This produces an alternating magnetic field in the center of the transducer which induces a signal into the secondary windings (S &S) depending on the position of the core. Movement of the core within this area causes the secondary signal to change (Fig.102.B).

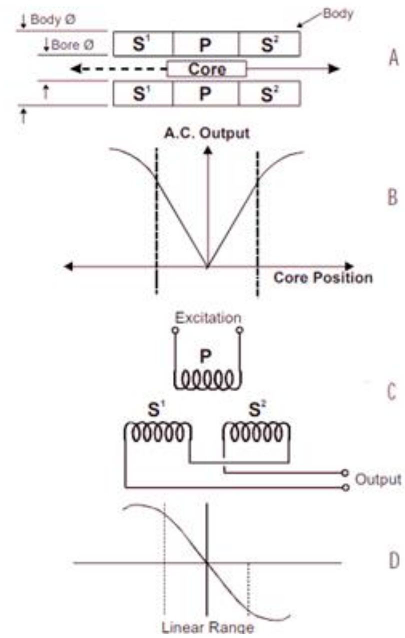


*Fig.102. LVDT working principle*

As the two secondary windings are positioned and connected in a set arrangement (push-pull mode), when the core is positioned at the center, a zero signal is derived. Movement of the core from this point in either direction causes the signal to increase (Fig.102.C). As the windings are wound in a particular precise manner, the signal output has a linear relationship with the actual mechanical movement of the core. The secondary output signal is then processed by a phase-sensitive demodulator which is switched at the same frequency as the primary energizing supply. This results in a final output which after rectification and filtering gives D.C. or 4-20mA proportional to the core movement and also indicates its direction, positive or negative form the central zero point (Fig.102.D). The distinct advantage of using an LVDT displacement transducer is that the moving core does not make contact with other electrical components of the assembly, as with resistive types, as so offers high reliability and long life. Further, the core can be so aligned that an air gap exists around it, ideal for applications where minimum mechanical friction is required.
The transducer used has a maximum stroke of +-150 mm and an output of 4...20mA.

## 11- Force transducer Lorenz K-25 20kN [43]

The force transducer is used to measure the loading force between the actuating cylinder and the loading one. This type is a tension and compression force sensor with nominal force of 20kN.

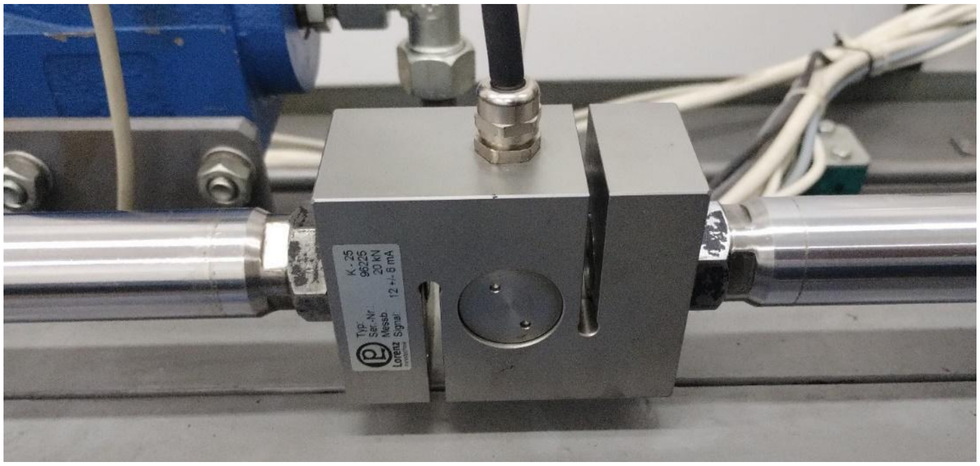

*Fig.103. Lorenz K-25 force transducer*

| Tension and Compression Force Sensor K-25 | | | | |
|---|---|---|---|---|
| Nominal force $F_{nom}$ | kN | 0.02 | 0.05 ... 1 | 2 ... 50 |
| Nominal load $F_{nom}$ | kg | 2 | 5 ... 100 | 200 ... 5000 |
| Accuracy class compression force or tension force | % $F_{nom}$ | 0.1 | | |
| Accuracy class compression force and tension force | % $F_{nom}$ | 0.2 | | |
| Rel. repeatability error in unchanged mounting position $b_{rg}$ | % $F_{nom}$ | 0.08 | | |
| Relative creep | % $F_{nom}$/30 min | <±0.06 | | |
| Rated characteristic value $C_{nom}$ | mV/V | 1.00 ±0.1% | 2.00 ±0.1% | |
| Input/output resistance $R_e/R_a$ | Ω | 350 | | |
| Insulation resistance $R_{is}$ | Ω | $>2*10^9$ | | |
| Rated range of excitation voltage $B_{U,\ nom}$ | VDC | 2 ... 12 | | |
| Electrical connection | | Cable, PVC, 3 m with free strands | | |
| Reference temperature $T_{ref}$ | °C | 23 | | |
| Rated temperature range $B_{T,\ nom}$ | °C | 0 ... 60 | | -10 ... 70 |
| Operating temperature range $B_{T,\ G}$ | °C | -10 ... 70 | | -30 ... 80 |
| Storage temperature range $B_{T,\ S}$ | °C | -30 ... 95 | | -50 ... 95 |
| Temperature effect on zero signal $TK_0$ | % $F_{nom}$/10 K | ±0.04 | | |
| Temperature effect on characteristic value $TK_C$ | % $F_{nom}$/10 K | ±0.12 | | |
| Maximum operating force $F_G$ | % $F_{nom}$ | 130 | | |
| Force limit $F_L$ | % $F_{nom}$ | 150 | | |
| Breaking force $F_B$ | % $F_{nom}$ | >300 | | |
| Permissible oscillation stress $F_{rb}$ | % $F_{nom}$ | 70 | | |
| Lateral force resistance | % $F_{nom}$ | 50 | | |
| Rated displacement $S_{nom}$ | mm | <0.25 | | |
| Preferential direction | | Tension direction | | |
| Material | | Aluminum | | Stainless steel |
| Level of protection | | IP60 | | IP67 |

*Fig.104. Lorenz K-25 force transducer data sheet*

**12.1...12.4 1 Bar check valves type S10A1.0** [44]
The check valve permits the flow to pass just in one direction, this type of valve having a cracking pressure of 1 bar.

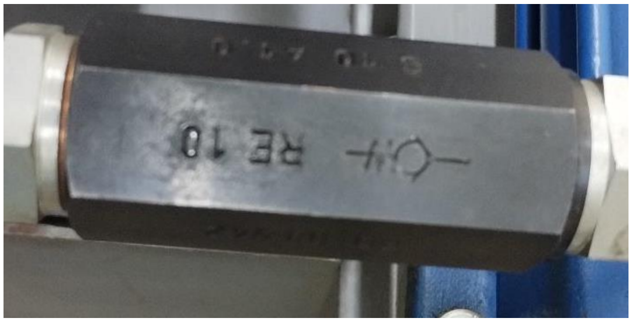


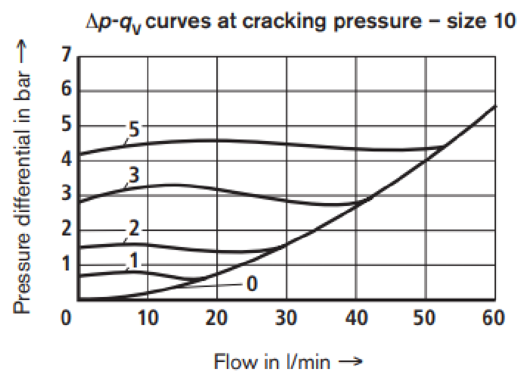


*Fig.105. S10A1.0 Check valve and pressure drop vs. flow curve*

**13. Pressure relief valve DBDH 10 G1A/100** [45]
The pressure relief valve 13 is used to simulate the force on the blade. It can be adjusted from 5 to 100 bar, creating a loading force. The set pressure can be seen with the manometer 6.2.
*Pressure relief valve coding explanation*
**DBD-** Pressure relief valve, direct operated;
**H-** With rotary knob;
**10-** With G 1/2 port;
**G-** For threaded connection;
**100-** Pressure setting up to 100 bar.

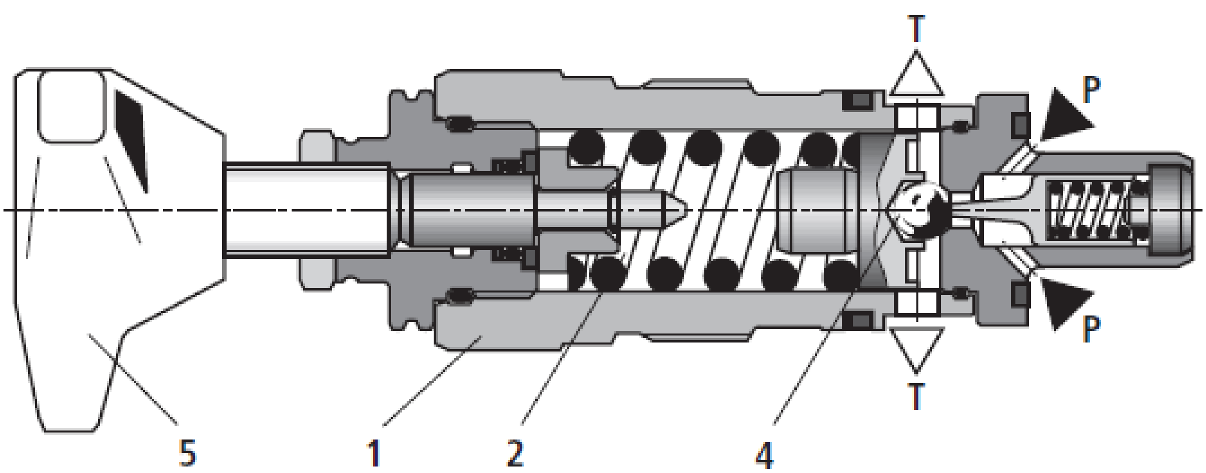


*Fig.106. Direct acting pressure relief valve*

These direct acting pressure relief valves as can be seen in Fig. 106, basically consist of sleeve (1), spring (2), ball (4) and adjustment element (5).
The system pressure setting can be infinitely varied by means of adjustment element (5). Spring (2) presses the ball (4) onto its seat. Channel P is connected to the system. The pressure prevailing in the system acts on the ball area.
When the pressure in channel P rises above the value set on spring (2), the ball (4) opens against spring (2). Hydraulic fluid can now flow from channel P into channel T. To obtain good pressure settings, the entire pressure range was subdivided into 7 pressure ratings. A pressure rating corresponds to a certain spring, which can be used for setting a maximum operating pressure.
The characteristic curves are presented in Fig.107, 108 and 109.

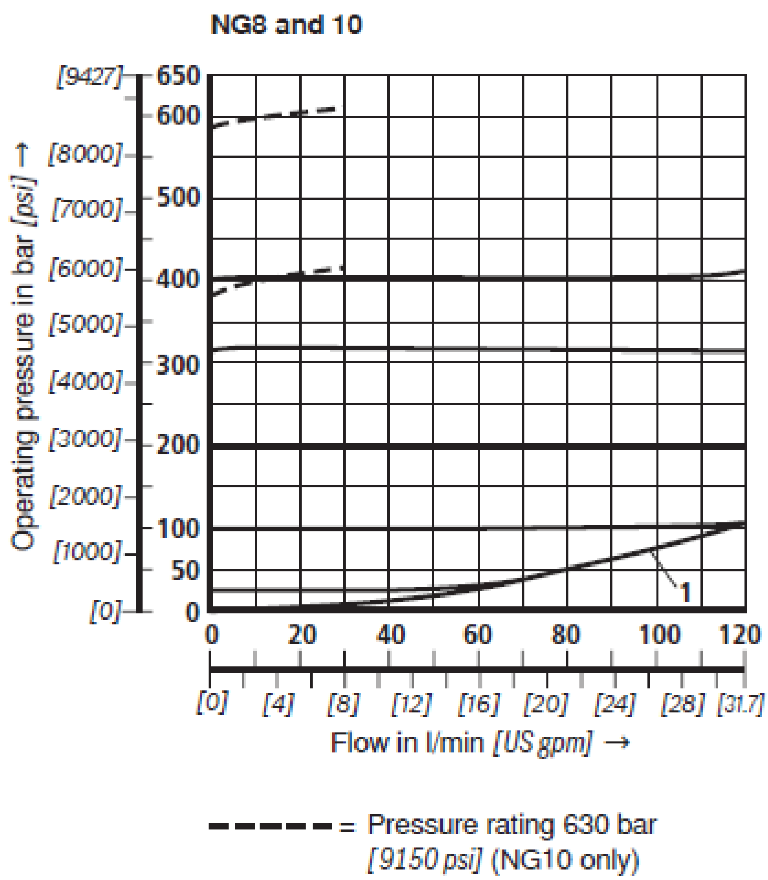


*Fig.107. Characteristic curves (measured with HLP46, Toil = 40 °C ±5 °C )*

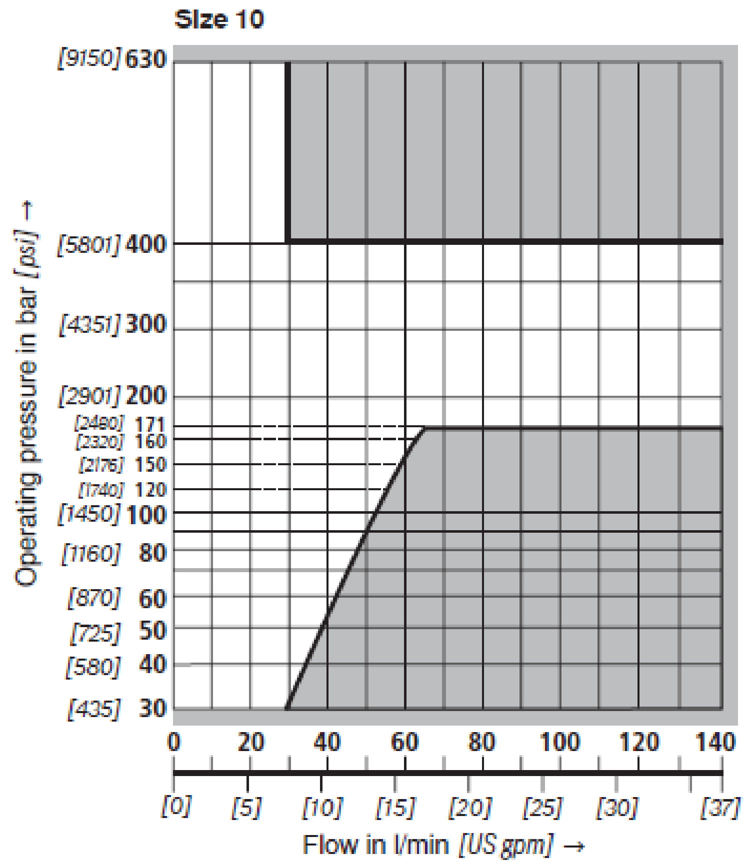


*Fig.108. Pressure vs flow curves for type DBD safety valve*

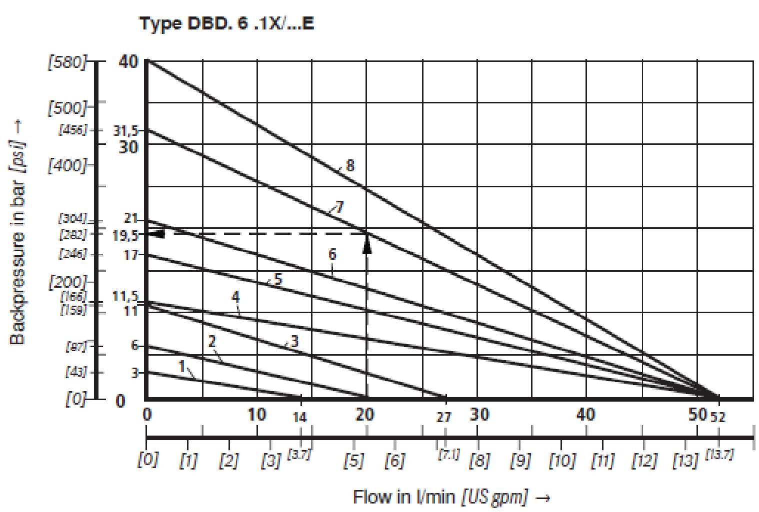


| Charac-teristic curves | Response pressure $p_A$ in bar [psi] |
|---|---|
| 1 | 30 [435] |
| 2 | 60 [870] |
| 3 | 110 [1595] |
| 4 | 115 [1668] |
| 5 | 170 [2465] |
| 6 | 210 [3046] |
| 7 | 315 [4568] |
| 8 | 400 [5800] |

Characteristic curves for intermediate values can be generated by interpolation. Further explanations can be found on page 16.

*Fig.109. Permissible maximum flow qVmax in dependence upon backpressure pT in the drain line*

**14-Flow meter OMNI-RT** [46]

The flow meter is used to measure the volumetric flow rate in the actuating circuit.


*Fig.110. OMNI-RT flow meter*

A turbine acts as the primary sensor; its rotational speed is proportional to the flow rate. The rotational speed is detected by means of pre-tensioned Hall sensors, i.e. there are no magnets in the flow space. The OMNI transducer located on the sensor has a backlit graphics LCD display which is very easy to read, both in the dark and in bright sunlight. The graphics display allows the presentation of measured values and parameters in a clearly understandable form. The measured values are displayed to 4 places, together with their physical unit, which may also be modified by the user. The electronics have an analog output (4..20 mA or 0..10 V) and two switching outputs, which can be used as limit switches for monitoring minima or maxima, or as two-point controllers. The switching outputs are designed as push-pull drivers, and can therefore be used both as PNP and NPN outputs. Exceeding limit values is signaled by a red LED which is visible over a long distance, and by a cleartext in the display. The stainless steel case has a hardened non-scratch mineral glass pane. It is operated by a programming ring fitted with a magnet, so there is no need to open the operating controls housing, and its leak proofness is permanently ensured.

**Technical data**

| | |
|---|---|
| **Sensor** | turbine with pre-tensioned Hall sensor |
| **Nominal width** | DN 15..50 |
| **Process connection** | G $^1/_2$ A...G 2 A |
| **Metering ranges** | see table "Ranges" |
| **Measurement accuracy** | ±1 % of full scale value<br>in the specified metering range<br>including linearity and repeatability |
| **Medium temperature** | -20..+85 °C<br>optionally -20..+150 °C (for 8 bar min.) |
| **Ambient temperature** | -20..+70 °C |
| **Storage temperature** | -20..+80 °C |
| **Max. particle size** | 0.5 mm |
| **Pressure loss** | maximum 0.3 bar at $Q_{max.}$ |
| **Pressure** | PN 250 bar |
| **Materials medium-contact** | Housing: stainless steel 316<br>Turbine: stainless steel 430<br>Bearing: tungsten carbide |
| **Materials Electronic housing** | Housing: stainless steel 1.4305<br>Glass: mineral glass hardened<br>Magnet: samarium-Cobalt<br>Ring: POM |
| **Supply voltage** | 18..30 V DC |
| **Power consumption** | < 1 W |
| **Analog output** | 4..20 mA / max. load 500 Ω or<br>0..10 V / min. load 1 kΩ |
| **Switching outputs** | transistor output "push-pull"<br>(resistant to short circuits and polarity reversal)<br>$I_{out}$ = 100 mA max. |
| **Hysteresis** | adjustable, position of the hysteresis depends on minimum or maximum |
| **Display** | backlit graphical LCD-Display (transreflective), extended temperature range -20..+70 °C, 32 x 16 pixels, background illumination, displays value and unit, flashing LED signal lamp with simultaneous message on the display. |
| **Electrical connection** | for round plug connector M12x1, 5-pole |
| **Ingress protection** | IP 67 / (IP 68 when oil-filled) |
| **Weight** | see table "Dimensions" |
| **Conformity** | CE |

*Fig.111. OMNI-RT flow meter technical data*

**15-Pressure relief valve, pilot operated DBW 10 BG2-52/200S6EG24N9K4R12** [47]

The pilot operated pressure relief valve is used to set the maximum pressure in the system.

*Pressure relief valve coding explanation*

**W-** With built-on directional valve;
**10-** Pilot valve with main spool insert size 10;
**B-** Normally open;
**G-** For threaded connection;
**2-** Sleeve with hexagon and protective cap;
**52-** Component series;
**200-** Pressure setting up to 200 bar;
**S -** With switching shock damping feature;

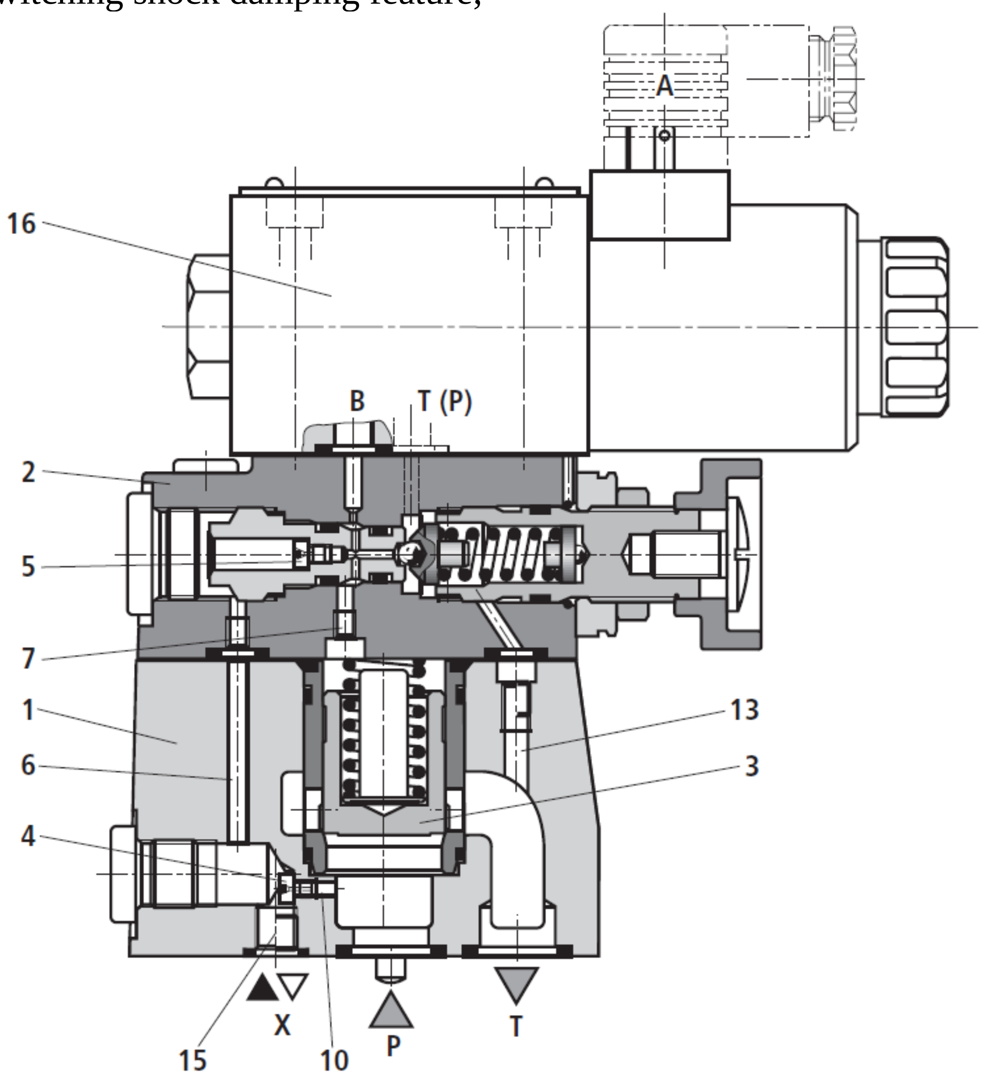


*Fig.112.Pressure relief valve with switching shock damping*

Pressure control valves of types DB and DBW are pilot operated pressure relief valves. They are used for the limitation (DB) or limitation and solenoid operated unloading (DBW) of the operating pressure. Pressure relief valves (DB) basically consist of main valve (1) with main spool insert (3) and pilot valve (2) with pressure adjustment element. The pressure present in channel P acts on the main spool (3). At the same time, the pressure is applied via pilot lines (6) and (7) that are provided with orifices (4) and (5) to the spring-loaded side of main spool (3) and to ball (8) in pilot valve (2). When the pressure in channel P rises to a value above that set on spring (9), ball (8) opens against spring (9). The signal for this process is provided internally via pilot lines (10) and (6) from channel P. The hydraulic fluid on the spring-loaded side of main spool (3) can now flow via pilot line (7), orifice bore (11) and ball (8) into spring chamber (12). From here, it is fed internally via pilot line (13) in the case of type DB…–, or externally via pilot line (14) in the case of type DB…Y, back to the tank. Orifices (4) and (5) generate a pressure differential across main spool (3), and the connection from channel P to channel T opens. The hydraulic fluid now flows from channel P to channel T while the set operating pressure is maintained.

The pressure relief valve can be unloaded or changed over to another pressure (second pressure stage) via port “X” (15).

Pressure relief valve type DBW

In principle, the function of this valve corresponds to that of type DB. However, unloading through main spool (3) is achieved by operating the built-on directional spool valve (16).

The characteristic curves of the pilot operated valve are presented in Fig.113, 114 and 115.

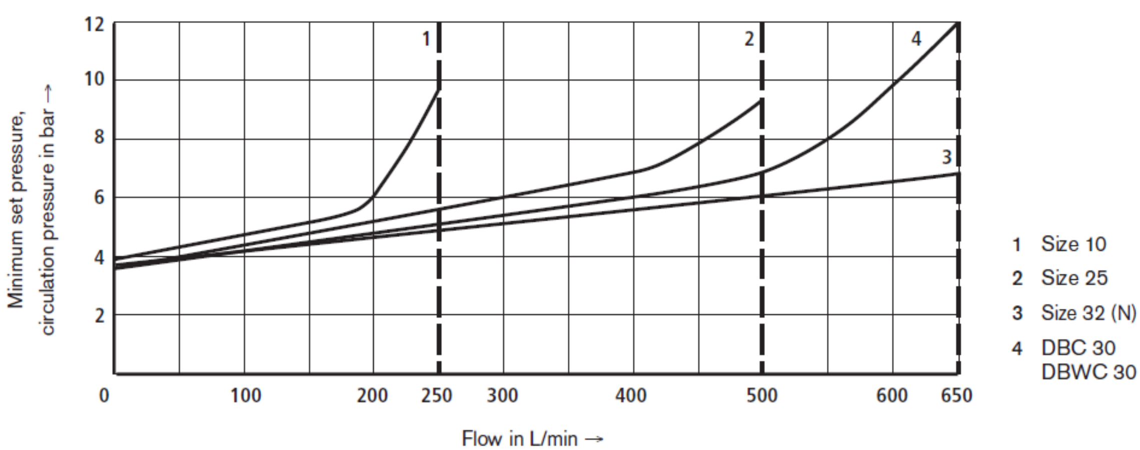


*Fig.113.Minimum set pressure and circulation pressure in dependence upon the flow*

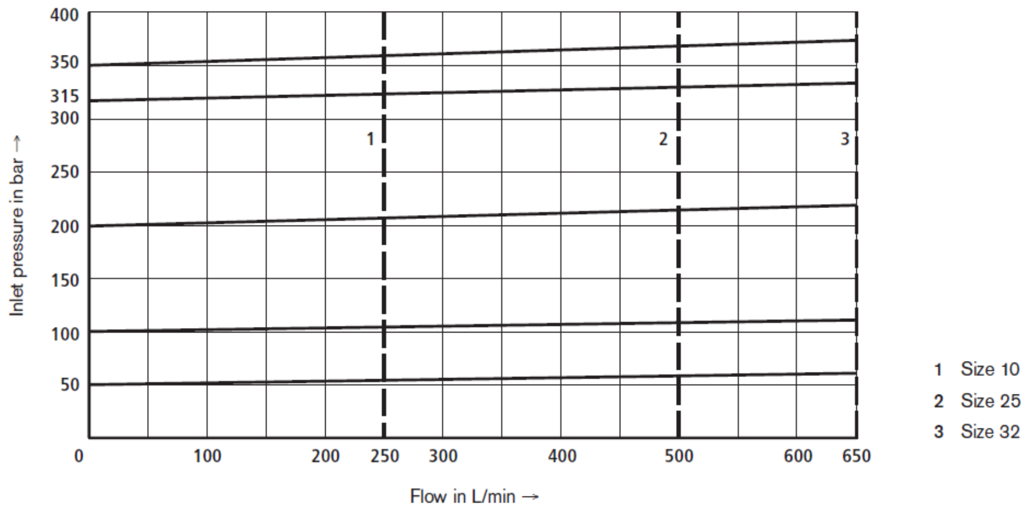


*Fig.114. Inlet pressure in dependence upon the flow*

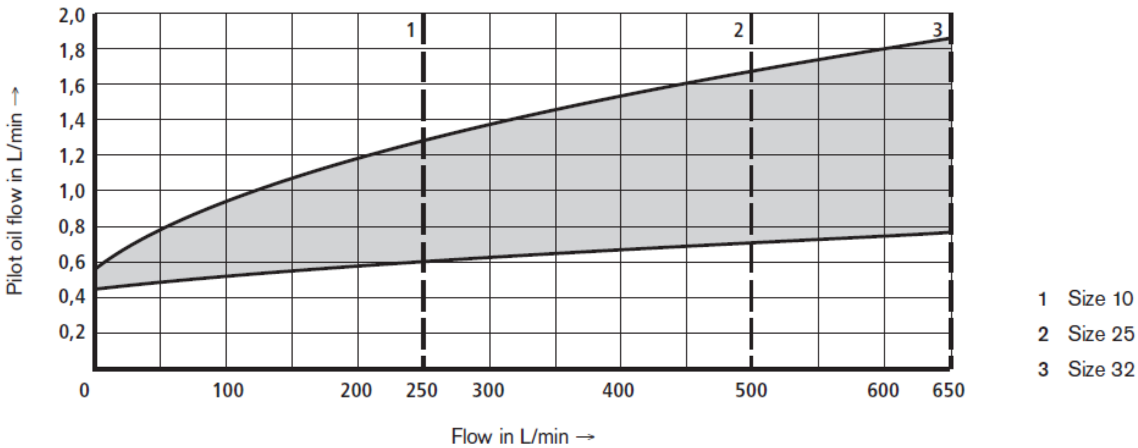


*Fig.115. Pilot oil flow*

**16- 5 Bar check valve type S10A1.0** [44]
This check valve has the role of maintaining a 5 bar pressure in the return line where the loading cylinder is connected.

### II.1.2 The data acquisition system

The data acquisition system consists of the following components and transducers, presented as a block scheme in Fig.116:
- the signal generator;
- the data acquisition board;
- the servo valve 7;
- the flow transducer 14;
- the pump line pressure transducer 5;

- the cylinder left side pressure transducer 8.1, the cylinder right side pressure transducer 8.2;
- the cylinder position transducer 10;
- the cylinder force transducer 11.

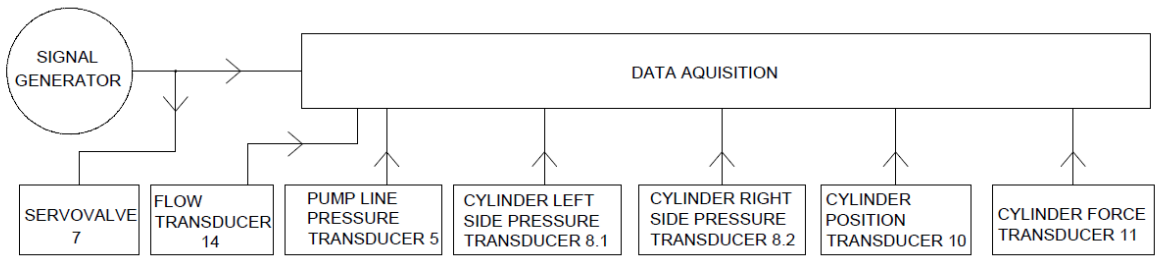


*Fig.116. The data acquisition system*

The sensors and the servovalve were presented in chapter II.1.1, in this chapter being presented the signal generator and the data acquisition board.

### **The Signal generator Tektronix CFG253** [48]

The Tektronix CFG253 Function Generator can produce sine, square and sawtooth waves and TTL signals in a frequency range from 0.03 Hz up to 3 MHz. It can be used to test and calibrate audio, ultrasonic equipment, servo systems and it can also directly control the amplitude and DC offset. The function generator has a symmetry function to control the rise and fall times of sine or sawtooth waves and the duty cycles of square waves. It also has a sweep function that makes the output signal traverse a range of frequencies.

| Characteristic | Measurement | |
|---|---|---|
| Outputs | Square wave, sine wave, sawtooth wave, TTL pulse, and sweep functions for all outputs | |
| Line Voltage Range | 90 to 110, 108 to 132, 198 to 242, and 216 to 250 VAC at 50–60 Hz | |
| Frequency ranges, nonskewed waveform (Freq/1) | **Range Setting** | **Variable** |
| | 1 | 0.3 to 3.0 Hz |
| | 10 | 3.0 to 30 Hz |
| | 100 | 30 to 300 Hz |
| | 1 K | 0.3 K to 3.0 kHz |
| | 10 K | 3 K to 30 kHz |
| | 100 K | 30 K to 300 kHz |
| | 1 M | 0.3 M to 3.0 MHz |
| Frequency ranges, skewed waveform (Freq/10) | **Range Setting** | **Variable** |
| | 1 | 0.03 to 0.3 Hz |
| | 10 | 0.3 to 3.0 Hz |
| | 100 | 3.0 to 30 Hz |
| | 1 K | 30 to 300 Hz |
| | 10 K | 0.3 K to 3.0 kHz |
| | 100 K | 3.0 K to 30 kHz |
| | 1 M | 30 K to 300 kHz |
| Frequency multiplier | Variable 0.3 to 3.0 times the selected frequency range | |
| Frequency/1 dial accuracy | ±5% of full scale of frequency/1 | |
| Frequency/10 dial accuracy | ±5% of full scale of frequency/10 | |
| Sine wave distortion | <1% from 10 Hz to 100 kHz | |

| Characteristic | Measurement |
|---|---|
| Sawtooth linearity | 20 Hz to 200 kHz ≥ 99%<br>200 kHz to 3 MHz ≥ 97% |
| Square response | ≤ 100 ns rise/fall time maximum output into 50 Ω load |
| Main output amplitude | Two ranges:<br>0–20 V peak-to-peak<br>100 mV to 20 $V_{p-p}$ (open circuit)<br>50 mV to 10 $V_{p-p}$ (50 Ω load)<br>0–2 V peak-to-peak<br>10 mV to 2 $V_{p-p}$ (open circuit)<br>5 mV to 1 $V_{p-p}$ (50 Ω load) |
| Impedance | 50 Ω ±10% |
| DC offset | <–10 V to >+10 V (open circuit), and<br><–5 V to >+5 V (into 50 Ω load) |
| Duty cycle | 5:1 minimum duty cycle change (50% at Center:Cal position), with symmetry button (Freq ÷ 10) pushed in |
| Sweep rate | Continuously variable from 0.5 to 50 Hz |
| Sweep width | Variable from 1:1 to 100:1 |

*Fig.117. Signal generator warranted characteristics*

**The data acquisition board DT9804** [49]

The DT9800 Series is a family of isolated, multifunction USB data acquisition modules. All DT9800 Series modules feature 16 single-ended (SE)/8 differential (DIFF) inputs with 12- or 16-bit resolution, up to 100 kS/s aggregate sample rate, 16 digital I/O lines, 2 counter/ timers, and optional 12- or 16-bit analog outputs.

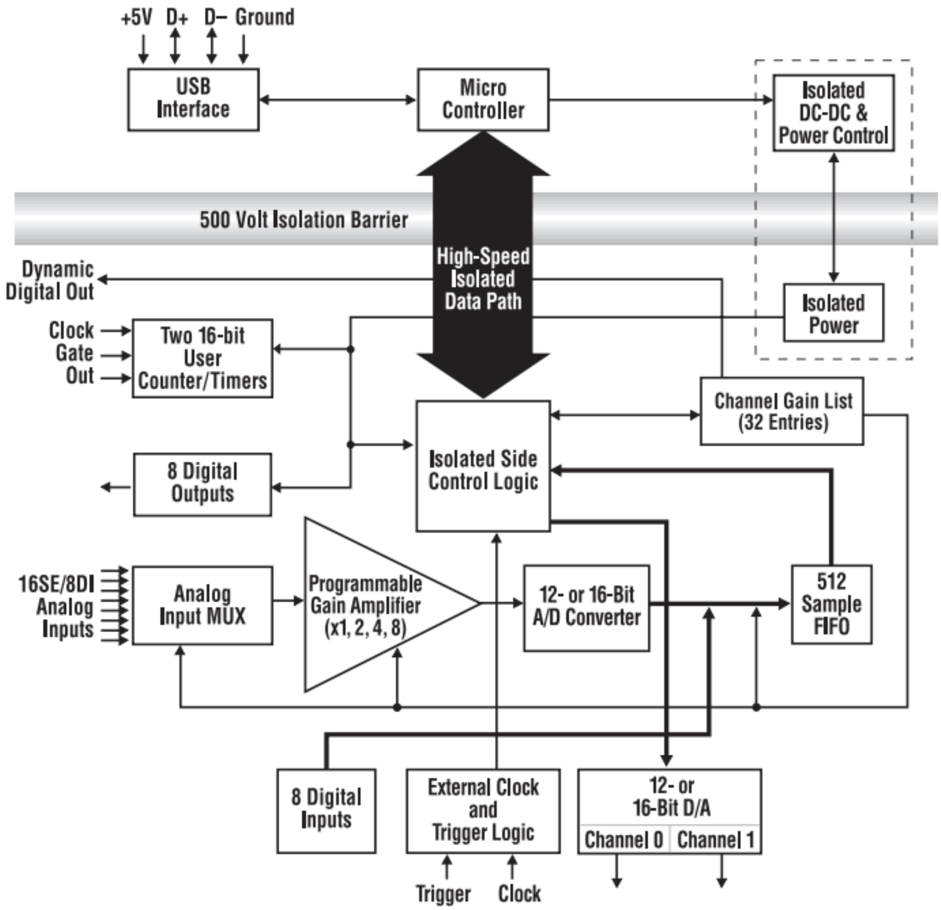


*Fig.118. Data acquisition board block diagram*

*Key Features*

• ±500 V galvanic isolation prevents ground loops, maximizes analog signal integrity, and protects the computer;

• Runs on USB power ideal for portable applications – no external power supply needed;

• 16 SE/8 DIFF analog input channels, 12- or 16-bit resolution;

• Fast sampling: up to 100 kS/s sample rate;

• Analog output channels: optional 12- or 16-bit • 16 DIO, two 16-bit counter/timers;

• Flexible acquisition modes for input operations: single value, continuous, and triggered scan;

## II. 2. The mathematical model [34, 50, 51]

In the current section, the main mathematical models of the servo-valve controlled hydraulic cylinder operating under variable load are presented.

### *II.2.1. Servo-valve model*

The servo-valve dynamics can be approximated with a first-order equivalent system when they operate at frequencies up to 50 Hz ($\omega_n \leq 50$Hz):

$$H(s) = \frac{Q}{\Delta U_c} = \frac{K}{1+\tau \cdot s} \tag{76}$$

Where Q [$m^3/s$] is the servo-vale volumetric flow rate, $\Delta U_c$ [V] is the input voltage (command) of the servo-valve, K proportional coefficient in stationary operating regime, $\tau$ is the servo-valve time constant.

### *II.2.2. Double acting hydraulic cylinder*

The mathematical model of the double acting hydraulic cylinder starts from continuity equation of the hydraulic cylinder:

$$Q = S_p \cdot \frac{dX_p}{dt} + C_{tp} \cdot P_L + \frac{V_t}{4 \cdot E_u} \cdot \frac{dP_L}{dt} \tag{77}$$

Where $S_p$ represents the cylinder active surface [$m^2$], $X_p$ represents the hydraulic cylinder stroke [m]; $V_t$ represents active volume of cylinder [$m^3$]; $C_{tp}$ represents the total leakage of the cylinder [$m^3/s$]; $E_u$ the bulk modulus of the fluid [Pa] and $P_L$ is the differential (load) pressure between the cylinder chambers [Pa].

Applying the Laplace transform in equation 77 results:

$$Q = S_p \cdot X_p \cdot s + \left(C_{tp} + \frac{V_t}{4 \cdot E_u} \cdot s\right) \cdot P_L \tag{78}$$

The piston force is expressed as:

$$F_P = S_p \cdot P_L = M_t \cdot \frac{d^2 X_p}{dt^2} + B_L \cdot \frac{dX_p}{dt} + K_a \cdot X_p + F_z \qquad (79)$$

Where $F_P$ is the force exerted by the piston [N]; $M_t$ is the total mass (load + piston mass + road mass) [kg]; $B_L$ the total damping factor (load + piston+ road) [N s/m]; $K_a$ is the total stiffness [N/m] and $F_z$ is the perturbation force [N] being so small that can be neglected.
After applying the Laplace transform in equation 79, $P_L$can be determined as:

$$P_L = \frac{1}{S_p} \cdot \left(M_t \cdot X_p \cdot s^2 + B_L \cdot X_P \cdot s + K_a \cdot X_p + F_z\right) \qquad (80)$$

Combining equations (77-80) results in the following equivalent transfer function (equation 81 with its parameters presented in equation 82) of the entire system (the servo-valve controlled hydraulic cylinder operating under variable load):

$$\frac{X_p}{\Delta U_c} = \frac{4 \cdot E_u \cdot S_p \cdot K}{A \cdot s^4 + B \cdot s^3 + C \cdot s^2 + D \cdot s + 4 \cdot E_u \cdot C_{tp} \cdot K_a} \qquad (81)$$

With

$$\begin{gathered} A = V_t \cdot M_t \\ B = V_t \cdot M_t + 4 \cdot E_u \cdot C_{tp} \cdot \tau + V_t \cdot B_L \cdot \tau \\ C = 4 \cdot E_u \cdot C_{tp} + V_L \cdot B_L + 4 \cdot E_u \cdot \tau \cdot \left(S_p\right)^2 + 4 \cdot E_u \cdot C_{tp} \cdot B_L \cdot \tau \\ D = 4 \cdot E_u \cdot \left(S_p\right)^2 + 4 \cdot E_u \cdot C_{tp} \cdot B_L + 4 \cdot E_u \cdot C_{tp} \cdot K_a \cdot \tau \end{gathered} \qquad (82)$$

## II. 3. Experimental system identification

The experimental data acquisition and also the system identification was done in MATLAB.
The data logger used was DT9804 which is a multifunction USB data acquisition module featuring 16 single-ended (SE)/8 differential (DIFF) inputs with 12- or 16-bit resolution, up to 100 kS/s aggregate sample rate, 16 digital I/O lines, 2 counter/timers, and optional 12- or 16-bit analog outputs, connected to a HP Gaming Pavilion—15-dk0022ns 8PK68EA.
Several experiments have been conducted in order to cover the entire operating range in terms of servo-valve signal shape (sinusoidal), frequency (0.45 Hz, 0.6 Hz, 0.75

Hz), amplitude (±2 V, ±5 V, and ±10 V) and load (pressure variation on the hydraulic cylinder acting as a load for 5 bars, 30 bars and 70 bars).
The raw experimental data have been acquired using seven of the available input channels of the DT9804 and logged on MATLAB (version R2024b), the position of cylinder rod on Analog Input Channel 0, p31 on Analog Input Channel 1, p32 on Analog Input Channel 2, flow on Analog Input Channel 3, force on Analog Input Channel 4, p33 on Analog Input Channel 5 and the servo-valve command, Analog ±10 V, given by the signal generator on Analog Input Channel 6 with a sampling rate of 1000 values/second (one value/1 millisecond).
The raw value given by the position transducer (Analog ±10 V) the data logged on MATLAB is converted to corresponding physical units according to equation (83):

$$Pos = a \cdot Pos_A + b \tag{83}$$

where *Pos* represents the extension of the hydraulic cylinder rod in mm, $Pos_A$ represents the raw analog value (±10 V), $a$ = 15.676 represents the calibration slope, and $b$ = 0.748 represents the calibration offset ($a$ and $b$ coefficients being obtained by calibrating the transducer so that the value measured by it, to be the same as the cylinder piston stroke (±150 mm) and the value 0 to represents the cylinder in the middle position).
The experimental data stored in MATLAB have been filtered using a lowpass filter designed in MATLAB in order to attenuate the frequencies above the specified passband frequency ($F_{pass}$). The upper limit of the passband frequency of the filter was chosen to be higher than the maximum frequency at which the servo-valve can make the cylinder oscillate. The maximum oscillation frequency of the cylinder is calculated considering the maximum flow rate given by the servo-valve $Q$ = 12 L/min in the system and the maximum stroke of the cylinder ($L$ = 0.15 m), using Equation (3):

$$F_{pass} = \frac{1}{t} = \frac{1}{L/v} = \frac{1}{L/(Q/S)} = 2.1\ Hz \approx 3\ Hz \tag{84}$$

With

$$S = \frac{\pi \cdot (D^2 - d^2)}{4} = 0.000641\ m^2 \tag{85}$$

where $T$ represents the time interval during which the cylinder makes an entire stroke, $v$ represents the cylinder's maximum velocity, $S$ represents the active surface of the hydraulic cylinder ($S$ = 0.000641 m$^2$), and $D$ represents the diameter of the cylinder ($D$ = 40 mm) and $d$, representing the diameter of the rod ($d$ = 28 mm).

For experimental system identification, MATLAB System Identification tool was used. Based on the measured data (having as input the servo-valve command and as output the actuating cylinder position), a model was emulated, considering a transfer function (TF) with 4 poles and 0 zeroes (based on the mathematical model presented above), the TF was generated and fit checked. If the curve fitting percent was higher than 85%, the generated transfer function was considered acceptable and kept. If the fitting was under the specified percentage another transfer function with 0 zeros and 3 poles, was considered. This new TF was also curve fit checked and if it was over 85% that was the considered TF. The logic scheme is presented in Figure 120.

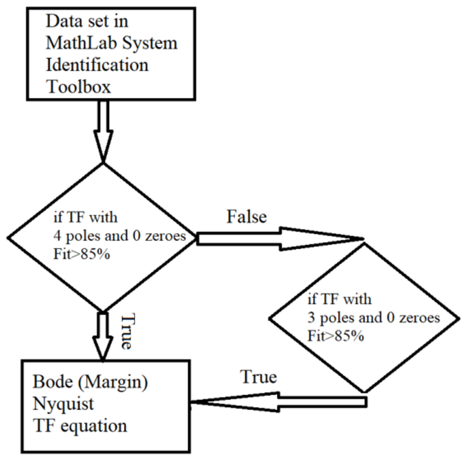


*Fig.120. System Identification logic*

***II.3.1. The results for the sinusoidal shape signal with a frequency of 0.45 Hz***

***II.3.1.1. 2V amplitude on command signal***

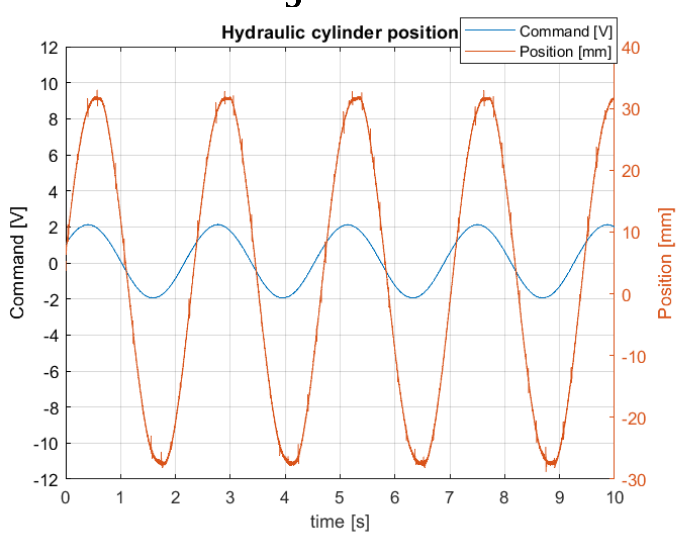


*a) 5 bar load*

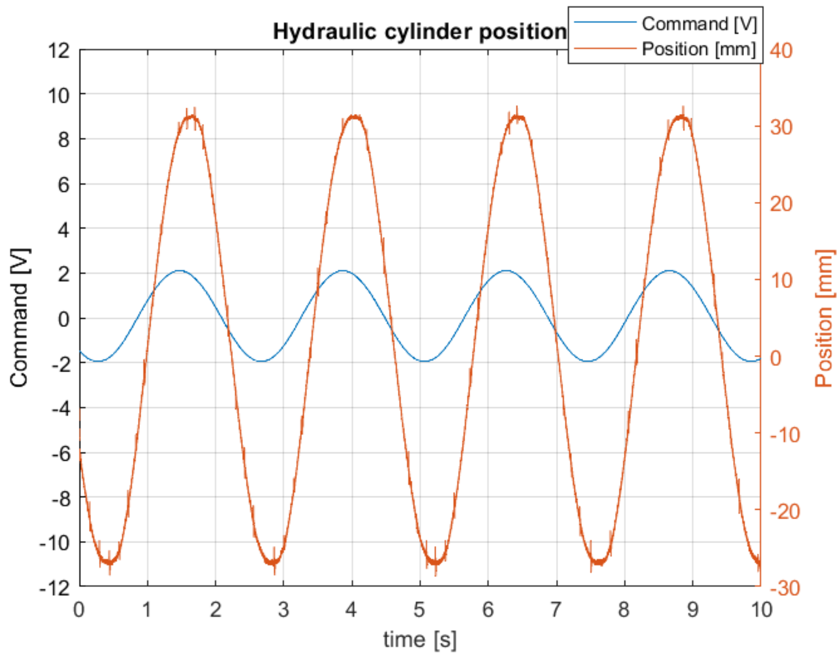


*b)30 bar load*

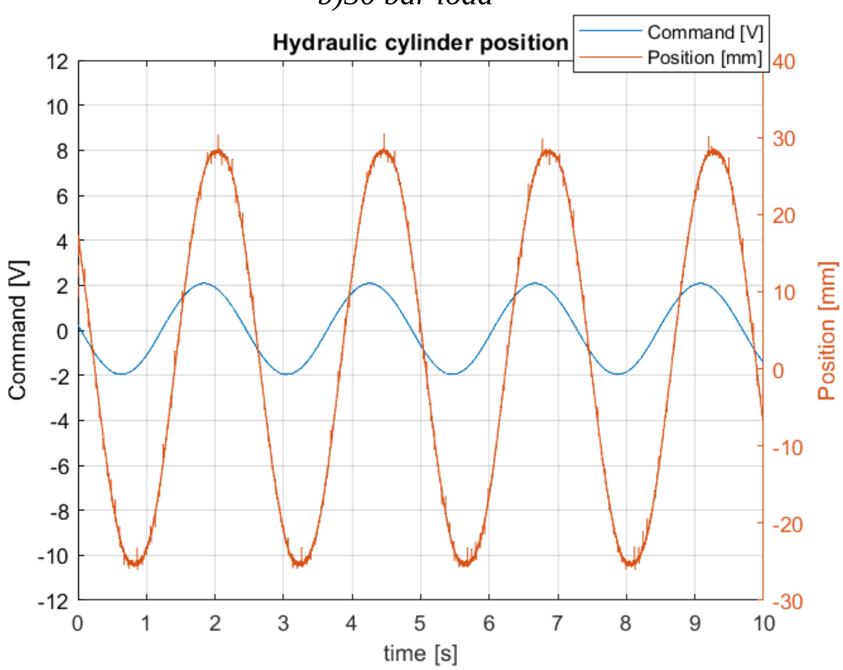


*c)70 bar load*

*Fig.121. The variation command signal of 5V vs position with different loads*

Based on the fitting logic presented in figure 120 there were chosen the following transfer functions:

$$TF_{2V5bar0.45Hz} = \frac{2.618 \cdot 10^4}{s^3 + 7.359 \cdot s^2 + 232.1 \cdot s + 1708} \tag{86}$$

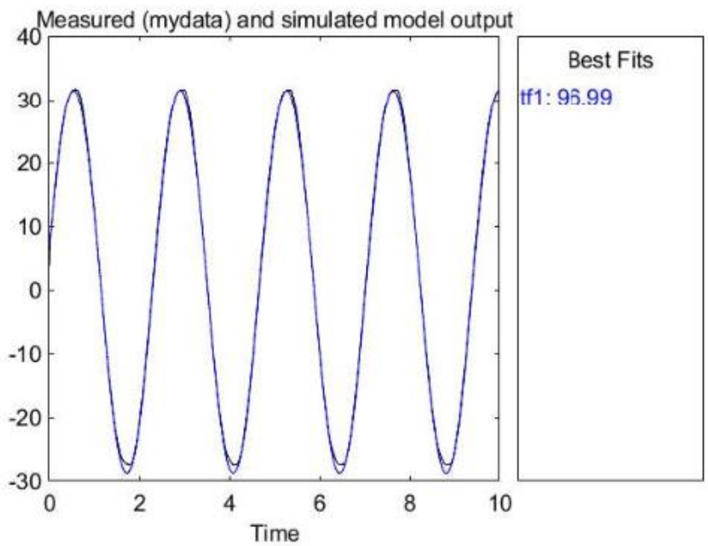


Fig.122.a. The transfer functions TF fit at command signal of 2V with 5 bar load

$$TF_{2V30bar0.45Hz} = \frac{5.035 \cdot 10^5}{s^4 + 16.12 \cdot s^3 + 416.7 \cdot s^2 + 4862 \cdot s + 3.472 \cdot 10^4} \tag{87}$$

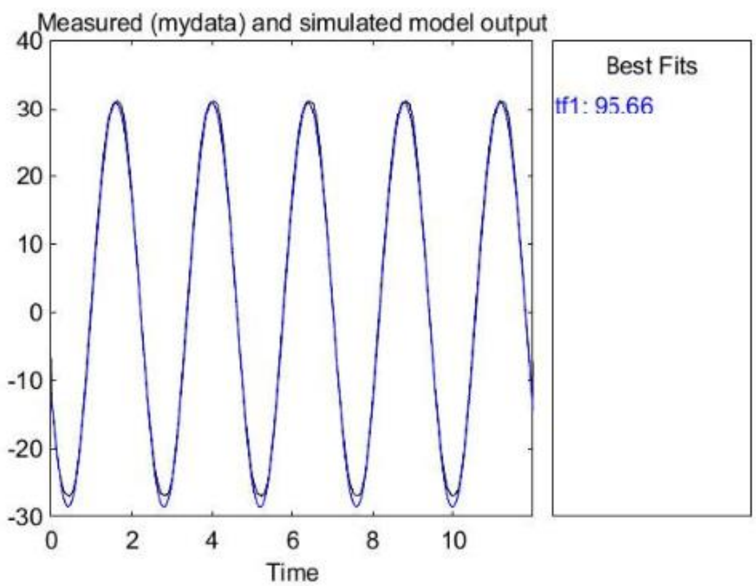


*Fig.122.b. The transfer functions TF fit at command signal of 2V with 30 bar load*

$$TF_{2V70bar0.45Hz} = \frac{2.295 \cdot 10^5}{s^4 + 15.21 \cdot s^3 + 296.1 \cdot s^2 + 3367 \cdot s + 1.655 \cdot 10^4} \tag{88}$$

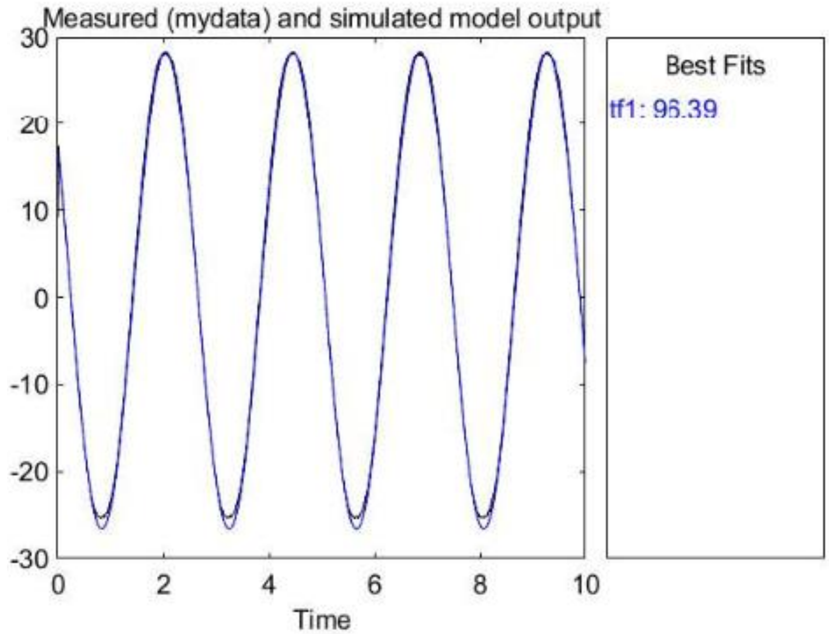


*Fig.122.c. The transfer functions TF fit at command signal of 2V with 70 bar load*

The **margin** [52] function plots the Bode diagram of the system on the screen and indicates the gain and phase margins on the plot. Gain margins are expressed in dB, and phase margin in $^{0}$.

Solid vertical lines mark the gain margin and phase margin. The dashed vertical lines indicate the locations of $\boldsymbol{\omega_{cp}}$, the frequency where the phase margin is measured, and $\boldsymbol{\omega_{cg}}$, the frequency where the gain margin is measured. The plot title includes the magnitude and location of the gain and phase margin.

***Gm*** and ***Pm*** of a system indicate the relative stability of the closed-loop system formed by applying unit negative feedback to the open loop system, as shown in the following figure.

m is the amount of gain variance required to make the loop gain unity at the frequency $\omega_{cg}$ where the phase angle is –180° (modulo 360°). In other words, the gain margin is 1/*g* if *g* is the gain at the –180° phase frequency. Similarly, the phase margin is the difference between the phase of the response and –180° when the loop gain is 1.0. The frequency $\omega_{cp}$ at which the magnitude is 1.0 is called the *unity-gain frequency* or *gain crossover frequency*. When the system has more than one crossover, margin indicates the frequencies with gain margin closest to 0 dB and phase margin closest to 0°.

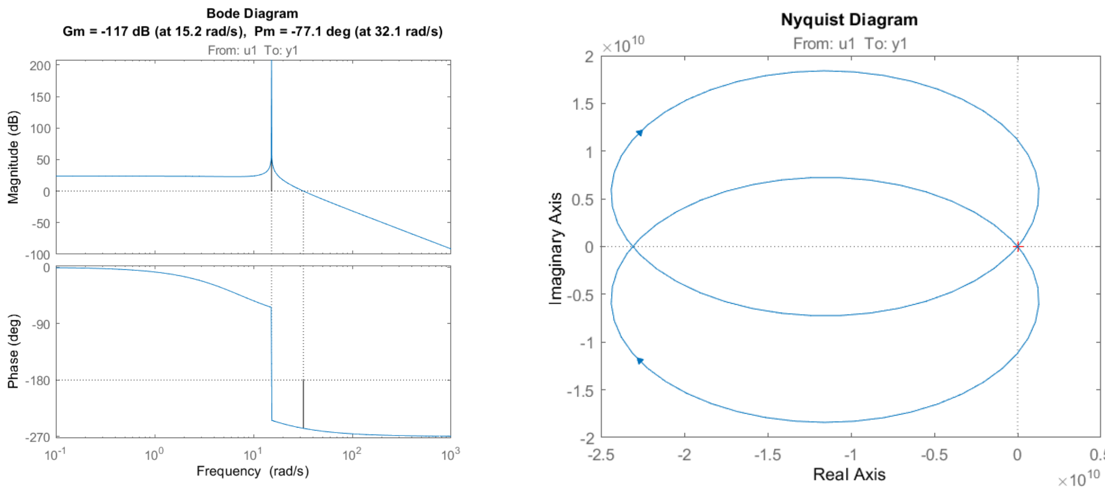


*a) 5 bar load*

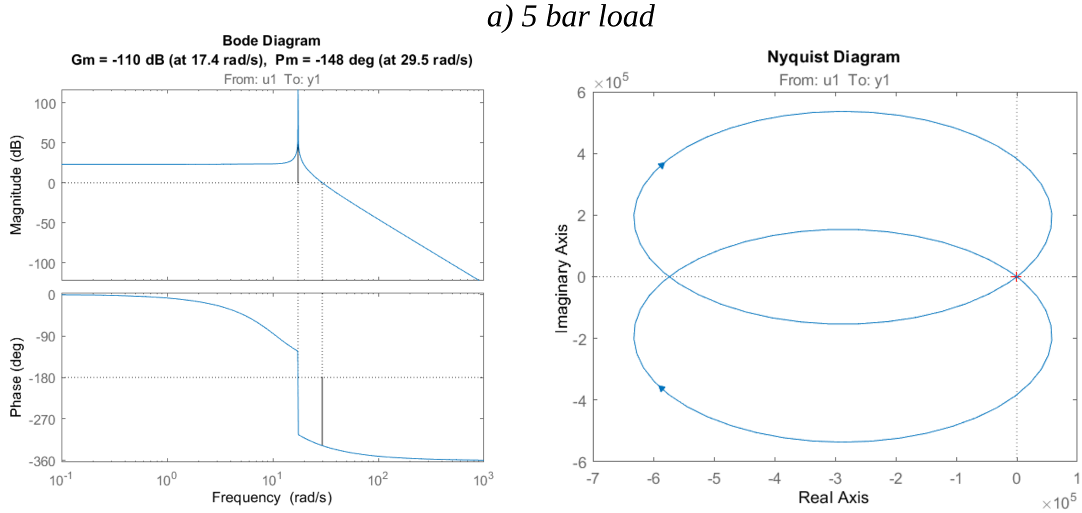


*b) 30 bar load*

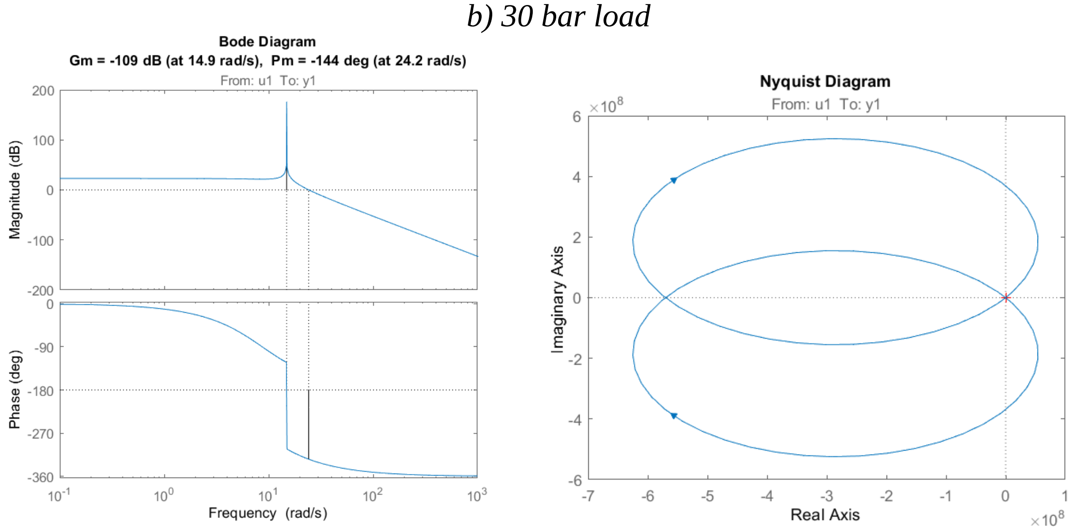


*b) 70 bar load*

*Fig.123. The Margin and Nyquist plots of the transfer functions at 2V amplitude of the input signal and a frequency of 0.45Hz with different loads*

The ***Nyquist*** [53] diagram is a parametric plot of a frequency response used in automation and signal processing. Nyquist plots are commonly used for assessing the stability of a system with feedback. In Cartesian coordinates, the real part of the transfer function is plotted on the X-axis while the imaginary part is plotted on the Y-axis. The frequency is swept as a parameter, resulting in one point per frequency. The same plot can be described using polar coordinates, where the transfer function is the radial coordinate, and the phase of the transfer function is the corresponding angular coordinate.

### *II.3.1.2. 5V amplitude on command signal*

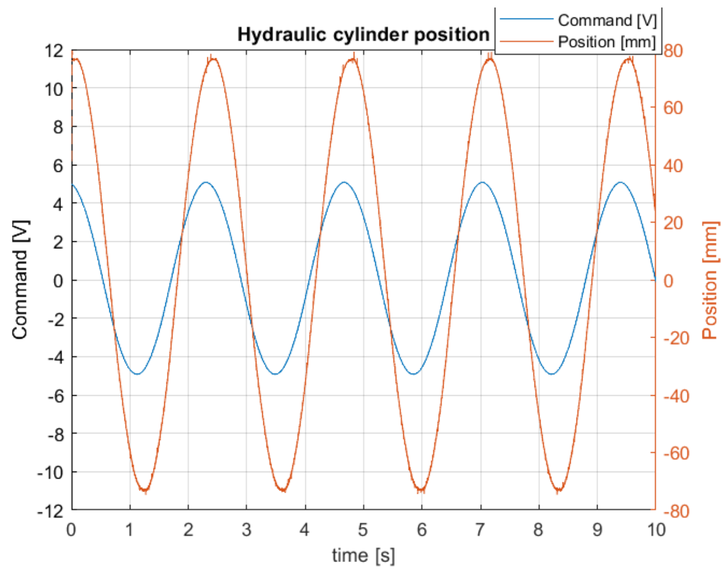


*a) 5 bar load*

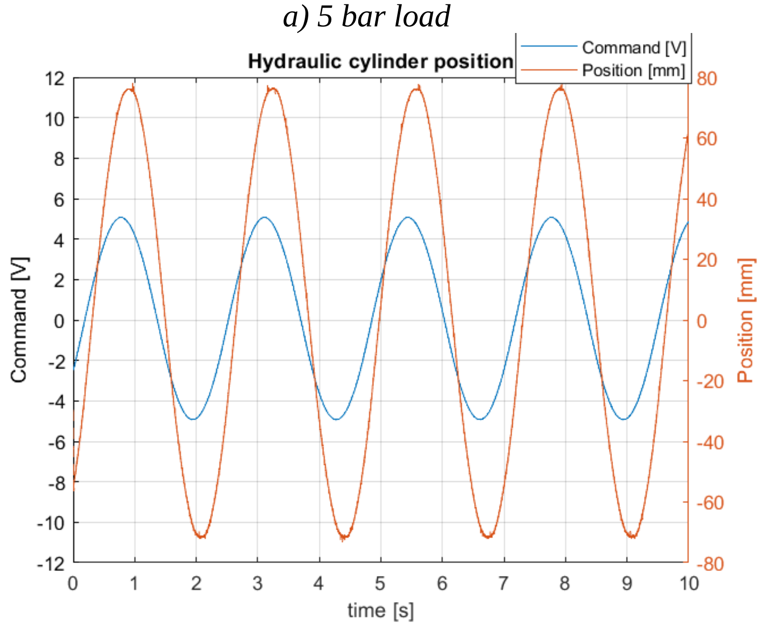


*b) 30 bar load*

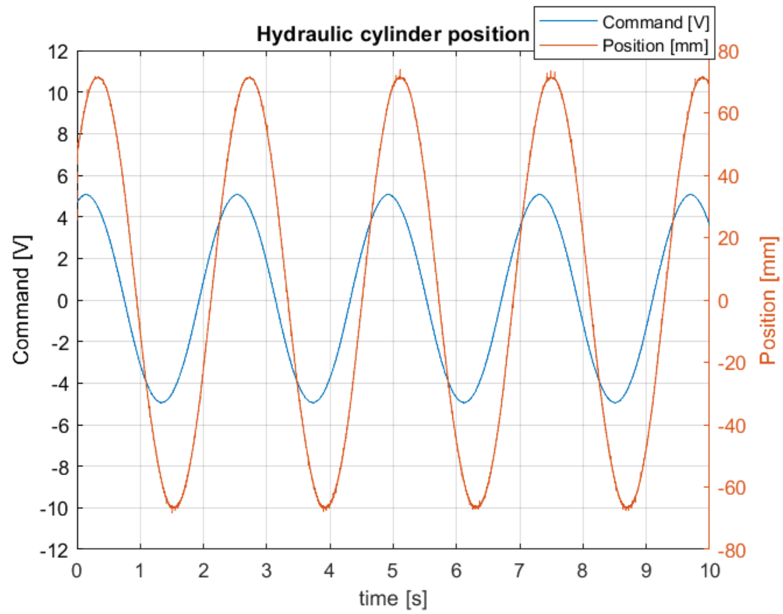


*b) 70 bar load*

*Fig.124. The variation command signal of 5V vs position with different loads*

$$TF_{5V5bar0.45Hz} = \frac{4.723 \cdot 10^4}{s^4 + 8.292 \cdot s^3 + 213.7 \cdot s^2 + 406.8 \cdot s + 4455} \qquad (89)$$

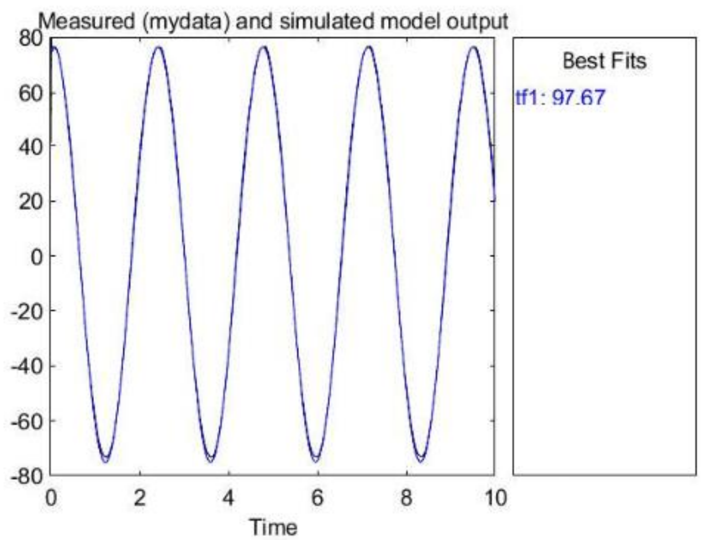


*Fig.125.a. The transfer functions TF fit at command signal of 5V with 5 bar load*

$$TF_{5V30bar0.45Hz} = \frac{1.889 \cdot 10^5}{s^3 + 9.112 \cdot s^2 + 1570 \cdot 10^{-6} \cdot s + 1.202 \cdot 10^4} \tag{90}$$

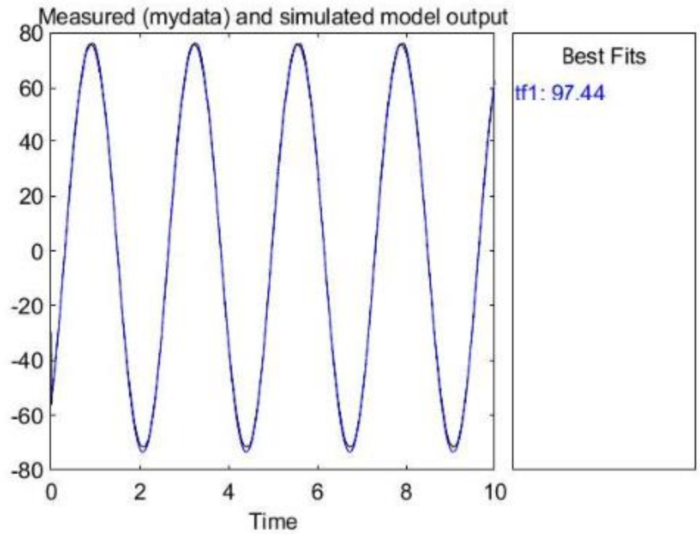


*Fig.125.b. The transfer functions TF fit at command signal of 5V with 30 bar load*

$$TF_{5V70bar0.45Hz} = \frac{2581}{s^3 + 4.768 \cdot s^2 + 41.02 \cdot s + 195.6} \tag{91}$$

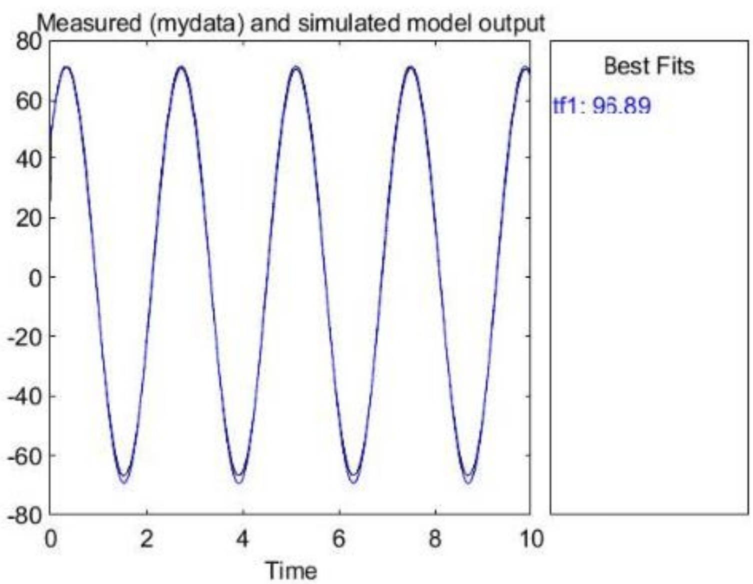


*Fig.125.c. The transfer functions TF fit at command signal of 5V with 70 bar load*

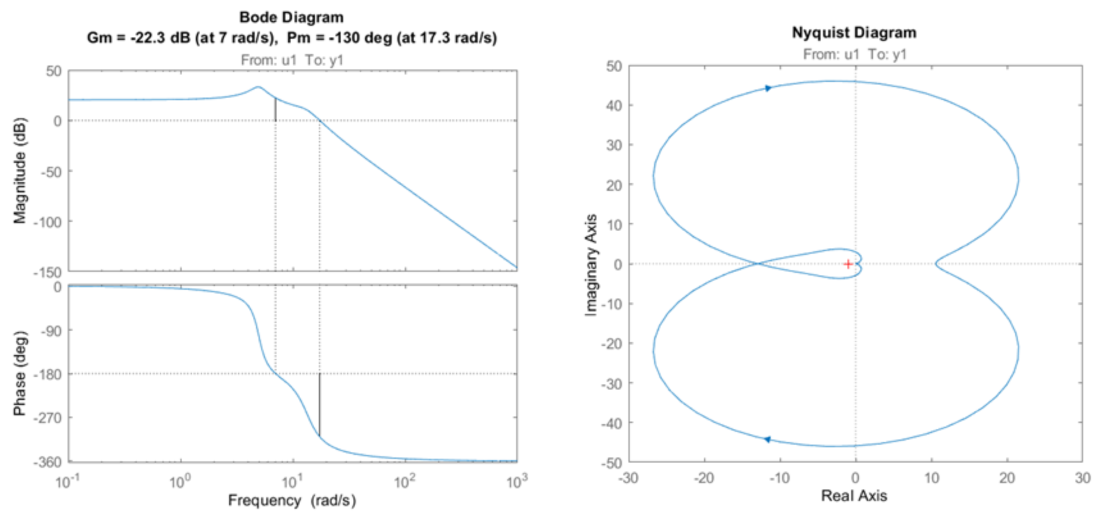


*a) 5 bar load*

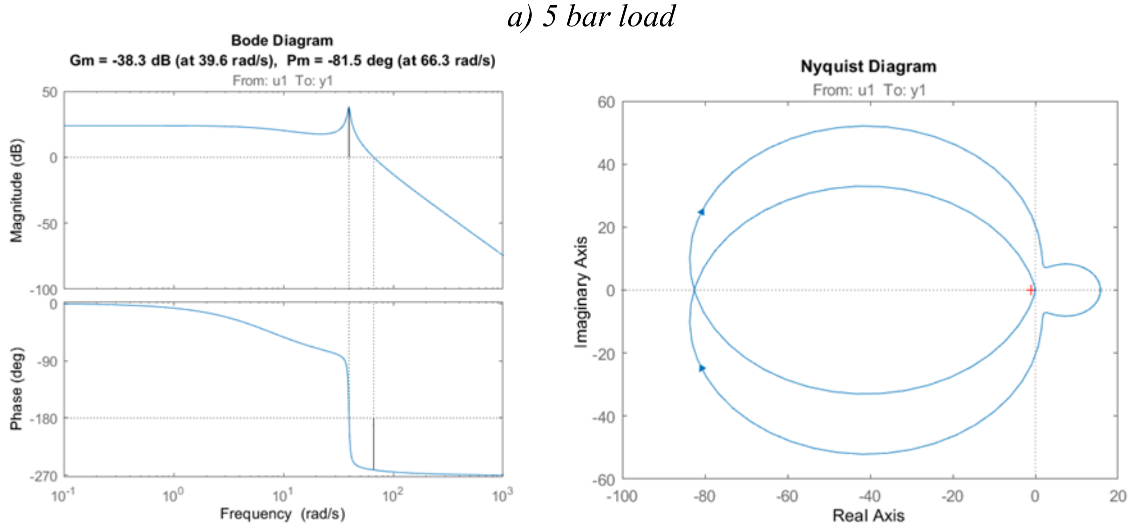


*b) 30 bar load*

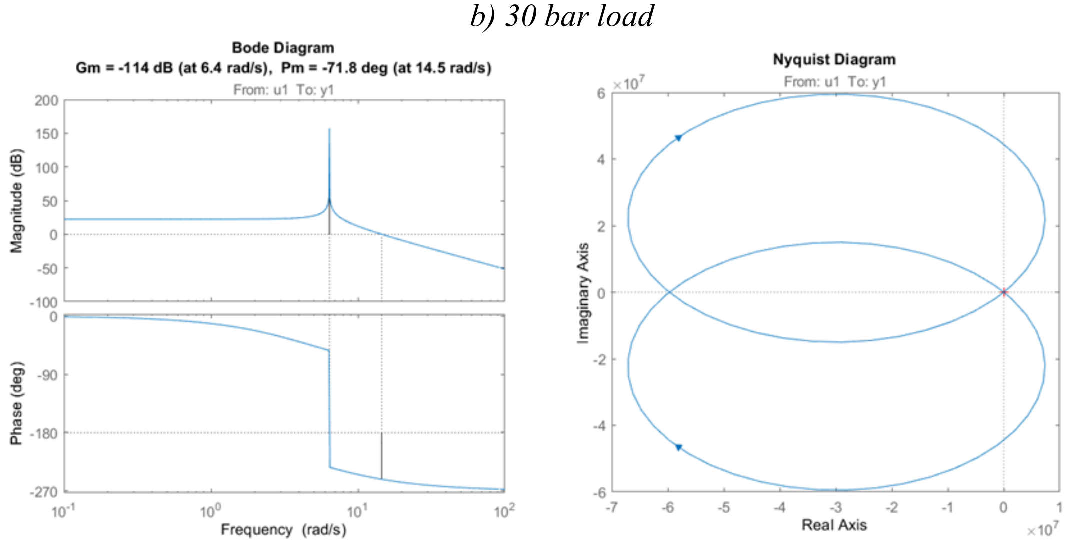


*c) 70 bar load*

*Fig.126. The Margin and Nyquist plots of the transfer functions at 5V amplitude of the input signal and a frequency of 0.45Hz with different loads*

### *II.3.1.3. 10V amplitude on command signal*

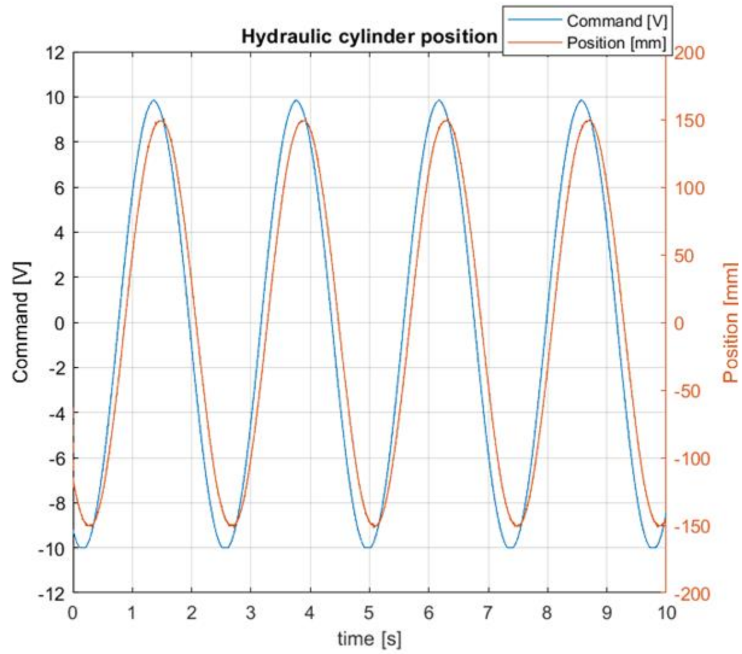


*a) 5 bar load*

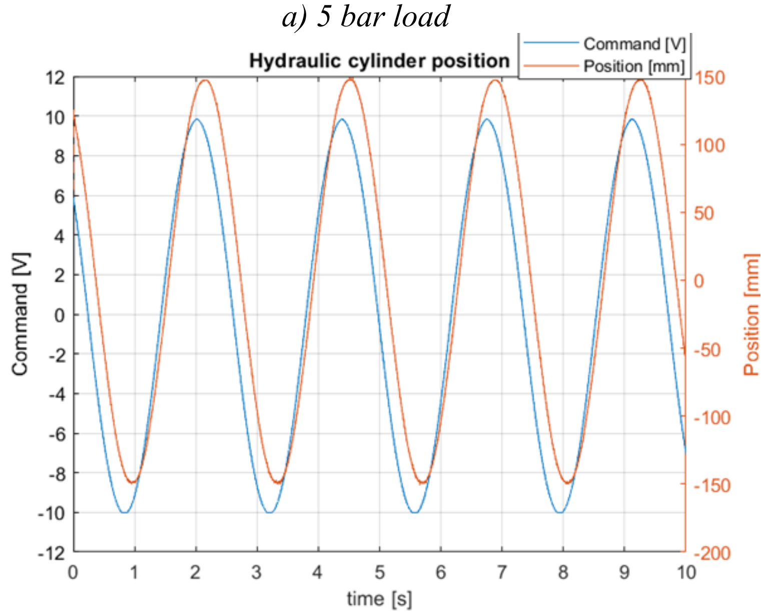


*b) 30 bar load*

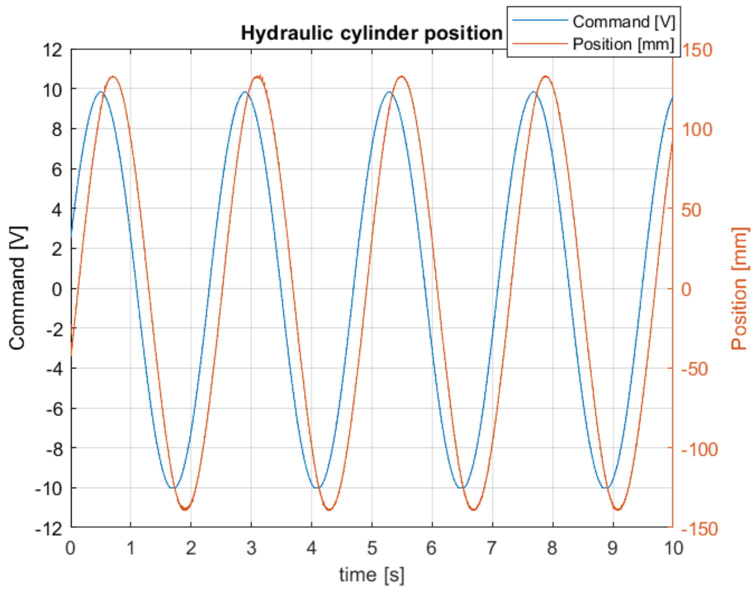


*c) 70 bar load*

*Fig.127. The variation command signal of 10V vs position with different loads*

$$TF_{10V5bar0.45Hz} = \frac{1.071 \cdot 10^4}{s^4 + 3.042 \cdot s^3 + 173.7 \cdot s^2 + 97.54 \cdot s + 1821} \tag{92}$$

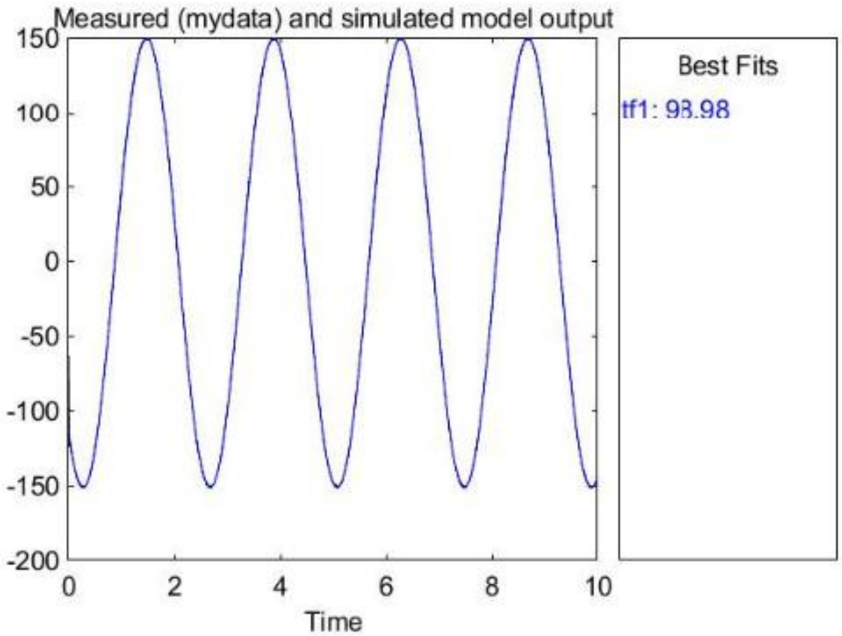


Fig.128.a. The transfer functions TF fit at command signal of 10V with 5 bar load

$$TF_{10V30bar0.45Hz} = \frac{4.516 \cdot 10^4}{s^4 + 1.881 \cdot s^3 + 224.6 \cdot s^2 + 381.8 \cdot s + 4394} \quad (93)$$

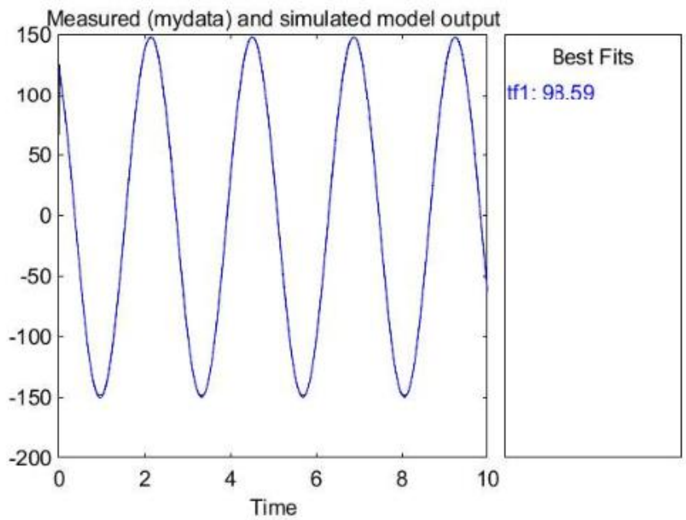


*Fig.128.b. The transfer functions TF fit at command signal of 10V with 30 bar load*

$$TF_{10V70bar0.45Hz} = \frac{4.423 \cdot 10^5}{s^4 + 19.85 \cdot s^3 + 439.9 \cdot s^2 + 6608 \cdot s + 3.079 \cdot 10^4} \quad (94)$$

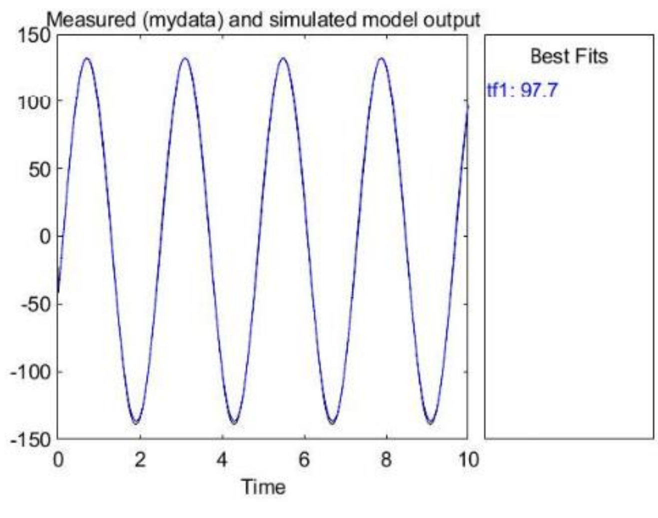


*Fig.128.c. The transfer functions TF fit at command signal of 10V with 70 bar load*

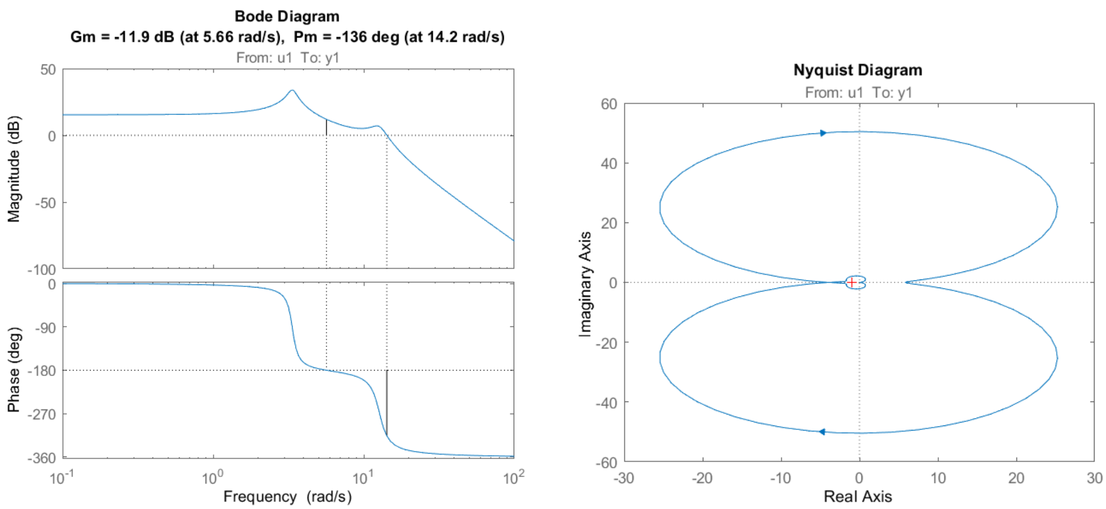


*a) 5 bar load*

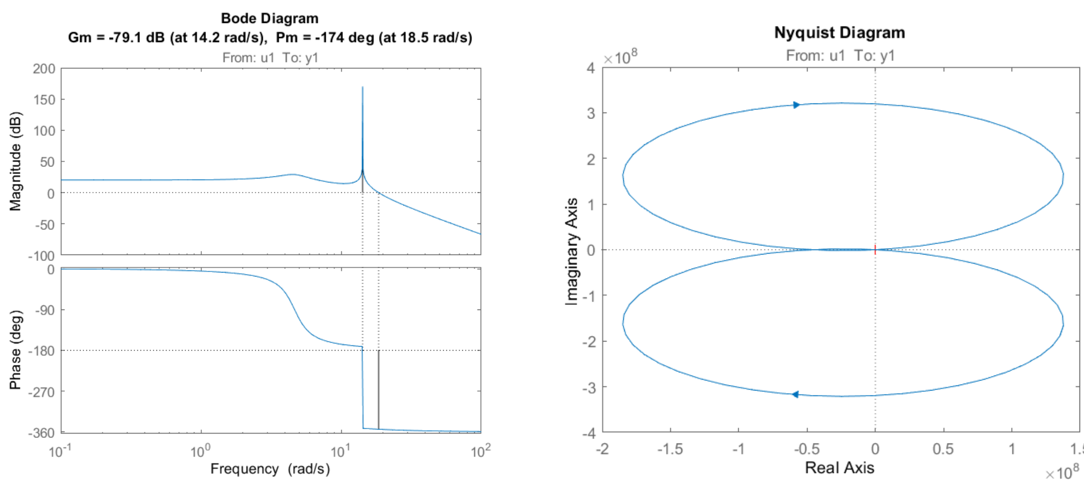


*b) 30 bar load*

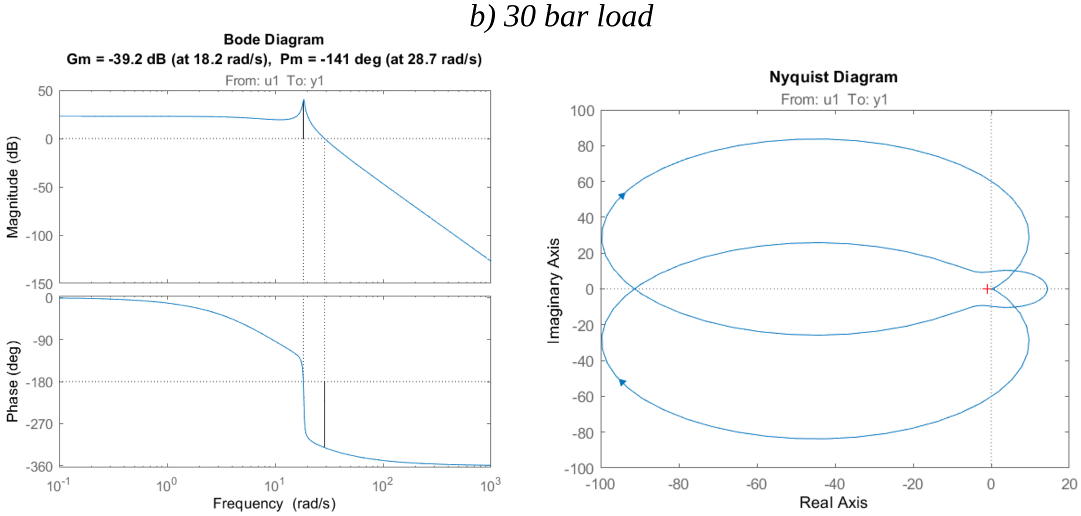


*b) 70 bar load*

*Fig.129. The Margin and Nyquist plots of the transfer functions at 10V amplitude of the input signal and a frequency of 0.45Hz with different loads*

### *II.3.2. The results for the sinusoidal shape signal with a frequency of 0.6 Hz*

#### *II.3.2.1. 2V amplitude on command signal*

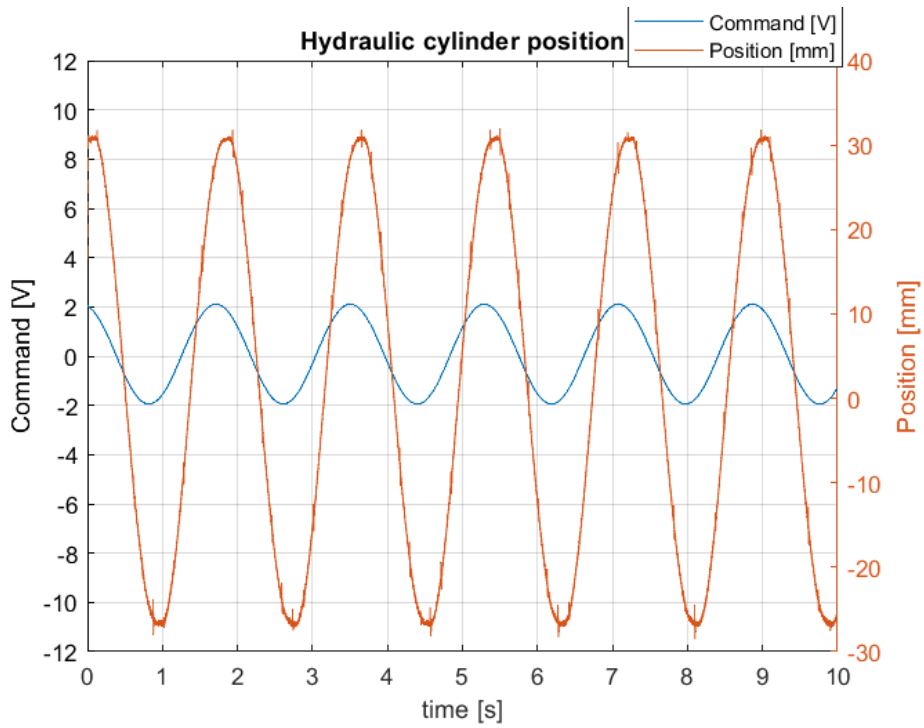


*a) 5 bar load*

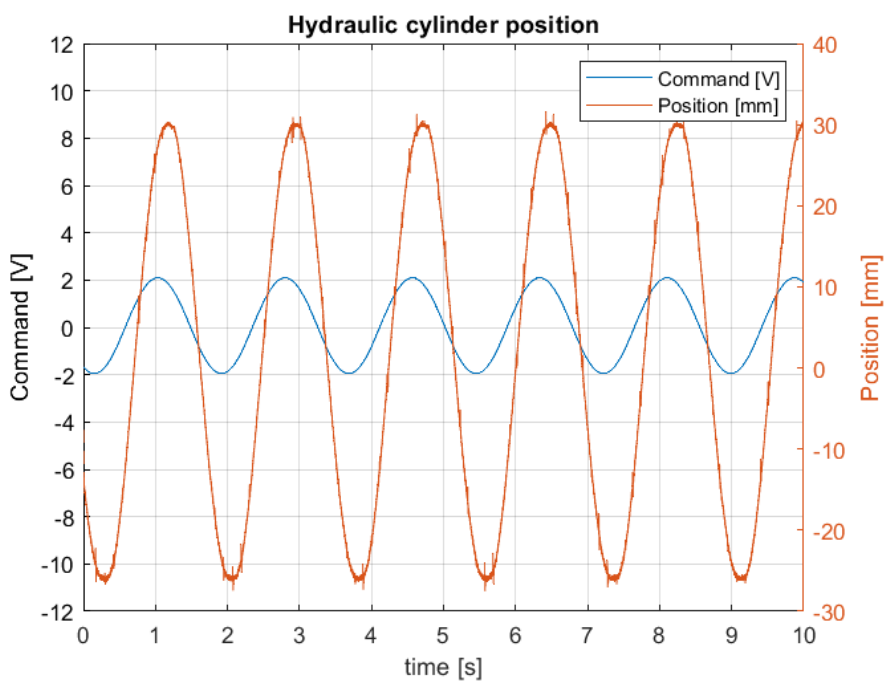


*b) 30 bar load*

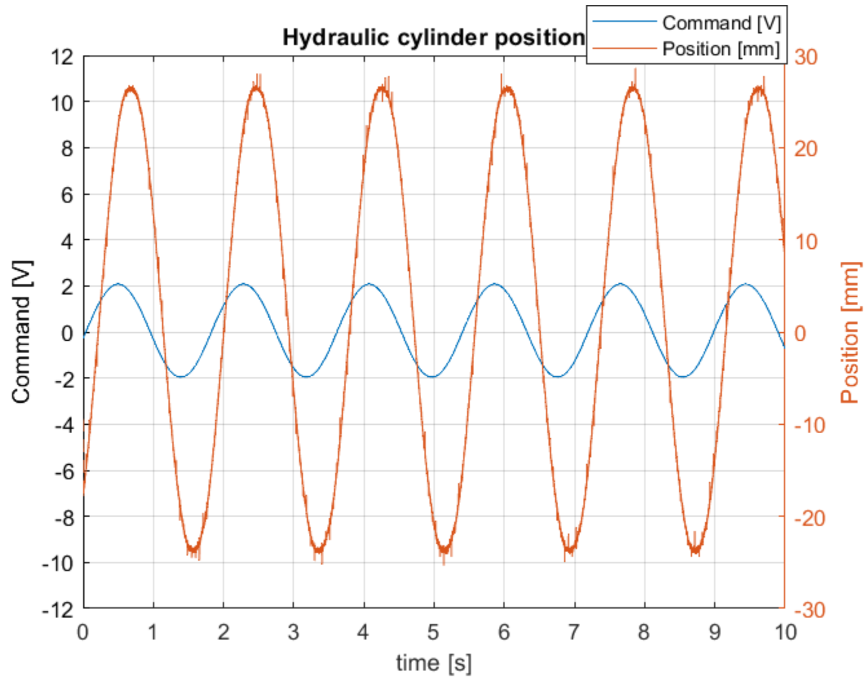


*b) 70 bar load*

*Fig.130. The variation command signal of 2V vs position with different loads*

$$TF_{2V5bar0.6Hz} = \frac{-53.5}{s^4 + 0.2121 \cdot s^3 + 15.89 \cdot s^2 + 2.402 \cdot s + 39.76} \qquad (95)$$

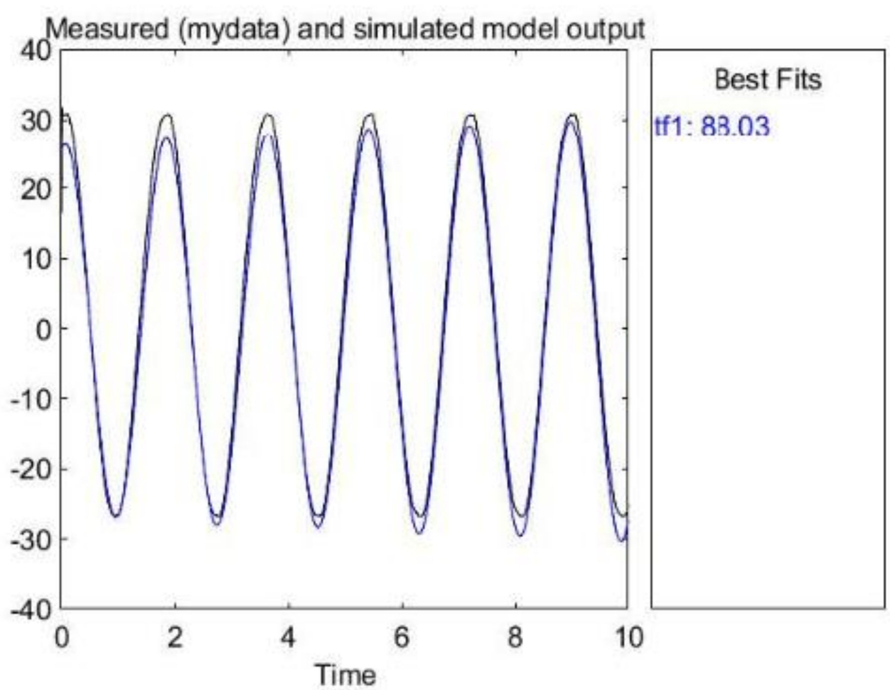


Fig.131.a. The transfer functions TF fit at command signal of 2V with 5 bar load

$$TF_{2V30bar0.6Hz} = \frac{6.608 \cdot 10^5}{s^4 + 6.777 \cdot s^3 + 943.6 \cdot s^2 + 5984 \cdot s + 5.346 \cdot 10^4} \quad (96)$$

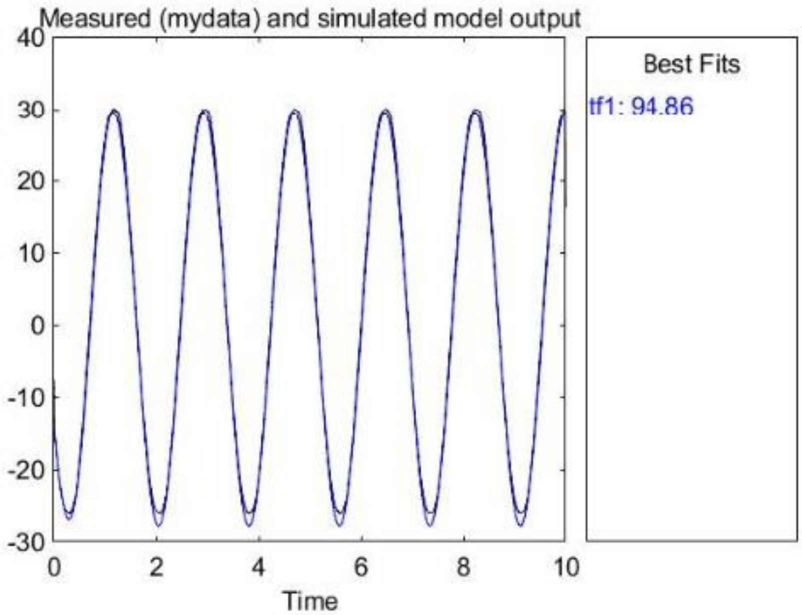


*Fig.131.b. The transfer functions TF fit at command signal of 2V with 30 bar load*

$$TF_{2V70bar0.6Hz} = \frac{5.408 \cdot 10^5}{s^4 + 19.97 \cdot s^3 + 483.7 \cdot s^2 + 7573 \cdot s + 3.965 \cdot 10^4} \quad (97)$$

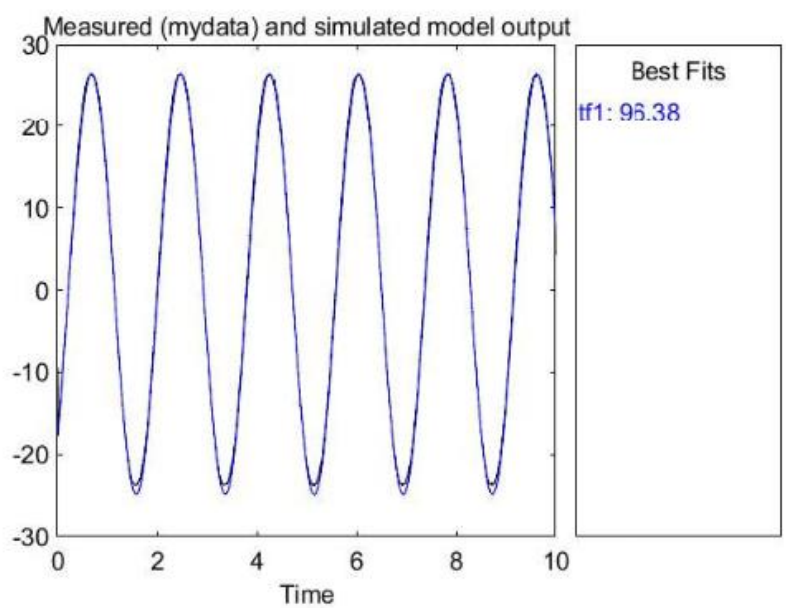


*Fig.131.c. The transfer functions TF fit at command signal of 2V with 70 bar load*

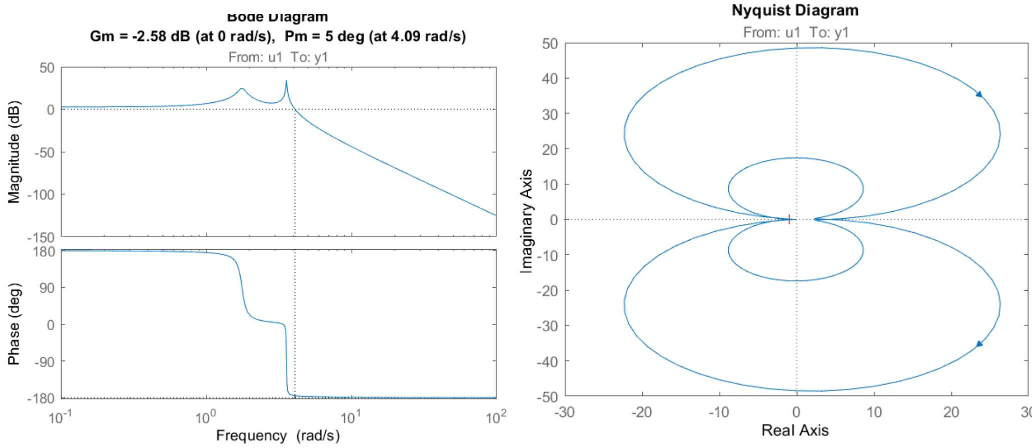


*a) 5 bar load*

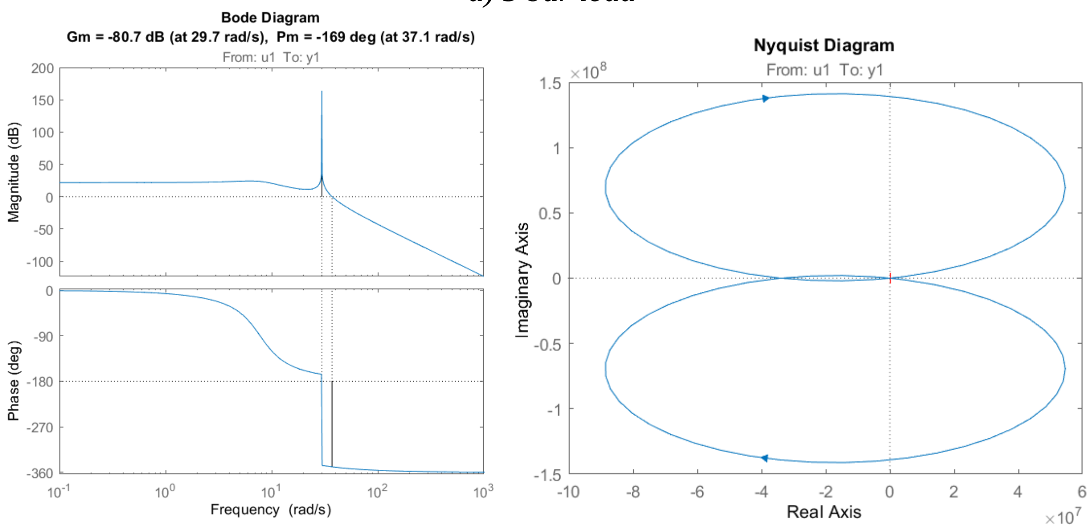


*b) 30 bar load*

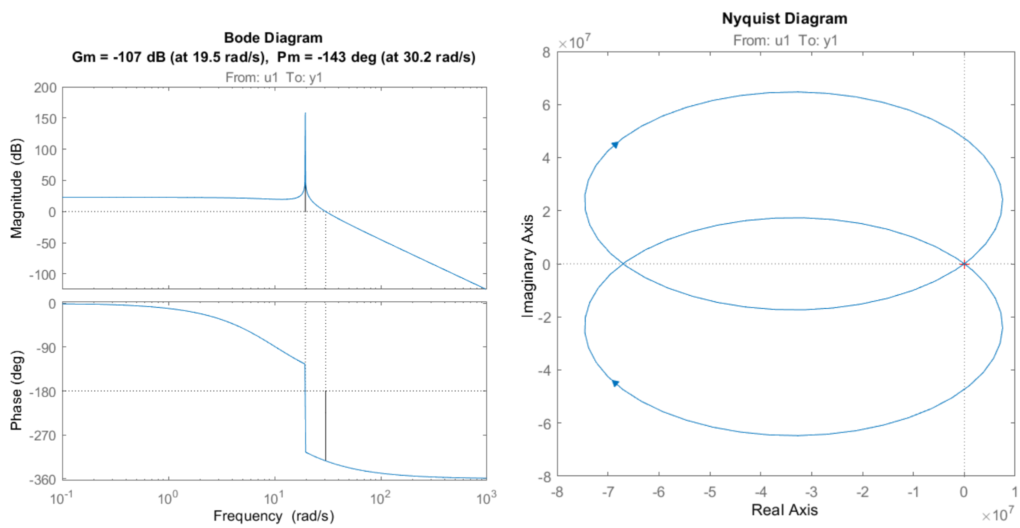


*b) 70 bar load*

*Fig.132. The Margin and Nyquist plots of the transfer functions at 2V amplitude of the input signal and a frequency of 0.6 Hz with different loads*

### *II.3.2.2. 5V amplitude on command signal*

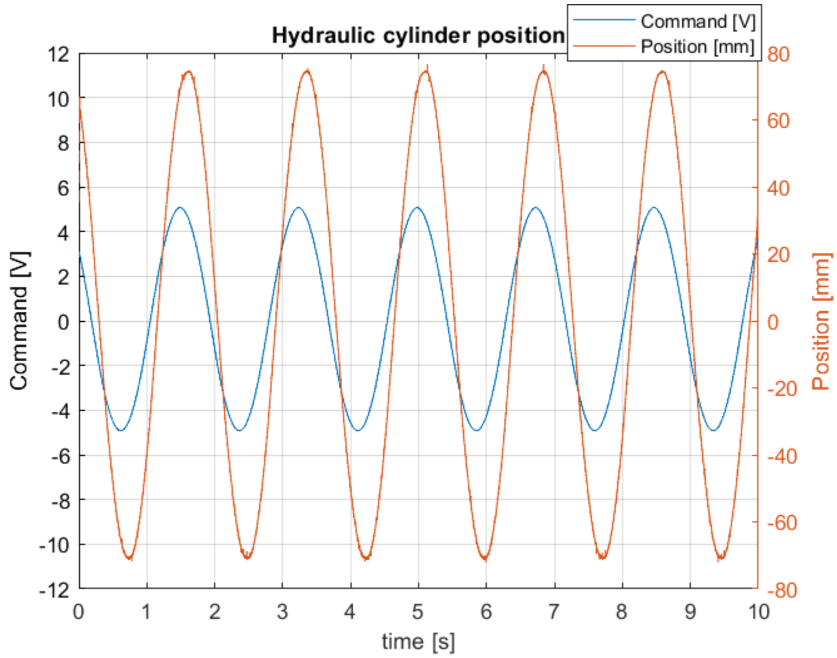


*a) 5 bar load*

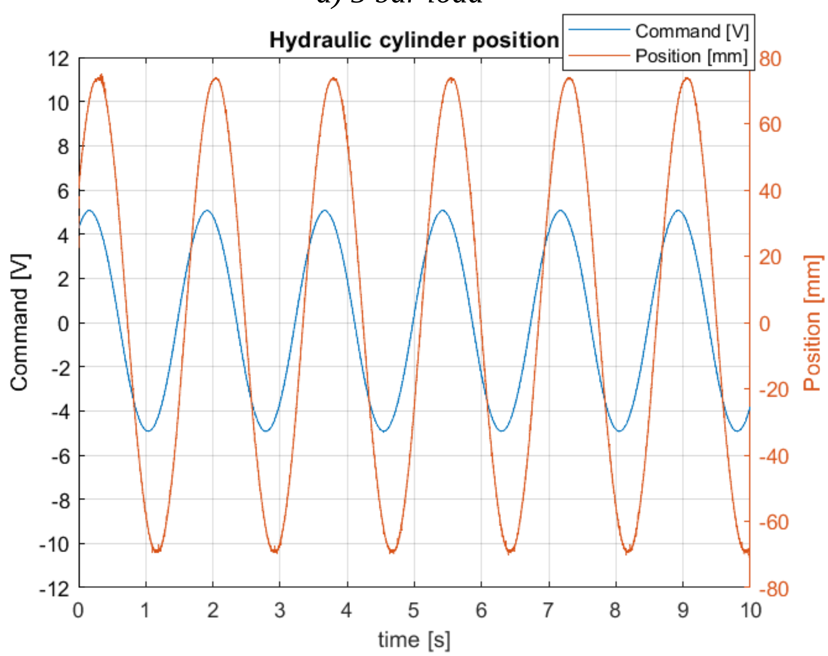


*b) 30 bar load*

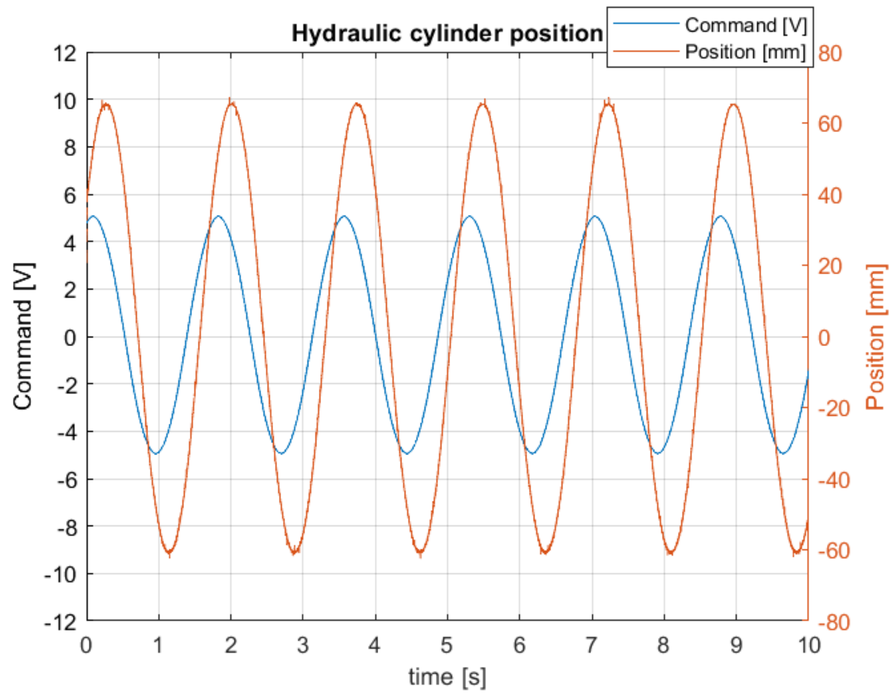


*b) 70 bar load*

*Fig.133. The variation command signal of 5V vs position with different loads*

$$TF_{5V5bar0.6Hz} = \frac{2.651 \cdot 10^5}{s^4 + 38.85 \cdot s^3 + 582.5 \cdot s^2 + 2422 \cdot s + 2.41 \cdot 10^4} \qquad (98)$$

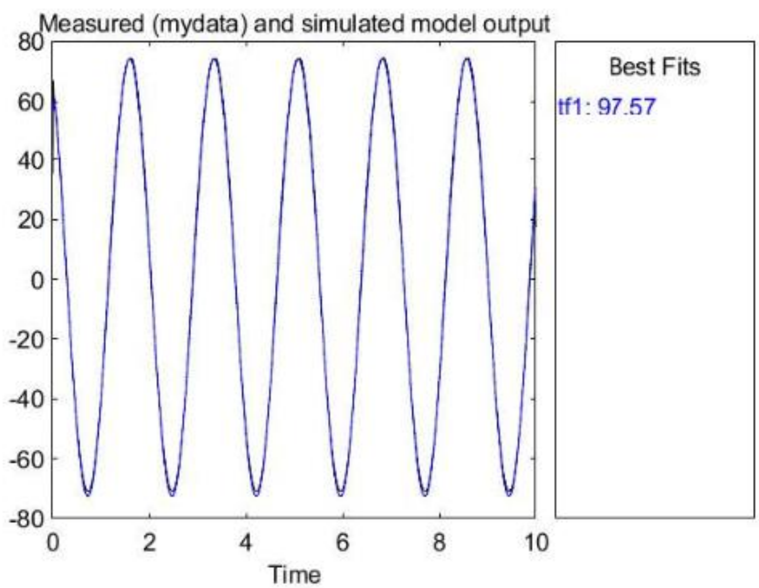


Fig.134.a. The transfer functions TF fit at command signal of 5V with 5 bar load

$$TF_{5V30bar0.6Hz} = \frac{-186.9}{s^4 + 0.8256 \cdot s^3 + 15.56 \cdot s^2 + 9.194 \cdot s + 22.44} \quad (99)$$

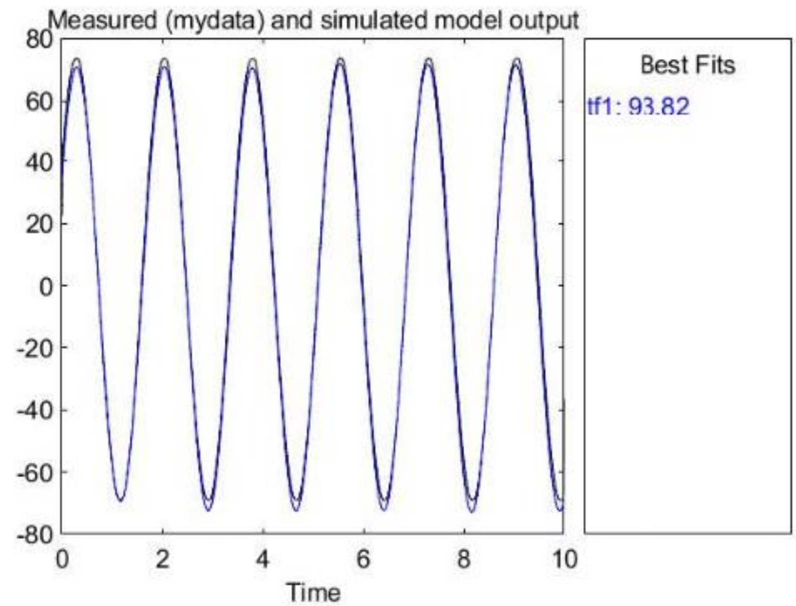


*Fig.134.b. The transfer functions TF fit at command signal of 5V with 30 bar load*

$$TF_{5V70bar0.6Hz} = \frac{1.86 \cdot 10^4}{s^3 + 4.648 \cdot s^2 + 262 \cdot s + 1218} \quad (100)$$

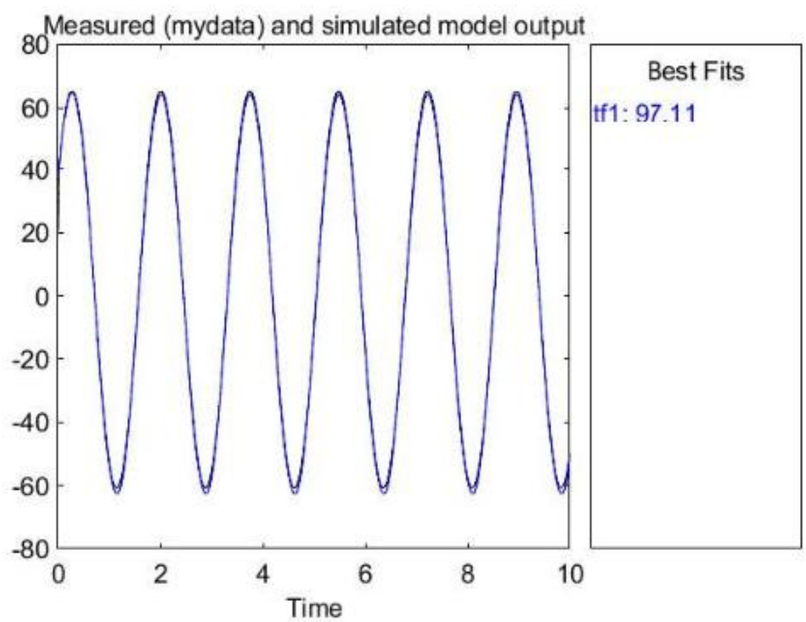


*Fig.134.c. The transfer functions TF fit at command signal of 5V with 70 bar load*

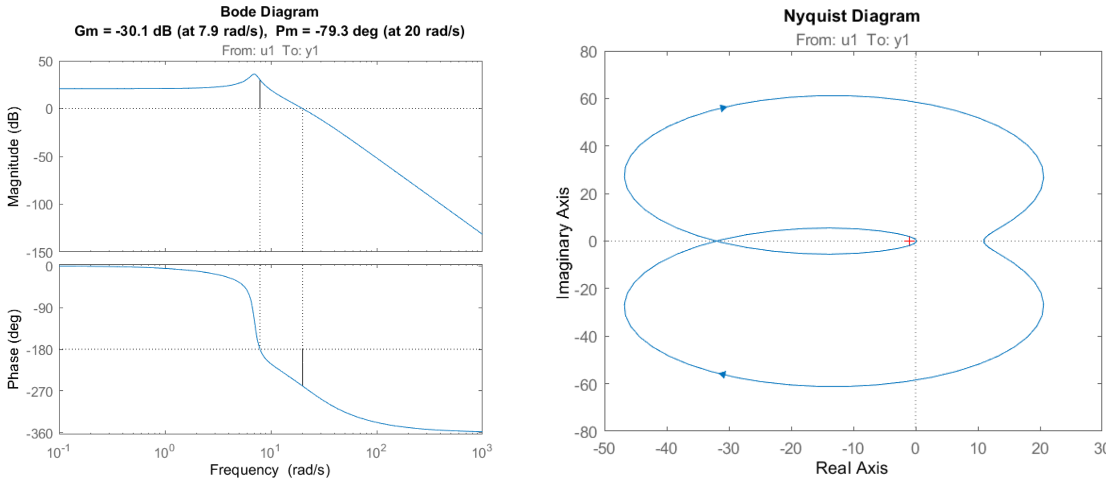


*a) 5 bar load*

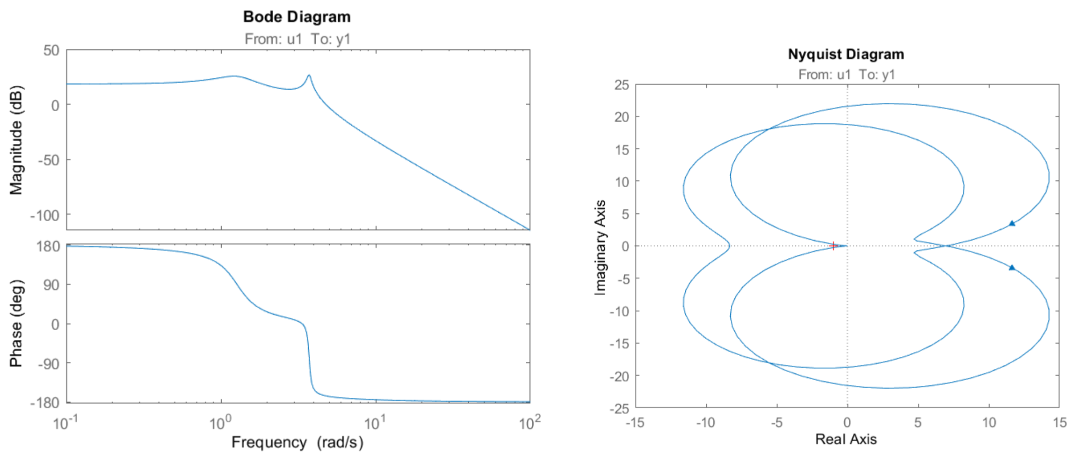


*b) 30 bar load*

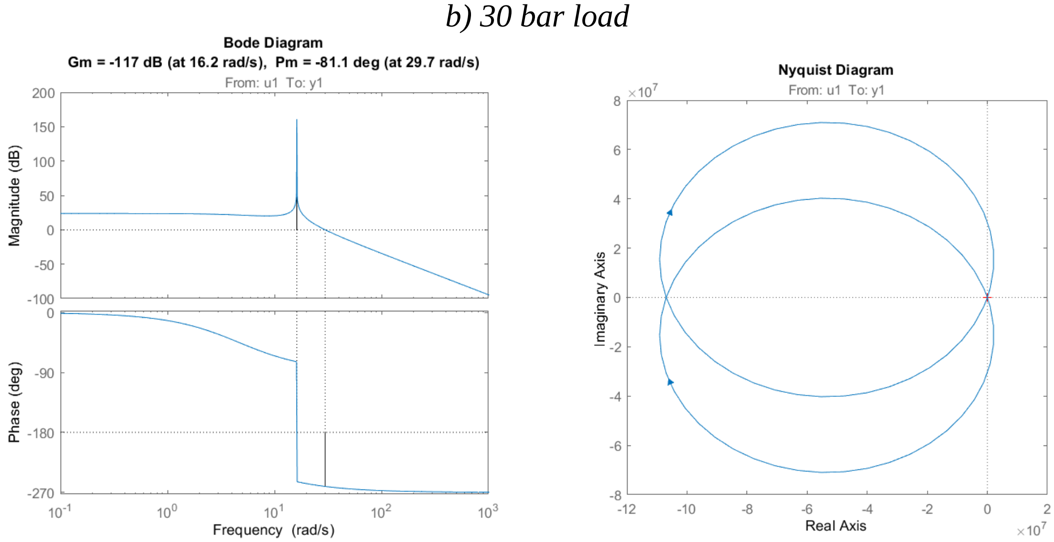


*b) 70 bar load*

*Fig.135. The Margin and Nyquist plots of the transfer functions at 5V amplitude of the input signal and a frequency of 0.6 Hz with different loads*

### *II.3.2.3. 10V amplitude on command signal*

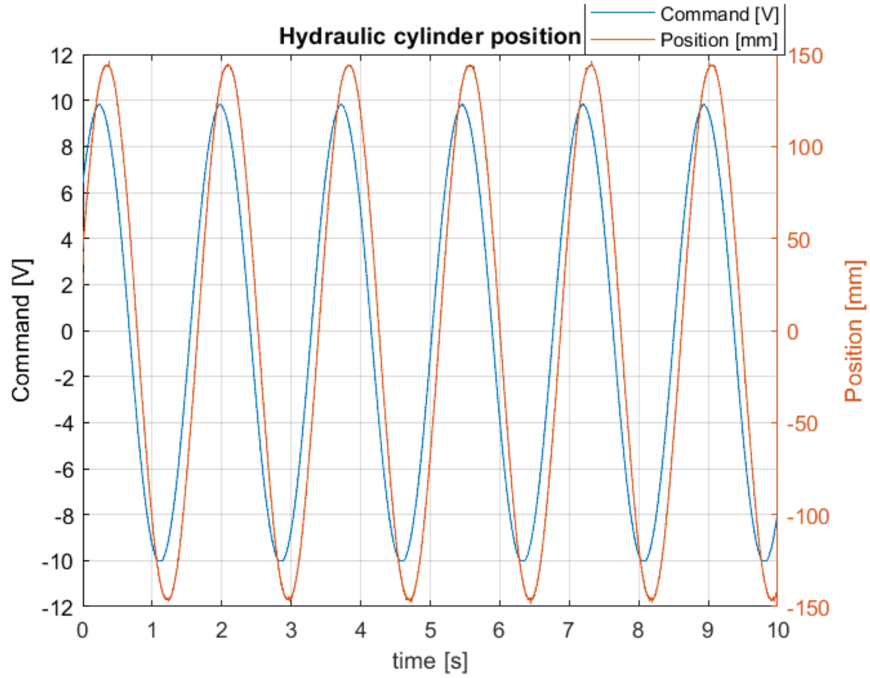


*a) 5 bar load*

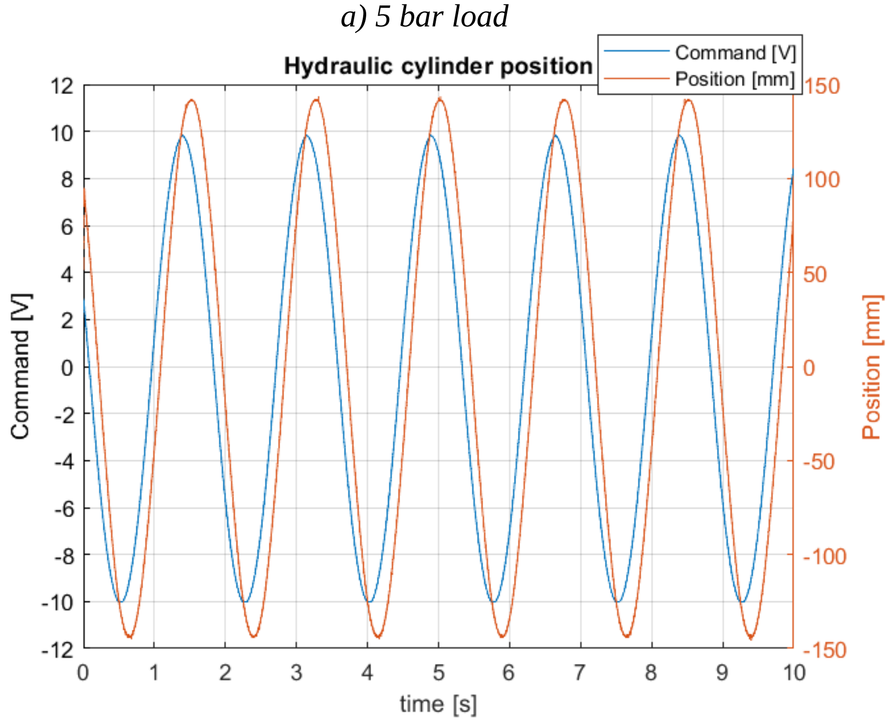


*b) 30 bar load*

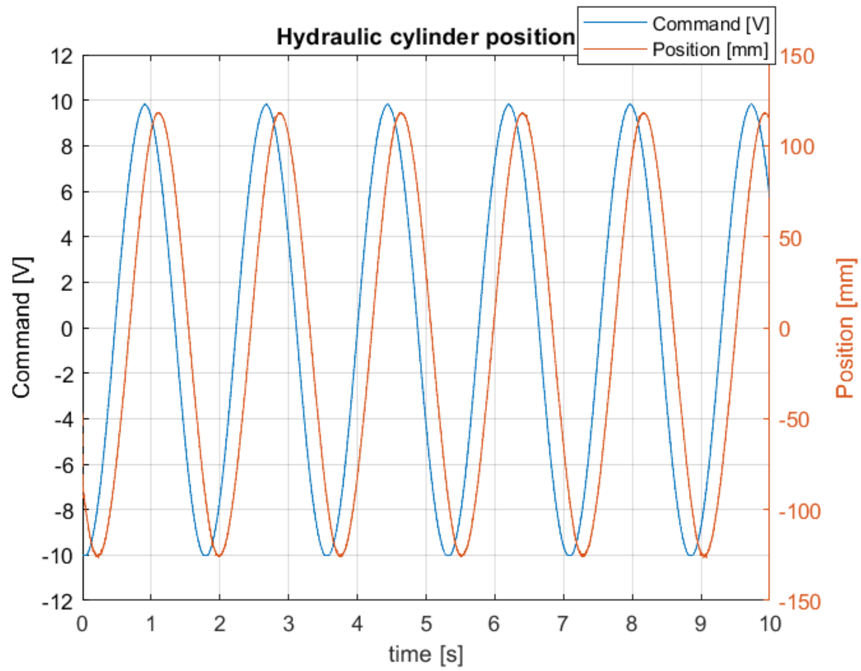


*b) 70 bar load*

*Fig.136. The variation command signal of 10V vs position with different loads*

$$TF_{10V5bar0.6Hz} = \frac{-37.34}{s^4 + 1.318 \cdot s^3 + 13.42 \cdot s^2 + 16.98 \cdot s + 2.585} \tag{101}$$

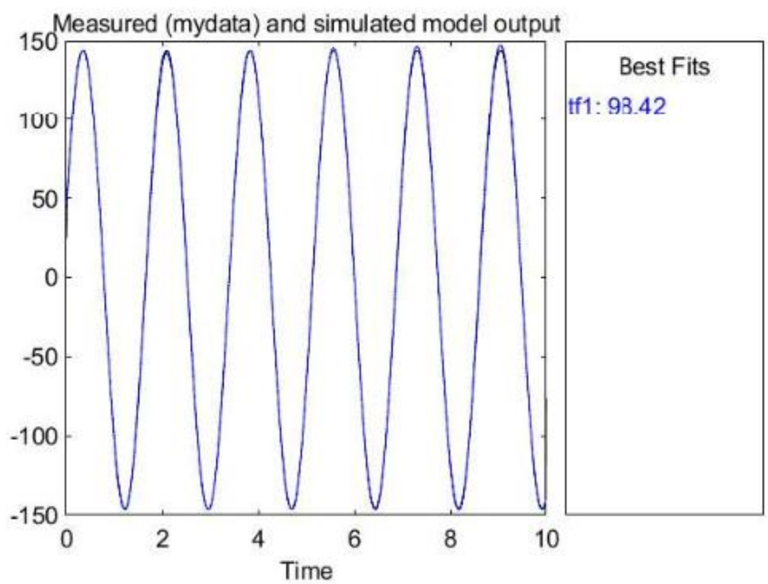


Fig.137.a. The transfer functions TF fit at command signal of 10V with 5 bar load

$$TF_{10V30bar0.6Hz} = \frac{3.889 \cdot 10^5}{s^4 + 61.04 \cdot s^3 + 1158 \cdot s^2 + 4038 \cdot s + 3.927 \cdot 10^4} \quad (102)$$

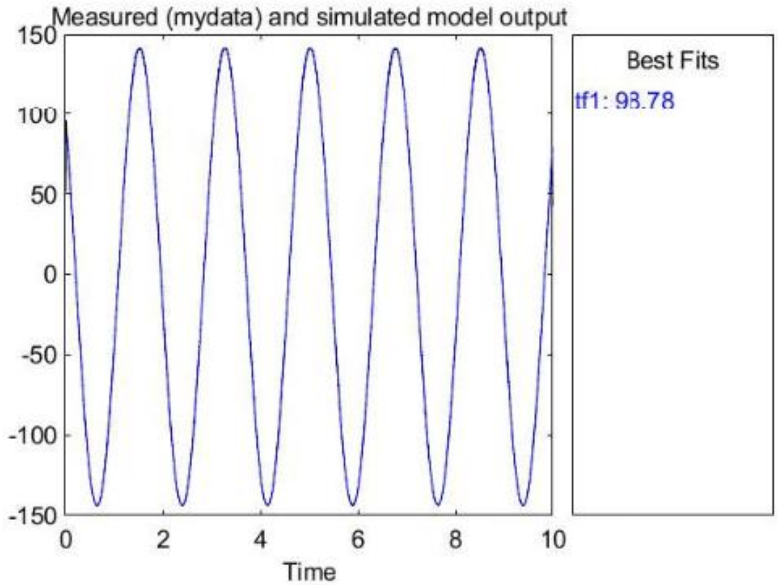


*Fig.137.b. The transfer functions TF fit at command signal of 10V with 30 bar load*

$$TF_{10V70bar0.6Hz} = \frac{5241}{s^3 + 4.028 \cdot s^2 + 93.19 \cdot s + 375.3} \quad (103)$$

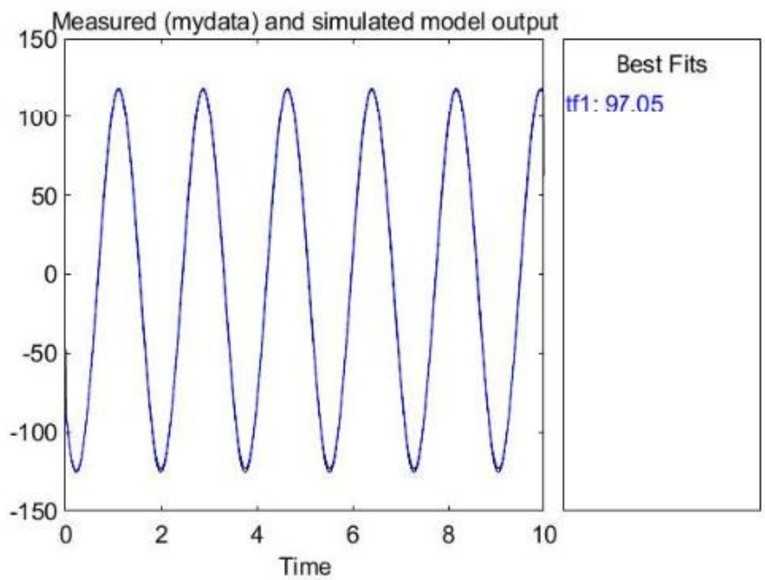


*Fig.137.c. The transfer functions TF fit at command signal of 10V with 70 bar load*

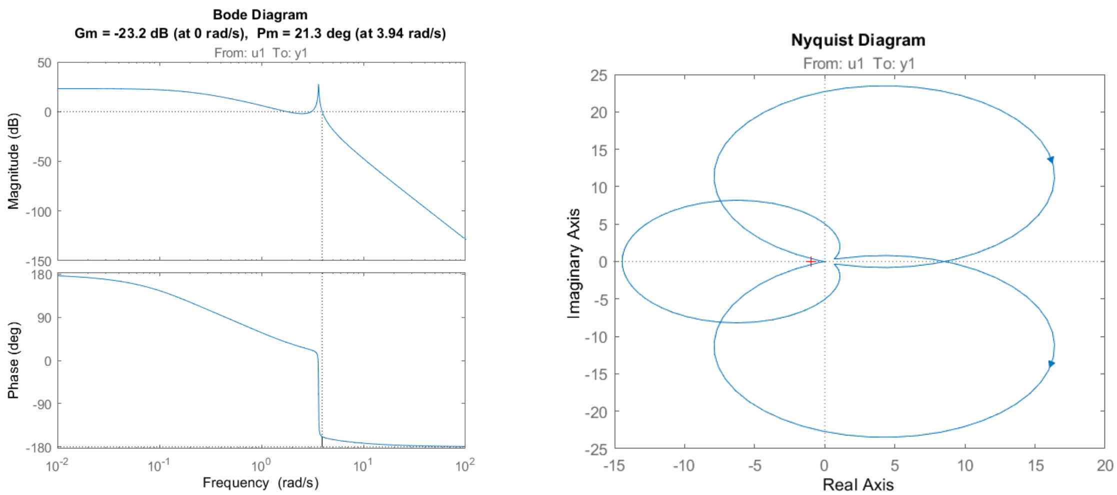


*a) 5 bar load*

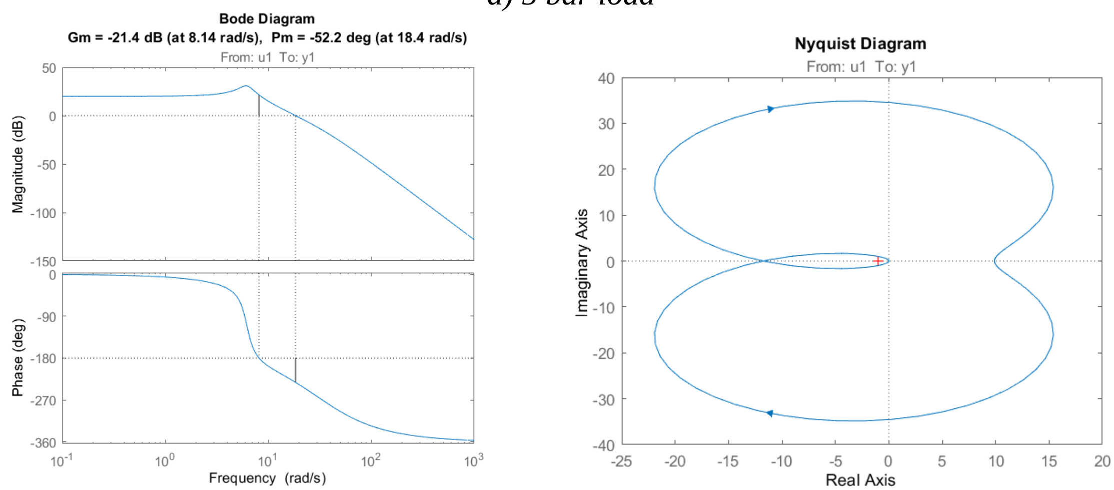


*b) 30 bar load*

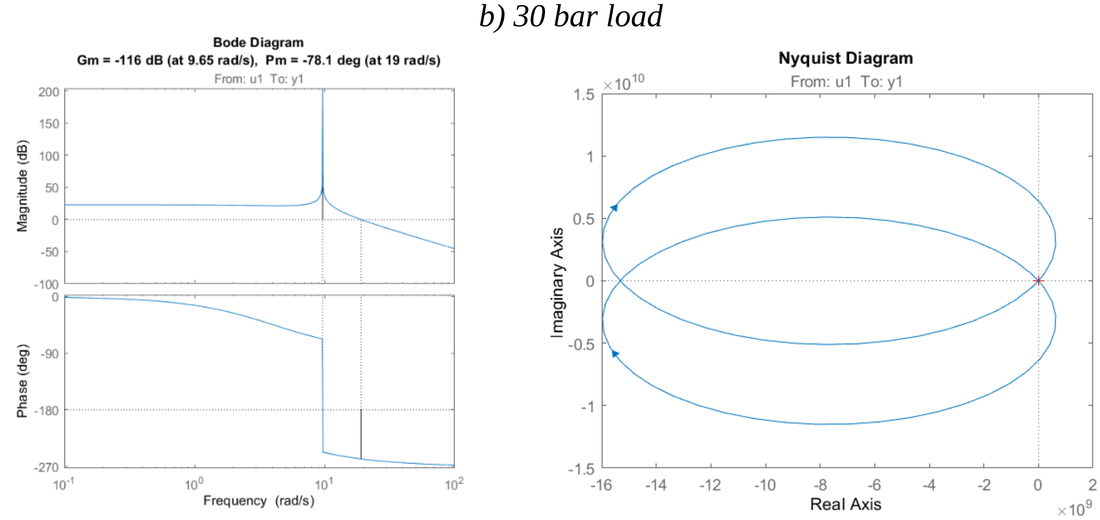


*b) 70 bar load*

*Fig.132. The Margin and Nyquist plots of the transfer functions at 10V amplitude of the input signal and a frequency of 0.6 Hz with different loads*

### *II.3.3. The results for the sinusoidal shape signal with a frequency of 0.75 Hz*

#### *II.3.3.1. 2V amplitude on command signal*

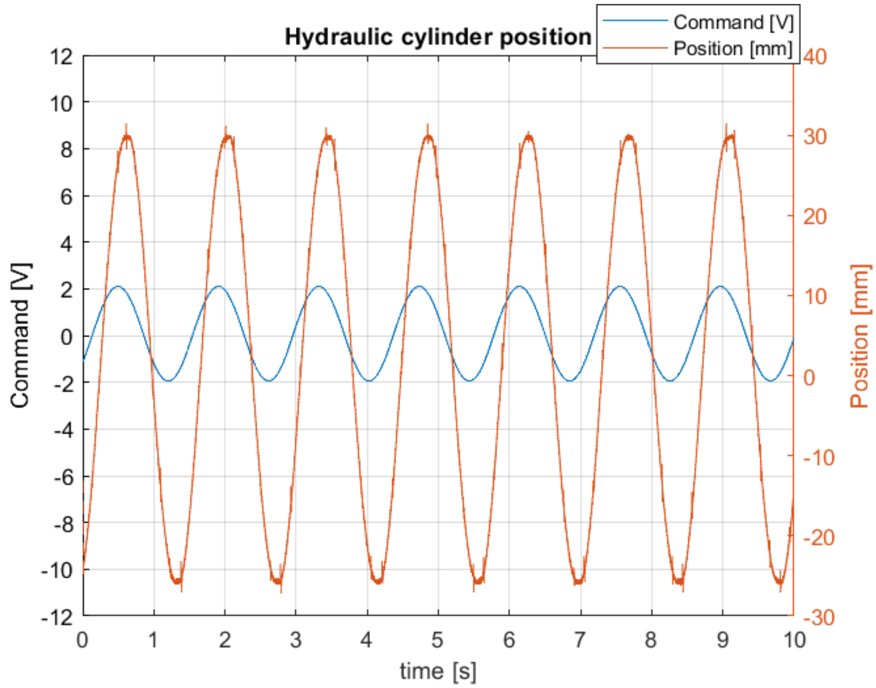


*a) 5 bar load*

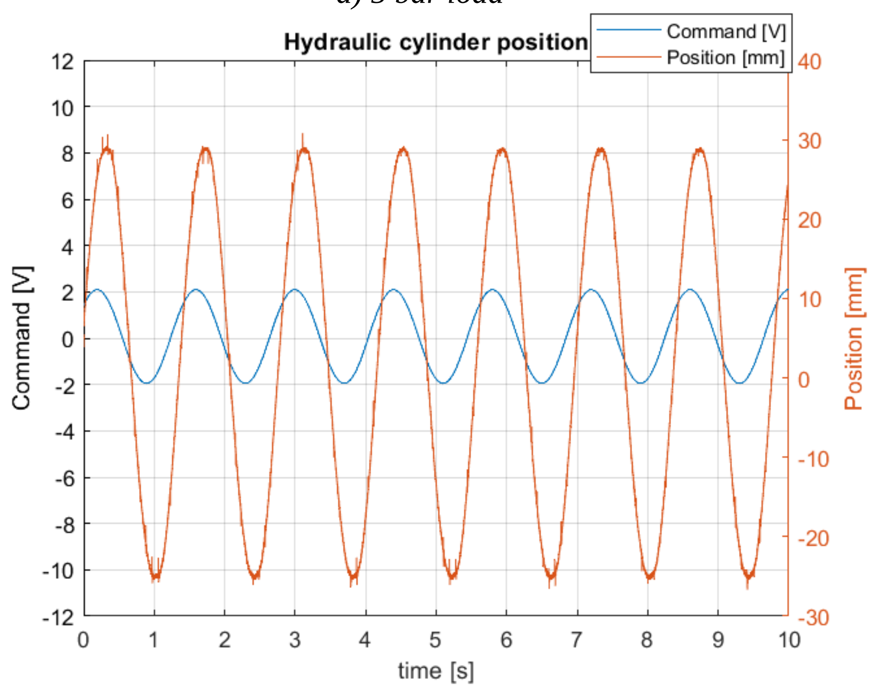


*b) 30 bar load*

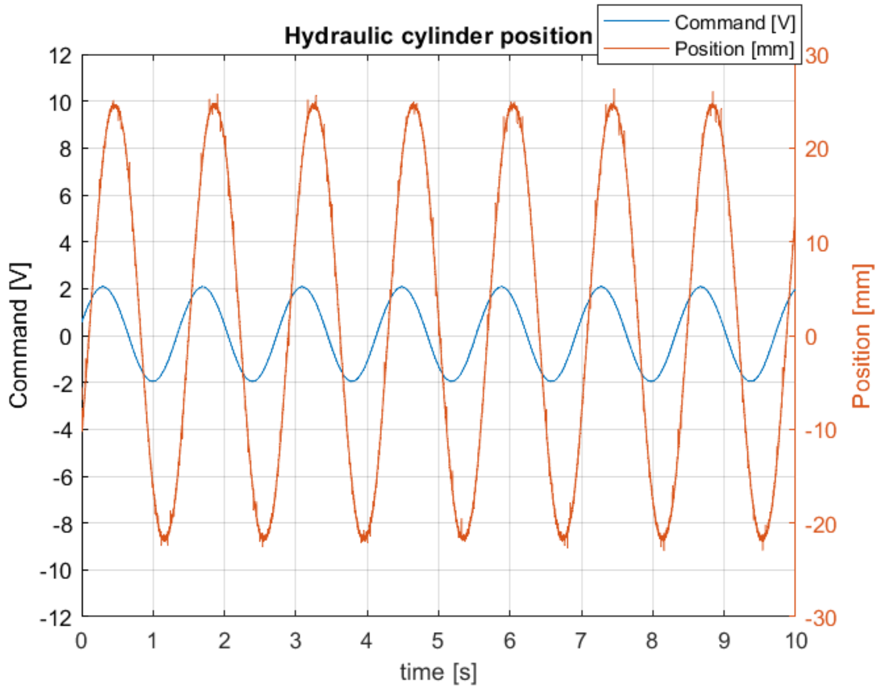


*b) 70 bar load*

*Fig.133. The variation command signal of 2V vs position with different loads*

$$TF_{2V5bar0.75Hz} = \frac{2.003 \cdot 10^5}{s^3 + 7.738 \cdot s^2 + 1621 \cdot s + 1.254 \cdot 10^4} \tag{104}$$

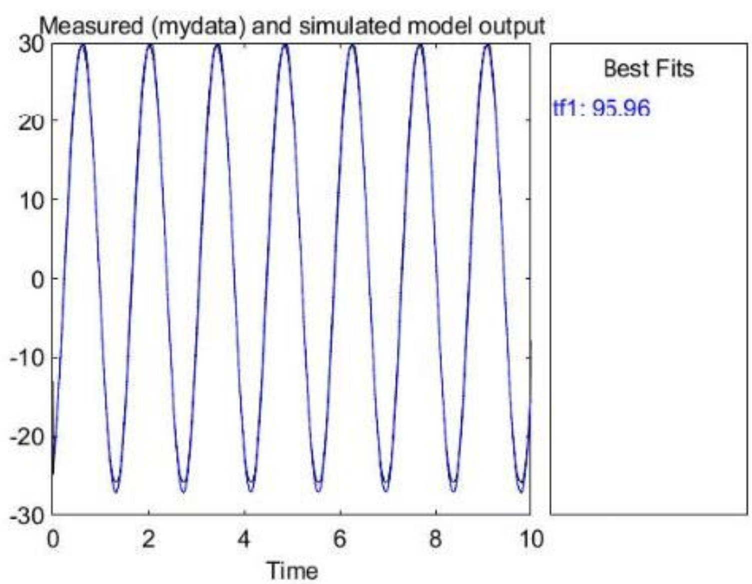


Fig.134.a. The transfer functions TF fit at command signal of 2V with 5 bar load

$$TF_{2V30bar0.75Hz} = \frac{-75.99}{s^4 + 0.3468 \cdot s^3 + 33 \cdot s^2 + 6.593 \cdot s + 255.2} \tag{105}$$

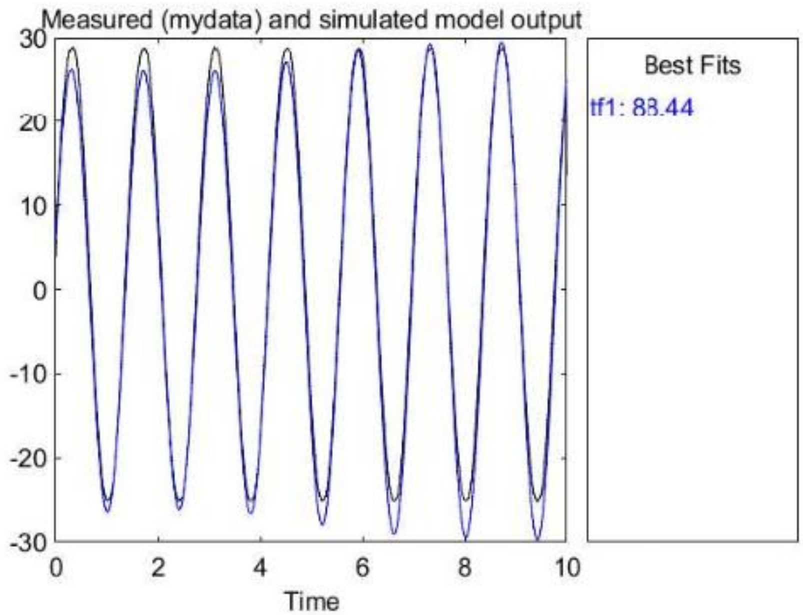


*Fig.134.b. The transfer functions TF fit at command signal of 2V with 30 bar load*

$$TF_{2V70bar0.75Hz} = \frac{1.442 \cdot 10^7}{s^4 + 591.9 \cdot s^3 + 8152 \cdot s^2 + 2.011 \cdot 10^5 \cdot s + 1.067 \cdot 10^6} \tag{106}$$

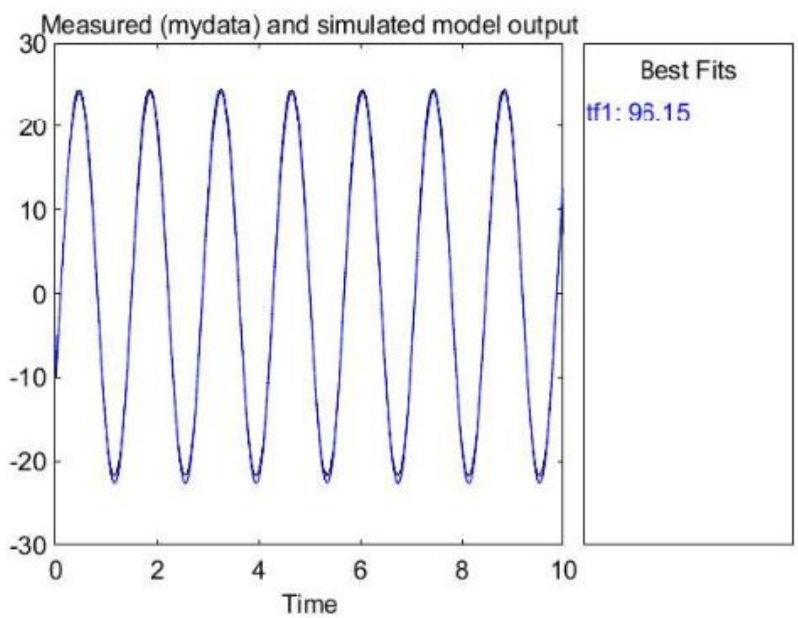


*Fig.134.c. The transfer functions TF fit at command signal of 2V with 70 bar load*

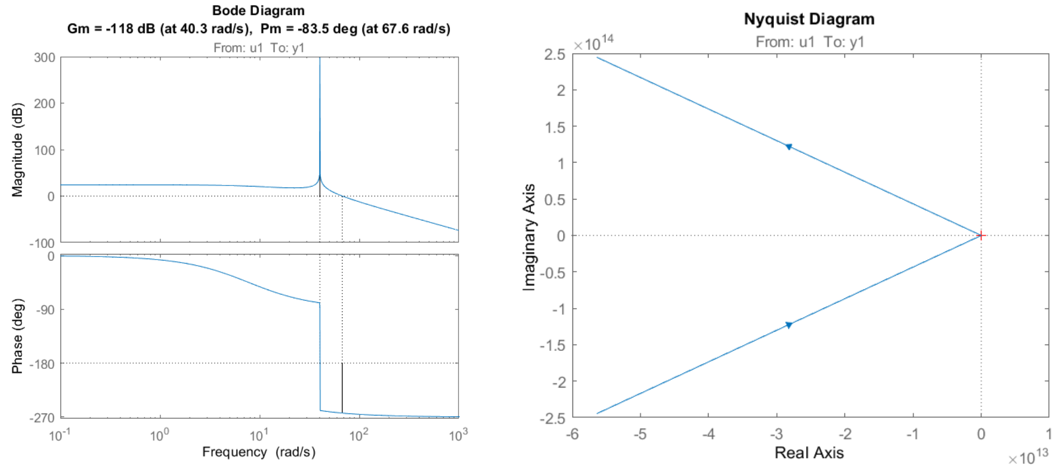


*a) 5 bar load*

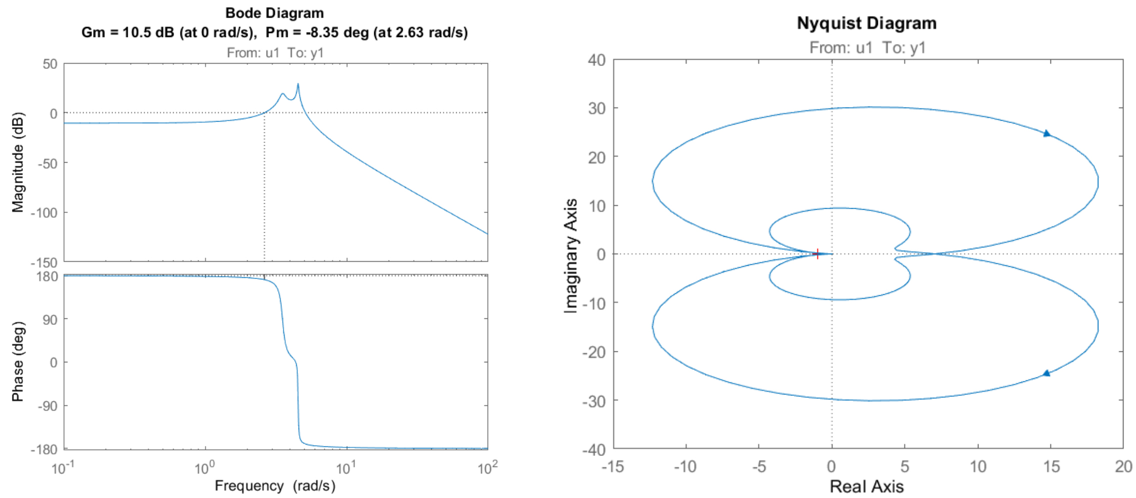


*b) 30 bar load*

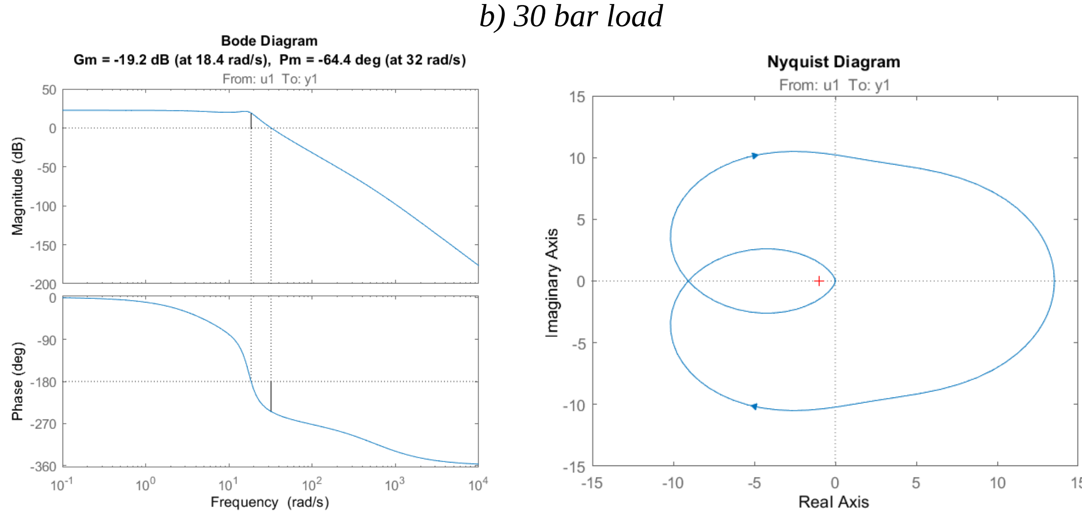


*b) 70 bar load*

*Fig.135. The Margin and Nyquist plots of the transfer functions at 2V amplitude of the input signal and a frequency of 0.75 Hz with different loads*

### *II.3.3.2. 5V amplitude on command signal*

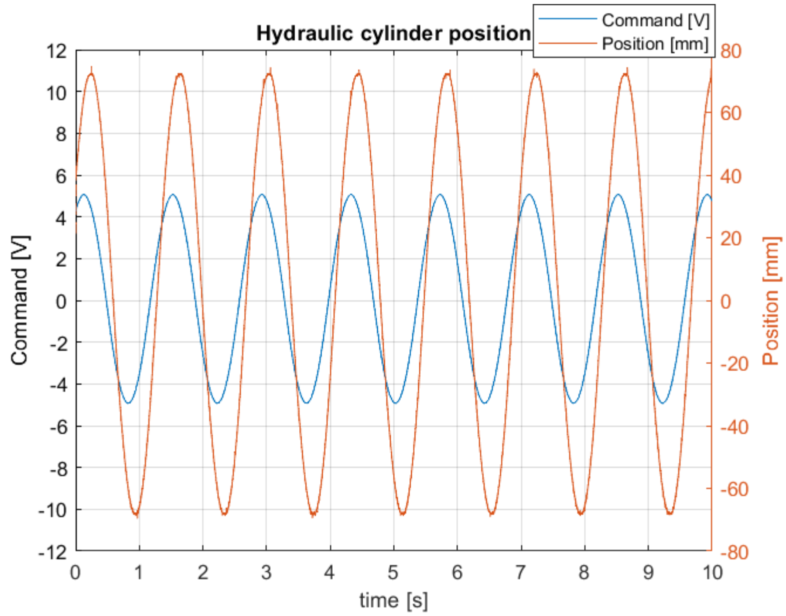


*a) 5 bar load*

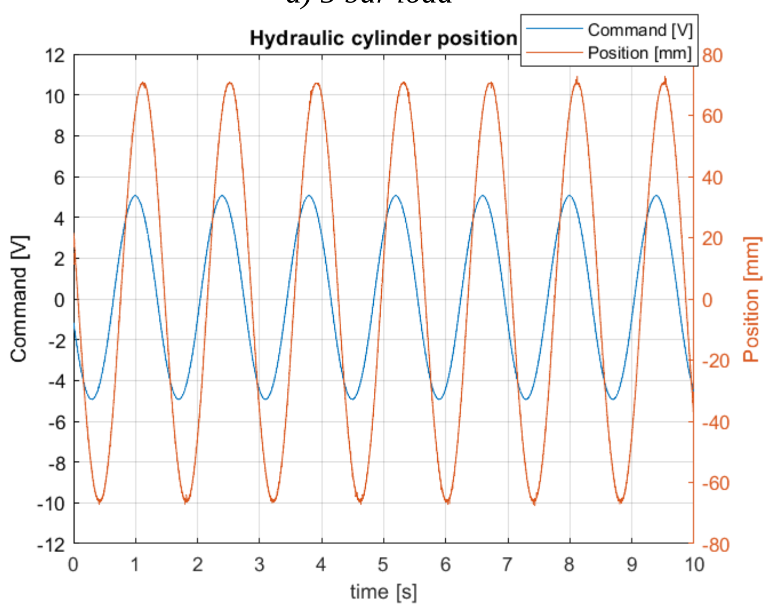


*b) 30 bar load*

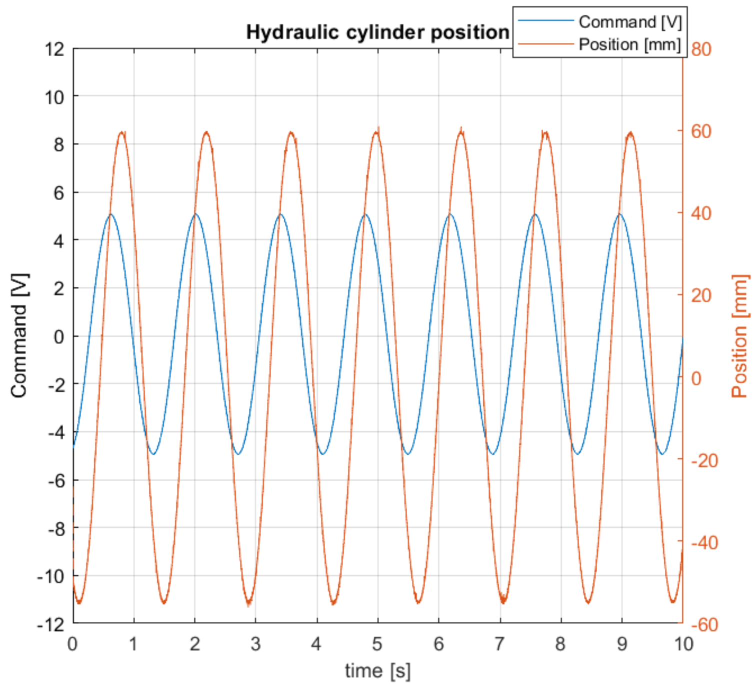


*b) 70 bar load*

*Fig.136. The variation command signal of 5V vs position with different loads*

$$TF_{5V5bar0.75Hz} = \frac{1.112 \cdot 10^5}{s^3 + 8.769 \cdot s^2 + 816.4 \cdot s + 7159} \tag{107}$$

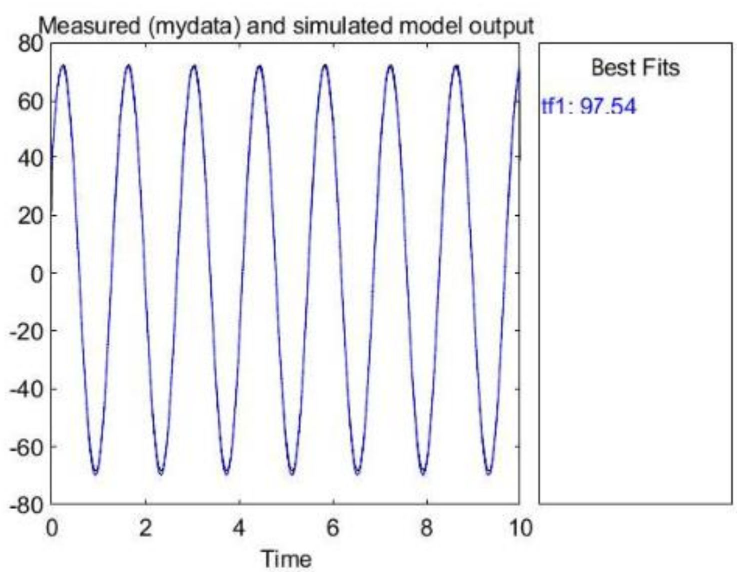


Fig.137.a. The transfer functions TF fit at command signal of 5V with 5 bar load

$$TF_{5V30bar0.75Hz} = \frac{5.87 \cdot 10^{6}}{s^{4} + 75.88 \cdot s^{3} + 2659 \cdot s^{2} + 5.001 \cdot 10^{4} \cdot s + 4.199 \cdot 10^{5}} \qquad (108)$$

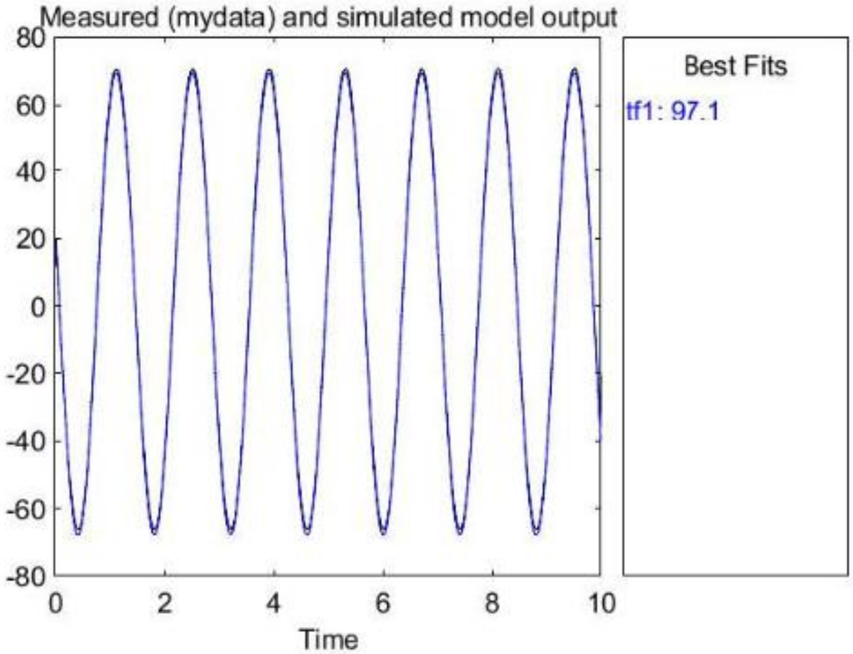


*Fig.138.b. The transfer functions TF fit at command signal of 5V with 30 bar load*

$$TF_{5V70bar0.75Hz} = \frac{1.817 \cdot 10^{4}}{s^{3} + 4.493 \cdot s^{2} + 268.4 \cdot 10^{4} \cdot s + 1206} \qquad (109)$$

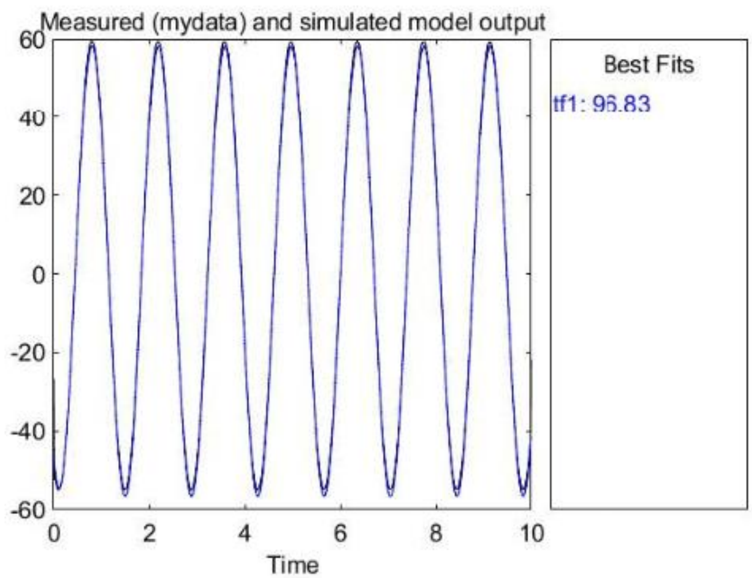


*Fig.139.c. The transfer functions TF fit at command signal of 5V with 70 bar load*

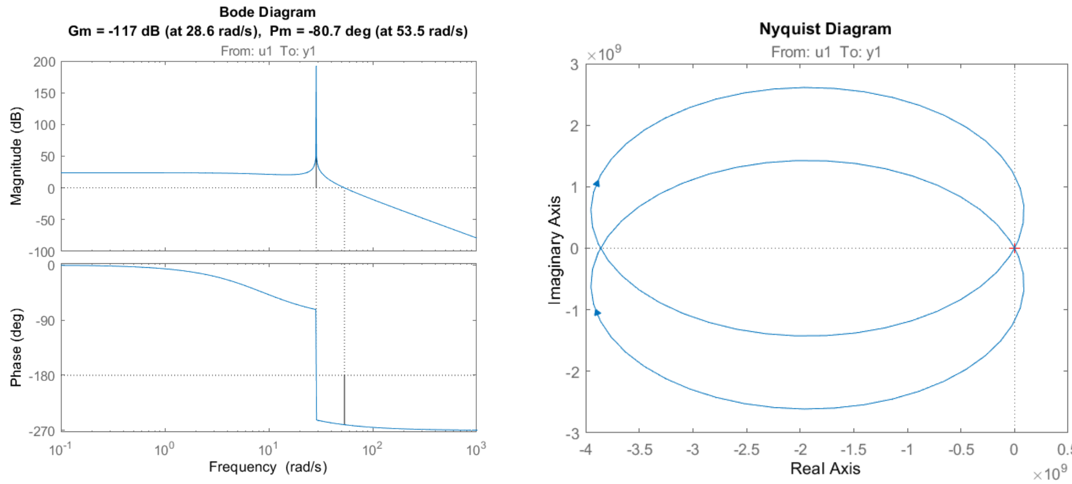


*a) 5 bar load*

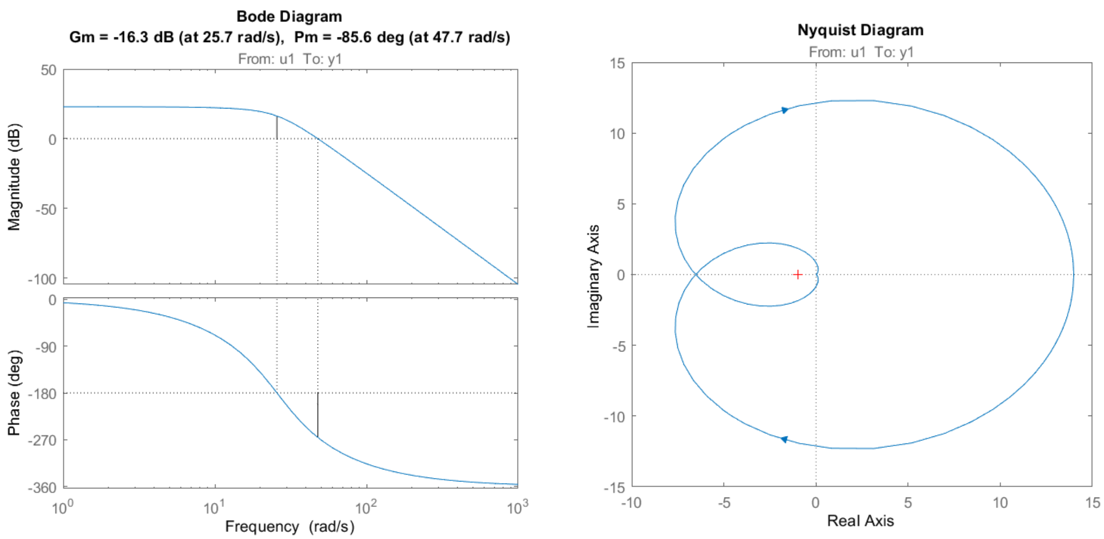


*b) 30 bar load*

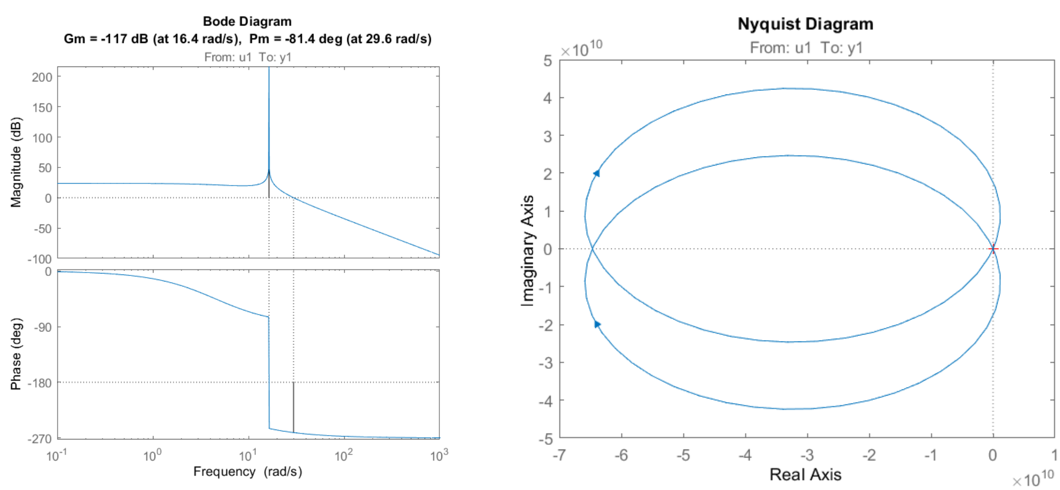


*b) 70 bar load*

*Fig.140. The Margin and Nyquist plots of the transfer functions at 5V amplitude of the input signal and a frequency of 0.75 Hz with different loads*

### *II.3.3. 10V amplitude on command signal*

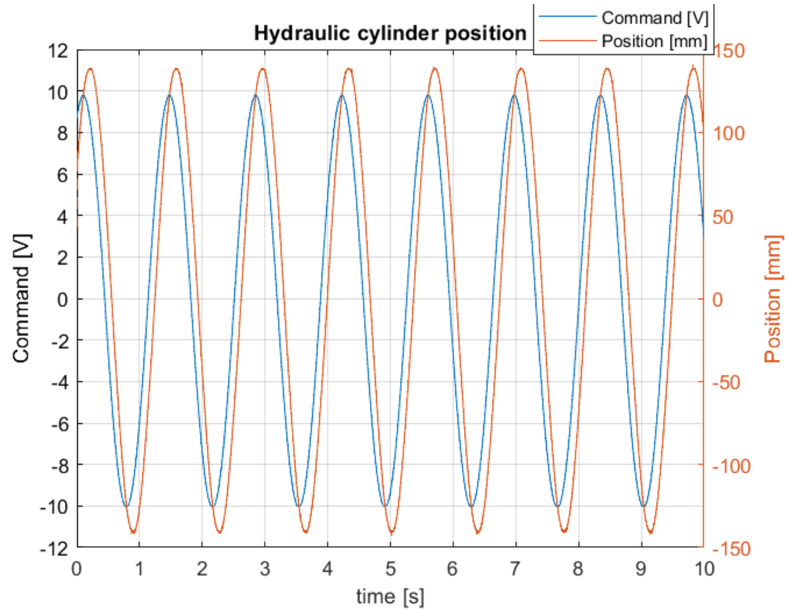


*a) 5 bar load*

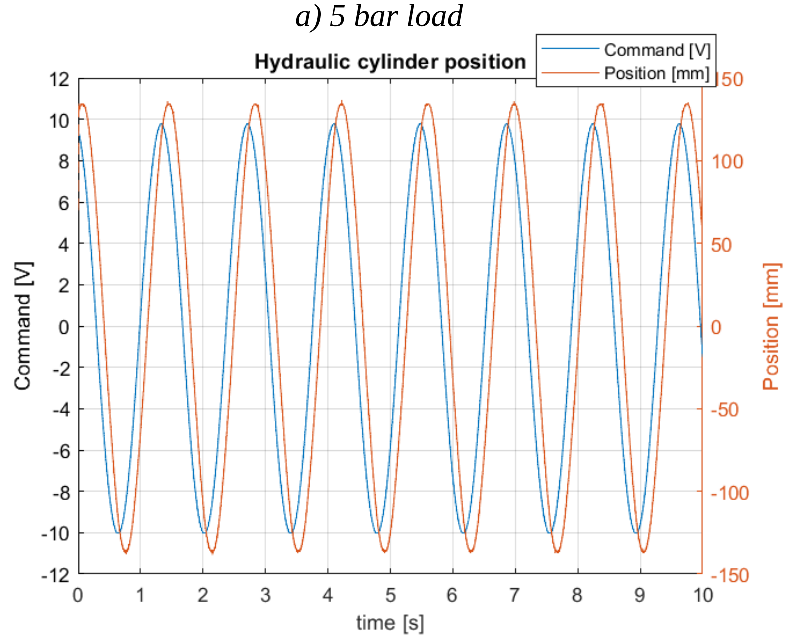


*b) 30 bar load*

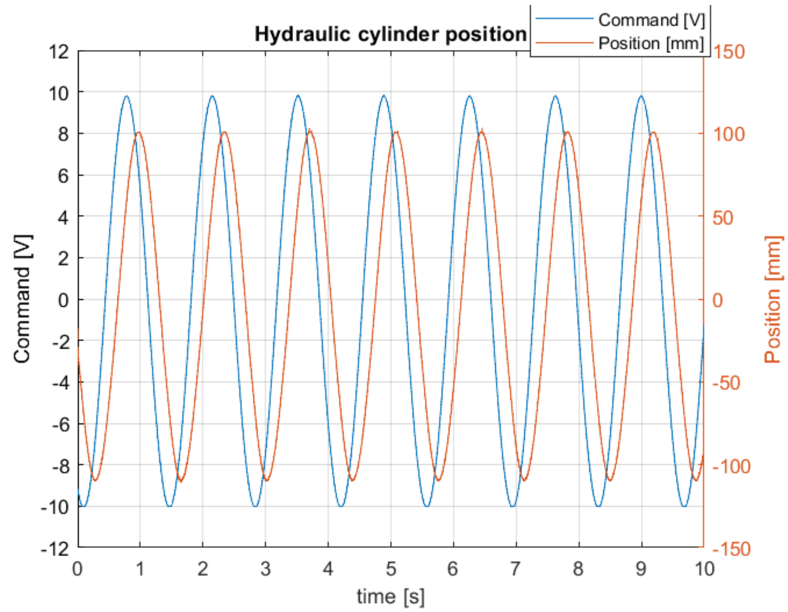


*b) 70 bar load*

*Fig.141. The variation command signal of 10V vs position with different loads*

$$TF_{10V5bar0.75Hz} = \frac{-264.7}{s^4 + 0.1627 \cdot s^3 + 24.31 \cdot s^2 + 1.694 \cdot s + 54.42} \quad (107)$$

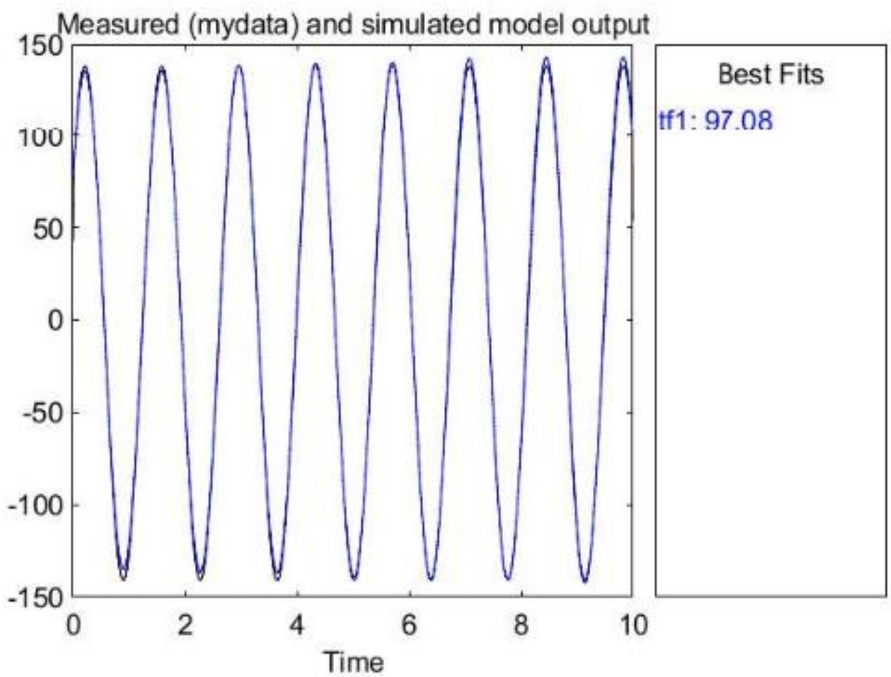


Fig.142.a. The transfer functions TF fit at command signal of 10V with 5 bar load

$$TF_{10V30bar0.75Hz} = \frac{5.905 \cdot 10^4}{s^4 + 3.665 \cdot s^3 + 234.1 \cdot s^2 + 584.6 \cdot s + 8099} \tag{108}$$

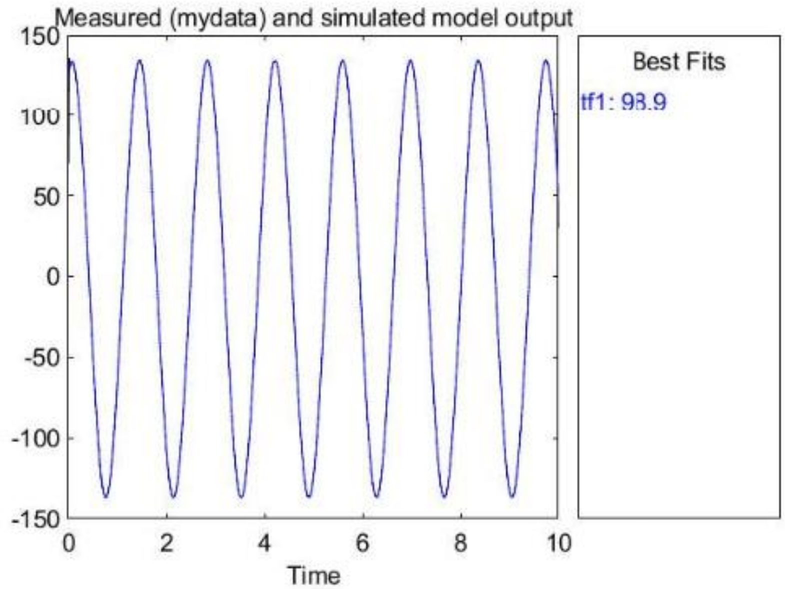


*Fig.142.b. The transfer functions TF fit at command signal of 10V with 30 bar load*

$$TF_{10V70bar0.75Hz} = \frac{-116.9}{s^4 + 0.9334 \cdot s^3 + 24.05 \cdot s^2 + 18.35 \cdot s + 56.16} \tag{109}$$

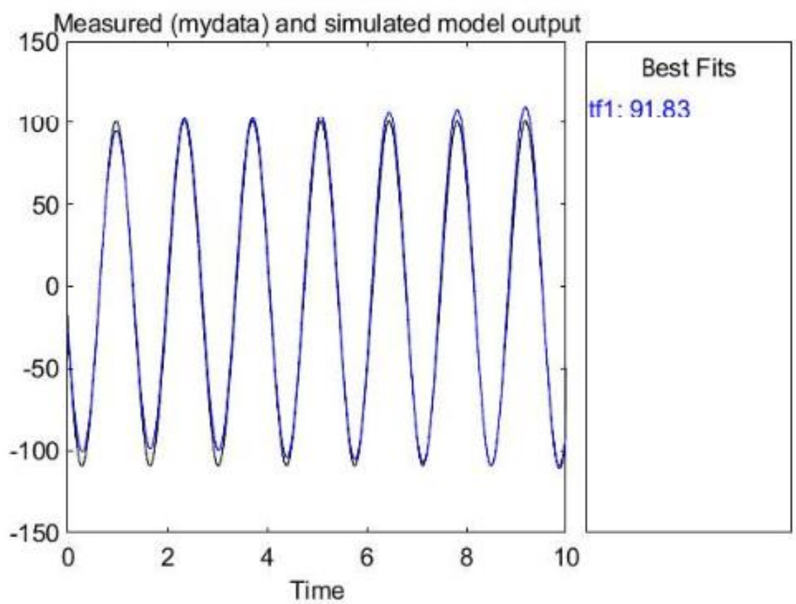


*Fig.142.c. The transfer functions TF fit at command signal of 10V with 70 bar load*

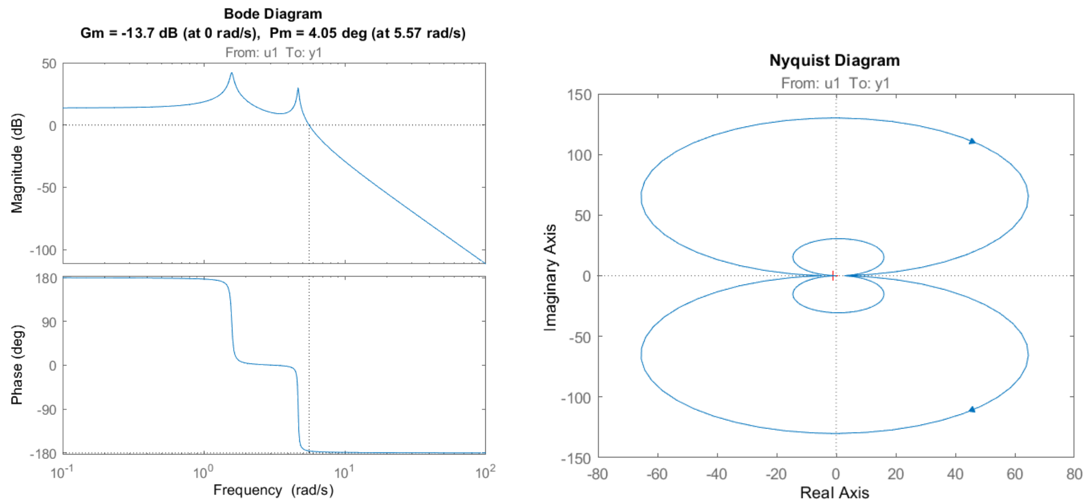


*a) 5 bar load*

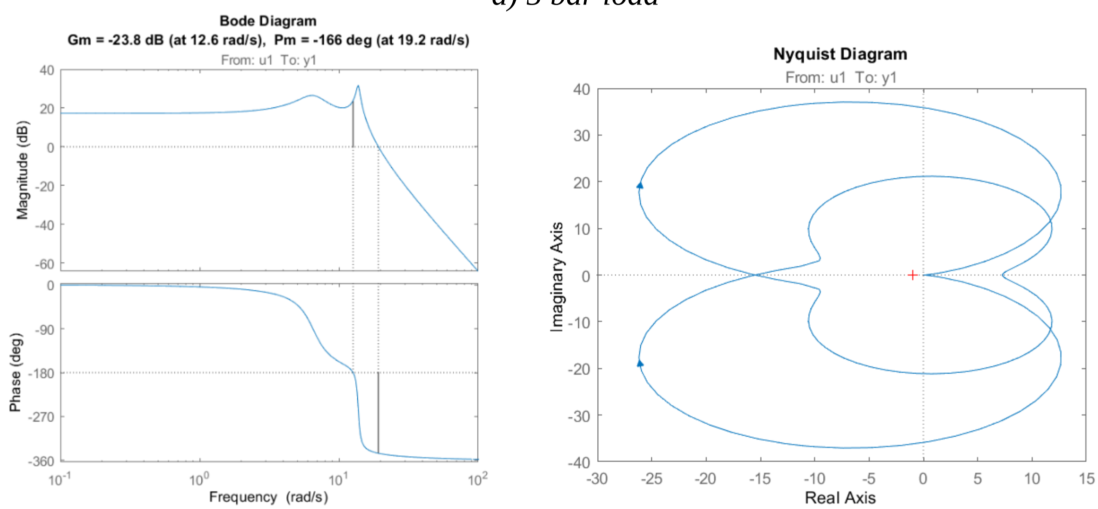


*b) 30 bar load*

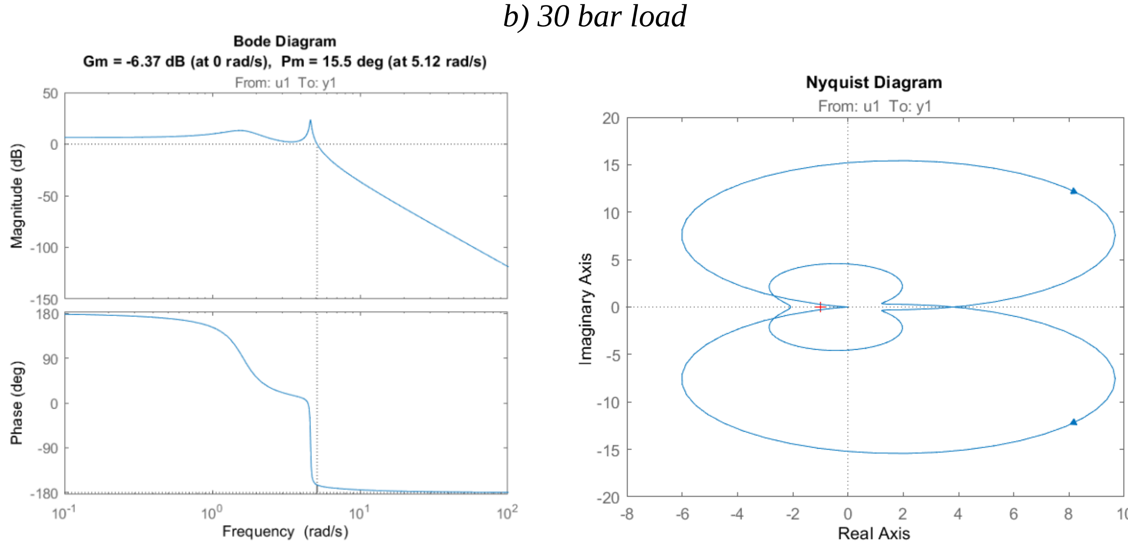


*b) 70 bar load*

*Fig.143. The Margin and Nyquist plots of the transfer functions at 10V amplitude of the input signal and a frequency of 0.75 Hz with different loads*

## II.4. Conclusions

The most valid dynamic characteristics of the industrial systems in operation are obtained experimentally. In general, these systems have various resistances, delays and nonlinear functions, therefore the analytical determination of their dynamic properties according to physical and constructive data is complicated.

As part of the experimental determination of the dynamic properties of the object subject to automation, are analyzed the character of the transient regime, or of the permanent one that appears as a result of the application of deterministic signals to the system input.

The frequency characteristics of the analyzed system are determined according to the variation curves of the input and output quantities.

Based on the two electro-hydraulic components in section II.2, it was proposed a mathematical model, obtaining a transfer function with 4 poles and 0 zeros.

In our research, in order to determine the dynamic characteristics of the wind turbine blade pitch system, there were used sinusoidal periodic signals of determined frequency, having as input the servo-valve command (V) and as output the position of the actuating cylinder (mm).

There were studied 3 reference frequencies 0.45, 0.6 and 0.75 Hz with 3 amplitudes on the servo-valve input command 2 V (20% of maximum input signal), 5V (50% of maximum input signal) and 10V (100% of maximum input signal).

Analyzing the variation of the cylinder position with the load it can be seen that at high loads, at all studied frequencies and amplitudes, the actuating cylinder stroke is affected, it moves less with the load increase, observing that at 30 bar load the actual system follows precisely the input command.

Based on the measured data there were obtained 27 transfer functions using MATLAB System Identification tool, all with fit over 85% and most of them over 93%.

Most of the transfer functions (TF) obtained were with 4 poles and 0 zeros, which confirms that the proposed mathematical (analytical) model can be used as reference when experimental dynamic identification is not possible.

The Bode and Nyquist plots of each transfer functions permit the analysis and study of the dynamic behavior of the system.

The hydraulic system used in this paper replicates with remarkable fidelity the operational characteristics of the blade pitching systems currently used in industrial wind turbines, considering also the variable load on it, performed through the loading system. The loading system is also protected against cavitation occurrence through a pressurized system composed of a feeding pump and a check valve system.

## II.5. The design and setup of the Hydraulic equipment testing stand

In 2021 I was a member of the team led by Prof. Dr. Ing. Ilare Bordeașu, where I was responsible for the design and setup of the hydraulic stand for testing the hydraulic equipment.

The concept of the stand was done by the team from "Politehnica" University of Timisoara together with INOE Bucharest, who has also produced it. The stand was placed in the The Hydraulic Machines "Aurel Barglazan" Laboratory of the Mechanical Faculty.

This testing stand can be used to test almost all components of a hydraulic drive system: pumps, rotary hydraulic motors, linear hydraulic motors and various devices (pressure valves, directional valves, proportional equipment, etc.). The stand's equipment allows for the following tests, trials, and verifications: static functional tests of didactic nature within the "Hydraulic Drives" discipline in the curriculum of technical universities, dynamic tests for researching components in the structure of hydraulic drive systems, functional checks (type or batch tests) of hydraulic devices and components at the request of economic agents. The stand can also be used for practical training at any level (workers, technicians, engineers) of people specializing and/or improving in the field of hydraulic drives.

*Fig.144. The Hydraulic equipment testing stand*

## Chapter III. Professional and academic career development plan

*The secret of excellence is the continuous development in both directions, teaching and research.*

Based on the experience gained in these past years since I defended my Ph.D. Thesis, as university teacher, as researcher and as hydraulic equipment design engineer, I am very confident that I can bring significative contributions in the field of turbomachinery, wind and water turbines, hydraulic pumps, hydraulic drives, leading the future PhD. theses with great significance in the domain of mechanical engineering.

In my teaching activity, I will be directly concerned with the continuous optimization of the quality of the educational act. Improving the quality of education will follow the permanent updating of the quality of the teaching materials.

The training of very high-quality engineers, who will have the opportunity to work in industry and beyond, will be my main priority. In this way, I will maintain a close connection with the specialized companies from the country and from abroad, which require well-trained engineers, trying to follow as many of their requirements as possible through the subjects taught.

The analytical programs of the subjects that I will teach will be continuously compared with those from other universities from the country and from abroad.

The bibliography recommended to students will be constantly updated.

I will use modern teaching aids and I will approach interesting ways of presenting the subject, which will capture the attention and arouse the interest of the students.

The concern for cultivating a positive relationship between the teaching staff and the students promotes the pedagogy of creativity in the learning process, so that the students are also prepared for future research activities.

The role that I intend to have in the relationship with the students will be, in addition to that of information provider, of counselor and guide.

Communication will be open, empathetic, based on trust and mutual respect.

I will continue to offer support to students in carrying out research projects, personal development, diploma theses and dissertations and why not PhD theses.

I will also be involved in the design of the new test stands, that can be used in both didactics and research.

I will also try to create international collaborations with prestigious universities and laboratories from abroad that act in the same domain of activity proposing different studies and research grants that could be done together.

I will also launch applications of new research projects/grants in the field of hydraulic and pneumatic drives that are commonly used in almost all engineering domains.

I will also continue to be involved in projects that arise with the industry, where I will try to attract students in order to provide the best possible professional training for the current market demand in the engineering field.
Regarding my publicist activity I will continue to write new highly quoted papers where I will present my current and future research.
My main focus when I am habilitated will be to work with PhD. students interested in the domain of hydraulics that I will lead, counsel and guide, professionally within both industrial and academic research, resulting in high quality PhD. theses.

## References

[1]. https://www.nov.com/products/pipe-handling-systems
[2]. https://www.nov.com/products/top-drive-systems
[3]. https://www.frigstadgroup.com/files/5035-fel-z-sa10-0001_-_rev_01_ _d90_mid_water_he_%28n%29_-_final_-_printed_file.pdf
[4]. https://www.youtube.com/watch?v=n-VctbPFpAc
[5]. https://vimeo.com/411579968
[6]. M Bărglăzan, E. Dobândă, T. Miloş, D. C. Stroiţă, *Theoretical Investigations of Temperature Variation in Torque Converters Operating with Two-Phase Flow,* 3rd International Conference on Energy and Enviroment 22-23 November 2007, ISSN 1454-234x, Bucharest, Romania.
[7]. M. Bărglăzan, E. Dobanda, Adriana Manea, C. Velescu, D. C. Stroiţă, *Experimental results of temperature variation in torque converters operating with two-phase flow,* CIEM 2007, Universitatea Politehnica Bucuresti, Sci. Bull. Series C, vol 69, nr. 4, 2007, ISSN 1454-234x.
[8]. Manea, AS; Dobanda, E; Barglazan, M; Stroita, DC, *Two-Phase Flow In Hydrodynamic Torque Converter*, Proceedings of The 20th International DAAAM Symposium, DAAAM Int Vienna, 1726-9679, 2009;
[9]. Stroita Daniel Catalin, Adriana Sida Manea, *Frequency modelling and dynamic identification of cross-flow water turbines*, Thermal Science 26 (2 Part C), 1665-1674.
[10]. Stroita Daniel Catalin, Adriana Sida Manea, Anghel Cernescu, *Blade Polymeric Material Study Of A Cross-Flow Water Turbine Runner*, Materiale plastice / ISSN 2537-5741 ISSN-L 0025-5289, Vol. 56(2), pag(366-369), 2019.
[11]. Tokar, D; Stroita, C; Tokar, A; Rusen, A, *Hybrid System that Integrates the Lost Energy Recovery on the Water-Water Heat Pump Exhaust Circuit*, IOP Conference Series-Materials Science and Engineering/4TH WORLD MULTIDISCIPLINARY CIVIL ENGINEERING-ARCHITECTURE-URBAN PLANNING SYMPOSIUM - WMCAUS/1757-8981, 2019.
[12]. Tanasa C., Stuparu A., Stroita C.,Popescu C.,Susan-Resiga R., *3D numerical analysis of pulsating water jet in the draft tube cone of hydraulic machinery,* AIP Conference Proceedings, Volume 2186, Article number 1800002, 2019.
[13]. M. Bărglăzan, I. Bordeaşu, M Popoviciu, V. Bălăşoiu,l L. Mădăras, C. Stroiţă, *Improving the reliability of a guide vane actuating mechanism for bulb – type units*, Conferinţa Hervex 2009 ediţia a XVII-a Râmnicu Vâlcea, ISSN 1454-8003, pag 97-103;
[14]. M. Gafitanu, s.a.: *Organe de Masini vol I*, Ed. Tehnicã,Bucuresti, 1999, p.191
[15]. C. Severineanu, *Organe de Masini*, Ed. Didactica si Pedagogica, Bucuresti, 1965, p.159;

[16]. Gh. Manea: Organe de Masini, Vol I, Ed. Tehnica, Bucuresti, 1970, p. 355
[17]. N. N. Kovalev: Ghidroturbini, Masghiz, Moskva, 1961, p. 224
[18]. Teodor Milos, Eugen Dobanda, Adriana Manea, Rodica Badarau, Daniel Stroita, *The Automatic Adjustment of The Optimum Operating Point Depending on the Requirements of The Water Supply Using an Intelligent Pump*, Scientific Bulletin of the "Politehnica" University of Timisoara, Romania, Transaction on Mechanics, Special Issue ISSN 124-6077, Tom 53(67), The International Conference on Hydraulic Machinery and Equipments, Timisoara, October 16-17, 2008, Romania, pag. 247-252
[19]. Miloş T., Dobândă E., Manea A., Bădărău R., Stroiţă D., *Computational Graph Theory for Find out Optimal Routes of Pipeline Supply*, IEEE International Joint Conferences on Computational Cybernetics and Technical Informatics ICCC-CONTI 2010, IEEE Catalog Number CFP10575-CDR, ISBN 978-1-4244-7431-8, 27-29 may 2010, Timisoara, Romania, pg,577-580, 2010.
[20]. Miloş T., Bărglăzan M., Dobândă E., Manea A., Bădărău R., Stroiţă D, *Optimal Routes of Pipeline Supply Using the Bellman-Kalaba Algorithm,* The International Conference on Design, Technologies & Management in Manufactoring, Iaşi, May 14th – 16th 2010. Published in Buletinul Institutului Politehnic din Iaşi, publicat de Universitatea Tehnică „Gheorghe Asachi" din Iaşi, Tomul LVI (LX), Fasc. 2, Secţia Construcţii de Maşini, ISSN 1011-2855, pag. 205-213 (9 pag.)
[21]. Miloş T., Bej, A., Dobândă E., Manea A., Bădărău R., Stroiţă D., *Blade Design using CAD Technique for Small Power Wind Turbine*, IEEE International Joint Conferences on Computational Cybernetics and Technical Informatics ICCC-CONTI 2010, IEEE Catalog Number CFP10575-CDR, ISBN 978-1-4244-7431-8, 27-29 May 2010, Timisoara, Romania, pg,571-575, 2010.
[22].Teodor Miloş, Francisc Gyulai, Eugen Dobândă, Adriana Manea, Rodica Bădărău, Daniel Stroiţă, *Wind power set of small powers for the emplacement with moderate wind, the international scientific conference design,* TECHNOLOGY AND MANAGEMENT IN MANUFACTURING, "D.T.M.M. - 2010", IASI, 14th – 16th MAY 2010, R O M A N I A, Buletinul Institutului Politehnic Iaşi, Tomul LVI, (LX), Fasc. 2b, ppg. 133-140.
[23]. Adriana Sida Manea, Daniel Catalin Stroita, Ilare Bordeasu, Cristian Ghera, Alexandru Nicolae Luca, *Air-Dynamic Measurements on "S" Shape Hydrofoils, KOD 2024.*
[24]. Manea A. S., Muntean S., Stroiță D.C., *Analitycal approach and numerical methodology validated against experimental data on S shape airfoil for wide flow angles of attack*, Proceedings of the Romanian Academy Series A - Mathematics Physics Technical Sciences Information Science/1454-9069, Vol 21/2, 2020.

[25]. Adriana Sida Manea, Dobândă Eugen, Daniel Cătălin Stroiţă, *Wind Tubine For Individual Sites, Energetika 2011, pag. 184-187, List Saveza energeticara, Broj 2/ Godina XIII, Mart 2011, UDC 620.9, ISSN br. 0354-8651.*

[26]. Mircea BĂRGLĂZAN, Teodor MILOŞ, Analytical models for characteristic curves of wind turbines, *WSEAS Intern. Conferences Timisoara, Romania, October 21-23, 2010, ISBN 978-960-474-237-0, ppg. 298-300.*

[27]. Ilare BORDEASU, Brandusa GHIBAN, Cristian GHERA, Cornelia Laura SALCIANU, Lavinia Madalina MICU, Daniel Catalin STROITA, Mihai Alin DEMIAN, Andreea Daniela BUZATU, *The effect of hardening obtained after tig remelting on the resistance of the 7075 alloy structure to cavitation erosion, UNIVERSITY POLITEHNICA OF BUCHAREST SCIENTIFIC BULLETIN, SERIES B-CHEMISTRY AND MATERIALS SCIENCE, 2025.*

[28]. Ilare Bordeasu, Cristian Ghera, Alexandru-Nicolae Luca, Adriana-Sida Manea, Daniel-Catalin Stroita, Cornelia Laura Salcianu, Brandusa Ghiban, Lavinia Madalina Micu, *Investigation of Cavitation Resistance of Biocompatible Zinc Based Alloys for Biomedical Applications, KOD 2024.*

[29]. Ilare Bordeasu, Cristian Ghera, Dionisie Istrate, Laura Sălcianu, Branduşa Ghiban, Dumitru Viorel Băzăvan, Lavinia Mădălina Micu, Daniel-Cătălin Stroiţă, Alexandra Suta, Ileana Tomoiagă, Alexandru Nicolae Luca, *Resistance and Behavior to Cavitation Erosion of Semi-Finished Aluminum Alloy 5083*, Hidraulica, Numărul 4, Pagini 17-24, 2021.

[30]. Dionisie Istrate, Cristian Ghera, Laura Sălcianu, Ilare BORDEAȘU, Brândușa GHIBAN, Dumitru Viorel Băzăvan, Lavinia Mădălina Micu, Daniel-Cătălin STROIȚĂ, Daniel Ostoia, *Heat Treatment Influence of Alloy 5083 on Cavitational Erosion Resistance,* Hidraulica, Numărul 3, Pagini 15-25, 2021.

[31]. Alexandru Nicolae Luca, Ilare Bordeasu, Brânduşa Ghiban, Cristian Ghera, Dionisie Istrate, Daniel-Cătălin Stroiţă, *Modification of the Cavitation Resistance by Hardening Heat Treatment at 450 C Followed by Artificial Aging at 180 C of the Aluminum Alloy 5083 Compared to the State of Cast Semi-Finished Product,* Hidraulica, Numărul 1, Pagini 39-45, 2022.

[32]. Cristian Ghera, Iosif Lazăr, Daniela Alexa, Ilare Bordeaşu, Nicușor Alin Sîrbu, Daniel Ostoia, Mihai Hluscu, Cornelia Laura Salcianu, Daniel Catalin Stroita, Dumitru Viorel Bazavan, Marcela Sava, Lavinia Madalina Micu, *New Results Regarding the Cavitation Destruction Behavior of Heat-Treated CuZn39Pb3 Brass with Different Parameters,* Advanced Materials Research, Vol. 1172, Pages 1-8, Editor Trans Tech Publications Ltd, 2022.

[33]. Daniel Cătălin Stroiță, Identificarea dinamică a turbinelor cu dublu flux, teză de doctorat, Ed. Politehnica, Timișoara, 2009.

[34]. DC Stroita, D Bordeasu, F Dragan, System Identification of a Servo-Valve Controlled Hydraulic Cylinder Operating Under Variable Load, Mathematics 13 (3), 341.
[35]. Carroll, J.; McDonald, A.; McMillan, D. Failure rate, repair time and unscheduled O&M cost analysis of offshore wind turbines.
Wind Energy 2016, 19, 1107–1119.
[36]. https://www.hidraulica-ph.ro/produse/pmrd/detalii/assets/carcat_prd.pdf
[37].https://static.mercateo.com/93/986f0946fb5c4a09a9ec8ea992d97080/pdf/boschrexroth-re50076.pdf?v=1
[38].https://static.mercateo.com/08/986f0946fb5c4a09a9ec8ea992d97080/pdf/boschrexroth-re29932.pdf?v=16
[39].https://store.boschrexroth.com/Hydraulics/Valves/Directionalvalves/Directional-servo-valves/SERVO-DIRECTIONAL VALVE_R900772317?cclcl=en_US
[40]. https://www.kanflu.com/assets/PDFs/CDT3-CYLINDERS.pdf
[41].https://aesensors.nl/assets/uploads/2015/07/AEsensors_LDVT_02_Economy.pdf
[42]. https://masautomazione.it/wp-content/uploads/2015/04/lvdt-catalogo.pdf
[43]. https://www.lorenz-messtechnik.de/pdfdatbl/f/080815c_k-25_en.pdf
[44]. https://www.kanflu.com/assets/PDFs/CHECK-VALVE-S-RE20375logo.pdf
[45]. https://docs.rs-online.com/778c/0900766b80061997.pdf
[46]. http://orangetech.com.tn/wp-content/uploads/2013/12/pi-ho-ftu-omni rt_e1.pdf
[47].https://www.kanflu.com/assets/PDFs/PRESSURE-RELIEF-DB-and-DBW-10-32-PILOT-OPERATED-RE25802.pdf
[48]. https://download.tek.com/manual/070836204.pdf
[49]. https://files.digilent.com/datasheets/DT9800-Series-Datasheet.pdf
[50]. Balasoiu, V.; Cristian, I.; Bordeasu, I., Echipamente si Sisteme Hidraulice de Actionare si Automatizare; Editura Orizonturi Universitare Timisoara, Romania, 2008; Volume 2, pp. 480–483.
[51]. Merritt, H.E. Hydraulic Control Systems;Wiley: Hoboken, NJ, USA; JohnWiley & Sons, Inc: New York, NY, USA, 1991; pp. 212–216.
[52]. https://www.mathworks.com/help/control/ref/dynamicsystem.margin.html
[53]. https://en.wikipedia.org/wiki/Nyquist_stability_criterion